Numerical quantification of barite reservoir scaling and the resulting injectivity loss in geothermal systems

Morgan Alan Tranter

Kumulative Dissertation

zur Erlangung des akademischen Grades
“doctor rerum naturalium” (Dr. rer. nat.)
in der Wissenschaftsdisziplin “Hydrogeologie”

eingereicht an der
Mathematisch-Naturwissenschaftlichen Fakultät
Institut für Geowissenschaften
der Universität Potsdam

Date of defense: 29.06.2022

Potsdam, 2022

To Eva

Gutachter

Prof. Dr. Michael Kühn
Deutsches GeoForschungsZentrum GFZ
Department Geochemie
Sektion Fluidsystemmodellierung
und
Universität Potsdam
Mathematisch-Naturwissenschaftliche Fakultät
Institut für Geowissenschaften

Prof. Dr. Traugott Scheytt
Technische Universität Bergakademie Freiberg
Fakultät für Geowissenschaften, Geotechnik und Bergbau
Institut für Geologie
Lehrstuhl für Hydrogeologie und Hydrochemie

Prof. Dr. Sergey Churakov
Paul Scherrer Institute
Nuclear Energy and Safety Research Division
Laboratory for Waste Management

Published online on the
Publication Server of the University of Potsdam:
https://doi.org/10.25932/publishup-56113
https://nbn-resolving.org/urn:nbn:de:kobv:517-opus4-561139

Abstract

Our understanding of the role of greenhouse gas emissions on climate change has issued us to change course in advancing energy technologies away from fossil fuels towards alternatives. Deep geothermal energy is one such alternative with promising features, such as low-carbon emissions, base-load capability, untapped potential in many areas of the world, and long-lasting thermal reserves. The common principle of a deep geothermal power plant with two wells is to produce hot fluids from the subsurface on one side, extract the heat above ground, and re-inject the cooled water into the reservoir on the other side. In Germany, the widespread adoption of this technology is still hampered in spite of the thermal potential it has in selected areas. This can be traced back to unresolved challenges revolving around finding risk of high hydraulic yields and temperature anomalies as well as specific operational demands for a long-term deployment.

Here, the issue of barite reservoir scaling and the according deterioration of hydraulic rock properties is addressed. Barite precipitation is thermodynamically favoured within the cold side of a geothermal power plant due to its prograde solubility. Furthermore, there are no viable counter-measures available to remove barite once it has formed as it is low-soluble and acid-resistant. Its formation in the reservoir over time is hypothesised to be a main obstacle for maintaining high efficiency and could even be responsible for a shutdown. However, direct field measurements are not feasible, thus, hydro-geochemical models are essential to quantify and predict the effects of precipitates on the reservoir's permeability.

In this thesis, the relevant precipitation processes of barite reservoir scaling and their impact on the effective hydraulic rock properties are investigated with numerical and analytical reactive transport simulations. The fractured-porous reservoirs of the German geothermal regions North German Basin (NGB) and Upper Rhine Graben (URG) are considered here for calculations. At various sites of both respective regions, barite has been observed to be a major contributor to scale formation within the system. The aim of this thesis, is to identify the decisive hydro-geochemical and reservoir-characteristic parameters in this context as well as to quantify the potentially induced injectivity loss for the investigated regions. Furthermore, the objectives include developing a screening method for readily approximating the specific reservoir scaling risk, which can aid in their early identification for exploration and operational purposes.

Precipitation can be generally subdivided into two relevant steps: nucleation and crystal growth. While pristine barite in the reservoir provides the base reactive surface area for crystal growth, nucleation may introduce additional growth locations. Therefore nucleation is an inherent risk for geothermal systems as it enhances and facilitates precipitation. Yet, there exists a specific threshold supersaturation, dependent on temperature and fluid content, below which nucleation is effectively inhibited. The presented geochemical models using thermodynamics and classical nucleation theory show that it is not a rate-determining step for the investigated reservoirs with depths between 2000 m and 3000 m, i. e., Landau and Neustadt-Glewe, since barite saturation ever stays below this threshold. Conversely, for deeper utilised reservoirs, e. g., Groß Schönebeck (> 4000 m), the modelled saturation is high enough so that nucleation becomes relevant, increasing the overall risk of reservoir scaling.

The results of the conducted reservoir simulations with precipitation kinetics show that the impact of reservoir scaling on injectivity is mostly determined by the total precipitation amount and the subsurface

distribution. The main driving force for precipitation is the temperature difference between reservoir and injection, but it is also influenced by the fluid's ionic strength and the barium to sulfate ratio. These three effects are positively correlated with depth, resulting in higher precipitation potential and thus generally higher risk for deeper reservoirs. A higher kinetic rate results in scales forming closer to the well, increasing the impact of scales on injectivity loss logarithmically. The enhancing effect of higher ionic strengths on the precipitation rate is especially noteworthy in the context of the investigated sites. The injection flow rate controls the range of scaling influence around the well and the overall substance input, thus it principally accelerates the related injectivity loss.

Fractures are preferential flow paths in the subsurface and therefore influence the subsurface scaling distribution. Simulation results of fractured reservoirs show that the larger the fracture aperture, the more it will extend the scaling reach and cause precipitates to spread away from the well. Accordingly, if there are active fractures present crossing the well section, the scaling impact on injectivity will be mitigated compared to purely porous reservoirs. However, it is emphasised that fractures with lower apertures experience more permeability loss compared to larger ones due to their higher specific reactive surface area. Thus, a fractured reservoir with larger fracture apertures is considered to the most robust regarding injectivity loss due to scaling.

The investigated sites in the NGB and the URG regions both reach similar depth-dependent precipitation potentials for barite (2.8–20.2 g/m^3 fluid). Yet, the conducted reservoir simulations give evidence that injectivity loss due to barite scaling is significant in the NGB (1.8%–6.4% injectivity loss per year) and can affect the longevity of the plant, especially for deeper reservoirs (3000 m). In contrast, the results of the URG sites do not indicate a significant role of barite ($< 0.1\%$–1.2% injectivity loss per year). The crucial differences are the reservoir thickness and existence of fractures as well as the ionic strength. The URG generally exhibits fractured-porous reservoirs with comparably higher thicknesses, which spread scale formation and mitigate the impairing effect. Furthermore, the ionic strengths are higher in the NGB, increasing the precipitation rate and thus skewing scales more towards the well.

A workflow for quick risk approximation related to reservoir scaling is established by combining the discovered parameter relationships into an analytical scaling score. The major advantage is its practicability compared to cumbersome reservoir-scale numerical models, which can both take a lot of time to set up and to carry out. By calibration with numerical reservoir simulation results, it can provide a quick and accurate estimate of the induced injectivity loss over time. It is an ideal tool for plant operators and decision makers, especially intended for an initial stage of site investigation when reservoir parameters are uncertain. Thus, it can find a broad application in geothermal engineering, e. g., in search of potential plant sites and estimation of long-term efficiency.

Zusammenfassung

Aufgrund der tragenden Rolle der Treibhausgasemissionen für den globalen Klimawandel ist die Entwicklung von alternativen, nicht-fossilen Energietechnologien essenziell. Die Tiefengeothermie stellt eine solche Alternative dar, welche vielversprechende Eigenschaften wie eine geringe Kohlenstoffemission, eine hohe Grundlastfähigkeit, lang anhaltende thermische Reserven sowie ein großes ungenutztes Potenzial in vielen Gebieten der Welt bietet. Das Prinzip einer geothermischen Anlage beruht auf dem Ansatz, dass heiße Fluide mit tief reichenden Bohrungen aus dem Untergrund gefördert, oberirdisch Wärme entzogen und das Wasser erneut in das Reservoir eingespeist wird. In Deutschland findet diese Technologie trotz des vielversprechenden thermischen Potenzials noch immer keine breite Anwendung. Dies ist vorrangig auf das Fündigkeitsrisiko von hydraulischen Ergiebigkeiten und Temperaturanomalien sowie hochspezifische betriebliche Anforderungen zurückzuführen, welche für einen langfristigen Betrieb unabdingbar sind.

Die vorliegende Arbeit befasst sich mit Barytausfällungen (im Folgenden auch *Scales* genannt) innerhalb geothermaler Reservoire und der damit verbundenen Verschlechterung der hydraulischen Gesteinseigenschaften. Eine Fällung ist aufgrund der prograden Löslichkeit von Baryt auf der kalten Seite eines Geothermiekraftwerks thermodynamisch begünstigt. Wenn sich Präzipitate gebildet haben, gibt es keine wirtschaftlich sinnvollen Gegenmaßnahmen, um diese zu entfernen, da Baryt schwer löslich und säurebeständig ist. Es wird angenommen, dass Scales im Reservoir ein Haupthindernis für die Aufrechterhaltung einer hohen Effizienz darstellt, was im Extremfall zur Aufgabe des Anlagenbetriebs führen kann. Da direkte Feldmessungen der Akkumulationen im Reservoir nicht möglich sind, ist die Entwicklung hydrogeochemischer Modelle unerlässlich, um die Auswirkungen von Ausfällungen auf die Durchlässigkeit des Reservoirs zu quantifizieren und vorherzusagen.

In dieser Arbeit werden die relevanten Fällungsprozesse von Baryt innerhalb des Reservoirs sowie die Auswirkungen derselben auf die hydraulischen Gesteinseigenschaften mittels numerischer und analytischer reaktiver Transportsimulationen untersucht. Für die Berechnungen werden die klüftig-porösen Reservoire der deutschen Geothermieregionen Norddeutsches Becken (NDB) und Oberrheingraben (ORG) betrachtet. An beiden Standorten wurde beobachtet, dass Baryt ein wesentlicher Bestandteil der auftretenden Scales ist. Ziel der vorliegenden Arbeit ist es, die in diesem Zusammenhang wesentlichen hydro-geochemischen und technischen Parameter zu identifizieren sowie den induzierten Injektivitätsverlust für die untersuchten Regionen zu quantifizieren. Darüber hinaus wurde eine Screening-Methode entwickelt, mit der das Risiko von Fällungen innerhalb des Reservoirs einer geothermalen Anlage begleitend zur Exploration oder im Betrieb umgehend quantifiziert werden kann.

Fällung kann im Allgemeinen in die zwei relevanten Schritte Nukleation und Kristallwachstum unterteilt werden. Während natürlich vorkommender Baryt im Reservoir bereits reaktive Oberfläche für Kristallwachstum bietet, kann diese durch Nukleation erhöht werden. Dies wiederum beschleunigt das Kristallwachstum, sodass Nukleation ein inhärentes Risiko für die Geothermie darstellt. Es gibt jedoch einen bestimmten temperatur- und lösungsinhaltabhängigen Sättigungsschwellenwert eines Minerals, unterhalb dessen Nukleation gehemmt ist. Die vorgelegten geochemischen Modelle unter Verwendung der Thermodynamik und der klassischen Nukleationstheorie zeigen, dass Nukleation bei den untersuchten Standorten Landau und Neustadt-Glewe mit Teufen zwischen 2000 m und 3000 m kein

relevanter Prozess ist, da die Barytsättigung stets unterhalb dieser Schwelle bleibt. Hingegen überschreitet die modellierte Sättigung diese Schwelle bei tiefer gelegene Lagerstätten, z.B. Groß Schönebeck (> 4000 m), sodass Nukleation stattfinden kann und das Gesamtrisiko durch Präzipitate im Reservoir erhöht ist.

Die Ergebnisse der durchgeführten Reservoirsimulationen mit berücksichtigter Fällungskinetik zeigen, dass die Auswirkung der Scales auf die Injektivität hauptsächlich durch die Gesamtfällungsmenge und derer Verteilung im Untergrund bestimmt wird. Der maßgebliche Faktor für die Fällung ist der Temperaturunterschied zwischen der warmen und der kalten Seite, aber sie wird auch durch die Ionenstärke und das Barium-Sulfat-Verhältnis beeinflusst. Diese drei Effekte sind positiv mit der Tiefe korreliert, sodass tiefere Reservoire allgemein ein höheres Fällungsrisiko aufweisen. Eine höhere kinetische Rate führt dazu, dass sich Scales näher am Bohrloch bilden, wodurch die Auswirkungen der Scales auf den Verlust der Injektivität logarithmisch zunehmen. Die verstärkende Wirkung höherer Ionenstärken auf die Fällungsrate ist im Zusammenhang mit den untersuchten Standorten besonders hervorzuheben. Die Injektionsrate steuert den radialen Einflussbereich der Scales um den Brunnen sowie den gesamten Stoffeintrag, und ist damit grundsätzlich positiv mit dem verbundenen Injektivitätsverlust korreliert.

Klüfte sind präferenzielle Fließwege im Untergrund und beeinflussen daher die Verteilung der Ablagerungen im Untergrund. Die vorgestellten Simulationsergebnisse für geklüftete Reservoir zeigen, dass sich die Scales umso weiter vom Bohrloch weg ausbreiten, je größer die Kluftöffnungen sind. Daher fällt die Auswirkung der Fällungen auf die Injektivität im Vergleich zu rein porösen Reservoiren geringer aus, wenn hydraulisch aktive Risse den Bohrlochabschnitt durchqueren. Risse mit kleineren Öffnungen weisen allerdings aufgrund ihrer größeren spezifischen reaktiven Oberfläche einen vergleichsweise größeren Permeabilitätsverlust auf. Geklüftete Reservoire mit großen Kluftöffnungen werden in Bezug auf Injektionsverluste durch Scales als am robustesten eingestuft und sollten für neue Projekte bevorzugt werden.

Für beide untersuchte Regionen konnte ein ähnliches, tiefenabhängiges Fällungspotenzial bestimmt werden ($2,8$–$20,2$ g/m^3 Fluid). Die durchgeführten Reservoirsimulationen zeigen jedoch, dass der Injektivitätsverlust aufgrund von Barytablagerungen im NDB erheblich ist ($1,8\%$–$6,4\%$ Injektivitätsverlust pro Jahr) und die Langlebigkeit der Anlage dadurch beeinträchtigt wird; dies gilt insbesondere für tiefere Reservoire (3000 m). Im Gegensatz dazu deuten die Simulationen der ORG-Standorte auf eine untergeordnete Rolle von Baryt hin ($< 0,1\%$–$1,2\%$ Injektivitätsverlust pro Jahr). Die entscheidenden Unterschiede zwischen den untersuchten Regionen sind die Reservoirmächtigkeiten und das Vorhandensein von Rissen im Gestein sowie die Ionenstärke der Fluide. Der ORG weist in der Regel klüftig-poröse Reservoire mit deutlich höheren Mächtigkeiten auf, was zu einer größeren Verteilung der Präzipitate im Untergrund führt. Weiterhin sind die Ionenstärken im NDB höher, was die Barytausfällungen wiederum stärker in Richtung des Bohrlochs verschiebt.

Durch die Zusammenführung der ermittelten Parameterbeziehungen zu einem analytischen Scaling-Score konnte ein Workflow für eine schnelle Risikoabschätzung im Zusammenhang mit Barytausfällungen in Reservoiren entwickelt werden. Der Hauptvorteil liegt in der Praxistauglichkeit im Vergleich zu aufwändigen numerischen Reservoirsimulationen, deren Erstellung und Durchführung viel Zeit in Anspruch nehmen kann. Nach einer Kalibrierung mit Simulationsergebnissen kann eine schnelle Schätzung des induzierten Injektivitätsverlustes über die Zeit vorgenommen werden. Es ist ein ideales Werkzeug für Anlagenbetreiber und Entscheidungsträger, insbesondere in der Anfangsphase der Standortuntersuchung, wenn die Reservoirparameter nur unsicher bestimmt sind. Somit kann insbesondere der Scaling-Score eine breite Anwendung innerhalb der Geothermie finden, z.B. bei der Suche nach potenziellen Anlagenstandorten und der Abschätzung der langfristigen Effizienz.

Acknowledgements

My biggest thank-you goes to my PhD supervisor Prof. Dr. Michael Kühn who put great faith in me from the beginning on of our cooperation and provided endless support throughout my studies. Particularly, he gave me all the space I needed to let my scientific endeavours run freely, but knew exactly when to pluck me off of the several dead-end pursuits and put me back on track. I would not be here at this stage without him. I am also very grateful to Prof. Dr. Traugott Scheytt and Prof. Dr. Sergey Churakov for accepting to review this work. Thank you to Maria, Christian, and Eva for proofreading parts of my dissertation.

I am very lucky to have been given the opportunity to work in the fluid systems modelling group of the GFZ. My gratitude goes to all former and present colleagues of our group, which have made the environment so pleasant and lively. My special thanks go to Dr. Marco De Lucia for always having an open door for me and for the many hours of fruitful discussions we had, which taught me a great deal. I would like to thank Dr.-Ing. Thomas Kempka, whose input I always valued highly, for believing in me and for providing the support I needed. Thank you, Dr. Maria Wetzel, for being a sunshine at work, and especially for your time and effort, which is much appreciated. I also want to thank my other PhD-fellows, Svenja Steding, Theresa Hennig, Zhen Li; we went through a lot of this together, but always had each other's backs. My gratitude goes to Benjamin Nakaten for introducing me to the command line. And, of course, to Jenny Meistring for keeping everything together.

This study was supported financially by the Federal Ministry for Economics and Energy of Germany (BMWi, grant no. 0324244C, project *ReSalt*) for which I am thankful for. My thanks go to all the researchers involved in *ReSalt* for their support, the instructive discussions in several meetings, and for sharing their scientific progress. Here, I would like to emphasise my thanks that go to Prof. Dr. Jürgen Schreuer, Philip Zuber, Dr. Guido Blöcher and Dr. Christian Kluge for their in-depth scientific exchange. Many thanks also to other co-workers of the GFZ Geoenergy department for sharing their expertise with me: Prof. Dr. Ingo Sass, Dr. Simona Regenspurg, Dr. Harald Milsch, and Anna Jentsch. Special thanks also to Dr. Markus Wolfgramm for his advice and contributions that significantly improved this work.

Above all, I want to thank my wife, Eva, for she has been a pillar of endless support and understanding. There is no chance this work would have been possible without her. I am indebted to my family for always being there for me during all these years. And, last but not least, my deepest gratitude to my friends and golems, who were always capable of brightening my day, making me laugh and picking me up during the occasional grim times.

Contents

List of Figures

List of Tables

CHAPTER 1

Introduction

1.1 Overview of geothermal energy utilisation

Escaping the fossil-fuel-dependency to reduce greenhouse gas emissions is one of the greatest challenges of our time. Global warming and its consequences are evident based on innumerable observations of most different aspects: global temperature rise, ocean warming, shrinking ice sheets, and an increase in extreme events, to name a few (IPCC 2021). The search for alternative energy sources and their technological development has become a race against increasing CO_2-concentrations in the atmosphere and draws heavily on classic concepts such as the utilisation of water, wind, and solar energy. Even immature or risky technologies, which arguably include nuclear energy (IAEA 2016), are under consideration as alternatives to coal and gas, despite their known risks, catastrophic incidences in history, and unresolved plans for waste disposal (Taebi and Roeser 2015); a reflection of a smouldering emergency. Our future energy market will be a product of complex interplay between climate-politics, economics, technology, social acceptance, and risk management (in no particular order). It is therefore crucial to put efforts into investigating and advancing all possible alternatives to ultimately find objectively the best solution for us and our earth.

Geothermal energy has an appealing position among low-emission energy sources in many aspects: it is base-load capable, takes up comparatively little space above surface, and is renewable to a certain extent (Bromley et al. 2010). It has untapped potential to further contribute to mitigating climate change, therefore it is of substantial interest to advance this technology. Geothermal energy is generally referred to as the energy stored in the earth's interior, in part as accretion heat (30%), as well as newly created through radioactive decay (70%) (Dickson and Fanelli 2013). The use of this energy source by man is illustrated in Cataldi et al. (1999), according to which indirect use has been taking place for several thousand years; on an industrial scale for almost 200 years. Today, geothermal energy is used in many regions of the world to provide thermal (direct use) and less often also electrical energy.

An additional incentive for deep geothermal energy lies in the fact that deep fluids are typically enriched in certain elements (Sanjuan et al. 2016; Stober et al. 2013; Wolfgramm et al. 2011b), which may become worthwhile extracting as a by-product (leach mining). While the idea is not new (Duyvesteyn 1992; Hano et al. 1992), the recent rapid price increase of Lithium as a consequence of the demand for more batteries (Martin et al. 2017), e. g., for electrical vehicles, has made it economically interesting (Li et al. 2018). Also, copper (Regenspurg et al. 2010) and rare earth elements (Smith et al. 2017) leaching from geothermal brines has been alluded to, but are both not economically viable at the current price state.

Direct use of geothermal energy is widespread globally and exists on many scales (Lund and Toth n.d.). The most common are small-sized, decentralised geothermal heat pumps (Fig. 1.1) used for heating and cooling of residential units and offices with about 60% of the total installed capacity (Lund and Toth n.d.). For this, either shallow open-hole wells or down-hole heat exchangers are employed; well depths are usually less than 100 m. In contrast, (centralised) deep geothermal energy utilises wells of

great depths > 400 m, sometimes even 2 000 m and more (Agemar et al. 2014), for district and space heating (Bloomquist 2003). If geothermal fluids are used directly as the heat carrier, the system is referred to as hydrothermal. In contrast, a petrothermal system exploits hot, low permeable rock by using it as a heat exchanger. Permeability enhancements are frequently needed in this case, thus it is also termed an Enhanced Geothermal System (EGS). A doublet is the most popular technical setup: water is pumped above ground with a production well, heat is extracted, and finally the cooled fluid is re-injected via an injection well due to waste management and aquifer recharge (Agemar et al. 2014; Dickson and Fanelli 2013). This approach has been tested and applied extensively with success (Dickson and Fanelli 2013; Stober and Bucher 2014).

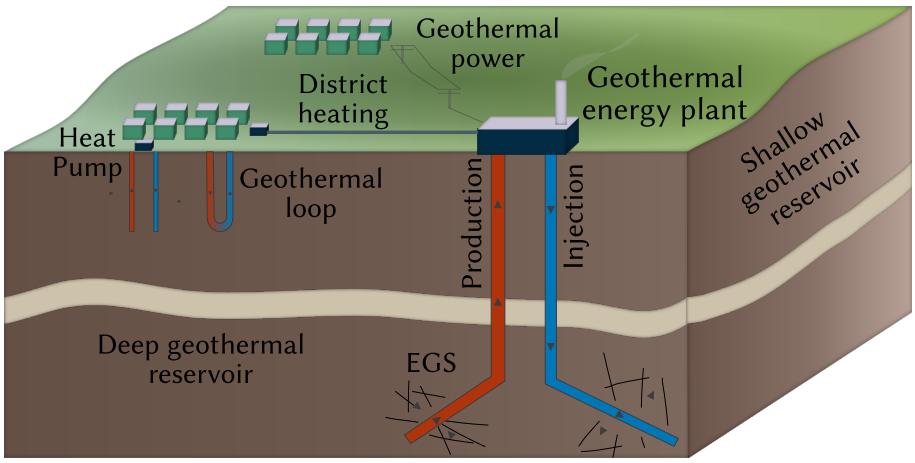

Figure 1.1: Geothermal energy is a low-emission alternative to fossil-fuels, has a comparably small area footprint, and is base-load capable. The most common setup for deep geothermal energy is a doublet (injection and production well). Low permeable, tight rock can be stimulated to activate flow paths for circulation, also referred to as Enhanced Geothermal Systems (EGS).

Geothermal power generation through dry-steam or flash steam cycles require comparatively high fluid temperatures (T) to achieve economic efficiencies (Chamorro et al. 2012). Reservoirs with corresponding down-hole $T > 200$ °C are called high-enthalpy reservoirs, in contrast to low-enthalpy reservoirs with $T < 200$ °C (Stober and Bucher 2014). However, binary plants with technologies using secondary working fluids with Organic Rankine (ORC) or Kalina cycle techniques enable power generation from as little as 100 °C, though at lower efficiencies (Heberle et al. 2016; Paschen et al. 2003); other sources even give a minimum value of 115 °C (Weber et al. 2016). Fluids must also be accessible at economically affordable depths, i. e., where favourable, geological conditions cause a high geothermal gradient (T increase with depth). It is often volcanically and tectonically active regions where these temperatures can be found. It stands to reason, that countries such as the United States, Indonesia, Philippines, and Mexico are among the world's largest producers. Most electrical energy from geothermal in Europe is produced in Turkey (1 549 MW_e), Italy (916 MW_e), and Iceland (755 MW_e) (Huttrer 2020), which are coincidentally known for elevated seismic activity (Grünthal et al. 2013).

While direct use of geothermal heat has become economically competitive in Germany (1.62% of the residential heat demand), geothermal energy currently plays only a minor role in electricity production (BMWi 2019). With an installed capacity of only 43 MW_e, it lags behind other nations in comparison (Huttrer 2020). This is primarily due to the moderately high geothermal gradient of 32 K/km, on average, which makes development economically-technologically challenging (Agemar et al. 2012). Accordingly, a mean borehole depth of 3 125 m is needed to reach at least 100 °C, though the drilling costs would outweigh the revenue at current energy prices in this case. Nevertheless, the German Federal Environment Agency has projected that geothermal electricity generation could increase more than a hundredfold by 2050 (from about 0.4 TWh/yr to 50 TWh/yr) if technological development makes tapping the available resources feasible (Umweltbundesamt UBA 2010). Despite there having

been recent advances in conceptualising power generation with ORC to be more efficient, even at these lower temperatures (Eyerer et al. 2020a; Eyerer et al. 2020b), the discovery of subsurface temperature anomalies through geophysical exploration and modelling has become a crucial step for success in this field (Birner et al. 2012; Przybycin et al. 2017).

In an official statement, the German institute for applied geophysics (LIAG) stresses that, in order to cover the renewable energy demand by 2050, heavily expanding use of geothermal energy is essential (Agemar et al. 2018). There are three main regions in Germany with known temperature anomalies: the North German Basin (NGB), along the Upper Rhine Graben (URG), and in the Molasse Basin (MB), where higher geothermal gradients of 40–50 K/km have been measured, locally even up to 100 K/km (Agemar et al. 2012). Almost exclusively, all currently running geothermal district heating and power plants in Germany are located there (Weber et al. 2016), indicating that temperature anomalies are vital for an economical utilisation. In the last decade, especially the region around Munich (in the MB region) has experienced rapid development of geothermal projects with six newly commissioned locations with an average installed capacity of about 5 MW_e, each (Dussel et al. 2016; Weber et al. 2016). The Upper Jurassic carbonate rock aquifer of the north Alpine foreland basin exhibits high permeabilities (Birner et al. 2012) and holds low mineralised fluids (Stober et al. 2013), which makes it an excellent target for geothermal utilisation. Besides the thermal potential, however, there also other demands that need to bet met, e. g., sufficient hydraulic yields and assurance for long-lasting operation. To also successfully tap the large geothermal potential in the other regions, further efforts in advancing reservoir engineering technologies and resolving operational issues are mandatory to ensure sufficient flow rates in the long-term.

1.2 Current challenges for geothermics in Germany

The success of a geothermal project is foremost measured in terms of the power that can be extracted from the subsurface, so the amount of energy that can be transferred per unit of time. This is determined by the fluid temperature and the flow rate, which accordingly are the prime parameters considered during prospection of geothermal reservoirs (Schumacher et al. 2020; Stober and Bucher 2014). The current challenges faced by geothermal plant operators today are to ensure sufficiently high flow rates and to overcome occurring productivity and injectivity loss.

In order to achieve these goals, the enhancement of tight rock and fault zones is currently being investigated (Blöcher et al. 2019; Kluge et al. 2021; Zimmermann et al. 2010). EGS aims at utilising rock formations with low, initial permeabilities for deep geothermal energy. Related rock formations with high thermal potential, but low matrix porosity, could be technically modified to yield the necessary rock permeability by re-activating natural fractures or generating new preferential flow paths. Pilot projects such as Groß-Schönebeck in the NGB (Zimmermann et al. 2010), as well as Landau in the URG (Schindler et al. 2010) have shown that it is principally possible to enhance fracture permeability, at least temporarily. If EGS becomes commercially viable, the use of suitable target formations from the Permian in Germany for power generation would be conceivable.

Another key component for success is the longevity of a plant's efficiency. A geothermal plant is usually conceptualised with a total life-time of at least 30 years (Karlsdottir et al. 2020), whereas the break-even point until any profit is made can be decades into continuous operation. However, there are many sources that can compromise the regular operation. (1) The down-hole temperature of the production well will drop over time because the injected cold water reaches the production well at some point (thermal breakthrough) as a consequence of the heat resources being consumed faster than they are recharged (Li et al. 2016). (2) Rock permeability decreases over time, which can be due to mechanical, thermal, or chemical reasons (Blöcher et al. 2016). (3) Plant components corrode or are affected by mineral scale formation, thus need restoration or even replacement at some point. Consequentially, either production/injection pressure must be varied, or the flow rate will go down. All these aspects

need to be taken into account during the design of a geothermal plant, for which model predictions are an essential component.

As an exemplary case, for which unforeseen issues dramatically impacted the longevity, we will consider the geothermal power plant Neustadt-Glewe (NG) in the NGB. The intermediate temperature anomalies in the NGB are vast, and hydrothermal reservoirs in depths up to around 2 500 m are often sufficiently permeable, porous aquifers (Mesozoic sandstones) with abundant groundwater circulation (Franz et al. 2018a,b). Thus, it holds a lot of potential for hydro-geothermal development and is a promising resource for district heating from this perspective. NG was the first plant in Germany to produce electrical power from geothermal energy, starting in 2004 with a capacity of about 0.45 MW_e (Paschen et al. 2003). A major challenge for operation, however, is the high mineralisation (> 200 g/L) of the local basinal fluids (Wolfgramm et al. 2011b). They are highly corrosive brines, and are prone to cause mineral scale formation in the technical system, pipes, and reservoir. Consequentially, technical elements needed replacing more frequently, and rock permeability declined over time (Birner et al. 2015; Wolfgramm et al. 2009, 2011a). All counter-measures that were applied were unsuccessful in mitigating the consequences sufficiently and lastingly (Wolfgramm et al. 2012, 2009). Based on this and related experience (Blöcher et al. 2016; Regenspurg et al. 2015), deep geothermal energy in the NGB appears to be only conditionally feasible until these issues are addressed. An in-depth understanding of the potential fluid-rock interactions and occurring scale formations in direct consequence of the geothermal exploitation is crucial and could help to mitigate these related issues.

1.3 Mineral scale formation in geothermal systems

Mineral scale formation is a known key issue of geothermal energy production around the globe (e. g., Brehme et al. 2018; Demir et al. 2014; Valdez et al. 2009; van den Heuvel et al. 2018; Wolfgramm et al. 2011a; Zarrouk et al. 2014). Many chemical reaction mechanisms and minerals have been observed, which all have the potential to reduce the efficiency of the system to some degree. The severity and the scaling type mainly depend on the fluid chemistry, the temperature, and pore pressure within the reservoir as well as their respective change within the system. Moreover, fluid interaction with technical material and microbially induced reactions have been observed to facilitate scaling (e. g., Regenspurg et al. 2015). The respective conditions can vary significantly from site to site, e. g., host rock composition, reservoir temperature, fluid origin and composition (Wolfgramm 2002). The prediction of scale formation requires a detailed determination of these parameters and reliable geochemical models, preferably before operation begins so that this can be taken into account.

There are different scale formation types in geothermal systems which can be categorised into (Wolfgramm et al. 2011a): (1) thermodynamically, (2) electrochemically, and (3) microbially mediated mechanisms. For instance, sulphides, hydroxides, and heavy-metals are attributed to microbial activity and electrochemical processes (Regenspurg et al. 2015; Wolfgramm et al. 2011a). The other main group of scales comprises carbonates, sulfates, and silicates, which are mostly related to changes in temperature and pressure within the system causing a thermodynamic disequilibrium. Fluid temperature reduction happens due to heat conduction through pipes, and foremost the deliberate heat extraction above ground in the heat exchanger. Thus, minerals with a prograde solubility, i. e., solubility increases with temperature, have the tendency to precipitate, provided the fluid is initially in thermodynamic equilibrium with the respective mineral in the host rock (Fig. 1.2). For example, massive halite scale formation in the borehole was observed at the Groß Buchholz site (NGB), presumably because the hydrothermal fluid was pristinely well saturated with NaCl and the temperature reduction during the uplift caused supersaturation (Hesshaus et al. 2013). Temperature reduction is among the most common causes for scaling in both low- and high-enthalpy systems.

Prograde-solubility related barite precipitation is one of the most prevalent scale formation minerals in low-enthalpy systems, where geothermal fluids are saline brines, i. e., > 100 g/L mineralisation (Wolfgramm et al. 2011a). Related scale formation in the pipework and in the system above ground are a

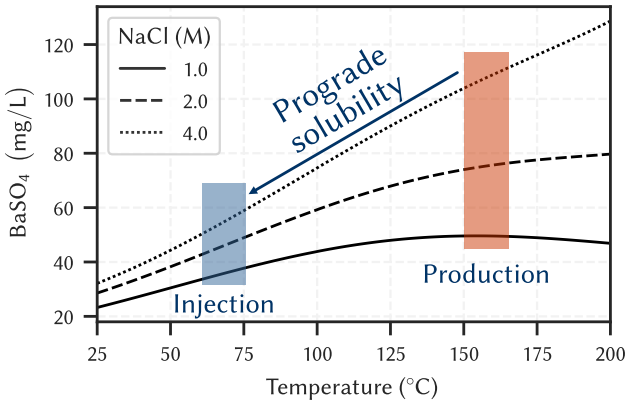

Figure 1.2: Solubility of barite in NaCl-solution increases with temperature (prograde) and ionic strength. The difference in solubility between the production and injection temperature corresponds to the precipitation potential, i. e., the maximum amount that can precipitate if thermodynamic equilibrium is assumed. For example, decreasing the temperature from 150 °C down to 60 °C of a 4 M-NaCl solution initially in equilibrium with barite results in a precipitation potential of around 103 mg/L − 52 mg/L = 51 mg per litre of fluid. Calculations were done with PHREEQC v3.7 (Parkhurst and Appelo 2013) and the `pitzer.dat` database.

well-known issue. For instance, Regenspurg et al. (2015) report barite-rich scale accumulation in the boreholes (sedimented at the bottom or grown on the casing) and in the particle filters/sieves at the Groß Schönebeck site (NGB). Barite scales were also verified in the surface system and the injection well of the Soultz-sous-Forêts site (URG) (Nitschke et al. 2014; Scheiber et al. 2013), and at Landau and Insheim (both URG) (Wolfgramm 2020). A further noteworthy site, where significant barite scale formation happened, is Neustadt-Glewe (Birner et al. 2015; Wolfgramm et al. 2012). In this instance, the formation of sparsely soluble minerals in the reservoir at the injection location, i. e., barite and sulphides, has been made accountable for the continuous injectivity decline over the years of operation (Birner et al. 2015).

Many geothermal sites are affected by declining injectivity over time (Birner et al. 2015; Blöcher et al. 2016), which may be attributed to mineral scaling in the reservoir. It has significant consequences for a plant's efficiency, depending on where the formation happens within the system. If the heat exchanger is covered with scales, this acts as an insulator and the capacity is impaired (fouling). If pipes are clogged, the flow-through diameter is reduced. Both cases are cost-intensive because the elements need to be either refurbished or replaced more regularly. However, there are strong indications for scale formation taking place also in the reservoir near the cool-water-injection location (reservoir scaling), although the explicit detection is inherently difficult. For example, barite scales have been detected in the surface equipment and in the injection well itself at various geothermal sites (Birner et al. 2015; Scheiber et al. 2013), so it must be assumed that to some extent scaling occurs also in the reservoir. Injectivity declines have been reported for other sites as well (Blöcher et al. 2016; Griffiths et al. 2016; Scheiber et al. 2013), but the causes have not been verified, yet.

Barite scale formation is particularly problematic due to the following reasons:

- Barite has the tendency to incorporate radionuclides into its crystal lattice, e. g., Ra, thus it must be handled accordingly as naturally occurring radioactive material (Degering et al. 2011; Sanjuan et al. 2016).
- Once precipitated, barite cannot be removed at reasonable technical and financial cost because of its low solubility, even at low pH, making acid-treatment unfeasible (Birner et al. 2015; Wolfgramm et al. 2011a).
- Barite is kinetically inhibited within the pipework system (Canic et al. 2011; Kaufmann-Knoke 1992; Kühn et al. 1997; Wolfgramm et al. 2011c), thus precipitation is delayed until the fluids reach the reservoir leading to reservoir scaling.

- Barite scale formation in the reservoir at the injection location can lead to substantial permeability loss of the reservoir and therefore injectivity loss.

One prevailing scientific question is to what extent barite scale formation is responsible for irreversible injectivity loss in low-enthalpy geothermal systems. The conceptual mechanism is that continuous accumulation of barite in the fracture-, pore-, and fissure-network of a geothermal reservoir leads to a microstructural change of the host rock, impairing the hydraulic properties over time. This may have severe consequences for geothermal plant operations, as it affects injectivity and potentially flow rate. As described above, it is inherently difficult to prove this with field-work alone because there are currently no tools available to monitor scale formations in the reservoir. In contrast, models could provide evidence whether barite plays a role on this account, and may be applied as a tool of practical importance for evaluating future geothermal sites in this regard. The development of geochemical and reactive transport models are therefore imperative for a reliable quantification and forecasting of occurring mineral scalings. If reservoir scaling were predictable and controllable, one major factor for achieving sustainable plant operation would be accounted for.

1.4 Thesis objectives

The overarching objective of this thesis is to develop and apply models for quantifying precipitation reactions in geothermal reservoirs, improving the prediction of permeability development in fractured-sedimentary rock reservoirs, and taking specific reservoir-chemical and temperature/pressure conditions into account. This was subdivided into the following key objectives:

- Evaluate the relevance of the individual precipitation steps leading to barite scaling in fractured and porous media, and establish approaches to map these into models.
- Assess parameter sensitivities in this regard for geothermal systems.
- Develop methods to transfer laboratory scale considerations to the reservoir scale.
- Quantify injectivity loss due to barite reservoir scaling for pertinent geothermal sites in the German geothermal regions North German Basin and Upper Rhine Graben.
- Develop readily accessible screening methods for geothermal plant operators and decision makers to quantify reservoir scaling risk.

1.5 Chapter summary and scientific contribution

1.5.1 Scientific publications

This cumulative doctoral thesis is composed of four articles published in peer-reviewed international journals, and an additional theoretical chapter. The thesis is finalised with a comprehensive discussion concerning the thesis objectives and concluded with the main findings. In all articles, I, as first author, designed and performed the research as well as analysed the data and illustrated the simulation results. Further, I was responsible for the manuscript preparation and revision. My co-author Michael Kühn supervised my related scientific activities, and contributed to the conceptualisation of the studies and the revision of the manuscripts. Marco De Lucia contributed as co-author of all articles to the methodological model development and the revision of the manuscripts. Markus Wolfgramm provided practical insights into geothermal plant operation contributing to one publication (Tranter et al. 2020). The studies are briefly summarised in the following.

Chapter 2 Morgan Tranter, Marco De Lucia, and Michael Kühn (2021b). Numerical Investigation of Barite Scaling Kinetics in Fractures. *Geothermics* 91:102027. DOI: 10.1016/j.geothermics.2020.102027

Barite precipitation kinetics in fractures are investigated on the laboratory scale to quantify the induced sealing rate and the theoretical range of influence due to the injection of supersaturated fluids. Precipitation is assumed to be a two-step process involving heterogeneous nucleation on the fracture walls and subsequent bulk reaction kinetics. A screening and global sensitivity analysis of the influential parameters is conducted considering their entire range of uncertainty in relevant geothermal systems. Crystal growth is instigated by nucleation, which however only happens when a certain threshold supersaturation is overstepped. Above the threshold supersaturation, the sealing rate is determined by crystal growth kinetics, which is mostly influenced by fracture aperture.

Chapter 3 Morgan Tranter, Maria Wetzel, Marco De Lucia, and Michael Kühn (2021c). Reactive Transport Model of Kinetically Controlled Celestite to Barite Replacement. *Advances in Geosciences* 56:57–65. DOI: 10.5194/adgeo-56-57-2021

The mineralogical evolution of a grain-packed column during simultaneous celestite ($SrSO_4$) dissolution and barite ($BaSO_4$) precipitation is modelled. Dissolution kinetics as well as two-step precipitation (spontaneous formation of small crystals and their subsequent growth) are coupled in reactive transport simulations to reproduce various reaction patterns. Explicitly defining these geochemical processes improves the usability of models for quantified prediction compared to models using empirical relationships. The process calibration provides valuable parameters for future forward modelling of similar systems.

Chapter 4 *unpublished*

Mathematical models and analytical solutions are developed for various mineral kinetic rate laws and advection-facilitated reactive mass transport in a radial diverging flow field. This contributes to the theoretical basis of the following chapters dealing with quantification of scaling potential around an injection well in a geothermal reservoir. While barite reservoir scaling was the main incentive, the results may find usefulness for other similar reactive transport problems and related mineral scale formation. Analytical solutions are generally useful for rapid estimates of reactive transport phenomena and for benchmarking numerical solutions, and also play a key part in performing sensitivity analyses for larger time- and spatial scales. In addition, the radial equilibrium length is derived, which represents the range of influence of quasi-stationary state coupled mass transport in radial flow. Therefore, it can be used as a central predictive value for quantifying the influential reach of reservoir scaling around an injection well.

Chapter 5 Morgan Tranter, Marco De Lucia, Markus Wolfgramm, and Michael Kühn (2020). Barite Scale Formation and Injectivity Loss Models for Geothermal Systems. *Water* 12(11):3078. DOI: 10.3390/w12113078

Impacts of fluid composition, temperature, and pressure variations on barite scaling and induced injectivity loss are investigated. Equilibrium models are applied to geothermal sites for approximating the specific scaling risk, in line with common practical approaches, but they only give indications and absolute precipitation amounts. Therefore, also reactive transport simulations with reaction kinetics are conducted to judge the site specific spatial and temporal scaling behaviour. Furthermore, an analytical scaling score is developed based on the Damköhler number, which aids in approximating injectivity loss without having to run complex reactive transport simulations, and thus holds great value for upscaling models to the reservoir scale.

Chapter 6 Morgan Tranter, Marco De Lucia, and Michael Kühn (2021a). Barite Scaling Potential Modelled for Fractured-Porous Geothermal Reservoirs. *Minerals* 11(11):1198. DOI: 10.3390/

min11111198

Dual-layer, hydro-chemical simulations of fractured-porous geothermal reservoir are conducted to study the long-term impact of barite scale formation on well injectivity. A scenario analysis is presented that covers a broad range of flow distribution through porous and fractured aquifers as this is often uncertain in enhanced geothermal systems utilising multiple stratigraphic units. The models show that mineral scalings are distributed more along the preferential flow paths of fractures, which is significant if their flow rate share is high. Thus, geothermal reservoirs with higher transmissivity-share regarding fractures are affected significantly less by scale formation. Finally, the scaling score, first established in Tranter, De Lucia, Wolfgramm, and Kühn (2020), is extended to be generically applicable to fractured and porous aquifers with varying thickness and porosity, therefore providing a quick initial screening tool for assessing scaling risk of geothermal sites in advance.

1.5.2 Software publications

The software publication phreeqsim[1] presents a modelling framework for coupled geochemical and reactive transport modelling. It is a Python-PHREEQC (Parkhurst and Appelo 2013)-interface with the aim of providing a geochemical package for calculating aqueous equilibrium or kinetic reactions and making the results readily available for further coupling (Fig. 1.3). I developed and applied it in close relationship with the models of the present thesis. The process library for complex precipitation mechanisms such as nucleation and crystal growth makes it singular compared to alternative projects (De Lucia and Kühn 2013). It ships with a transport module, the basis for carrying out reactive transport simulations by sequentially coupling reactive processes. The process interface is built, so additional processes can be integrated easily. Further benefits of this interface are that data evaluation methods such as parameter optimisation and sensitivity analysis can be performed readily within the popular Python infrastructure using state-of-the-art methods. High-resolution, thermo-hydro-mechanical-chemical (THMC) coupled transport models are often bottlenecked by geochemical calculations regarding simulation time. Some approaches to reduce these calculation times are already implemented in its current state, which facilitated the simulations for the current work (e. g., unique cell filtering, caching and reusing results, and multiprocessing). Other approaches, e. g., surrogates for geochemical modelling utilising modern machine learning algorithms, are envisaged and subject to future development.

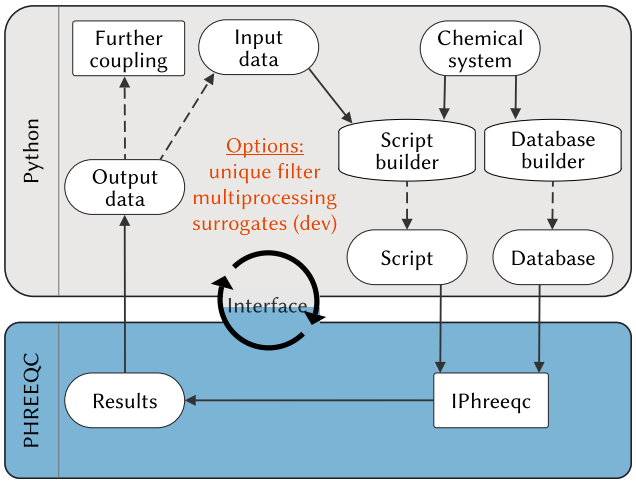

Figure 1.3: Flowchart of the basic implementation in the software code phreeqsim (Tranter 2021) for carrying out geochemical batch calculations in Python using PHREEQC (Parkhurst and Appelo 2013).

[1]Morgan Tranter (2021). *Phreeqsim*. Version 0.3.0. Zenodo. DOI: 10.5281/ZENODO.5482132.

CHAPTER 2

Numerical investigation of barite scaling kinetics in fractures

This is a reprint of an article published in the journal Geothermics (Elsevier)[1].

Abstract

Barite stands out as one of the most ubiquitous scaling agents in deep geothermal systems, responsible for irreversible efficiency loss. Due to complex parameter interplay, it is imperative to utilise numerical simulations to investigate temporal and spatial precipitation effects. A one-dimensional reactive transport model is set up with heterogeneous nucleation and crystal growth kinetics. In line with geothermal systems in the North German Basin, the following parameters are considered in a sensitivity analysis: temperature (25 to 150 °C), pore pressure (10 to 50 MPa), fracture aperture (10^{-4} to 10^{-2} m), flow velocity (10^{-3} to 10^{0} m s^{-1}), molar volume (50.3 to 55.6 cm^3 mol^{-1}), contact angle for heterogeneous nucleation (0° to 180°), interfacial tension (0.07 to 0.134 J m^{-2}), salinity (0.1 to 1.5 mol kgw^{-1} NaCl), pH (5 to 7), and supersaturation (1 to 30). Nucleation and consequently crystal growth can only begin if the threshold supersaturation is exceeded, therefore contact angle and interfacial tension are the most sensitive in terms of precipitation kinetics. If nucleation has occurred, crystal growth becomes the dominant process, which is mainly controlled by fracture aperture. Results show that fracture sealing takes place within months (median 33 days) and the affected range can be on the order of tens of metres (median 10 m). The presented models suggest that barite scaling must be recognised as a serious threat if the supersaturation threshold is exceeded, in which case, large fracture apertures could help to minimise kinetic rates. The models further are of use for adjusting the fluid injection temperature.

2.1 Introduction

Deep geothermal systems are a potential source of renewable energy, which is becoming increasingly important in the context of the German energy transition. Numerous pilot projects have shown that significant thermal energy or even electricity is available in a couple of regions in Germany, such as the Molasse Basin, the Upper Rhine Graben (URG), and parts of the North German Basin (NGB) (Seibt et al. 2010a). In order for them to be used in an efficient operation for energy production, the down-hole temperature should exceed at least 100 °C. In Germany, depending on the local geothermal gradient, these temperatures are expected to be encountered at depths of more than 1 800 m (Stober et al. 2013). Sufficient productivity and injectivity are also required for an economical plant. The target reservoir's properties in this regard are porosity and permeability, hence the local geology is decisive in this context.

[1]Morgan Tranter et al. (2021b). Numerical Investigation of Barite Scaling Kinetics in Fractures. *Geothermics* 91:102027. DOI: 10.1016/j.geothermics.2020.102027.

While promising temperatures are met at practicable depths in regions of the NGB (Stober et al. 2013), non-sufficient rock permeabilities in related sedimentary horizons are potentially an issue (Wolfgramm et al. 2008). Previous concepts and applications, for example at the geothermal test-site Groß Schönebeck located in the NGB (Zimmermann et al. 2010), require enhancing the fracture network by hydraulic stimulation. However, decreasing productivity and injectivity are observed over time. Blöcher et al. (2016) propose that this may be explained by the following processes: accumulation of mineral scaling in the reservoir and the wellbore, thermo-mechanically induced fracture closing, and two-phase flow as a consequence of outgassing. There is evidence that chemical reactions are accountable for reduced injectivity (Blöcher et al. 2016; Griffiths et al. 2016; Regenspurg et al. 2015; Scheiber et al. 2013; Stober et al. 2013).

Precipitation of certain minerals, termed scaling in this context, is a key issue for many geothermal sites in Germany. This is due to the chemical characteristics of the formation waters as well as the perturbation of the system due to changing temperature and pressure during production and re-injection. Total dissolved solids (TDS) of basinal brines in the NGB are correlated with depth, temperature, and corresponding stratigraphical units. The chemistry of these brines are dominated either by Na and Cl or by Na, Ca and Cl, and their TDS range from (100 to 400) $\mathrm{g\,l^{-1}}$, increasing with depth and temperature (Stober et al. 2013; Tesmer et al. 2007; Wolfgramm et al. 2011b). Scaling has a damaging and potentially lasting effect by accumulating and hence clogging parts of the system, e.g., the wells, the surface equipment, and notably the reservoir itself.

In regions of the NGB and the URG, brines produced at geothermal sites from depths of 2 000 m and more have increased concentrations of Ba (Wolfgramm et al. 2011b), coinciding with observed scalings consisting predominantly of barite (Regenspurg et al. 2015; Scheiber et al. 2013; Wolfgramm et al. 2011a,c). In this regard, barite is the focus of many current investigations (e.g., Bozau et al. 2015; Griffiths et al. 2016; Heberling et al. 2017; Regenspurg et al. 2015; Scheiber et al. 2013). They stand out to be exceptionally hard to remove once accumulated, as no economically viable solvents are available. Although nucleation and crystal growth kinetics of barite have been studied for many years (e.g., Christy and Putnis 1993; Dove and Czank 1995; Fernandez-Diaz et al. 1990; He et al. 1995; Kühn 1997; Prieto 2014; Scheiber et al. 2013; Zhen-Wu et al. 2016), its formation in relation to temperature and pressure change along a geothermal system path still need to be resolved. It is a necessity for plant operation that temporal and spatial precipitation effects of barite can be anticipated so as the right prevention measures can be taken.

The aim of this study is to investigate the role of barite scaling associated to fracture sealing and reduced fracture permeability near the injection well. It further provides the basis for designing complementary fracture permeability investigations on the laboratory scale, similar to Blöcher et al. (2019). The main questions addressed here are its adverse effect on the injectivity of a geothermal system and the sensitivity in terms of the parameters that control precipitation kinetics. For assessing the overall impact on fracture permeability, the critical time t_{crit} for permeability to decrease by one order of magnitude as well as the saturation length scale (SLS) are used as key figures. Numerical, one-dimensional Darcy flow simulations of coupled transport and geochemical processes are carried out on the laboratory scale. Specifically, precipitation is studied by heterogeneous nucleation on the fracture wall and subsequent bulk crystal growth kinetics. The results of a global sensitivity analysis are presented and discussed regarding their implications for geothermal applications.

2.2 Methods

2.2.1 Model setup

A one-dimensional, numerical reactive transport model was set up with a sequential non-iterative approach, consisting of advective solute transport and chemical kinetic reactions.

The conceptual model adopted for the present study is in accordance with experimental core flooding set-ups, where the cores exhibit a single fracture, similar to laboratory and modelling experiments carried out by Blöcher et al. (2019). Laminar, single-phase flow between two plates with smooth, impermeable walls was assumed and hence a single-continuum approach was chosen (Fig. 2.1).

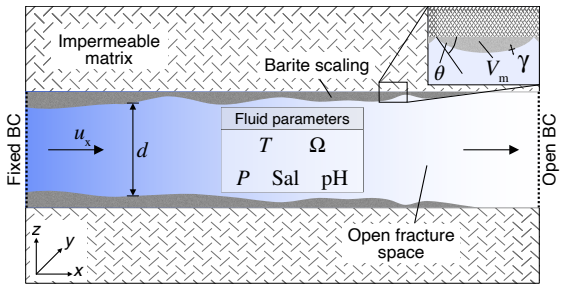

Figure 2.1: Conceptual model for the reactive transport setup of the one-dimensional fracture flow between two plates with smooth, impermeable walls. Barite scalings are assumed to accumulate on fracture walls. The following parameters are shown: fracture aperture (d), flow velocity (u_x), temperature (T), pressure (P), pH, saturation ratio of barite (SR), fluid background salinity (Sal), molar volume (V_m), contact angle (θ) and interfacial tension (γ).

The model domain was discretised in the flow direction ($\Delta x = 3 \times 10^{-2}$ m, six nodes). As only the free fracture space was considered, the geometry of the whole domain is effectively a cuboid of the size ($x \times y \times d$), where the sample length is $x = 0.15$ m, the fracture width is $y = 0.10$ m, and the distance between the plates, i.e., the fracture aperture, is d.

The one-dimensional flow-field was imposed with a homogeneous flow velocity u_x and kept constant throughout the simulation. Advection was assumed to be the dominant solute transport process. Hydro-mechanical diffusion as well as thermal and density driven transport processes were neglected for flow through the fracture. Conservation of mass was numerically solved with an explicit finite differences scheme using first-order upwind. The time step length Δt was chosen so that the Courant-Friedrichs-Lewy condition is always satisfied ($|\frac{u_x \Delta t}{\Delta x}| \leq 1$). Four species were considered in solute transport (see below). The initial and boundary conditions where implemented as follows: solute concentrations and solids in the model domain are initially set to zero. Solute concentrations at the inlet are fixed and the outlet was set to an open flux boundary condition.

2.2.2 Geochemical modelling

Geochemical batch reaction calculations were carried out using the PHREEQC software package, version 3.5.0 (Parkhurst and Appelo 2013) and its module IPhreeqc (Charlton and Parkhurst 2011). During a transport simulation, the chemical state of each node at each time step is passed on to PHREEQC, where a batch kinetic reaction is calculated. The results are then passed back to the transport simulator.

The chemical system implemented was kept to a minimum in order to illustrate the effects of barite precipitation on fracture permeability. Barite precipitation was considered the sole phase transition reaction:

$$SO_4^{2-}{}_{(aq)} + Ba^{2+}{}_{(aq)} \rightarrow BaSO_{4(solid)}. \tag{2.1}$$

Therefore, the dissolved species Ba^{2+} and SO_4^{2-}, as well as H^+ and e^- were transported. Note that for solute transport, total Ba and S concentrations were treated as though their only species are Ba^{2+} and SO_4^{2-}, respectively, which is valid for the redox and pH state considered. H^+ and e^- virtually stayed constant, but were nevertheless considered as PHREEQC needs them as an input (as pH and pe) and to have a generally valid model. All other dissolved species were kept constant.

The saturation ratio of barite in a solution is defined as:

$$SR_{barite} = \frac{a_{Ba^{2+}}\, a_{SO_4^{2-}}}{K_{sp,barite}} \tag{2.2}$$

where a denotes the activities of the respective species denoted in the subscript and $K_{\mathrm{sp,barite}}$ is the solubility constant of barite. The subscript barite will be omitted hereafter. If SR < 1, then the fluid is undersaturated, and if SR > 1, then the fluid is supersaturated with respect to barite and precipitation becomes possible from a thermodynamic point of view. The saturation state was calculated with PHREEQC using the database supplied `pitzer.dat` (Appelo et al. 2014; Parkhurst and Appelo 2013), where the activities are calculated from concentrations and activity coefficients derived from the Pitzer ion-interaction approach (Pitzer 1973). The Pitzer approach is known to produce more accurate estimates than the extended Debye-Hückel approach especially at high ionic strengths (Appelo et al. 2014). Indeed, making use of the underlying activity model as well as the temperature and pressure dependent correction of the solubility constant (Appelo 2015; Parkhurst and Appelo 2013), Hörbrand et al. (2018) have shown that using `pitzer.dat` yields the best results at conditions relevant to the present case.

2.2.3 Classical nucleation theory

Based on classical nucleation theory (CNT), the nucleation rate J ($\mathrm{m^{-3}\,s^{-1}}$) for homogeneous nucleation (HON) is given by (Nielsen 1964):

$$J = \Gamma \exp\left(-\frac{\Delta G_c}{k_\mathrm{B}\,T}\right) \tag{2.3}$$

where Γ ($\mathrm{m^{-3}\,s^{-1}}$) is a pre-exponential factor that quantifies the diffusive flux of molecules to the growing cluster, ΔG_c (J) is the free energy change, k_B ($1.381 \times 10^{-23}\,\mathrm{J\,K^{-1}}$) is Boltzmann's constant, and T (K) is the temperature. Changing the supersaturation in a solution potentially has an immense impact on the nucleation rate because it significantly determines ΔG_c as a log function in the denominator (Nielsen 1964):

$$\Delta G_\mathrm{c} = \frac{\beta\, V_\mathrm{m}^2\, \gamma^3}{k_\mathrm{B}\,T\,\ln \mathrm{SR}} \tag{2.4}$$

where β is a shape factor depending on the nucleus geometry (here $16\pi/3$, as a sphere was assumed), V_m ($\mathrm{m^3\,mol^{-1}}$) is the molar volume, and γ ($\mathrm{J\,m^{-2}}$) is the interfacial tension. There are various propositions to approximate Γ (e.g., Kashchiev 2000; Lasaga 1998; Nielsen 1964). Nielsen proposes the following:

$$\Gamma = \frac{2\,D_\mathrm{mol}}{d_\mathrm{ion}^5} \tag{2.5}$$

where D_mol ($\approx 10^{-9}$ $\mathrm{m^2\,s^{-1}}$) is the diffusion coefficient, and d_ion ($\approx 10^{-9.5}$ m) is taken as the mean diameter of an ion. Prieto (2014), on the other hand, applied the approach proposed by Kashchiev, which takes additional parameters into account, such as available monomers and sites for nucleation. The Nielsen-approach was adopted for the present study, as fewer uncertain parameters need to be assumed.

If a substrate is in contact with the solution, the formation of a nucleus at the interface is termed heterogeneous nucleation (HEN). In this case, the energy barrier to form a stable nucleus at the phase boundary is lowered as a function of its contact angle θ:

$$\Delta G_\mathrm{c,HEN} = \Delta G_\mathrm{c}\, f(\theta). \tag{2.6}$$

This is due to a higher structural similarity between nucleus and substrate compared to nucleus and solution, and effectively results from tensional forces between each the solid, fluid, and crystal phases. A spherical droplet nucleus was assumed, hence the reduction factor was calculated as (Lasaga 1998):

$$f(\theta) = \frac{1}{4}\left(2 - 3\,\cos\theta + \cos^3\theta\right) \tag{2.7}$$

Another overall decisive parameter is the interfacial tension γ, which is demanding to quantify experimentally and is only scarcely available in the literature for barite in respective solutions. Reported

values range from (0.08 to 0.134) $\mathrm{J\,m^{-2}}$ (Fernandez-Diaz et al. 1990; He et al. 1995; Nielsen and Söhnel 1971).

In any case, it becomes clear that, compared to HON, a lower supersaturation threshold ($\mathrm{SR_{th}}$) suffices for HEN to take place. Hence, if a substrate is in contact with the solution, HEN is likely to be the dominant nucleation process. It has been shown experimentally that this is the case for barite at saturation conditions $\log_{10} \mathrm{SR_{barite}} < 3$ (Poonoosamy et al. 2020b). For the present case this is relevant, as the fracture walls were considered as substrate material. However, the value of the relevant parameter θ is uncertain, as it theoretically depends on the minerals accessible to the solution. Even though He et al. (1995) report a standard value of 0.4 for $f(\theta)$, the whole range from 0 to 1 was considered here, as it describes an uncertain process. Other studies also treat it as a fitting parameter (Liu 1999; Poonoosamy et al. 2016; Prieto 2014).

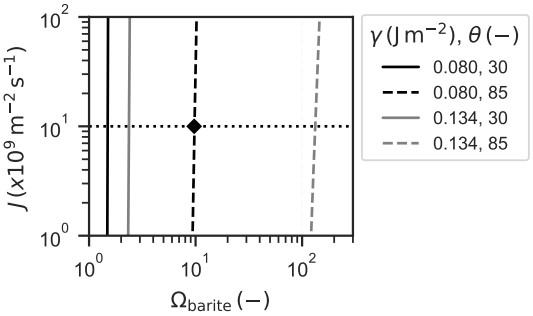

Figure 2.2: Schematic illustration of the influence of interfacial energy (γ) and contact angle (θ) on the heterogeneous nucleation rate (J) using Eqs. (2.3)–(2.7). Temperature was set to 60 °C. Vertical curves imply that a supersaturation threshold $\mathrm{SR_{thresh}}$ can be assumed. It is often arbitrarily set to the point, where $J = 10^{10}\ \mathrm{m^{-2}\,s^{-1}}$ (dotted line). Hence for $\gamma = 0.08\ \mathrm{J\,m^{-2}}$ and $\theta = 85°$, $\mathrm{SR_{thresh}}$ is about 10 (diamond marker).

Figure 2.2 illustrates, how vast the impact of the two parameters γ and θ can be on the heterogeneous nucleation rate. It also becomes clear that, depending on these parameters, there is a supersaturation threshold, from which nucleation becomes relevant. It is often (arbitrarily) related to the point, where nucleation rate is $10^{10}\ \mathrm{m^{-2}\,s^{-1}}$ (Lasaga 1998; Prieto 2014).

On the basis of the findings above, the size of a nucleus that is potentially stable in solution is dependent on its supersaturation. Only when this critical nucleus radius r_{crit} is overcome, the nucleus becomes thermodynamically stable. r_{crit} is largely dependent on the ratio of the free energies concerning the nucleus' surface and volume. It can be shown that (Lasaga 1998):

$$r_{\mathrm{crit}} = \frac{2\,\gamma\,V_{\mathrm{m}}}{R\,T\,\ln \mathrm{SR}} \tag{2.8}$$

In the case of HEN, a nucleus is in contact with a flat surface, hence the resulting surface area in contact with the solution is (Lasaga 1998):

$$\mathrm{SA_{nucleus}} = 2\,\pi\,r_{\mathrm{crit}}^2\,(1 - \cos\theta) \tag{2.9}$$

During simulations, the accumulated surface area of all nuclei formed was calculated at every time step and for every cell. Considering $\mathrm{SA} = \min(\mathrm{SA_{frac}}, \mathrm{SA_{nuclei}})$, the resulting reactive surface area SA for crystal growth was then passed on to PHREEQC. Note the assumption that the reactive surface area and hence chemical reaction was restricted to the fracture surface area ($\mathrm{SA_{frac}} = 2\,\Delta x\,y$).

2.2.4 Crystal growth

Precipitation and dissolution reaction kinetics of minerals can be modelled on a macroscopic scale using rate constants derived from bulk reaction experiments. A general form for calculating the precipitation rate was used (Lasaga 1998):

$$r = -\frac{\mathrm{SA}}{m_{\mathrm{water}}} k\,(1 - \mathrm{SR}^p)^q \tag{2.10}$$

where m_{water} (kg) is the mass of water in solution, k (mol m^{-2} s^{-1}) is the rate constant, and the dimensionless exponents p and q are empirical parameters describing reaction order and deviation from equilibrium according to the transition state theory (Lasaga 1998). Zhen-Wu et al. (2016) currently provide the only source for bulk precipitation rates in NaCl-solutions. They conducted experiments on dissolution and precipitation kinetics of barite in solutions with salinities up to 1.5 M NaCl, temperatures from (25 to 90) °C, and pH from 2 to 9. Further, they derived lumped rate constants from this that incorporate temperature, ionic strength, and pH dependent mechanisms, by fitting the experimentally measured time series to Eq. (2.10), and setting q and p each to unity. More commonly, the reaction rate equation Eq. (2.10) is further decomposed into separate terms, each representing a factor-dependent reaction mechanism. For example, influencing effects at varying pH can be described by using an acid, a neutral, and a base term, or temperature can be represented by using an Arrhenius term (Lasaga 1998). Based on transition state theory, Palandri and Kharaka (2004) provide a set of rate parameters for calculating kinetic reactions in this fashion for a range of minerals, among them barite. However, since there is only limited data available on precipitation rates at saline conditions (Christy and Putnis 1993; Dove and Czank 1995; Zhen-Wu et al. 2016), it was decided to use a more general rate equation. In the present study, rate constants were derived by using data from Zhen-Wu et al. (2016) in order to process calculations on precipitation rates, which was implemented using Eq. (2.10). For predicting rate constants at varying conditions for the reactive transport models, a linear regression was carried out.

The dimensionless Damköhler number for advective transport quantifies the ratio of a characteristic time for advective transport to a characteristic time for reaction. It therefore gives an indication on the nature of the reaction front with regard to the spatial discretisation. It was calculated with (Steefel 2008):

$$t_{\mathrm{adv}} = \frac{\Delta x}{u_{\mathrm{x}}} \tag{2.11}$$

$$t_{\mathrm{react}} = \frac{c_{\mathrm{eq}}}{\mathrm{SA}\,k} \tag{2.12}$$

$$Da_{\mathrm{adv}} = \frac{t_{\mathrm{adv}}}{t_{\mathrm{react}}} \tag{2.13}$$

where c_{eq} is the solubility of barite in equilibrium.

In a homogeneous case, equilibrium is reached within a grid cell if $Da_{\mathrm{adv}} > 1$. From this, the saturation length scale SLS was derived, which describes the flow length, beyond which equilibrium is reached (Steefel 2008):

$$\mathrm{SLS} = \frac{\Delta x}{Da_{\mathrm{adv}}} \tag{2.14}$$

The mean SLS of all nodes was taken as one key figure for the sensitivity analysis (see below) and is an indication for the influencing range of barite scaling around an injection well.

2.2.5 Permeability evolution

Fracture transmissivity is an important parameter when evaluating the suitability of a target reservoir. To derive a quantifiable value for this, the change of fracture aperture as a consequence of barite precipitation needs to be related to change in fracture permeability K (m^2). Assuming laminar flow and parallel fracture walls, exhibiting smooth surfaces and 'no-slip' boundary conditions, the permeability

of a fracture can be approximated with the cubic law (e.g., Neuzil and Tracy 1981). If a single fracture is considered, it is given as:

$$K_i = \frac{d_i^2}{12} \tag{2.15}$$

where the subscript i signifies a respective cell in flow direction at a given time. Change in fracture aperture due to barite precipitation was derived by calculating the volume fraction in each cell at each time step and relating it to the initial aperture:

$$d_i = d_0 \left(1 - \frac{n_{\mathrm{i,barite}}\, V_{\mathrm{m}}}{\Delta x\, y\, d_0}\right) \tag{2.16}$$

where n_{barite} (mol) is the amount of barite, Δx (1×10^{-3} m) is the cell spacing in flow direction, y (0.1 m) is the fracture length (diameter of core), and the subscript 0 signifies the initial state. It follows that the permeability K_i in each cell can then be calculated from the initial permeability K_0:

$$K_i = K_0 \left(\frac{d_i}{d_0}\right)^2 \tag{2.17}$$

The effective permeability of the whole fracture was then taken as the harmonic mean of the respective permeability in each cell.

For assessing a decisive indicator of the coupled simulations with regard to permeability change, the time for the permeability to change by one order of magnitude was taken as another key figure for the sensitivity analysis (see below). This value was presumed to be the critical time t_{crit} for the fracture to be virtually sealed in the present application, as it would render the geothermal system as uneconomic. It was taken advantage of the fact that the closing rate of the fracture $r_d = \mathrm{d}d/\mathrm{d}t$ approaches a constant value, since the reactive surface area is limited by fracture surface area. If the closing rate is assumed to be constant, it can be shown from Eq. (2.15) that:

$$t_{\mathrm{crit}} = \frac{d_{\mathrm{initial}} \left(1 - \frac{1}{\sqrt{10}}\right)}{r_d} \tag{2.18}$$

A simulation was terminated if either r_d approached a constant value, i.e., the change compared to the previous advection step is smaller 1%:

$$\mid 1 - \frac{r_{d,\mathrm{t}}}{r_{d,\mathrm{t+1}}} \mid < 0.01 \tag{2.19}$$

Or if no nucleation has taken place at all after at least 18 advection steps (3 × nodes). In the latter case, this would result in $t_{\mathrm{crit}} = \infty$, but $t_{\mathrm{crit}} = 10^{99}$ s was adopted here in order to have comparable numerical values.

2.2.6 Sensitivity analysis

A sensitivity analysis was carried out with respect to the model outputs t_{crit} and SLS for assessing the temporal and spatial effects of barite scaling, respectively. The parameters covered and their respective ranges for the present study are summarised in Tab. 2.1. All parameters were treated independently from another. For a more complete list, see Tab. A.1.

The parameters fracture aperture (d), darcy velocity (u_x), temperature (T), pore pressure (P), pH, and saturation state (SR) were chosen so as to capture typical values that can be expected in the fracture network near an injection well. For this, the geothermal reservoir Groß Schönebeck (Blöcher et al. 2016; Regenspurg et al. 2015; Zimmermann et al. 2010) was taken as a reference. The geochemistry of the respective formation water can be seen in Tab. 2.2 (Regenspurg et al. 2010).

Table 2.1: Ranges of model parameters chosen for the sensitivity analysis selected to capture expected conditions in a fracture network near an injection well in a geothermal system.

Input parameter	Abbreviation	Unit	Varied ranges	Source
fracture aperture	d	m	$\log(-3 \pm 1)$	(Zimmermann et al. 2010)
flow velocity	u_x	$m\,s^{-1}$	$\log(-1.5 \pm 1.5)$	(Zimmermann et al. 2010)
temperature	T	°C	60 ± 10	(Blöcher et al. 2016)
pressure	P	Pa	$\log(7.35 \pm 0.35)$	(Blöcher et al. 2016)
pH	pH	-	6 ± 1	(Regenspurg et al. 2015)
saturation ratio	SR	-	16 ± 15	(Regenspurg et al. 2015)
fluid salinity	Sal	M NaCl	0.8 ± 0.7	(Zhen-Wu et al. 2016)
molar volume	V_m	$cm^3\,mol^{-1}$	52.9 ± 2.7	(Appelo 2015)
contact angle	θ	-	$90^\circ \pm 90^\circ$	(Lasaga 1998)
interfacial tension	γ	$J\,m^{-2}$	0.102 ± 0.032	see Section 2.2.3

Table 2.2: Geochemistry and state of the formation water in the geothermal reservoir Groß-Schönebeck. The equilibrated column is calculated with PHREEQC (`pitzer.dat`), where the measured column is the input data, barite was equilibrated (SR = 1), and charge balance was done with Cl^-.

Parameter	Measured (Regenspurg et al. 2015)	Equilibrated
T	150 °C	150 °C
P	500 bar	500 bar
pH	5.7	5.7
Na^+	1.67 M	1.67 M
K^+	7.40×10^{-2} M	7.40×10^{-2} M
Ca^{2+}	1.35 M	1.35 M
Mg^{2+}	1.80×10^{-2} M	1.80×10^{-2} M
Ba^{2+}	2.50×10^{-4} M	2.88×10^{-3} M
Sr^{2+}	2.20×10^{-2} M	2.20×10^{-2} M
Cl^-	4.71 M	4.52 M
SO_4^{2-}	1.50×10^{-3} M	4.13×10^{-3} M
HCO_3^-	3.10×10^{-4} M	3.10×10^{-4} M

It is assumed that the formation water is in equilibrium with barite in the reservoir. Therefore, the formation water was equilibrated with barite using PHREEQC and the database `pitzer.dat`. If temperature and pressure is then reduced, as it were produced, the fluid will become supersaturated with respect to barite (Fig. 2.3). As can be seen, due to a temperature decrease from 150 °C (reservoir state) to 70 °C (injection state), SR is expected to be on the order of 30. The influence of decreasing pressure is noticeably lower.

It is furthermore expected that some barite will readily precipitate before the fluids reach the reservoir surrounding the injection well. Hence, scenarios at lower supersaturation were also investigated. Salinity is an important factor for the rate constants introduced and is bound to the respective experimental data. The molar volume (V_m) is given in the Pitzer database (Parkhurst and Appelo 2013), but it was varied arbitrarily to ±5% in order to account for inhomogeneous scaling morphology along the fracture. The contact angle (θ) was varied within the two limiting cases for heterogeneous nucleation, and the

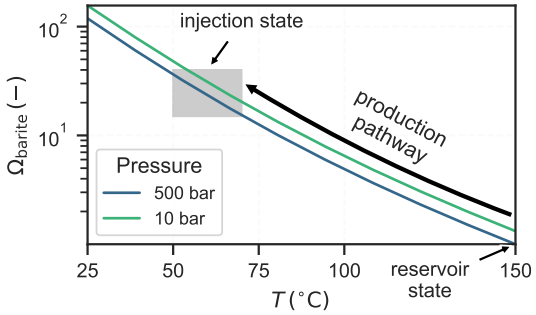

Figure 2.3: Expected supersaturation of barite, if temperature and pressure are reduced along the production pathway of a geothermal power plant. It is assumed that the fluid is in equilibrium at the reservoir state (SR = 1). The grey box highlights the presumed temperature and pressure injection state, which corresponds to a saturation ratio in the range of 15–30.

range of the interfacial tension (γ) was obtained from literature data (Fernandez-Diaz et al. 1990; He et al. 1994a; Nielsen and Söhnel 1971; Prieto 2014).

The relative importance of each parameter was firstly ascertained by a screening method, which illustrates varying effects and processes on a general level. The one-at-a-time (OAT) method of Morris (1991) was utilised for this so as to yield the mean elementary effects and their standard deviation of each parameter in the model output. The sampling is carried out on a regularly spaced grid, varying each parameter at a time. This is done for a limited amount of model runs and is utilised to retain non-influential parameters. The number of model runs results from $t(p+1)$, where p is the number of parameters and t is the number of trajectories (Morris 1991). $p = 10$ and t was set to 1 000, resulting in 11 000 model runs for the OAT screening.

In a next step, the global, variance based sensitivity analysis of Sobol′ (2001) was applied, which implements a more elaborate parameter sampling procedure than the OAT method (Saltelli 2002). From this, the interaction effects and total sensitivity indices for each parameter were derived and they quantify a parameter's total influence on the system. Due to the model termination criteria ($t_{crit} = 10^{99}$ s), the mechanism of HEN potentially conceals parameter dependencies important for governing crystal growth. So as to highlight the effect of crystal growth, noteworthy scenarios at saturation ratio 15, 20 and 30 were considered. Further, parameters controlling HEN were fixed at this stage to $\gamma = 0.08$ J m^{-2} and $\theta = 85°$. These standard values proposed by He et al. (1994a) result in a threshold supersaturation of $SR_{th} \approx 10$ (Fig. 2.2). This leaves seven factors ($p = 7$) for the global sensitivity analysis. The number of model runs needed for this follows from $n(2p+2)$, where p is the number of parameters and n is the number of samples (Saltelli 2002). n was set to 1 000, resulting in 16 000 model runs.

2.3 Results

2.3.1 Rate constants

The lumped rate constant (k) for evaluating crystal growth rates from Eq. (2.10) was calculated with a linear regression at respective temperature (T) and salinity (Sal) conditions, as shown in Tab. 2.3. Comparing various first-order linear regression models with interaction terms, to prevent over-fitting given only nine data points are available, the following model yielded the lowest averaged residuals:

$$\log_{10} k_{model} = k_1 T^{-1} + k_2 \,\mathrm{Sal}^{\frac{1}{2}} + k_3 \tag{2.20}$$

The regressed coefficients are $k_1 = -0.453$, $k_2 = 0.291$, and $k_3 = -7.279$, with an adjusted $R^2_{adj} = 0.88$. The resulting rate constants using this model at respective experimental conditions are shown in Tab. 2.3.

A detailed description of the experimental data is given in Zhen-Wu et al. (2016). In general, k is positively correlated with temperature and ionic strength. The temperature dependency can be described by an Arrhenius term (Lasaga 1998). Hence, the reciprocal of the temperature was chosen to predict $\log_{10} k$. The influence of the ionic strength is much higher at lower salinities. This dependency levels off at higher salinities, therefore the root of salinity for the linear model was used.

Table 2.3: Rate constants for bulk precipitation of barite at varying conditions used for the linear regression. The parameters T and Sal are the input features, which were transformed and scaled for the regression. Comparing experimental and model rates yields $R^2_{\text{adj}} = 0.88$.

T (°C)	Sal (M NaCl)	$\log_{10} k^{\text{a}}_{\text{exp}}$ ($\text{mol/m}^2\,\text{s}$)	$\log_{10} k_{\text{model}}$ ($\text{mol/m}^2\,\text{s}$)
25	0.0	−8.46	−8.21
25	0.1	−7.62	−7.99
25	1.0	−7.60	−7.51
25	1.5	−7.55	−7.36
60	0.1	−7.22	−7.09
60	0.7	−6.60	−6.73
60	1.0	−6.54	−6.62
60	1.5	−6.52	−6.46
25	1.0	−7.40	−7.51

(a) Experimental data on bulk precipitation (Zhen-Wu et al. 2016)

The linear model obtained for determining the rate constant was introduced into the reactive transport model. Together with the reactive surface area and the supersaturation, it is the basis for the kinetic crystal growth calculations using Eq. (2.10) as implemented in PHREEQC.

2.3.2 Parameter screening

In the parameter screening, the bandwidths of all parameters shown in Tab. 2.1 were evaluated. The results of the OAT sensitivity analysis with regard to the temporal model output t_{crit} (Eq. (2.18)) are shown in Fig. 2.4.

The absolute mean elementary effects ($\mu^*_{t_{\text{crit}}}$) and respective standard deviations ($\sigma_{t_{\text{crit}}}$) of most parameters are high ($> 10^{94}$ d), which is due to the model termination criteria. The value 10^{99} s was used as a numerical placeholder, which signifies that t_{crit} is infinite due to negligible crystal growth. Indeed, 9 080 of the total 11 000 model runs terminated because no HEN happened at all. Thus, notably the parameters, defining whether the threshold supersaturation (SR_{th}) is exceeded or not, i.e., supersaturation, contact angle, and interfacial tension, have the strongest impact on the total model outcome. This can be derived from Fig. 2.4, in which the parameters the furthest away from the point of origin are more influential in the parameter space investigated. The elementary effects of darcy velocity, molar volume and temperature, and salinity are similarly high, but one or two orders lower. In contrast, it becomes apparent that the parameters fracture aperture, pH, and pore pressure only have a comparably small sensitivity. Customarily, the uncertainties of parameters, which have small elementary effects, are neglected in further analyses. But in fact, they are on the order of $\gg 50$ years, even though they have near to no impact on the nucleation mechanism. Hence, the model exhibits two distinguishable mechanisms, each depending on different parameters. Both mechanisms have a decisive impact on the model output as the influences are by far higher than the life expectancy of a utilised geothermal system.

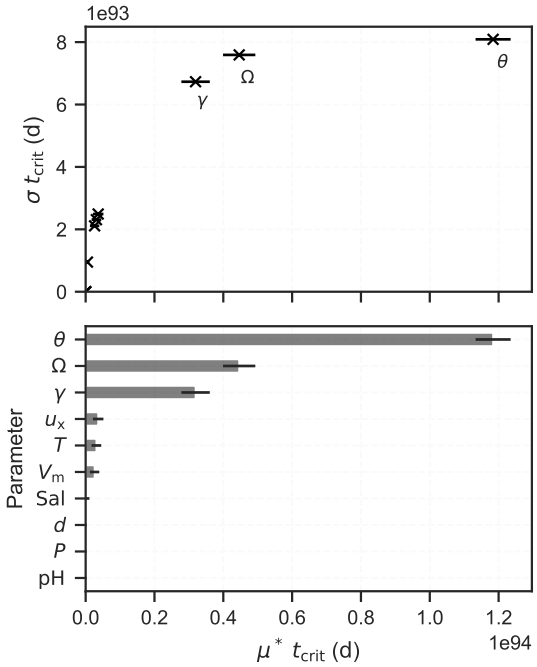

Figure 2.4: Absolute mean of the elementary effects (μ^*) and the respective standard deviations (σ) of the model parameters on t_{crit} derived from the one-at-a-time (OAT) method of Morris (1991). The solid, horizontal lines represent bootstrapped confidence intervals of μ^*. The ranges of the model input parameters are shown in Tab. 2.1.

2.3.3 Global sensitivity analysis

The role of the nucleation mechanism is shown to be important in the previous section. For evaluating the sensitivity of crystal growth with respect to the input parameters in more detail, time spans for fracture sealing were examined at a fixed supersaturation threshold ($SR_{th} \approx 10$) and three selected supersaturation states (A: SR = 15, B: SR = 20, C: SR = 30.). The distributions of t_{crit} with regard to the input parameters for all scenarios are shown in Fig. 2.5.

Comparing all three scenarios, it can be seen that the larger the supersaturation is, the smaller t_{crit} is. It should be noted that the time ranges are many orders of magnitude higher for C than for A and B. This becomes apparent through stronger scattering in the lower and especially the upper ranges, i.e., a higher variance. In all scenarios, a negative trend can be seen for the parameters T and Sal, whereas a pronounced, positive trend can be seen for d. For example, in B, the median of t_{crit} at a low fracture aperture of about 10^{-1} mm is approximately only 5 days, whereas for a fracture aperture of 10 mm the median is almost 200 days, about 40 times higher. For A, the respective t_{crit} values are only slightly lower (3 and 140 days), however they are significantly higher (> 2 000 days) for C and virtually independent of the fracture aperture. A slight positive trend can also be ascertained for V_m, though only for C; in A and B no correlation becomes apparent in this sense. Furthermore, pH and P exhibit no indication of correlation in all scenarios.

The distribution of the model results are described with summary statistics, as can be seen in Tab. 2.4. The median values of t_{crit} for scenarios B and C are on the order of tens of days. For scenario A, on the other hand, it is on the order of years. The negative trend of t_{crit} with respect to supersaturation becomes apparent again, as does the broader range of the outcome with a smaller supersaturation. Therefore, the uncertainty becomes increasingly larger, the closer the supersaturation is to the threshold supersaturation. While the maximum fracture sealing time in C is about 500 days, it is $\gg$ 50 years in A, suggesting that the variance increases as supersaturation decreases.

The results of the spatial impact, i.e., the distribution of SLS with respect to varying input parameters, are shown in Fig. 2.6. For scenarios B and C it becomes clear that the parameters flow velocity u_x and

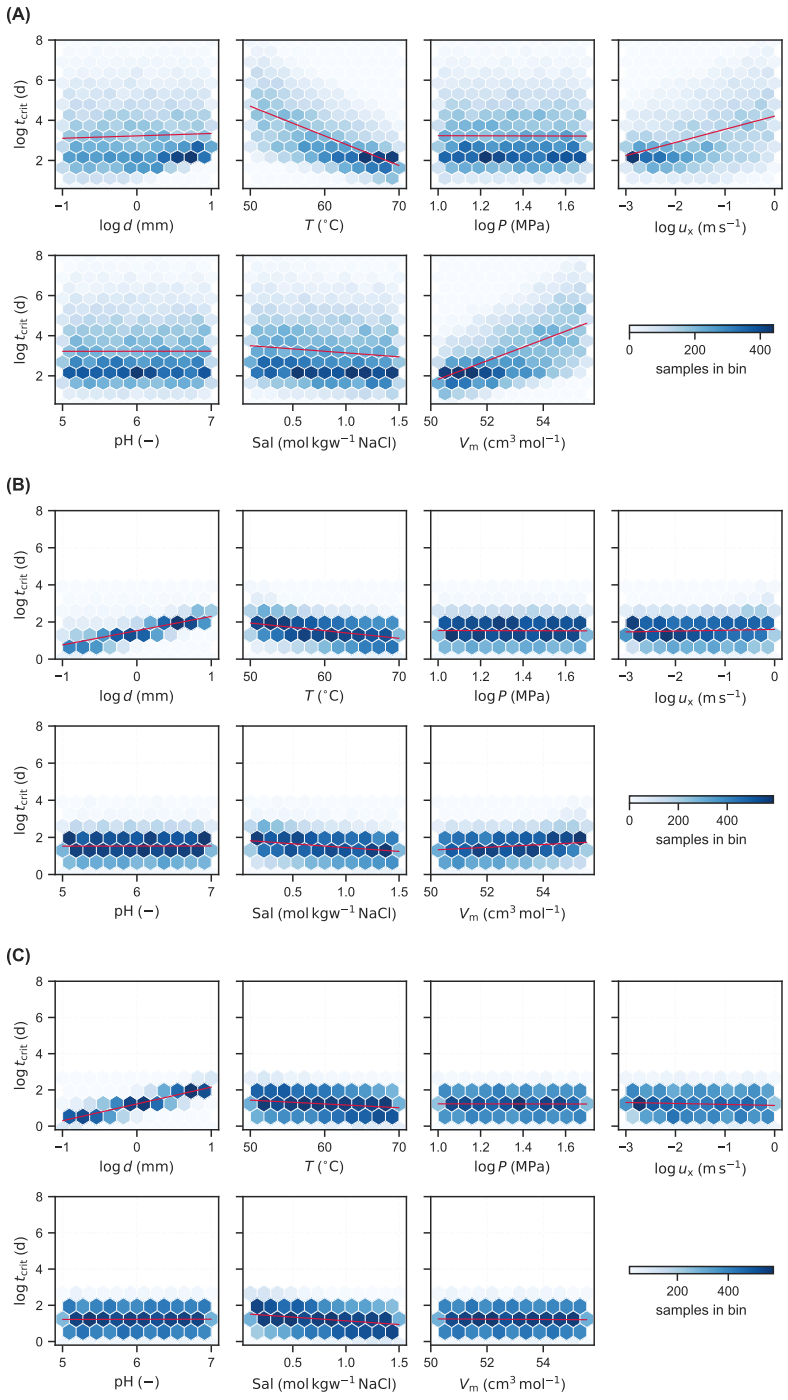

Figure 2.5: Distribution of t_{crit} with regard to varying model parameters for 16 000 model runs obtained from the global sensitivity analysis (Sobol′ 2001). The sampling implemented is based on Saltelli (2002). The solid lines represent the mean trend obtained from linear regression. The color in each hexagon represents the number of results of the model run plotted within the respective area. (A) SR = 15, (B) SR = 20, (C) SR = 30.

fracture aperture d have by far the largest influence on SLS and that both exhibit a positive correlation. All other parameters appear negligible in these cases. For scenario A, on the other hand, the range of the results is much larger and a strong dependency on T, V_m, and u_x can the seen. While the mean SLS at low velocities ($u_x = 10^{-3}$ m s^{-1}) is about 1 m, it is about 1 km at high velocities ($u_x = 1$ m s^{-1}). The describing statistics referring to this are also provided in Tab. 2.4. SLS is in the range of tens of

Table 2.4: Quantiles (Q) of the temporal and spatial model output obtained from the global sensitivity analysis (Sobol′ 2001) at various fixed saturation SR. They give an indication for when the permeability has decreased by one order of magnitude (t_{crit}) and how far along a fracture is sealed, i.e., the saturation length scale (SLS), due to barite scaling.

Scenario	SR	Output	25th Q	50th Q	75th Q
A	15		148	804	12 853
B	20	t_{crit} (days)	12	33	94
C	30		6	16	49
A	15		16	205	7 521
B	20	SLS (m)	3	14	92
C	30		2	12	70

metres for scenarios B and C. For scenario A, it is in the range of hundreds of metres or even kilometres and the uncertainty is also much larger.

As a primary result of the global sensitivity analysis, the first-order S_i and total interaction indices S_{Ti} of the model input parameters were derived (the subscript i signifies the respective parameters in this case). In Fig. 2.7, they are shown with respect to the model output t_{crit} for all three scenarios. As S_i signifies the contribution of a parameter i on the output variance by itself, it can be used to prioritise the input parameters. To evaluate, which parameters are rather non-influential and to also capture possible non-linear effects on the model output variance, S_{Ti} is used, which includes further interaction between the parameters. If S_{Ti} is negligibly small, the respective parameter can be assumed to be non-influential in this context. Generally, scenario C exhibits different parameter dependencies than A, while B can be described as a transition scenario. In C, temperature, flow velocity, molar volume and salinity have the highest impact on S_i. Combined, they only add up to 3% of the total variance of the model output, therefore significant variance is due to non-linear and interaction effects among the parameters, which is quantified by the respective S_{Ti} values. In all scenarios, pH and pore pressure have sensitivity indices of 0, hence they have no impact on the model output. In scenario C, the most sensitive parameter is the fracture aperture, which makes up for over 65% of the variance of the output by itself. To a slight extent, salinity and temperature also have an impact, although $S_{T,sal}$ and $S_{T,T}$ are both below 0.1, indicating at least some interaction. In total, S_i accumulates to approximately 0.8, hence the variance of the model output can mostly be explained by varying the parameters on their own and interaction effects are rather small. Scenario B appears to be somewhere between scenario A and C with regard to the parameter dependencies.

The sensitivity indices for the saturation length scale SLS are slightly differently distributed (Fig. 2.8). Here, scenario A and B reveal similar dependencies on T, u_x and V_m, with near to no primary interaction, but complex parameter interplay. For scenario C, on the other hand, apart from temperature, which has a minimal influence ($S_{T,T} = 0.01$), only flow velocity and fracture aperture determine the model output. All other parameters have a negligible influence. The first-order indices of flow velocity and fracture aperture combined make up for 40% of the variance of the model output. The rest of the variance is primarily determined by interaction effects between these two parameters. Flow velocity and fracture aperture therefore are the most influential parameters for the influencing range along a fracture at higher supersaturation. At lower supersaturation, the parameter dependencies are not as clear.

2.3.4 Scenario Groß Schönebeck

In the sensitivity analyses, all parameters were treated independently from one another. Some parameters that were fixed this way, however, may be dependent on others in a true case scenario. To illustrate

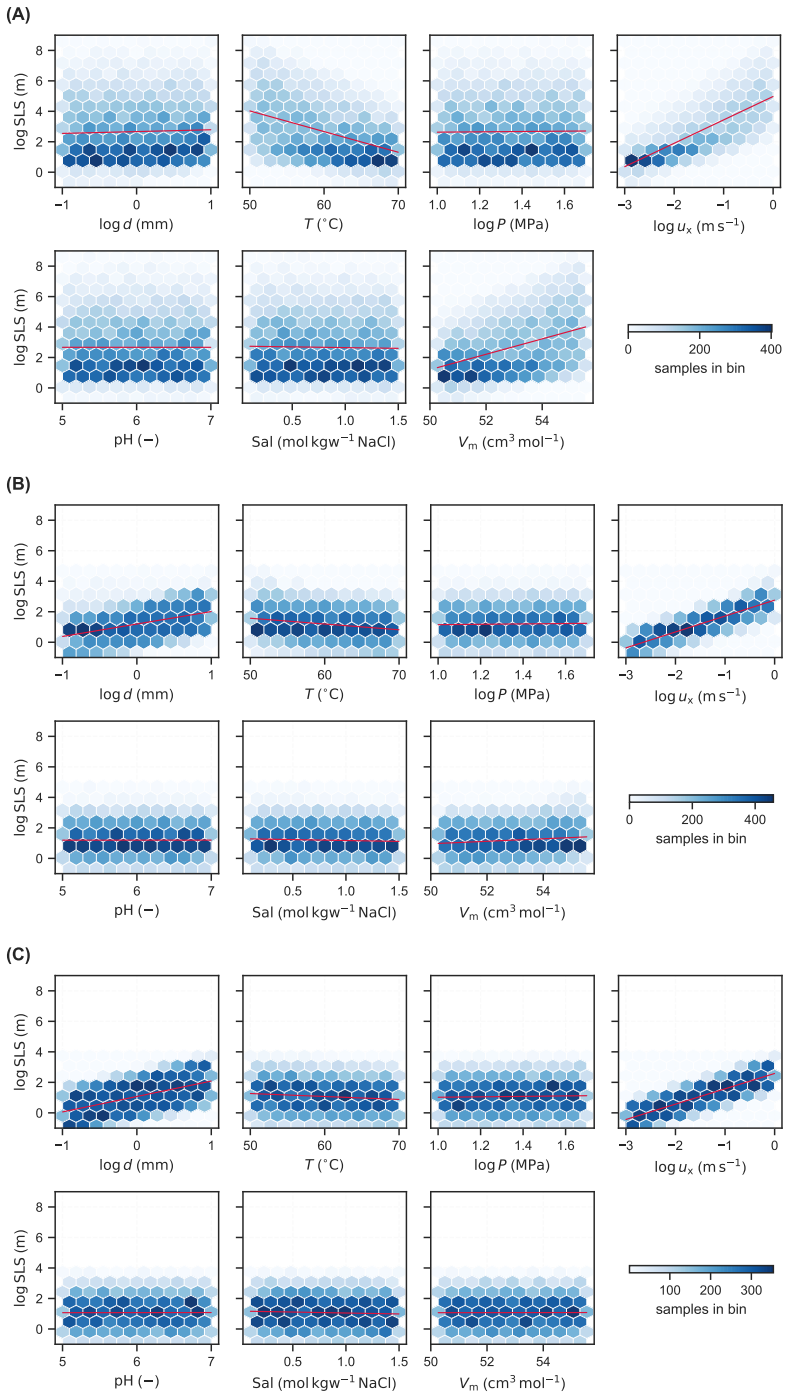

Figure 2.6: Distribution of SLS with regard to varying model parameters for 16 000 model runs obtained from the global sensitivity analysis (Sobol′ 2001). The sampling implemented is based on Saltelli (2002). The solid lines represent the mean trend obtained from linear regression. The color in each hexagon represents the number of results of the model run plotted within the respective area. (A) SR = 15, (B) SR = 20, (C) SR = 30.

the effect of coupled nucleation and crystal growth in a case where supersaturation is dependent on lowering temperature, we applied this model to the Groß Schönebeck site. Here, the equilibrated fluid chemistry was taken as the input condition (Tab. 2.2). The temperature was varied from 25 to 150 °C, and the fracture aperture was varied from 0.1 to 10 mm. All other parameters were kept constant (Tab. A.1). The resulting times for permeability of a fracture to decrease by one order of magnitude (t_{crit}) are shown in Fig. 2.9. Similarly to the previous results, it becomes clear that larger apertures exhibit

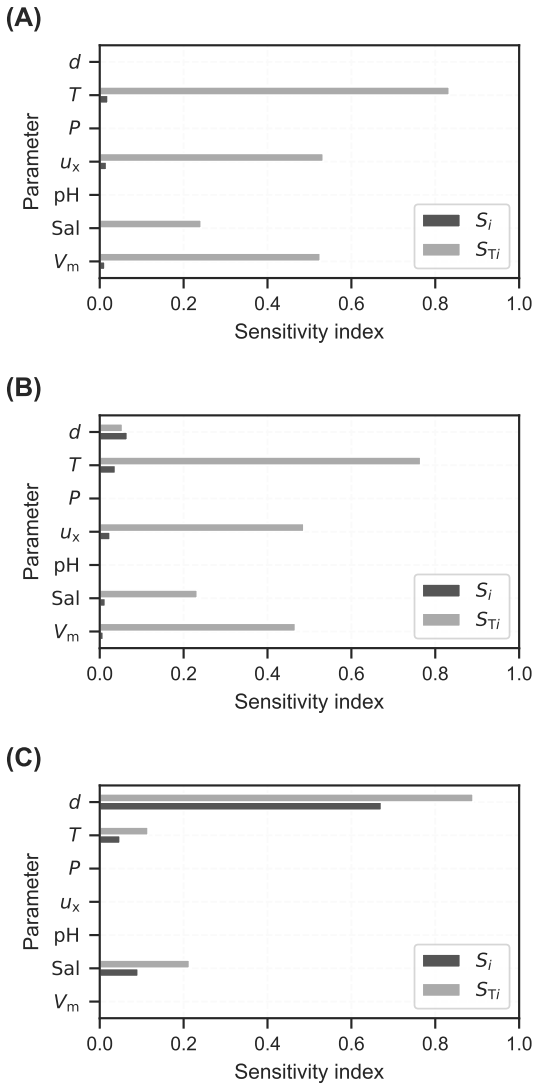

Figure 2.7: First-order S_i and total interaction indices S_{Ti} of the model input parameters with respect to the model output t_{crit}. All values are derived using the variance-based sensitivity analysis based on Sobol′ (2001). (A) SR = 15, (B) SR = 20, (C) SR = 30.

larger t_{crit}. For small apertures (< 1 mm), this is in the range of days, but for larger apertures, this is in the range of months. Three distinct domains on the temperature scale can be seen here. Decreasing the temperature from 150 °C to approximately 90 °C, nucleation begins, as the supersaturation threshold is exceeded. This coincides with a saturation ratio of about 10 (Fig. 2.3). Cooling further down, nucleation rate continues to become stronger up to a point, where nucleations will quickly cover the whole fracture surface (from about 70 °C downwards). From then on, supersaturation will further increase, but the kinetic rate constant, on the other hand, decreases. It can be seen that t_{crit} becomes larger again, which can be attributed to the fact that the kinetic rate constant decreases more strongly than supersaturation increases with regard to Eq. (2.10).

2.4 Discussion

Scaling is a common issue in geothermal systems, as scales may form in the wells and the surface system, but also in the reservoir. Barite is assumed to be originally in equilibrium with the reservoir fluids, since reservoir rock samples contain barite (Regenspurg et al. 2015). As temperature and pressure

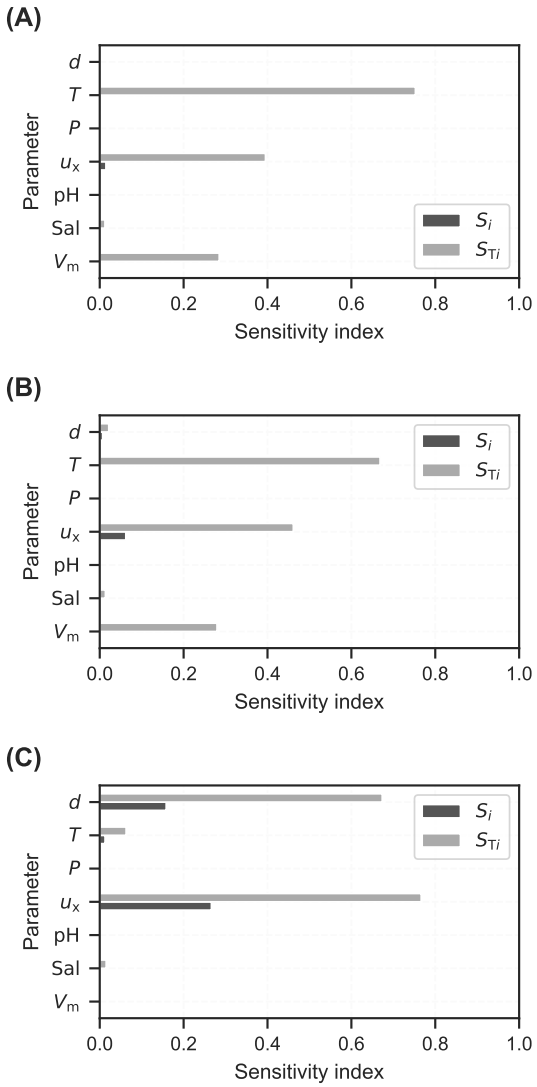

Figure 2.8: First-order S_i and total interaction indices S_{Ti} of the model input parameters with respect to the model output SLS. All values are derived using the variance-based sensitivity analysis based on Sobol′ (2001). (A) SR = 15, (B) SR = 20, (C) SR = 30.

decrease during production, the solubility of barite also decreases (Fig. 2.3), triggering the emergence of barite precipitates along the system pathway. In a continuous production-injection cycle, fluids cool down, while passing through the surface system, after which they are re-injected back into the reservoir through the injection well at about (50 to 70) °C (Griffiths et al. 2016; Zimmermann et al. 2010). The hypothesis is that scales may accumulate in the reservoir behind the injection well over time, if supersaturated fluids are constantly re-injected. This would eventually result in decreased permeabilities and likewise reduced injectivities over time; a highly unwanted effect as there is no solvent applicable for barite available. It is expected that mineral scales will also form before the fluids reach the reservoir, where supersaturation is the highest. Fluids will most likely have their steepest supersaturation gradient somewhere in the surface system near the production well or the heat exchanger. However, due to the low specific surface area compared to the fracture space, the formation of nuclei and subsequently crystal growth kinetics is assumed to be attenuated. Even if nuclei form in the surface system, they may be 'washed' into the reservoir. Therefore, longer shut-in periods potentially pose a problem in this context because in this case there is more time for nuclei to form larger clusters, settle on surfaces, and become immobile. Barite scales have been observed to form in the injection well of the geothermal site

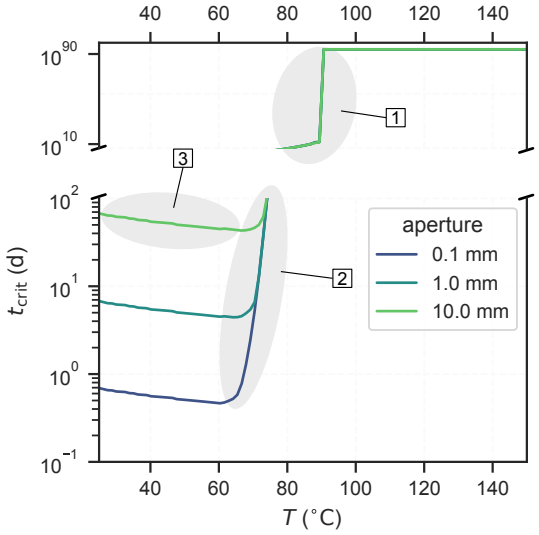

Figure 2.9: Scenario for the Groß Schönebeck site showing the time for permeability of a fracture to decrease by one order of magnitude (t_{crit}) at various apertures. (1): Supersaturation threshold is reached and nucleation begins (note $t_{crit} = 10^{94}$ d represents infinity.). (2): Whole fracture surface is covered with nucleations. (3): Kinetic rate constant decreases more than supersaturation increases. The input chemical state was taken from Tab. 2.2 (equilibrated at 150 °C). The model input file can be seen in Tab. A.1.

Soultz-sous-Forêts (Scheiber et al. 2013), but also to completely seal fractures in this context (Griffiths et al. 2016), supporting the hypothesis.

Numerical experiments were conducted for evaluating under which circumstances barite scales can form and if they potentially have an impact on fracture permeability on a time-scale of a geothermal power plant's lifetime. This was carried out for fractures on the laboratory scale as a precursor to laboratory experiments, but it can be transferred to reservoir scales. In order to capture the high dynamics of a geothermal system and to make estimations on spatial and temporal impacts, a coupled kinetics model was employed. The novel approach is that nucleation on fracture walls as well as crystal growth is taken into account. Other related studies either use an ad hoc precursor crystal surface, thereby circumventing the nucleation mechanism, or simply just use thermodynamics (e.g., Bozau et al. 2015; Griffiths et al. 2016).

The quantities and parameters required for making reliable predictions are to some extent uncertain or variable. A global sensitivity was carried out, using the key figures t_{crit} (Eq. 2.18) for the timescale and SLS (Eq. 2.14) for the range of influence of fracture sealing. System parameters are hereby highlighted that are either under-determined or that are most sensitive for the processes. This can be used as a guideline in practical applications for deciding which of these must be investigated in more detail and which can be neglected. Factors controlling nucleation, such as the interfacial tension or the contact angle, are experimentally under-determined in the respective geothermal in-situ conditions. In other words: the known range of the threshold supersaturation (SR_{th}) is too uncertain in order to predict with the necessary precision whether heterogeneous nucleation will take place in a respective system (Fig. 2.2). Moreover, down-hole parameters, such as saturation state and specific surface area, are not measurable, but each constitutes a decisive impact on scaling mechanisms.

The parameter screening shows that parameters controlling nucleation have the overall largest impact on the model outcome. No detailed information is available with regard to minerals on the fracture wall, accessible to the fluid. While a contact angle of a barite nucleus on quartz, for example, is expected to be high due to their dissimilarity, a much smaller value can be assumed for similar crystal structures, such as celestite. However, detailed data on this is not available in the literature, and furthermore it would vary within a certain range, depending on the reservoir rock. Hence, the whole bandwidth of

possible contact angles between a nucleus and substrate was evaluated. Interfacial tension γ also has a broad range, reported in the literature (Fernandez-Diaz et al. 1990; He et al. 1995; Nielsen and Söhnel 1971; Prieto 2014), and other studies have used it as a fitting parameter for models (e.g., Poonoosamy et al. 2016; Prieto 2014). Furthermore, it becomes obvious from laboratory experiments (Fernandez-Diaz et al. 1990; He et al. 1995) that γ is a system dependent parameter. Although He et al. (1995) proposed a strong dependency on ionic strength and temperature, there still is no comprehensive study available on how to reliably predict γ at varying conditions.

Using the parameter ranges considered, the parameter screening shows that slightly more than 80% of the model-runs terminated because the threshold supersaturation was too high for nucleation to take place. From many experiments and observations it is known, however, that nucleation does take place at respective conditions in geothermal systems (e.g., Kühn 1997; Regenspurg et al. 2015; Zhen-Wu et al. 2016). Currently, it is not possible to predict the threshold supersaturation for nucleation (SR_{th}) with high enough certainty, to definitively foresee if it is overstepped in a system. Though, knowing SR_{th} to a certain degree and its dependencies in a given system is crucial for a long-term operation because once nucleation has taken place, further permeability impairing crystal growth becomes more likely. It is further pointed out that, though heterogeneous nucleation is expected to be the dominant nucleation process, nucleation in the free solution is possible to some degree and is encouraged at increased flow velocities (Poonoosamy et al. 2020b). If these floating nuclei grow to sizeable colloids, clogging and decrease in rock permeability may take place. Thus, investigating these particular parameters in more detail could help to identify which of these can be manipulated in order to mitigate or even control nucleation. We refer to pertinent experimental studies (e.g., Poonoosamy et al. 2016; Poonoosamy et al. 2020a; Zhen-Wu et al. 2016), which are invaluable in narrowing down these uncertainties in geothermal conditions.

To further investigate the role of crystal growth, standard values for γ and θ with regard to barite nucleation in NaCl-solutions were used to fix these, as proposed by He et al. (1994a). The resulting SR_{th} is approximately 10, which coincides well with the results of experiments carried out by Zhen-Wu et al. (2016). There, evidence is reported for heterogeneous nucleation in a NaCl-solution at SR = 32, while none took place at SR = 8. Derived from the fluid composition at the Groß Schönebeck site (Regenspurg et al. 2016), the expected barite supersaturation due to reduced temperatures is on the order of 30 (Fig. 2.3). Although some barite may precipitate along the surface system pathway, it is assumed that fluids will still be supersaturated when they are re-injected into the reservoir. In all three scenarios considered (SR at 15, 20, and 30), SR_{th} is overstepped and crystal growth determines the outcome of the models.

When crystal growth becomes the dominant mechanism ($SR > SR_{th}$), the scenarios outlined show that the parameters fracture aperture, salinity, and temperature are most influential for fracture sealing. The former coincides with the specific reactive surface area within a fracture, while the others influence the kinetic rate constant. This is an important point because the relative amount of fluid in contact with the fracture wall compared to the total amount of fluid in the fracture space is inversely proportional to the fracture aperture. It follows that the permeability of fractures with larger apertures is less affected by mineral scaling over time. More fluid volume can flow through before having the same permeability impairing effect, therefore larger apertures could be a reasonable approach for keeping injection rates stable for a longer period. Therefore, for fracture sealing, a few large fractures are more favourable than producing a finely dendritic fracture network with an equivalent rock permeability.

Temperature and salinity have a strong impact on the precipitation mechanism (Risthaus et al. 2001; Zhen-Wu et al. 2016). Zhen-Wu et al. (2016) confirmed a previously postulated strong dependency of the rate constant on ionic strength (Risthaus et al. 2001) and temperature (Dove and Czank 1995), as well as a negligible influence of pH in the range 5 to 7 (Ruiz-Agudo et al. 2015). The role of temperature in this sense is ambivalent. On the one hand, if fluids are cooled down, the respective supersaturation with regard to barite is increased, which is the main driving force for crystal growth and nucleation. Yet, the kinetic rate for crystal growth is reduced at lower temperatures. The impact of these two effects must

be weighed up in detail for a specific system, to decide which is the ideal temperature. Of course, the necessary heat conversion must be taken into account. For the Groß Schönebeck site, it was shown that cooling fluids down to 70 °C indeed can be seen as a worst case scenario with respect to barite scaling (Fig. 2.9). At these temperatures, the resulting supersaturation and nucleation rate will be high enough to cover the whole fracture surface, leading to a highly reactive surface area for crystal growth. Only at even lower temperatures will the rate constant decrease further to counter this effect to some extent. It should be noted that the threshold supersaturation was assumed to be 10 and that supersaturation is reached instantaneously at the fracture inlet.

Results show further that sealing rates are on the order of days or months (Tab. 2.4, Fig. 2.9). On average, these closing rates are by far smaller than the target lifetime of a geothermally utilised system (tens of years). Griffiths et al. (2016) came to a similar conclusion, who presented a model with regard to the geothermal site Soultz-sous-Forêts. They modelled radial growth of a seed barite crystal within a fracture in order to approximate sealing rates. For a fracture with an aperture of 20 mm, they derived a sealing time of about one month. Indeed, these rates are consistent with observations at various geothermal sites, where significant barite scale build-ups have been reported in the well bore and the surface system within months of production (Griffiths et al. 2016; Nitschke et al. 2014; Regenspurg et al. 2015). Regenspurg et al. (2015) report that approximately two tons of solids precipitated in the production well during the production of 20 000 m^3 fluids at the Groß Schönebeck site; most of the residues in filters in the surface installation were composed of barite. They further report that this may have contributed to reduced flow rates over time.

2.5 Conclusions

This study assesses the impact of barite scaling on fracture permeability in the near field of the injection wells of geothermal systems by numerical simulations. It aims at illustrating the effects of respective parameter ranges on scaling in fractures on the laboratory scale and aids in designing complementary laboratory experiments. The geothermal test-site Groß Schönebeck is used as a basis, but the general physico-chemical conditions are applicable also to other sites, whose fluids exhibit increased Ba-supersaturation. For describing the precipitation mechanisms, a one-dimensional transport model is coupled with a two-step precipitation model that accounts for heterogeneous nucleation on fracture walls using classical nucleation theory as well as subsequent crystal growth kinetics using PHREEQC. A screening and sensitivity analysis with respect to fracture sealing times outlines, which of the hereby introduced parameters are most influential.

Nucleation and crystal growth both depend on supersaturation. Crystal growth is expected to only play a role, if nuclei have formed on the fracture wall. This happens if the respective threshold supersaturation is overstepped, which is determined by the interfacial tension and the contact angle. In the given range, these are the most influential parameters on the overall model outcome. In order to be able to predict the threshold supersaturation with sufficient certainty, these factors need to be determined in more detail in the laboratory and at in-situ conditions of geothermal applications.

Screening the parameter ranges shows that the threshold supersaturation is exceeded for a relevant chemical fluid composition, if temperature and pressure are reduced along the pathway of a geothermal power plant. In this case, crystal growth becomes the overall determining process, which is mainly controlled by the specific reactive surface area and the reaction mechanism. The surface area available in a fracture in proportion to the fluid is primarily defined by its aperture, while the rate constant depends on the fluid's temperature and salinity. The median times for fractures sealing are on the order of days or months. On average, these rates are considerably smaller than the economically required target lifetime of a geothermally utilised system, which is on the order of tens of years.

The presented results give time estimates for the impairing effect of barite scaling on fracture permeability and point out that they do pose a serious threat for the injectivity of geothermal wells,

if the supersaturation threshold is exceeded. The lowering of temperature along the system pathway increases supersaturation and requires site specific assessment, as it also determines the amount of heat that can be harnessed. This is countered to some degree because lower temperatures also result in slower kinetic rates, hence these effects must be weighed up. The model outlined constitutes a tool for predicting and quantifying the temperature range, which is advisable for the fluid injection temperature. It is further advised rather to produce few fractures with large apertures than many with small apertures during hydraulic stimulation, to minimise sealing times.

CHAPTER 3

Reactive transport model of kinetically controlled celestite to barite replacement

This is a reprint of an article published in the journal Advances in Geosciences (Copernicus)[1] *.*

Abstract

Barite formation is of concern for many utilisations of the geological subsurface, ranging from oil and gas extraction to geothermal reservoirs. It also acts as a scavenger mineral for the retention of radium within nuclear waste repositories. The impact of its precipitation on flow properties has been shown to vary by many orders of magnitude, emphasising the need for robust prediction models. An experimental flow-through column setup on the laboratory scale investigating the replacement of celestite ($SrSO_4$) with barite ($BaSO_4$) for various input barium concentrations was taken as a basis for modelling. We provide here a comprehensive, geochemical modelling approach to simulate the experiments. Celestite dissolution kinetics, as well as subsequent barite nucleation and crystal growth were identified as the most relevant reactive processes, which were included explicitly in the coupling. A digital rock representation of the granular sample was used to derive the initial inner surface area. Medium (10 mM) and high (100 mM) barium input concentration resulted in a comparably strong initial surge of barite nuclei formation, followed by continuous grain overgrowth and finally passivation of celestite. At lower input concentrations (1 mM), nuclei formation was significantly less, resulting in fewer but larger barite crystals and a slow moving reaction front with complete mineral replacement. The modelled mole fractions of the solid phase and effluent chemistry match well with previous experimental results. The improvement compared to models using empirical relationships is that no a-priori knowledge on prevailing supersaturations in the system is needed. For subsurface applications utilising reservoirs or reactive barriers, where barite precipitation plays a role, the developed geochemical model is of great benefit as only solute concentrations are needed as input for quantified prediction of alterations.

3.1 Introduction

Utilised subsurface systems are often affected by continuous changes in rock properties due to water-rock-interaction. There are applications, where mineral precipitation or dissolution induced rock alterations are intended, e.g., in reactive barriers for nuclear waste repositories (Curti et al. 2019). In other cases, they are an unwanted side effect, for example, barite scalings in geothermal systems or during oil and gas extraction, where they can induce a massive loss of injectivity or productivity (Tranter et al. 2020). A comprehensive understanding of the reactive processes taking place is crucial, so they

[1]Morgan Tranter et al. (2021c). Reactive Transport Model of Kinetically Controlled Celestite to Barite Replacement. *Advances in Geosciences* 56:57–65. DOI: 10.5194/adgeo-56-57-2021.

can be incorporated into prediction models that anticipate and quantify the behaviour of the system, paving the way for a successful utilisation. As opposed to commonly applied empirical formulations for describing rock property alterations, process-based models are more robust and flexible. In order to develop reactive transport models that are applicable to a broad range of boundary conditions and scenarios, it is necessary to identify, parametrise and calibrate the relevant processes with the aid of laboratory experiments.

A recent experimental study investigated the role of barite supersaturation on its precipitation mechanisms caused by concurrent celestite dissolution (Poonoosamy et al. 2020b). To this aim, quasi one-dimensional flow-through column experiments were conducted, providing insights into pore-scale evolution during mineral exchange reactions. Three different orders of magnitudes of barite supersaturation were applied, where each caused different precipitation patterns. The authors identified barite nucleation as a key process that becomes increasingly relevant at higher supersaturations. Nuclei formation increases exponentially with supersaturation, and in turn creates reactive surface area for consecutive crystal growth (Lasaga 1998). Thus, at high input concentrations, a passivation effect occurred due to complete or partial coverage of the celestite grains, preventing any further dissolution. At low input concentrations, nucleation played a lesser role, enabling the replacement reaction to take place. The authors tested the validity of conceptual models to describe precipitation induced reactive surface area development together with celestite dissolution kinetics and barite equilibrium reactions. They concluded that a single empirical relationship is insufficient, but rather two or more are needed to represent the observed responses at all input concentrations. However, it remains open which saturation threshold is to be used for switching instances, and how transition ranges should be treated.

In this study, we provide a comprehensive geochemical modelling approach to match the reported experimental responses. A digital rock representation of the granular celestite sample was applied. The derived rock properties were then used as initial conditions for one-dimensional reactive transport simulations. Next to bulk dissolution and precipitation kinetics, process-based heterogeneous nucleation applying classical nucleation theory and geometrical crystal growth were considered in the coupling. The modelled mineral phase volume fractions in the column and effluent chemistry were compared to the experimental results.

3.2 Methods

3.2.1 Experimental setup

A detailed description of the considered laboratory experiment is given in Poonoosamy et al. (2020b). The flow-through core experiment consisted of a granular celestite section (11 mm) enclosed by granular quartz sections on both ends (17 and 4 mm, respectively). Each cylindrical section was filled up with respective grains and then packed to attain a target porosity of 46%. The core diameter is 10 mm, thus it can be assumed to be a one-dimensional problem. In three such columns, $BaCl_2$-solutions with concentrations of 100, 10, and 1 mM, respectively, were injected for a duration of 500 h. Temperature and pressure were constant 25 °C and 0.1 MPa, respectively. Initial pH was reported to be 5.6. The influent is undersaturated with respect to celestite, causing celestite to dissolve. Due to the release of SO_4^{2-}-ions into solution the fluid becomes supersaturated with respect to barite, causing barite to precipitate. The injection flow rate Q was kept constant at $2.5 \cdot 10^{-10}$ m^3/s. The chemical composition (Ba^{2+}, Cl^-, Sr^{2+}, SO_4^{2-}) of the effluent was measured multiple times over the course of the experiment duration. After the injection period, the columns were cut into slices to investigate the chemical and structural alterations in the porous sections.

3.2.2 Reactive transport modelling

One-dimensional reactive transport simulations were carried out using the PHREEQC (Parkhurst and Appelo 2013) software code (version 3.6.2) to model the experiment. Only the enclosed celestite section was considered, as the quartz sections were assumed to be unreactive. The model domain was discretised into a regular grid of 30 elements each with a length of 0.37 mm (Fig. 3.1).

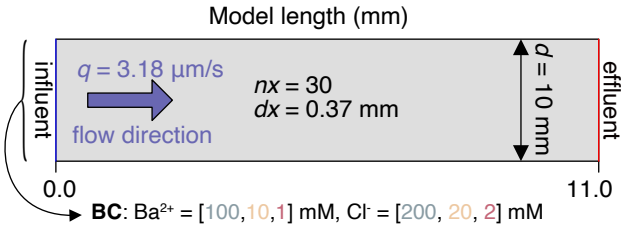

Figure 3.1: Numerical setup of the simulations based on the laboratory experiment from Poonoosamy et al. (2020b). Initial conditions in the column are $\varphi = 0.46$, $\varphi_{SrSO_4} = 0.56$, $\varphi_{BaSO_4} = 0.0$, SSA = 87 900 m^2/m^3 (this study), $Sr^{2+} = 0.621$ mM, $SO_4^{2-} = 0.621$ mM, $Ba^{2+} = 0$ mM, $Cl^- = 0$ mM. BC shows the boundary conditions of the flux inflow.

Flow velocity q was set to a constant value of 3.18 µm/s.

$$q = \frac{Q}{A} = \frac{4Q}{\pi d^2}$$

Feedback of porosity changes to pore flow velocity was not considered, as the final porosity decrease in the experiments from 0.46 to 0.43 only has a negligible influence. Diffusion was disregarded for solute transport as it is an advection-dominated system (Pe $\gg$ 1). At each integration step, PHREEQC calculates transport then kinetics in serial. In addition, nucleation and crystal growth were calculated in between advection and kinetics steps, altering the reactive surface areas. The reactive processes are shown schematically in Fig. 3.2.

Digital celestite sample

To determine the initial inner surface area of the celestite sample, a well sorted granular sample was generated exhibiting a grain size equivalent to the laboratory experiment. Therefore, the discrete element method (DEM) of Al Ibrahim et al. (2019) is applied. This approach considers interactions between individual particles, which are successively deposited under the influence of gravity. Combined with an additional grain cementation, this method enables to construct virtual sandstone samples with granulometric, hydraulic and elastic properties equivalent to those of the natural sample (Wetzel et al. 2020a, 2021). The geometry of the DEM is converted into a digital image comprising a rectangular uniform grid, in order to compute geometrical properties and perform additional grain pack alterations. The porosity of the very well sorted grain pack is with 38% considerably lower than that of the celestite sample from Poonoosamy et al. (2020b). For the reason of comparability, grain sizes of the deposited grain pack are uniformly reduced until the porosity of 46% is achieved. Finally, the constructed virtual sample (Fig. 3.3) comprises 3 198 individual grains with a mean diameter of 42 µm. The inner surface area of $8.79 \cdot 10^4$ m^2/m^3 is determined using MorphoLibJ (Legland et al. 2016).

Kinetics

Reaction kinetics for celestite dissolution and barite precipitation were taken into account. Solid-solutions were not taken into account. Dissolution of celestite and the successive release of SO_4^{2-} into solution causes barite to precipitate (Fig. 3.2):

$$Ba^{2+}_{(aq)} + SrSO_{4,(s)} \rightarrow BaSO_{4,(s)} + Sr^{2+}{}_{(aq)} \tag{3.1}$$

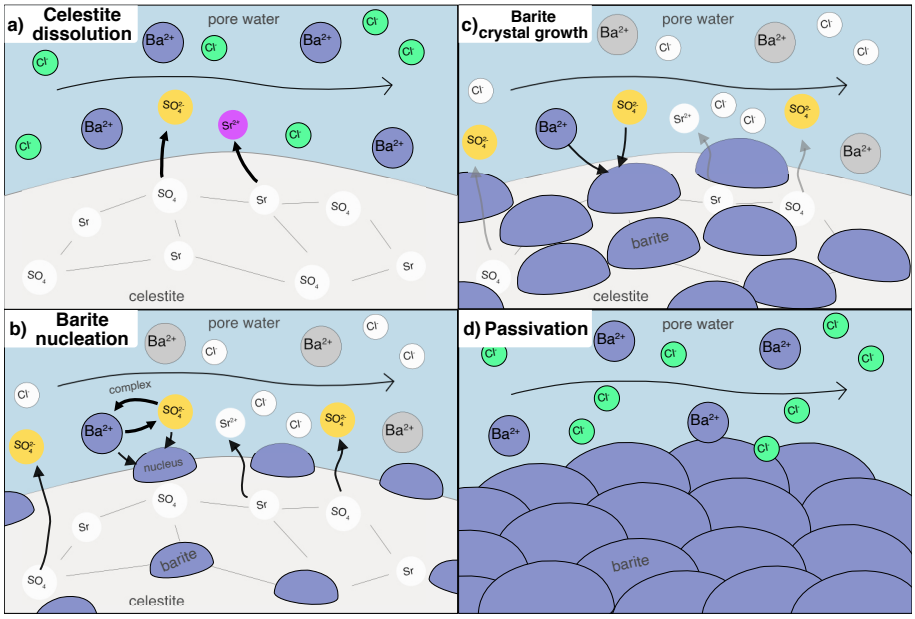

Figure 3.2: Conceptual illustration of the considered processes in the reactive transport simulations. (a) Celestite dissolves after $BaCl_2$ solution is injected into the column, as the solution is undersaturated with respect to celestite. (b) Heterogeneous barite nucleation on celestite substrate sets in after a barite supersaturation threshold is exceeded. The more celestite dissolves, the more sulfate is in solution, increasing barite supersaturation. (c) Creation of barite reactive surface area causes bulk precipitation to happen and the precipitated nuclei to grow. (d) When nucleation and crystal growth are fast, the celestite substrate may overgrow with barite crystals, leading to a passivation of the system.

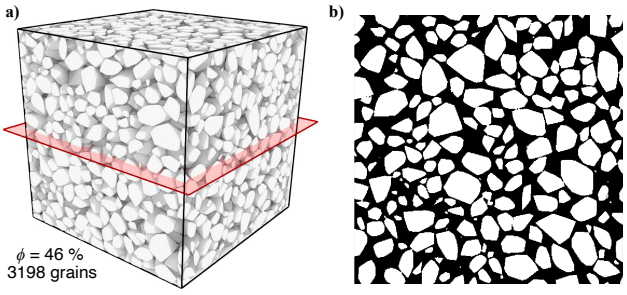

Figure 3.3: a) Three dimensional virtual sample of well sorted celestite grains with a mean grain diameter of 42 µm is used to determine the inner surface area. b) Two-dimensional slice through the virtual celestite grain pack (red plane in a).

Reaction rates are calculated using a general kinetics rate law for both dissolution and precipitation based on transition state theory (Lasaga 1998):

$$\frac{\mathrm{d}m_m}{\mathrm{d}t} = -\mathrm{SA}_m \, k_{\mathrm{r},m} \, (1 - \mathrm{SR}_m) \tag{3.2}$$

where dm (mol/s) is the rate of a mineral phase m, SA (m^2) is the reactive surface area, k_r (mol/m^2/s) is the rate constant, and SR (-) is the saturation ratio, i.e., the ratio of the ion activity product of the reacting species and the solubility constant. The saturation ratio is calculated with PHREEQC using the provided `phreeqc.dat` database. The dissolution rate constant of celestite is calculated at each kinetic step following the approach of Palandri and Kharaka (2004), using data from Dove and Czank (1995). For calculating the precipitation rate constant of barite, a linear regression was used that accounts for

temperature and ionic strength, which have been shown to have a significant impact (Tranter et al. 2021b; Zhen-Wu et al. 2016):

$$\log_{10} k_{\mathrm{r,barite}} = -\frac{2532}{T} + 0.694\sqrt{I} + 0.29 \tag{3.3}$$

where T (K) is the temperature and I (M) is the ionic strength of solution.

Nucleation

Classical nucleation theory was applied to calculate heterogeneous formation of barite on celestite substrate. Nucleation describes the spontaneous formation of stable clusters of a supersaturated phase. The formation of nuclei has the following impacts on reactive transport: (1) reactive surface area of the nucleating phase is created, which increases the subsequent precipitation rate, (2) minor amount of phase substance is precipitated, (3) substrate area is covered and therefore its reactive surface area is decreased (Fig. 3.2b).

Here, we followed the approach as reported in Prieto (2014) and Tranter et al. (2021b). The heterogeneous nucleation rate J (1/s) is calculated with

$$J = \Gamma \exp\left(\frac{\mathrm{d}G^*}{k_\mathrm{B}\, T\, \ln \mathrm{SR}}\right) \tag{3.4}$$

with the bulk free energy change $\mathrm{d}G^*$ (J):

$$dG^* = \frac{1}{4}(2 - 3\cos\theta + \cos^3\theta)\frac{\beta\,\gamma^3\,V_\mathrm{m}^2}{(R\,T\ln \mathrm{SR})^2} \tag{3.5}$$

where Γ ((1/t) is a pre-exponential factor, θ is the fitted contact angle of a nucleus and the substrate, β is a shape factor for spherical nuclei ($= 16\pi/3$), γ is the interfacial tension of the nucleating phase set to 0.134 J/m^2 (Prieto 2014), V_m (m^3/mol) is the molar volume of the nucleating phase set to $5.29 \cdot 10^{-5}$ m^3/mol (taken from `phreeqc.dat`), R (J/K mol) is the gas constant, and k_B (J/K) is Boltzmann's constant. The pre-exponential factor accounts for the attachment rate of monomers to a sub-critical nucleus:

$$\Gamma = \Gamma_0 \frac{Z\,D_m\,N_1\,N_0\,\mathrm{SA_{N-L}}}{r_\mathrm{N,crit}} \tag{3.6}$$

with the Zeldovic factor

$$Z = \left(\frac{dG^*}{3\pi\,k_\mathrm{B}\,T n_\mathrm{c}^2}\right)^{\frac{1}{2}} \tag{3.7}$$

where Γ_0 (1/s) is a fitting factor, D_m is the molecular diffusion coefficient set to $1 \cdot 10^{-9}$ m^2/s, N_0 (1/m^3) is the number of nucleation sites on the substrate ($= \mathrm{SA_S/SA_{N-S}}$), N_1 (1/m^3) is the number of available monomers in solution, and n_c is the number of monomers in a critical nucleus. As a precursor for nucleation, the neutral complex $[BaSO_4]^0$ was chosen, which was calculated with PHREEQC at each time step. The radius of a spherical, critical nucleus is calculated with

$$r_\mathrm{N,crit} = \frac{2\,\gamma\,V_\mathrm{c}}{k_\mathrm{B}\,T\,\ln \mathrm{SR}} \tag{3.8}$$

and its respective interfaces with the solution and the substrate are

$$\mathrm{SA_{N-L}} = \pi\, r_\mathrm{N}^2(1 - \cos^2\theta) \tag{3.9}$$

$$\mathrm{SA_{N-S}} = 2\pi\, r_\mathrm{N}^2(1 - \cos\theta) \tag{3.10}$$

where V_c is the volume of a monomer ($= V_m/N_A$). The changes in reactive surface areas were calculated at each time step for the nucleating and substrate phase:

$$\mathrm{dSA}_{\mathrm{barite},i} = J\,dt\,\mathrm{SA}_{\mathrm{N-L}} \tag{3.11}$$

$$\mathrm{dSA}_{\mathrm{celestite},i} = -J\,dt\,\mathrm{SA}_{\mathrm{N-S}} \tag{3.12}$$

For the following crystal growth step, the mean nucleus radius and total amount of nuclei in a cell were tracked. Only one mean nucleus size was taken into consideration for each cell. The precipitated phase amount in nuclei was taken into consideration and added to the system.

Crystal growth

Crystal growth was implemented as the homogeneous, three-dimensional spatial growth of barite nuclei. The basic geometry of a sphere cap nucleus was maintained, i.e., contact angle θ was kept constant, and only its radius was increased based on the added volume from bulk precipitation kinetics.

$$\mathrm{d}V_{\mathrm{barite}} = V_{\mathrm{m,barite}}\,\mathrm{d}m_{\mathrm{barite}} \tag{3.13}$$

In practical terms, the radius of a sphere-cap corresponds to a crystal height—or a rim thickness if we consider the overgrowth of a substrate material—which can be calculated with:

$$\mathrm{rim} = r_{\mathrm{N}}\,(1 - \cos\theta) \tag{3.14}$$

The mean nucleus volume in a cell at a time step i was calculated with its radius of the previous time step and the amount of newly precipitated phase volume from bulk precipitation.

$$V_{\mathrm{N},i} = r_{\mathrm{N},i-1}^3 \frac{\pi}{3}(2 - 3\cos\theta + \cos^3\theta) + \mathrm{d}V_{\mathrm{barite},i} \tag{3.15}$$

The new corresponding mean nucleus radius $r_{\mathrm{N},i}$ was saved for consecutive nucleation and crystal growth steps. The change of nucleus-solution and nuclei-substrate interfaces, as well as the total reactive surface areas of barite and celestite can then be derived:

$$\mathrm{dSA}_{\mathrm{barite},i} = n_{\mathrm{N}}\,\mathrm{SA}_{\mathrm{N-L}} \left(1 - \left(\frac{V_{\mathrm{N},i}}{V_{\mathrm{N},i-1}}\right)^{\frac{2}{3}}\right) \tag{3.16}$$

$$\mathrm{dSA}_{\mathrm{celestite},i} = -n_{\mathrm{N}}\,\mathrm{SA}_{\mathrm{N-S}} \left(1 - \left(\frac{V_{\mathrm{N},i}}{V_{\mathrm{N},i-1}}\right)^{\frac{2}{3}}\right) \tag{3.17}$$

Crystal growth was skipped if the celestite surface was completely covered ($\mathrm{SA}_{\mathrm{celestite}} = 0$).

3.3 Results

For matching the results of the reactive transport simulations with the experimental data, only the nucleation process was calibrated manually. By adjusting θ and Γ_0 to 32° and $7.0 \cdot 10^{-18}$ 1/s, these were found to be the best matching values to reproduce the experimental data with respect to effluent chemistry and mineral substance amount in the column. The results of the simulations using these parameters are presented in the following.

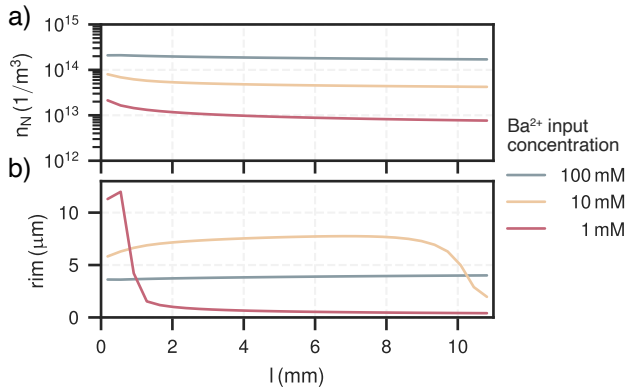

Figure 3.4: Spatial distribution of nuclei (a) and their corresponding radius (b) in the column for all experiments.

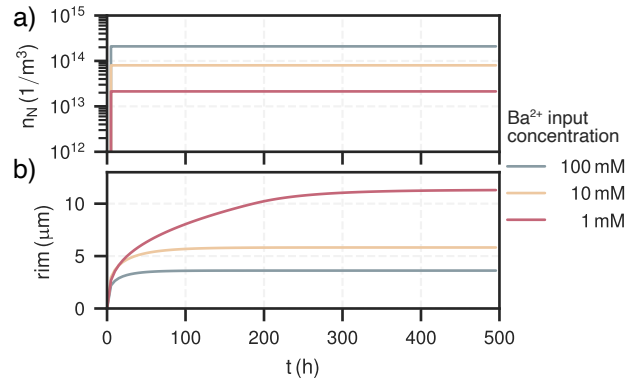

Figure 3.5: Temporal distribution of nuclei (a) and their corresponding rim thickness (b) in the first cell (0-0.37 mm) over the course of the experiment for all experiments.

3.3.1 Nucleation and crystal growth

The amount of nuclei and mean rim thicknesses were tracked for each cell. They are shown for all experiments for the length of the column after the experiment in Fig. 3.4a–b and for the first cell over the course of the experimental duration in Fig. 3.5a–b.

The amount of nuclei are evenly spread along the column for all experiments, ranging from $1 \cdot 10^{13}$ 1/m^3 to $2 \cdot 10^{14}$ 1/m^3. The experiment with $Ba^{2+}_{in} = 100$ mM had the most nuclei overall, about ten-times as many as the experiment with $Ba^{2+}_{in} = 1$ mM, which had the least. The nucleation process is characterised by a surge of nuclei formation in the beginning of the experiment within the first few hours (< 10 h). The early barite crystal rim thickness after the initial surge at around 10 h is similar for all cases, about 2 µm. Increase in size hereafter is solely due to bulk precipitation and crystal growth. Crystals in the experiment with high input concentration ($Ba^{2+}_{in} = 100$ mM) reach their final rim thickness of 4 µm after about 80 h, which are homogeneous throughout the column. In the medium input concentration experiment ($Ba^{2+}_{in} = 10$ mM), crystal sizes are proportional to the mole fraction of barite, reaching rim thickness between about (2–8) µm. The growth phase in each cell is only short-lived and happens within the moving reaction front, where the reactive surface area of celestite concurrently goes towards zero. Consequently, celestite dissolution rate and barite precipitation rate both also go towards zero. At the rear end of the column ($l > 9$ mm), crystal sizes are smaller because the reaction front has not reached this section yet. The low input concentration experiment ($Ba^{2+}_{in} = 1$ mM) mainly exhibits crystal growth in the first two millimeters of the column, although continuously until all celestite is dissolved (rim thickness up to 12 µm). Similar to the medium input concentration, barite crystals only grow within a sharp reaction front, which travelled about 1 mm in the low concentration mode.

3.3.2 Effluent chemistry and column mineral content

The effluent breakthrough curves from the reactive transport simulations are shown together with measured values from laboratory experiments for input concentrations 100 mM, 10 mM, and 1 mM in Figs. 3.6a, 3.7a, and 3.8a, respectively. The respective summed total mineral phase amounts of barite and celestite in the column are shown over the course of the experiment in Figs. 3.6b, 3.7b, and 3.8b. The corresponding mole fractions of barite and celestite at the end of the experiment are depicted in Fig. 3.9a–c. For all experiments, chloride stays constant after the advection front has reached the end of the column, equal to the injected concentration.

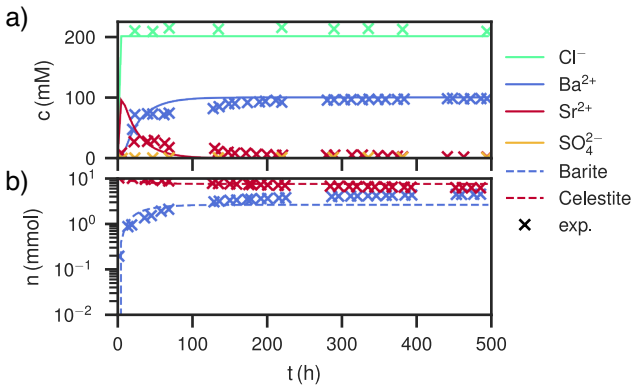

Figure 3.6: Comparison of experimental (Poonoosamy et al. 2020b) and simulation results for barium input concentration Ba^{2+} = 100 mM. (a) Breakthrough curves of the effluent, i.e., the chemical composition (Ba^{2+}, SO_4^{2-}, Sr^{2+}, Cl^-) of the last cell over the course of the experiment. (b) Total barite and celestite phase amount in the column over the course of the experiment.

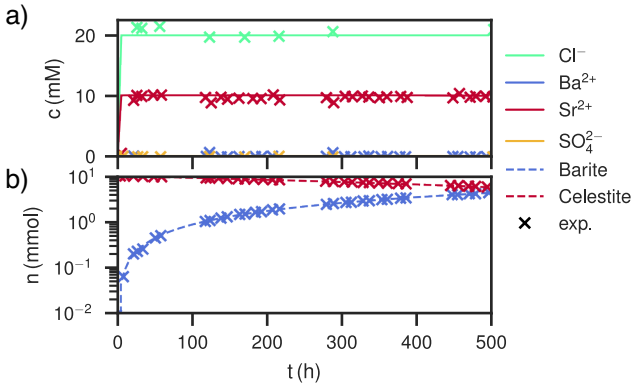

Figure 3.7: Comparison of experimental (Poonoosamy et al. 2020b) and simulation results for barium input concentration Ba^{2+} = 10 mM. (a) Breakthrough curves of the effluent, i.e., the chemical composition (Ba^{2+}, SO_4^{2-}, Sr^{2+}, Cl^-) of the last cell over the course of the experiment. (b) Total barite and celestite phase amount in the column over the course of the experiment.

High Ba^{2+} input concentration results in a peak concentration of almost 100 mM newly dissolved Sr^{2+}, arriving together with the chloride concentration, which slowly levels off over the course of 150 h (Fig. 3.6a). Contrastingly, Ba^{2+} breaks through with concentrations below 1 mM and then increases quickly, reaching the input concentration of 100 mM asymptotically after about 150 h. The calculated sulfate concentrations are always comparably small, but correspond to equilibrium conditions with respect to celestite in the beginning (< 10 h) and barite in the end (> 150 h). The measured values are matched well, except for Sr^{2+} had a lower peak (Fig. 3.6a). The total amount of substance in the column showed a continuous barite increase and celestite decrease in the first 80 h and then stays constant for

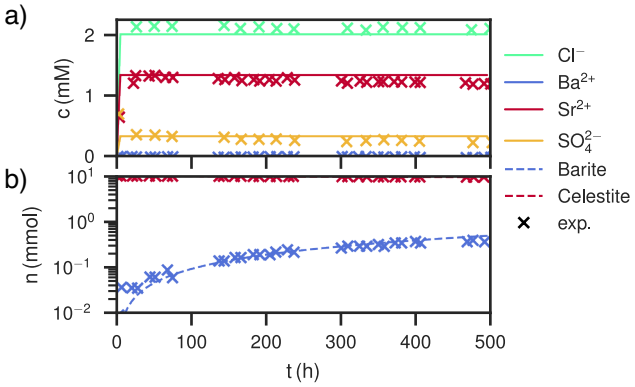

Figure 3.8: Comparison of experimental (Poonoosamy et al. 2020b) and simulation results for barium input concentration Ba^{2+} = 1 mM. (a) Breakthrough curves of the effluent, i.e., the chemical composition (Ba^{2+}, SO_4^{2-}, Sr^{2+}, Cl^-) of the last cell over the course of the experiment. (b) Total barite and celestite phase amount in the column over the course of the experiment.

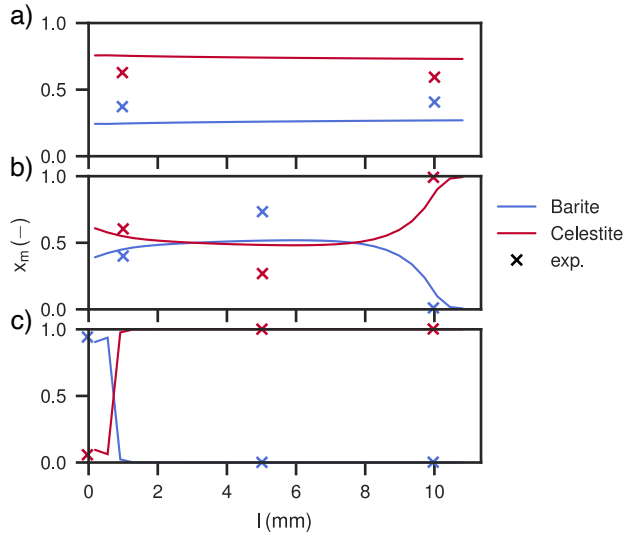

Figure 3.9: Mole fractions of barite and celestite in the column after the duration of experiments one (a), two (b) and three (c). Shown are also mole fractions derived in the experimental study (Poonoosamy et al. 2020b). Only barite and celestite are present in the column.

the rest of the time. The distribution in the column is homogeneous, with mole fractions ranging from $x_{\text{barite}} = 0.32$ at the entrance of the column to $x_{\text{barite}} = 0.37$ at the exit. Measured data correspond to slightly more precipitated barite ($x_{\text{barite}} = 0.37$ and $x_{\text{barite}} = 0.40$, respectively).

The medium input concentration experiment shows a quick increase of Sr^{2+} in the breakthrough curve together with chloride in the beginning, reaching 10 mM and staying constant for the remainder of the experiment (Fig. 3.7a). Sulfate concentration always corresponds to equilibrium with respect to celestite in the order of 0.1 mM. Ba^{2+} is in the order of 0.01 mM in the beginning, but gradually increases to 0.1 mM. The measured values are reproduced. During the whole time, the total amount of barite in the column increases linearly, while the amount of celestite decreases. After the experiment, the mole fraction of barite slightly increases along the column length up to 7 mm from 0.4 to about 0.5. From there on, the content decreases to zero again.

At low input concentrations, all species concentrations in the effluent are constant over the whole period (Fig. 3.8a), matching the laboratory data. Sr^{2+} is about 1.34 mM, SO_4^{2-} is about 0.34 mM and Ba^{2+} is about 10^{-4} mM, all corresponding to equilibrium with respect to celestite and barite. The amount of

barite in the column increases continuously over time, but less than for the medium input concentration experiment. The mole fractions along the column length at the end show that precipitation only happened in the first millimeter of the column, whereas the rest is mostly undisturbed. Close to complete mineral replacement happened at the entrance of the column.

3.4 Discussion

Continuum scale reactive transport simulations were applied to match the experimental results. Barite precipitation likewise caused the reactive surface area of barite to increase and that of celestite to decrease, up to five orders of magnitude. These large variations justify to take dissolution kinetics of celestite and precipitation kinetics of barite into account (Lasaga 1998). The precipitation mechanism of barite was identified to consist of two steps, heterogeneous nucleation on celestite substrate and subsequent growth of these nuclei to become larger crystals. Nucleation was treated deterministically with the classical theory (Kashchiev and van Rosmalen 2003). Crystal growth was implemented as the averaged geometrical growth of nuclei bodies, where the volume increase was taken from bulk precipitation rate.

The overgrowth of celestite with barite crystals had a passivation effect at high and medium input concentrations (Ba^{2+}_{in} = 100 mM and Ba^{2+}_{in} = 10 mM). This happened when a high enough number of nuclei formed during the initial surge of nucleation. The subsequent crystal growth covered all the celestite surface and prevented any further dissolution. At low supersaturations (i. e., for Ba^{2+}_{in} = 1 mM), the passivation effect was not observed, since significantly fewer nuclei formed in the beginning. Thus, fewer barite crystals grew to larger sizes compared to the experiments with 100 mM and 10 mM input concentration, covering the celestite surface only in parts. Therefore, a complete mineral replacement took place.

The modelled distribution patterns of barite crystals match well with the SEM images of the laboratory experiments for all input concentrations (Poonoosamy et al. 2020b). The experiment with high input concentration showed celestite grains overgrown uniformly with a thin barite rim ($\sim$ 3 µm). The other two experiments showed distinct zonation patterns across the column with mineral phase substitution of different degrees. The medium input concentration mode exhibited a transition zone in the center with thicker rims ($\sim$ 5 µm) and generally decreasing barite content on either end of the column. At low $BaCl_2$ input concentration, a sharp reaction front at the upstream was observed, where the average thickness of overgrowth was about $\sim$ 7 µm. Simulated crystal sizes are slightly larger, corresponding to final rim thicknesses of 4 µm, 8 µm, and 12 µm for experiments with high, medium, and low input concentration, respectively.

Nucleation was parametrised assuming spherical cap shaped nuclei and a respective interfacial tension from the literature (Prieto 2014). Two parameters were fitted to match the laboratory experiments: Γ_0 and θ. Γ_0 is part of the pre-exponential factor Γ of the nucleation rate (Eq. (3.4)), which quantifies the diffusive attachment rate of monomers from solution to sub-critical clusters. Compared to the exponential term, where parameter uncertainties are much more significant, approximating the order of magnitude of Γ is usually sufficient. However, many of the parameters for calculating Γ are challenging to quantify. It is uncertain, how many monomers in the pore fluid actually play a role in the nucleation process, or if only monomers in the diffusive layer surrounding the substrate should be considered. Furthermore, the available nucleation sites can only be judged from the total substrate surface area and the approximate size of a nuclei. Calibrating Γ_0 accounts for these uncertainties in the considered system. The contact angle θ of the nuclei and the substrate depends on the structural similarity between the substances. At 180° the contact is practically only one point, at 0° the nucleating phase completely 'wets'the substrate. The fitted value of 32° accounts for the similarity between barite and celestite, both crystallise in the orthorhombic system. It also compares well to the value of 30° used by Poonoosamy et al. (2016) for a similar system.

Modelling all three experiments with empirical relationships required at least two different models to account for the reactive surface area evolution (Poonoosamy et al. 2020b). However, for the modeller it remains impossible to know which empirical relationship to use a-priori. Furthermore, they seem insufficient to be used for the transitional case (Ba^{2+}_{in} = 10 mM). In this study, the identified chemistry-based processes are taken into consideration explicitly in coupled models. The resulting transient reactive surface areas are used in both kinetic rates for barite and celestite, compared to only celestite kinetics and barite equilibrium reactions (Poonoosamy et al. 2020b). After calibration of the here provided models, the effluent and column chemistry of laboratory experiments at medium (10 mM) and low (1 mM) barium input concentrations could be reproduced almost exactly, and at high (100 mM) input concentration the match was good with slight deviations. The main benefit is that no knowledge of the supersaturation in the system has to be known in advance, which also solves the transitional case well (medium input concentration).

Calibration of the presented models may be improved by further refining the grid size and increasing the iteration steps of nucleation and crystal growth between transport steps, thus coupling them more tightly together with the kinetics solver. However, model run times on a regular desktop working machine (2,3 GHz Quad-Core Intel Core i5) were in the range (12–20) h for one experiment run on a single CPU with 30 grid elements. Increasing the grid size would make manual calibration unfeasible due to too long model run times. In future work, this could be solved by using approaches for chemistry speed-ups in reactive transport simulations (De Lucia and Kühn 2021). Furthermore, a more detailed crystal size distribution map using digital pore-scale models instead of mean values in each cell may improve determination of transient reactive surface areas. However, nucleation happens predominantly in the beginning, thus the comparably low amount of new nuclei later on in the experiment do not change the mean crystal size of each cell significantly. The assumption of tracking only one mean size per cell appears sufficient as the models can describe the investigated system qualitatively well and moreover the data basis does not cover this in enough detail.

3.5 Conclusions

A geochemical modelling approach was presented to simulate barite formation in a celestite grain packed column. Celestite dissolution and barite precipitation kinetics, as well as barite nucleation and barite crystal growth were included explicitly as processes in the model coupling. After calibration of the nucleation process, of the three different precipitation patterns observed in the experiments, two were reproduced almost exactly and one was matched qualitatively well by only varying the input concentration. Compared to previous modelling approaches using various empirical relationships to take reactive surface area evolution into account, the provided models can be applied to systems with a broad range of input concentrations without a-priori knowledge of the prevailing barite supersaturations. This can be of great benefit for modelling the evolution of subsurface systems due to barite formation, where only the prevalent solute concentrations are known. This is foremost important in geothermal reservoirs or in reactive barriers near nuclear waste repositories, where it is crucial to predict the response of the system in advance, so it can be incorporated into the project design. In future work, it is planned to couple reactive transport and digital pore-scale models more tightly together. The aim is to track pore-scale alterations in detail and exploit the capabilities of digital rock physics for deriving rock properties: evolution of reactive surface areas and feedback of resulting geometrical and porosity changes on permeability evolution. Furthermore, the use of surrogate models to speed-up geochemical calculations will be a valuable improvement in the future, making higher grid discretisation and inverse modelling feasible for more accurate parameter determination.

CHAPTER 4

Reactive transport modelling with radial flow: governing equations and analytical solutions

4.1 Introduction

We consider the problem of injecting barite-supersaturated fluids into a geothermal reservoir on the borehole to reservoir scale. The injection of water into a porous aquifer through a fully-penetrating well results in a radially diverging flow field (Fig. 4.1). Seepage velocity then generally is a function of radial distance to the well and thus cannot be described by standard linear flow models. This also leads to unacceptable numerical dispersion if no adaptions are made to common finite differences numerical solvers. In this chapter, the governing equations for describing reactive solute transport under these conditions are derived by applying the principe of mass conservation. It provides the theoretical basis for the chapters hereafter dealing with barite scaling potential for geothermal systems. However, the investigated kinetic rates are not exclusively applicable to barite precipitation, but can also be applied to other mineral reaction mechanisms, provided they follow the respective rate law. Equally, the solutions of the radial flow advection-reaction equations are derived generically, and thus may be applicable to other use cases, too.

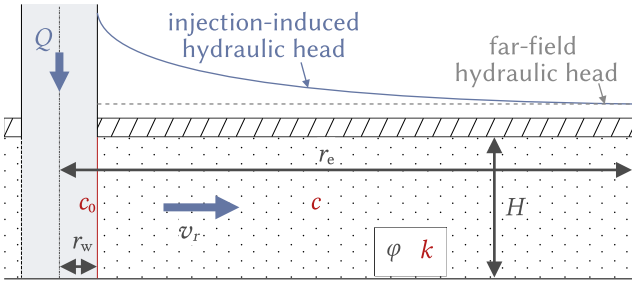

Figure 4.1: Schematic diagram of the reactive transport problem with radial diverging flow. Left is shown an injection well through which fluid is injected with a flow rate of Q into a horizontal, homogeneous, isotropic, porous aquifer with thickness H and a porosity of φ. It is bounded horizontally by aquitards. r_w is the well radius, r_e is the range of influence, and v_r is the pore velocity as a function of r. The solute has a concentration of c, a constant input function of c_0, and a rate constant of k.

The following additional specifications are made compared to well known studies on radial flow facilitated mass transport problems (Chen 1985; Hsieh 1986). Mineral precipitation reaction is included as the sole reactive process. Furthermore, transport is reduced to advection only, disregarding dispersion and molecular diffusion, which greatly simplifies the mathematical model and makes analytical solutions practically tangible (more on this later). Generally, hydrodynamic dispersion is crucial for adequately describing solute transport in porous media (Bear 1988). As the investigated flow path increases, dispersion has an increasingly larger impact on solute concentration profiles. Nevertheless, for the target use case in geothermics, advection greatly dominates in proximity of an injection well. Furthermore, the

close surroundings of the well is more important than the far field considering structural rock changes due to mineral precipitation. In fact, it can be shown that the impact on effective rock permeability declines logarithmically with radial distance (Renard and de Marsily 1997). The mentioned simplification thus is justified for practical applications.

Investigation of radial advection-dispersion equations is of practical and theoretical interest for hydrogeology problems, such as transport parameter determination from tracer well tests (Chen 1985; Chen et al. 2002; Lai et al. 2016; Moench and Ogata 1981; Wallis et al. 2012), contaminant or wastewater injection (Chen 1985), and aquifer performance for storage and recovery (Lu et al. 2011). Injection of mineral supersaturated fluids is a topic far less often investigated, but is of significance for geothermal (Banks et al. 2014; Regenspurg et al. 2015) as well as for gas- and oil industry (Granbakken et al. 1991; Haarberg et al. 1992; Sorbie and Mackay 2000), for example.

Analytical solutions are usually not as flexibly applicable compared to numerical solutions due to their specific (boundary) conditions. Still, they can be used for benchmarking numerical solutions, which can thus be first tested for simple conditions and then extended to include more complex objectives (Aichi and Akitaya 2018). Furthermore, they are useful for rapid estimates of reactive transport phenomena and play a key part in performing sensitivity analyses for larger time- and spatial scales (Toride et al. 1993). It should also be noted that, from a modellers' perspective, the underlying physico-chemical processes are retraced in more detail than perhaps with numerical solutions where most calculations happen 'under the hood'.

In the first section, some common kinetic rate reactions for describing mineral precipitation are introduced. Analytical solutions are derived for these, laying the basis for developing dimensionless numbers later, such as the instructive Damköhler number, which relates reaction and transport processes. The following sections deal with the governing advection-reaction equations and analytical solutions for specific boundary conditions. It is then demonstrated, how the Damköhler number and equilibrium length can be derived for a specific problem by using the introduced equations. These are key values for rapid forward modelling and have predictive capabilities for approximating the impact of reactive processes on subsurface systems. In the last section, it is shown how this problem can be solved numerically with the PHREEQC transport code.

4.2 Kinetic rate laws

Mineral kinetic laws for aqueous solutions commonly used in geosciences are investigated in the following to obtain analytical solutions and characteristic times for reaction (Fig. 4.2). This enables the derivation of so-called half-life time of reaction, i. e., the time when half of the reactant has reacted, and also characteristic times for calculating Damköhler numbers for reactive transport problems (cf. Section 4.4).

Consider a mineral phase M with a 1:1 stoichiometry with two species A and B:

$$\mathrm{M} \rightleftharpoons \mathrm{A} + \mathrm{B}. \tag{4.1}$$

A classical transition-state theory or Lasaga type rate expression for kinetic control of such reaction would be (Lasaga 1998):

$$\frac{\partial \mathrm{M}}{\partial t} = -k \left(1 - \frac{\mathrm{A}\,\mathrm{B}}{K_\mathrm{M}} \right), \tag{4.2}$$

where t (T) is time. Here we expressed all quantities M, A and B as unit substance mass (N) per unit mass of solvent (M). We assume dilute solutions and thus activity coefficients of unity. The term $\mathrm{A}\,\mathrm{B}/K_\mathrm{M}$ represents the saturation ratio (SR) of M, and $K_\mathrm{M} = \mathrm{A}_\mathrm{eq}\,\mathrm{B}_\mathrm{eq}$ the solubility product of M at thermodynamic equilibrium. In natural environments, A and B cannot be assumed to be equal. In the following cases, however, Eq. (4.2) admits simplifications:

- both of A and B are fixed. As a result, **the kinetic rate is constant**, i. e., zeroth-order kinetics (not further investigated here).
- one of A or B is fixed, for example as a result of assumed equilibrium of a third phase acting as a buffer (sink/source) for the solute fixing its activity and hence concentration. In this case, **the system reverts to first-order kinetics** (Subsection 4.2.1). In some cases, mineral reactions follow a first-order rate law because they only have a single reactant, e. g., quartz formation from $SiO_{2,(aq)}$ (Rimstidt and Barnes 1980).
- the ratio $A/B = v$ is constant: this corresponds to the assumption that the amount of reaction does not change the dissolved species concentrations (e. g., assuming volume of solution $\gg$ precipitated mineral). In this case, **the system reverts to second-order kinetics** for one species (Subsection 4.2.2), since Eq. (4.2) can be written as:

$$\frac{\partial M}{\partial t} = -k \left(1 - \frac{A^2}{v \cdot K_M} \right). \tag{4.3}$$

If activity coefficients change significantly during the reaction process, finding exact analytical solutions is not feasible and simplifications have to be made. Alternatively, numerical solvers can be used as a fallback approach, which have gained in popularity especially due to more user-friendly codes and accessible user interfaces (e. g., Leal et al. 2017; Parkhurst and Appelo 2013). Still, finding appropriate analytical solutions to existing problem of chemical reaction kinetics is invaluable as it provides quick prediction capabilities and has more explanatory value.

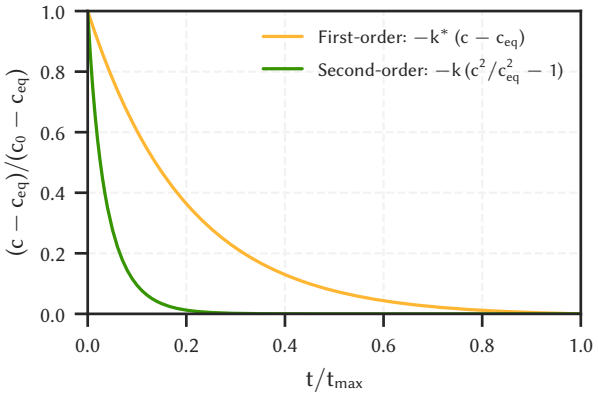

Figure 4.2: Concentration profiles for the three considered precipitation kinetic rate laws calculated with analytical solutions. The following parameters are used: $c_0 = 1.0$ N/M, $c_{eq} = 0.5$ N/M, and $k^* = 0.5$ 1/T, or respectively $k^* = 0.5$ N/MT.

4.2.1 First-order rate law

Coming from Eq. 4.2, let B be constant so a first-order rate law with respect to A can be assumed. Using the relationship $\partial M/\partial t = -\partial A/\partial t$ under the assumption that the solvent is fixed at unity, Eq. (4.2) can be rewritten:

$$\frac{\partial A}{\partial t} = -k \left(\frac{A}{K_M/B} - 1 \right). \tag{4.4}$$

For clarity, we use the definitions

$$\begin{aligned} c\ (\mathrm{N/M}) &:= A, \\ c_{eq}\ (\mathrm{N/M}) &:= K_M/B, \\ k^*\ (1/\mathrm{T}) &:= k/c_{eq}, \end{aligned}$$

where c_{eq} is the reactant concentration in thermodynamic equilibrium, to rewrite Eq. (4.4) into:

$$\frac{\partial c}{\partial t} = -k^* (c - c_{eq}). \tag{4.5}$$

to get the commonly used first-order reaction rate (Gardner and Nancollas 1983; Hina and Nancollas 2011; Lasaga 1998; Rimstidt and Barnes 1980). The general solution to this first-order ordinary differential equation (ODE) is:

$$c(t) = c_{eq} + F \exp(-k^* t), \tag{4.6}$$

where C is an integration constant. Let us substitute the initial conditions into the general solution, stating that we begin a reaction with the initial reactant concentration c_0:

$$\begin{cases} c = c_0, \\ t = 0. \end{cases}$$

For $c_{eq} > 0$, $c_0 > c_{eq}$, $t > 0$, and $k^* > 0$, we get $C = c_0 - c_{eq}$. Plugging this into Eq. (4.6) we get:

$$c(t) = c_{eq} + (c_{eq} - c_0) \exp(-k^* t). \tag{4.7}$$

Figure 4.3 shows this solution using the parameters $c_0 = 1.0$, $c_{eq} = 0.5$, and $k = 0.5$. The results are matched against a solution using the PHREEQC code with a third-order Runge-Kutta solver (Parkhurst and Appelo 2013).

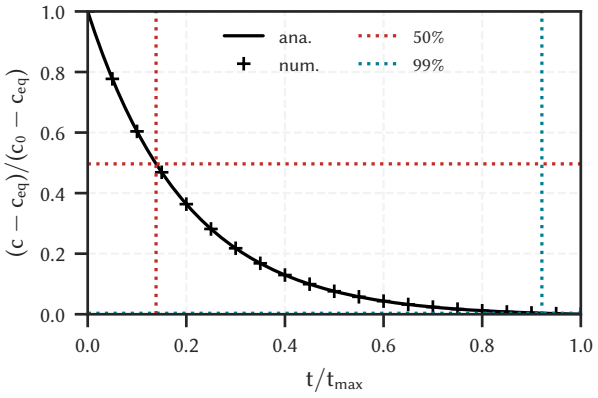

Figure 4.3: Concentration profile for a first-order precipitation reaction (Eq. (4.5)). The numerical results are computed using the numerical solver PHREEQC. The horizontal lines indicate where the reactant has reacted by 50% (dotted) and 99% (dashed) of $c_0 - c_{eq}$, respectively. The vertical lines correspond to the respective times calculated with Eqs. (4.8) and (4.9).

To find the time at which c has decreased by half the amount (half-life time), we set the left-hand side to $c_{50} = c_0 - 0.5\,(c_0 - c_{eq})$ and get

$$t_{50,A} = \frac{\ln 2}{k^*} \approx \frac{0.69}{k^*}. \tag{4.8}$$

The time at which close to all c has reacted, i. e., $c_{99} = c_0 - 0.99\,(c_0 - c_{eq})$ is

$$t_{99,A} = \frac{2\,(\ln 2 + \ln 5)}{k^*} \approx \frac{4.6}{k^*}. \tag{4.9}$$

Both times are also depicted in Fig. 4.3 for the given parameter set and match with the concentration profile.

Note that the following first-order rate law is also commonly found in the literature (e. g., Hina and Nancollas 2011; Steefel 2008):

$$\frac{\partial c}{\partial t} = -k\,(c/c_{\mathrm{eq}} - 1). \tag{4.10}$$

However, it is obviously almost identical to Eq. (4.5), only that it defines the rate constant as k, not as k^*. The characteristic times can be derived analogously, but are shown for the sake of completeness in the following. The time at which c has decreased by half the amount (half-life time) for this case is

$$t_{50,\mathrm{B}} = \frac{c_{\mathrm{eq}} \ln 2}{k} \approx \frac{0.69 c_{\mathrm{eq}}}{k}. \tag{4.11}$$

The time at which close to all c has reacted, i. e., $c_{99} = c_0 - 0.99\,(c_0 - c_{\mathrm{eq}})$ is

$$t_{99,\mathrm{B}} = \frac{2 c_{\mathrm{eq}}\,(\ln 2 + \ln 5)}{k} \approx \frac{4.6 c_{\mathrm{eq}}}{k} \tag{4.12}$$

4.2.2 Second-order rate law with one species

The following case is for a mono-species reaction following a second-order rate law, or for two species with equimolar concentrations (e.g. Christy and Putnis 1993):

$$\mathrm{AB} = \mathrm{A}^2$$
$$c\ (\mathrm{N/M}) \coloneqq \mathrm{A}.$$

Thus, we get to rewrite Eq. (4.2):

$$\frac{\partial c}{\partial t} = -k\,(c^2/c_{\mathrm{eq}}^2 - 1). \tag{4.13}$$

The general solution to this first-order ODE is:

$$c = \frac{2\,c_{\mathrm{eq}}}{C\,e^{\frac{2kt}{c_{\mathrm{eq}}}} - 1} + c_{\mathrm{eq}}, \tag{4.14}$$

where C is an integration constant. Let us substitute the initial conditions into the general solution, stating that we begin a reaction with the initial reactant concentration c_0:

$$\begin{cases} c = c_0, \\ t = 0. \end{cases} \tag{4.15}$$

For $c_{\mathrm{eq}} > 0$, $c_0 > c_{\mathrm{eq}}$, $t > 0$, and $k > 0$, we get $F = \dfrac{c_0 + c_{\mathrm{eq}}}{c_0 - c_{\mathrm{eq}}}$. Plugging this into Eq. (4.14) we get:

$$c(t) = \frac{2\,c_{\mathrm{eq}}}{\dfrac{(c_0 + c_{\mathrm{eq}})\,\exp(2kt/c_{\mathrm{eq}})}{c_0 - c_{\mathrm{eq}}} - 1} + c_{\mathrm{eq}}. \tag{4.16}$$

Figure 4.4 shows this solution using the parameters $c_0 = 1.0$ N/M, $c_{\mathrm{eq}} = 0.5$ N/M, and $k = 0.5$ N/M T. The results are matched against a solution using the PHREEQC code with a third-order Runge-Kutta solver (Parkhurst and Appelo 2013).

To find the time at which c has decreased by half the amount (half-life time), we set the left-hand side to $c_{50} = c_0 - 0.5\,(c_0 - c_{\mathrm{eq}})$ and get

$$t_{50,\mathrm{C}} = \frac{c_{\mathrm{eq}} \ln\left(\dfrac{3\,c_{\mathrm{eq}} + c_0}{c_{\mathrm{eq}} + c_0}\right)}{2k}. \tag{4.17}$$

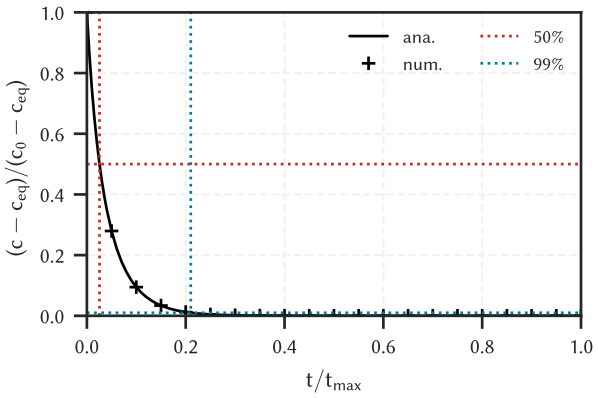

Figure 4.4: Concentration profile for a second-order precipitation reaction (Eq. (4.13)). The numerical results are computed using the numerical solver PHREEQC. The horizontal lines indicate where the reactant has reacted by 50% (dotted) and 99% (dashed) of $c_0 - c_{eq}$, respectively. The vertical lines correspond to the respective times calculated with Eqs. (4.17) and (4.18).

The time at which close to all c has reacted, i. e., $c_{99} = c_0 - 0.99\,(c_0 - c_{eq})$ is

$$t_{99,C} = \frac{c_{eq} \ln\left(\dfrac{199\,c_{eq} + c_0}{c_{eq} + c_0}\right)}{2k}. \tag{4.18}$$

Both times are also depicted in Fig. 4.3 for the given parameter set and match with the concentration profile.

4.2.3 Multi-species kinetics

In the general case, the assumptions above are not applicable, i. e., mineral reaction kinetics are multi-species dependent. Solving the equations for two changing species is more complex. The general concept to yielding analytical solutions for this case is demonstrated in the following. Specific solutions are not derived, here, but readers may find the approach useful, nevertheless.

Consider a closed system constituted by a fixed and constant amount of solvent m_w and solute concentrations A and B with initial values A_0 and B_0, respectively.

$$\frac{\partial M}{\partial t} = \begin{cases} -\dfrac{\partial A}{\partial t}, \\ -\dfrac{\partial B}{\partial t}. \end{cases} \tag{4.19}$$

Integrating the two Eqs. (4.19) we obtain the straightforward relationship between mineral amount and concentration changes in solution:

$$M(t) - M_0 = A_0 - A(t) = B_0 - B(t). \tag{4.20}$$

Equation (4.19) can hence be written as:

$$\frac{\partial M}{\partial t} = -k\left(1 - \frac{(M_0 + A_0 - M)\cdot(M_0 + B_0 - M)}{K_M}\right) \tag{4.21}$$

Setting for clarity $a = M_0 + A_0$ and $b = M_0 + B_0$, Eq. 4.21 becomes:

$$\frac{\partial M}{\partial t} = \frac{k}{K_M}\left[M^2 - (a+b)\cdot M - (ab - K_M)\right] \tag{4.22}$$

Equation (4.22) is a first-order ordinary differential equation quadratic in the unknown function M. This class of differential problems is called **Riccati equation** and can be solved, e. g., by reducing it to a second-order linear equation (cf. Wikipedia entry). The general solution of Eq. (4.22) is:

$$M = \begin{cases} \dfrac{\sqrt{-4K_M + b^2 + 6ab + a^2}}{2} + \dfrac{a+b}{2} & \text{for } C = 0 \\ \dfrac{\sqrt{-4K_M + b^2 + 6ab + a^2}}{2} - \dfrac{a+b}{2} & \text{for } C = \infty \\ \dfrac{\sqrt{4K_M - b^2 - 6ab - a^2}\,\tan\left(\frac{k\sqrt{4K_M - b^2 - 6ab - a^2}\,t + C}{2K_M}\right)}{2} + \dfrac{b}{2} + \dfrac{a}{2} & \text{otherwise.} \end{cases} \tag{4.23}$$

4.3 Reactive transport with radial flow

4.3.1 The governing equation for advection-reaction

The general one-dimensional advection-diffusion-reaction equation can be written in cartesian coordinates (Bear 1988):

$$\frac{\partial c}{\partial t} = \nabla \cdot (D \nabla c) - \nabla \cdot (\mathbf{v} c) + R. \tag{4.24}$$

In the vicinity of an injection well, the advective component of flow dominates (Phillips 1991), thus without the diffusive term the equation reduces to

$$\frac{\partial c}{\partial t} = -\nabla \cdot (\mathbf{v} c) + R. \tag{4.25}$$

v_x is dependent on x (Fig. 4.5) for radially diverging flow. Eq. (4.25) is thus to be written in cylindrical coordinates (x, z, ω) because the right-hand-side no longer simplifies in

$$\frac{\partial c}{\partial t} = -\|\mathbf{v}\| \frac{\partial c}{\partial x} + R,$$

and the divergence of $\mathbf{v}$ is no longer zero. The formula for the divergence in cylindrical coordinatesreads:

$$\nabla \cdot \mathbf{A} \equiv \frac{1}{r} \frac{\partial (r A_r)}{\partial r} + \frac{1}{r} \frac{\partial A_\omega}{\partial \omega} + \frac{\partial A_z}{\partial z}.$$

Further, assuming homogeneous and isotropic conditions, we can now transform Eq. (4.25) into cylindrical coordinates by using the velocity tensor

$$\mathbf{v} = \begin{cases} v_r &= \frac{Q}{2\pi r H \varphi} = \frac{V}{r}, \\ v_\omega &= 0, \\ v_z &= 0, \end{cases} \tag{4.26}$$

into

$$\frac{\partial c}{\partial t} = -\frac{V}{r} \frac{\partial c}{\partial r} + R. \tag{4.27}$$

In the above equations, c (N/L^3) is the solute concentration in the radial flow field, r (L) is the radial distance from the center of the injection well, x (L) is the distance from the injection well in cartesian coordinates, t (T) is time from the start of solute injection, v (L/T) is the pore flow velocity, D (L^2/T) is the hydrodynamic dispersion, Q (L^3/T) is the injection flow rate, H (L) is the thickness of the aquifer, φ is the effective porosity, R (N/L^3 T) is a solute source (> 0) or sink (< 0) term, and V (L^2/T) is a flow constant.

4.3.2 Analytical solution for a first-order reaction

Setting $R = -k(c - c_{\mathrm{eq}})$ as a sink term that is representative for a first-order mineral precipitation reaction (Eq. (4.5)), the governing equation reads:

$$\frac{\partial c}{\partial t} = -\frac{V}{r}\frac{\partial c}{\partial r} - k(c - c_{\mathrm{eq}}). \tag{4.28}$$

We further consider the injection of solution into the domain not at $r = 0$, but at the well exit $r = r_{\mathrm{w}}$. The total solute travel distance thus is $\epsilon = r - r_{\mathrm{w}}$ and the equation must be modified to account for this by substitution:

$$\frac{\partial c}{\partial t} = -\frac{V}{r_{\mathrm{w}} + \epsilon}\frac{\partial c}{\partial \epsilon} - k(c - c_{\mathrm{eq}}). \tag{4.29}$$

This PDE (partial differential equation) may be solved readily using symbolic algebra or mathematical software (e. g., *Wolfram|Alpha* 2021), i. e., CAS (computer algebra systems). The general form of the solution for Eq. (4.29) is:

$$c(\epsilon, t) = c_{\mathrm{eq}} + F\left(t - \frac{\epsilon^2 - 2\epsilon\, r_{\mathrm{w}}}{2V}\right) \exp\left(-\frac{k\epsilon(\epsilon + 2r_{\mathrm{w}})}{2V}\right), \tag{4.30}$$

where F is an arbitrary function corresponding to a constant of integration. Re-substitution with $\epsilon = r - r_{\mathrm{w}}$ and simplification yields:

$$c(r, t) = c_{\mathrm{eq}} + F\left(t - \frac{r^2 - r_{\mathrm{w}}^2}{2V}\right) \exp\left(-\frac{k(r^2 - r_{\mathrm{w}}^2)}{2V}\right), \tag{4.31}$$

We now consider the IBVP (Initial-Boundary Value Problem) consisting of initial concentration c_{eq} everywhere, and injection of a concentration $c = c_0 > c_{\mathrm{eq}}$ at the well exit $r_{\mathrm{w}} > 0$:

$$\left\{\begin{array}{ll} c(r, 0) & = c_{\mathrm{eq}} \quad \text{for } r > r_{\mathrm{w}}, \\ c(r_{\mathrm{w}}, t) & = c_0 \quad \text{for } t \geq 0. \end{array}\right\} \tag{4.32}$$

Plugging the two conditions Eq. (4.32) into the general solution Eq. (4.31), we get:

$$\begin{cases} c_{\mathrm{eq}} & = c_{\mathrm{eq}} + F\left(-\frac{r^2 - r_{\mathrm{w}}^2}{2V}\right) \exp\left(-\frac{k(r^2 - r_{\mathrm{w}}^2)}{2V}\right), \\ c_0 & = c_{\mathrm{eq}} + F(t). \end{cases} \tag{4.33}$$

For the first of Eqs. (4.33) we conclude that the argument $\xi = r^2 - r_{\mathrm{w}}^2/2V$ of function F is always negative because $r > r_{\mathrm{w}}$ and $V = Q/(2\,\pi\, H\, \varphi)$ has only positive physical quantities; for the other case it is $\xi = t \geq 0$:

$$F(\xi) = \begin{cases} 0 & \text{if } \xi < 0 \iff t - (r^2 - r_{\mathrm{w}}^2)/2V < 0, \\ c_0 - c_{\mathrm{eq}} & \text{if } \xi \geq 0 \iff t - (r^2 - r_{\mathrm{w}}^2)/2V \geq 0. \end{cases} \tag{4.34}$$

Finally, by plugging the function F (Eq. (4.34)) for this IBVP into Eq. (4.31), we can write the corresponding full analytical solution:

$$c(r, t) = \begin{cases} c_{\mathrm{eq}} & \text{if } t < (r^2 - r_{\mathrm{w}}^2)/2V, \\ c_{\mathrm{eq}} + (c_0 - c_{\mathrm{eq}}) \exp\left(-\frac{k(r^2 - r_{\mathrm{w}}^2)}{2V}\right) & \text{if } t \geq (r^2 - r_{\mathrm{w}}^2)/2V. \end{cases} \tag{4.35}$$

For validating Eq. (4.35), we use the upwind differences in space numerical method.

$$c_i^{n+1} = c_i^n - \frac{V}{r_i}\frac{\mathrm{d}t}{\mathrm{d}r}(c_i^n - c_{i-1}^n) - \mathrm{d}t\, k\,(c_i^n - c_{\mathrm{eq}}), \tag{4.36}$$

where superscript n represents the time step, subscript j represents the domain node, $\mathrm{d}t$ is the time step length, and $\mathrm{d}r$ is the grid length. This scheme is stable for $\mathrm{d}t \leq \min\left(\mathrm{d}r\, r_j/V\right)$. Equations (4.35) and (4.36) are compared in Fig. 4.5. The resulting concentration profiles match save for numerical errors, which are grid-resolution dependent.

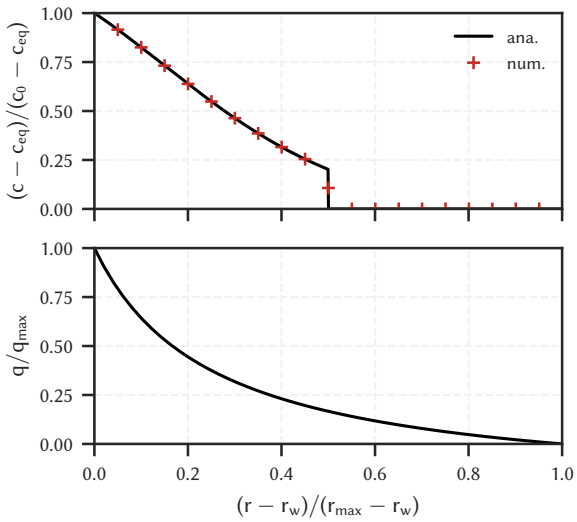

Figure 4.5: Concentration and velocity profiles of the advection-reaction-equation for radial flow. The analytical Eq. (4.35) and numerical Eq. (4.36) solutions of Eq. (4.29) are matched for the following parameters: $r_w = 0.2$ L, $r_{max} = 1.0$ L, $t = 0.16$ T, $c_{eq} = 0.1$ N/L^3, $c_0 = 1.0$ N/L^3, $k = 10$ 1/T, $V = 1.0$ L^2/T, and 1 000 nodes for the numerical setup. The bottom figure illustrates the non-constant flow velocity along the r-axis due to the diverging flow.

4.3.3 Analytical solution for a first-order reaction (steady-state)

Flow in a confined aquifer induced by water injection through a fully penetrating well cannot reach true steady-state, but can be assumed approximately for long injection periods (so called quasi-steady-state). This case holds if rock permeability is assumed to be constant by disregarding any effects chemical reactions have on the pore structure. Pore flow velocity then is only a function of r, but not of t. If also constant reaction rates are assumed within the whole domain, Eq. (4.29) further reduces to

$$\frac{V}{r_w + \epsilon}\frac{\partial c}{\partial \epsilon} + k(c - c_{eq}) = 0 \quad \text{for } t \geq (r_{eq}^2 - r_w^2)/2V, \tag{4.37}$$

where r_{eq} (L) is the equilibrium length (cf. Section 4.4), which is the flow length the solution needs to reach equilibrium for the investigated reaction under the specified conditions.

The general form of the solution of theis ordinary differential equation (4.37) then reads

$$c(\epsilon) = \frac{F}{\exp\left(k\frac{\epsilon^2 + 2\epsilon r_w}{2V}\right)} + c_{eq}. \tag{4.38}$$

Re-substitution with $\epsilon = r - r_w$ and simplification yields:

$$c(r) = \frac{F}{\exp\left(k\frac{r^2 - r_w^2}{2V}\right)} + c_{eq}. \tag{4.39}$$

We consider the boundary value problem with injection of a constant concentration $c_0 > c_{eq}$ at the well-aquifer boundary, i. e., at $r = r_w > 0$:

$$c(r_w) = c_0. \tag{4.40}$$

By plugging Eq. (4.40) into Eq. (4.39) we get the following definition for F:

$$F = c_0 - c_{eq}. \tag{4.41}$$

Finally, by inserting Eq. (4.41) into Eq. (4.39) we get to write the full analytical steady-state solution:

$$c(r) = \frac{c_0 - c_{\mathrm{eq}}}{\exp\left(k\frac{r^2 - r_{\mathrm{w}}^2}{2V}\right)} + c_{\mathrm{eq}} \text{ for } r \geq r_{\mathrm{w}}. \tag{4.42}$$

For validation purposes of Eq. (4.42), we use the upwind differences in space numerical method Eq. (4.36) (see Fig 4.6). In this case, up to j iterations are necessary to reach the specified conditions. The resulting concentration profiles match save for numerical errors.

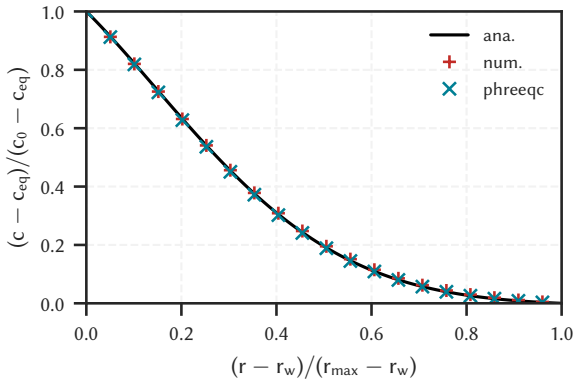

Figure 4.6: Comparison of the analytical Eq. (4.42), numerical Eq. (4.36), and PHREEQC solution (see Section 4.3.4) for the quasi-stationary state concentration profile of the advection-reaction-equation for radial flow Eq. (4.29). The following parameters were used: $r_{\mathrm{w}} = 0.2$ L, $r_{\mathrm{max}} = 1.0$ L, $c_{\mathrm{eq}} = 0.1$ N/L^3, $c_0 = 1.0$ N/L^3, $k = 10$ 1/T, $V = 1.0$ L^2/T, and 100 nodes for the numerical setup. t must be ≥ 0.48 T.

4.3.4 Numerical implementation in PHREEQC

It was shown that analytical solutions are often only available under specific conditions and—not seldomly drastic—simplifications. Numerical solvers are more flexible in this sense, but need to be validated against analytical solutions first to gain credibility, which is commonly referrred to *benchmarking*. Let us therefore now derive a way to solve the reactive transport equation with radial flow numerically using the PHREEQC code v3.7 (Parkhurst and Appelo 2013). With this code, significantly more complex chemical systems can be modelled, e. g., species activity coefficients as functions of time or multi-mineral kinetic reactions (Appelo and Postma 2010).

We begin with a similar equation to Eq. (4.27), but now define advection with the Darcy velocity q instead of specific discharge v:

$$\frac{\partial}{\partial t}(\varphi\, c_i) = -q\,\frac{\partial c_i}{\partial r} + \varphi\, R. \tag{4.43}$$

with

$$q = \frac{Q}{2\pi\, r\, H} = \frac{V}{r},$$

and where c (N/L^3) is the solute concentration, and R (N/L^3 s) is the reaction rate. Given that PHREEQC's current one-dimensional transport module only accepts constant flow velocities, Eq. (4.43) cannot be readily solved because the considered q is a function of radial distance r. There are two options to resolve this: (1) a non-uniform grid is used, where each grid step length corresponds to the mean flow velocity of the respective cell to fulfil the Courant-Friedrichs-Lewy stability criteria:

$$q(r)/\varphi \leq \Delta r/\Delta t.$$

Flow velocity decreases with r, thus grid step lengths have to decrease with r accordingly. The main downside to this is that the grid is coarse close to the well and gets increasingly finer with r. However, it

is especially important to resolve the section near the well highly if permeability alterations are assessed, as the closer change happens to the well, the larger the impact on the effective permeability, i. e., well injectivity. (2) Another option, which was adopted here, is to assume quasi-stationary state (Eq. (4.37)) and to multiply the equation with $q'/q(r)$ (constant for $t > 0$, Eq. (4.44)).

$$q' \frac{\partial c_i}{\partial r} - \frac{q'}{q(r)} \varphi R = 0, \tag{4.44}$$

where q' (L/T) is the substitute Darcy velocity. It should be in the range $q(r)_{\text{med}} \leq q' \leq q(r)_{\text{max}}$ to avoid numerical errors. Using q_{med} gives the largest possible time steps. By making this adaption, the advection term is constant and the reaction term changes with r. This is easily implementable in PHREEQC by using separate kinetics blocks for each cell and varying the respective reaction volume and thus reactive surface area. A comparison of this solution and the analytical solution for the steady-state case is shown in Fig. 4.6. Importantly, calculated phase changes $\mathrm{d}\varphi_m^*$ of a mineral m using this method have to be rescaled after the simulation with:

$$\mathrm{d}\varphi_m = \mathrm{d}\varphi_m^* V/r\, q'. \tag{4.45}$$

4.4 Radial damköhler number and equilibrium length

The Damköhler number (Da) relates the characteristic solute transport time to reactive time and corresponds to a respective transport equation, e. g., the advection-reaction equation (Eq. 4.25). In general, its value is used to determine whether the dominant part of reaction happens within an arbitrarily defined flow section, thus indicating if the system is advection or reaction dominated within the considered space. This has practical relevance, e. g., for numerical solvers of reactive transport, as the Da can indicate which approximate grid size is needed to resolve the respective problem. In a one-dimensional, advection-dominated flow column on the length section $[0, l_c]$, the advective time τ_A (T) is defined with Eq. (4.46).

$$\tau_A = \varphi \int_0^{l_c} \frac{1}{q(x)} \mathrm{d}x, \tag{4.46}$$

where l_c (L) is the characteristic length and x (L) is the flow distance. If $q(x)$ is constant over x, we get the commonly cited term (e. g., Lichtner 1988, 1996; Steefel 2008):

$$\tau_A = \varphi\, l_c/q. \tag{4.47}$$

The reactive time τ_R (T) depends on the kinetic rate law and the respective reaction order of the considered mineral. Using a first-order rate law of the form given in Eq. (4.10), the reactive time is:

$$\tau_R^* = \frac{\varphi\, 4.6\, c_{\text{eq}}}{k'},$$

where k' ($\mathrm{N/L^3_{rock}}$) $= \varphi\, k$ is the volumetric rate constant. This corresponds to $t_{99,\text{B}}$ given in Eq. (4.12) and is commonly used in the literature (Lichtner 1988, 1996; Steefel 2008), though the 4.6 is seen to be omitted. In this regard, it is usually not specified, which condition defines the reactive time, i. e., how far the reaction has progressed. The factor of 4.6 takes into account that 99% of the potential reaction from initial to equilibrium condition has taken place, which appears to be a resonable approach. Depending on the objective, other assumptions (e. g., half-life) may be valid, also. Here, we use the simplified first-order rate law given in Eq. (4.5) that yields the following reactive time for the 99%-progression case:

$$\tau_R = \frac{\varphi\, 4.6}{k'}. \tag{4.48}$$

A solution for a second-order rate law, e. g., that describes the barite precipitation reaction (Zhen-Wu et al. 2016), cannot be readily found, as it usually depends on two non-equimolar reacting species SO_4^{2-}

and Ba^{2+}. In this case, either the simplified form given in Eq. (4.48) for a first-order rate, or alternatively the solution for a second-order rate with equimolar reactants should be used (Eq. (4.18)).

We now yield the advective Damköhler number Da (-) with Eq. (4.49) assuming constant k' over $[0, l_c]$.

$$\mathrm{Da} = \frac{\tau_A}{\tau_R} = \frac{l_c\, k'}{q\, 4.6}. \tag{4.49}$$

The diffusive Damköhler number, which relates diffusive to reactive rates, can be derived analogously, but is not elaborated further here, as it was not considered in the transport problem.

The equilibrium length l_{eq} (L) can be derived from the same concept of relating advective and reactive rates, but by also assuming quasi-stationary state (Lichtner 1988). Its value gives the approximate magnitude of flow length, over which a transported solution has reached thermodynamic equilibrium with respect to a specific mineral reaction. For its derivation, we set the characteristic length to the unknown equilibrium length when calculating the advective time (Eq. 4.50) and also set the Damköhler number to 1, i. e., characteristic advective time and reactive time are balanced out (Eq. (4.51)).

$$\tau_{A,eq} = \frac{\phi}{q} \int_0^{l_{eq}} \mathrm{d}x = \frac{\phi\, l_{eq}}{q} \tag{4.50}$$

$$\mathrm{Da}_{eq} = \frac{l_{eq}\, k'}{4.6\, q} = 1 \tag{4.51}$$

$$l_{eq} = \frac{4.6\, q}{k'} \tag{4.52}$$

If $q(x)$ is non-constant over x, however, the derivation of the Damkähler number and the corresponding equilibrium length for the steady-state case is slightly different. Now, q needs to be integrated over the considered flow section to get the time for a solute entity to travel this distance. Thus, the advective time in a radial diverging flow field $\tau_{A,rad}$ (T) is given by:

$$\tau_{A,rad} = \varphi \int_{r_w}^{r_c} \frac{1}{q(r)}\, \mathrm{d}r = \frac{\varphi}{V} \int_{r_w}^{r_c} r\, \mathrm{d}r = \frac{\varphi}{2V}(r_c^2 - r_w^2). \tag{4.53}$$

Note that instead of integrating over $[0, l_c]$ as in Eq. (4.46), we now consider the flow section from the well exit to a characteristic flow radius $[r_w, r_c]$. Again, assuming a constant reaction rate over this section, we get the radial Damköhler number:

$$\mathrm{Da}_{rad} = \frac{\tau_{A,rad}}{\tau_R} = \frac{k'}{9.2V}(r_c^2 - r_w^2). \tag{4.54}$$

The radial equilibrium length Eq. (4.57) can be derived analogously to the linear case by using the definition of $\tau_{A,rad}$ instead of τ_A:

$$\tau_{A,rad,eq} = \varphi \int_{r_w}^{r_{eq}} \frac{1}{q(r)} \mathrm{d}r = \frac{\varphi}{2V}(r_{eq}^2 - r_w^2) \tag{4.55}$$

$$\mathrm{Da}_{rad,eq} = \frac{k'}{9.2V}(r_{eq}^2 - r_w^2) = 1 \tag{4.56}$$

$$r_{eq} = \sqrt{\frac{9.2V}{k'} + r_w^2} \tag{4.57}$$

4.5 Conclusions

The whole narrative of this chapter was focussed on barite precipitation in porous media as a consequence of injecting supersaturated fluid into an aquifer. It is—in parts—the theoretical background for the

mathematical model of the next two chapters. Yet, the respective equations are applicable to any mineral dissolution or precipitation reactions alike if the reaction rate is adapted.

Some common first- and second-order rate laws for describing mineral reactions were introduced and corresponding analytical solutions were derived. This made it possible to evaluate characteristic times of reaction, which are an important factor in calculating the Damköhler number. The results were validated with numerical solutions. However, analytical solutions to these rate laws can only be found for either mono-species-dependency, or two-species-dependency at equimolality. This restricts the applicability to mineral reactions dependent on only one aqueous species (e.g., Quartz), and to pseudo-first-order reactions, i. e., when one aqueous reactant species is much larger than the other. This is commonly the case for barite precipitation in natural environments, where sulfate concentrations are much larger than barium.

The governing equations were derived for the reactive solute transport in radial flow problem. An analytical solution for the one-dimensional case is derived, which was shown to match the results of a numerical solution using finite-differences for a simple steady-state case. This validates that the numerical and analytical solution give the same results, save for numerical errors, given the same boundary conditions. Thus, the numerical method can be used with confidence to calculate more complex problems, i. e., the sink term R cannot be simplified to a first-order reaction. Furthermore, the analytical solution is a valuable finding, which can be of practical use for rapid assessment of transport problems if the respective conditions are met.

Common definitions of the Damköhler number for linear flow problems are not applicable to radial flow problems. The radial Damköhler number is derived based on the previously stated advection-reaction equation. It quantifies whether the dominant part of reaction happens within an arbitrary characteristic radial distance. For numerical solvers, this can be applied to approximate the necessary grid resolution to ensure that reaction happens not only within a single cell. Assuming steady-state, the equilibrium length can be calculated if the characteristic reactive and transport times are balanced out. Under the given assumptions, the range of influence of the reactive process can be determined with this value. Regarding the topic of this thesis, it gives an approximate reach of barite scaling within a geothermal reservoir, which is an important indicator for assessing the scaling induced injectivity loss.

CHAPTER 5

Barite scale formation and injectivity loss models for geothermal systems

This is a reprint of an article published in the journal Water (MDPI)[1].

Abstract

Barite scales in geothermal installations are a highly unwanted effect of circulating deep saline fluids. They build up in the reservoir if supersaturated fluids are re-injected, leading to irreversible loss of injectivity. A model is presented for calculating the total expected barite precipitation. To determine the related injectivity decline over time, the spatial precipitation distribution in the subsurface near the injection well is assessed by modelling barite growth kinetics in a radially diverging Darcy flow domain. Flow and reservoir properties as well as fluid chemistry are chosen to represent reservoirs subject to geothermal exploration located in the North German Basin (NGB) and the Upper Rhine Graben (URG) in Germany. Fluids encountered at similar depths are hotter in the URG, while they are more saline in the NGB. The associated scaling amount normalised to flow rate is similar for both regions. The predicted injectivity decline after 10 years, on the other hand, is far greater for the NGB (64%) compared to the URG (24%), due to the temperature- and salinity-dependent precipitation rate. The systems in the NGB are at higher risk. Finally, a lightweight score is developed for approximating the injectivity loss using the Damköhler number, flow rate and total barite scaling potential. This formula can be easily applied to geothermal installations without running complex reactive transport simulations.

5.1 Introduction

The North German Basin (NGB) and the Upper Rhine Graben (URG) are two of the main regions in Germany for geothermal exploration, exhibiting promising hydrothermal resources (Agemar et al. 2014). The success of a geothermal project greatly depends on the target reservoir' transmissivity and temperature (Schumacher et al. 2020). The high fluid mineralisation in Mesozoic sandstones (Naumann 2000; Pauwels et al. 1993; Sanjuan et al. 2016; Stober et al. 2013; Wolfgramm and Seibt 2008; Wolfgramm et al. 2011b), however, gives rise to challenges for their long-term utilisation (Regenspurg et al. 2015; Wolfgramm et al. 2011a). One of which the present study focused on is barite scale formation ($BaSO_4$), originating from lowering the fluid's state temperature and pressure during the production–injection cycle. Barite is a low-soluble scaling mineral, typically found at geothermal installations located in the NGB and the URG area that handle fluids produced from reservoirs of depths greater 2 000 m (Nitschke et al. 2014; Seibt et al. 2010a; Wolfgramm et al. 2011a). Scalings are undesirable because they lower

[1]Morgan Tranter et al. (2020). Barite Scale Formation and Injectivity Loss Models for Geothermal Systems. *Water* 12(11):3078. DOI: 10.3390/w12113078.

tubing diameters or reduce efficiency of heat exchangers, which leads to restoration costs (Birner et al. 2015; Seibt et al. 2010b; Wolfgramm et al. 2011a,b). Scale formation in the host rock at the injection site (Fig. 5.1a), however, may constitute a more serious threat, as the related pore clogging affects the reservoir's hydraulic properties. In case of barite scaling, this leads to irreversible injectivity loss and thus reduced overall efficiency (Birner et al. 2015; Scheiber et al. 2013).

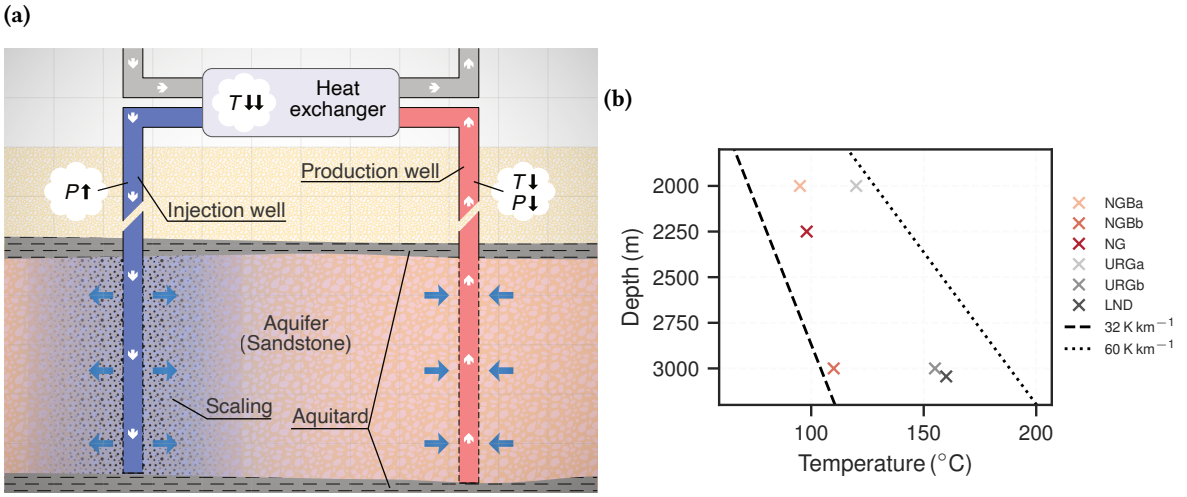

Figure 5.1: (**a**) Schematic diagram of a geothermal doublet, showing the core technical installations consisting of a production and an injection well, as well as a heat exchanger. Brine temperature (T) and pressure (P) change along the flow path. Scalings at the injection site clog the pores, which results in reduced injectivity. (**b**) Fluid temperatures at respective depths for the test cases Neustadt-Glewe (NG), Landau (LND) as well as for the hypothetical sites in the North German Basin (NGB) and the Upper Rhine Graben (URG). The dashed line represents the average geothermal gradient for Germany (Agemar et al. 2012).

Due to the prograde solubility dependency of barite, reduction of temperature along the flow path results in supersaturated conditions (Blount 1977; Templeton 1960). Hence, the initial reservoir fluid's state and chemistry as well as the surface system state need to be known in advance for evaluating the scaling potential of barite for a specific geothermal site. This can be done using geochemical modelling software that applies the law of mass action together with an appropriate thermodynamic database (Hörbrand et al. 2018). The resulting equilibrium models yield a specific potential scaling mass based on the temperature and pressure change as well as according change in solubility. While they are easy to implement, this potential scale formation amount, however, only indicates whether precipitation can be expected and if there is a respective risk. These commonly applied equilibrium models (e.g., Bozau et al. 2015; Haarberg et al. 1992; Schröder et al. 2007) are insufficient in predicting the related temporal impact on injectivity because they provide no data on the distribution near the injection well. This can be achieved by using a reactive transport simulator that implements respective solute transport and a kinetic rate law. The advantage is that further site specific parameters are accounted for, such as the injection flow velocity and the precipitation rate.

Barite growth is promoted when barite-supersaturated fluids come into contact with barite in the formation rock (Lasaga 1998). Whether scalings grow dispersed or at specific locations has a significant impact on effective macro-scale permeability and injectivity (Beckingham 2017; Phillips 1991). It is crucial to take precipitation kinetics and flow into account to make assumptions on the expected scaling distribution in the subsurface for assessing this issue for long-term utilisation of geothermal systems.

Precipitation kinetics of barite have been the focus of numerous experimental studies (Christy and Putnis 1993; Gardner and Nancollas 1983; Godinho and Stack 2015; Liu et al. 1976; Nancollas and Purdie 1963; Nancollas and Liu 1975; Risthaus et al. 2001; Ruiz-Agudo et al. 2015; Zhen-Wu et al. 2016), demonstrating complex dependencies on nucleation, temperature, pH, ionic strength and ion

ratios. Associated pore clogging and permeability loss effects have been also studied by means of core experiments (Kühn et al. 1997; Orywall et al. 2017) and with regard to specific pilot sites (e.g., Birner et al. 2015; Bozau et al. 2015; Canic et al. 2011; Griffiths et al. 2016; Wolfgramm et al. 2011c), which highlights that barite scale formation is in fact a potential risk for geothermal systems in need of quantification and prevention measures.

Three representative cases for each geothermal region are considered in the present study. For the NGB, the geothermal plant Neustadt-Glewe (NG) was chosen, which actively produces brine from a Rhaetian sandstone aquifer (Naumann 2000). Barite scalings have been observed in the filters and in the heat exchanger within the surface installations. A gradual injectivity decline over the course of many years has been attributed to this issue (Birner et al. 2015). The geothermal site Landau (LND) was taken as a representative example for the URG. In the URG, a multi-horizon approach has been shown to be feasible, lowering exploration risk due to matrix permeability (Bär 2012; Baumgärtner et al. 2010). The well section is stretched over stratigraphical units of the Bunter sandstone, the Muschelkalk and the Permian granitic basement and also exploits a hydraulically active fault zone (Baumgärtner et al. 2010). Furthermore, two additional cases for each region were chosen based on averaged properties, representing hypothetical sites at various depths (Wolfgramm and Seibt 2008). Hereafter, they are called NGBa/NGBb and URGa/URGb, respectively. The corresponding depths and temperatures are shown in Fig. 5.1b, where it can be seen that all sites have anomalously high temperature gradients compared to the German average (Agemar et al. 2012).

This paper provides a new approach for calculating potential barite scaling amounts near the injection well and assessing the resulting impact on injectivity loss for geothermal systems in the NGB and the URG. By applying equilibrium models, the total precipitation amounts are calculated for the various sites based on the initial chemical composition of the formation fluid as well as temperature and pressure change along the flow path. One-dimensional reactive transport simulations are conducted considering radially-diverging Darcy flow and precipitation kinetics to model the constant injection of supersaturated fluids into a porous aquifer. The altered reservoir's effective permeability and thus injectivity are assessed based on the scale formation distribution. The relevant operational parameters temperature, flow velocity and reaction rate are subjected to a sensitivity analysis in order to further provide implications for a geothermal project. Finally, a score is proposed, which aims at approximating the injectivity loss using quickly accessible parameters, applicable also to planned geothermal projects.

5.2 Materials and methods

5.2.1 Geochemistry

Fluid chemistry

Formation fluid chemistry is determined by flow path history, contact with different rock types and structures, and also temperature and pressure. The amount of total dissolved solids or salinity thus can vary strongly between geothermal sites. The physico-chemical parameters and chemical compositions of the considered cases are shown in Tab. 5.1. The URG has generally higher temperature gradients than the NGB (Fig. 5.1b). Measured pH levels are all slightly acidic in the range 5.1–6.0.

The shown fluids are all $Na-Cl$ or $Na-Ca-Cl$ dominated brines. NGB fluids are generally more saline than those from the URG. Ionic strengths for the NGB range from about (4.0–6.2) M, and for the URG from (1.3–2.4) M). The calculated charge balance errors lie between −2% and 0.03%, indicating that the chemical analyses show sufficient quality. Ba-content is rarely reported due to its low solubility.

Table 5.1: Physico-chemical parameters (upper part) and chemical composition (lower part) of the considered geothermal fluids. Measured chemical compositions are taken from given literature and converted from (mg/L) to (M) using calculated solution densities. Reservoir chemical compositions have been calculated to achieve thermodynamic equilibrium with respect to quartz, barite, anhydrite, celesite, and calcite at respective reservoir conditions, using the measured values as the basis. Cl^- has been additionally adjusted to achieve charge balance.

Parameter	Unit	NGBa[a]		NGBb[a]		NG[b,c]		URGa[a]		URGb[a]		LND[d]	
		measured	reservoir	measured	reservoir	measured	reservoir	measured	reservoir	measured	reservoir	measured	reservoir
T	°C	25	95	25	110	25	98	25	120	25	155	25	160
P^e	MPa	0.1	20	0.1	30	0.1	23	0.1	20	0.1	30	0.1	30
ρ_s^f	kg/m^3	1 130	1 110	1 190	1 150	1 150	1 110	1 050	1 000	1 080	1 010	1 070	996
pH	–	5.60	5.33	6.00	4.91	5.20	5.64	5.80	5.66	5.50	5.28	5.15	5.41
IS	M	4.05	4.00	6.21	6.11	4.50	4.48	1.37	1.32	2.29	2.31	2.05	2.01
Ba^{2+}/SO_4^{2-}	–	NA	$3.42 \cdot 10^{-3}$	NA	$2.89 \cdot 10^{-2}$	$8.33 \cdot 10^{-3}$	$5.47 \cdot 10^{-3}$	NA	$3.19 \cdot 10^{-3}$	NA	$2.64 \cdot 10^{-2}$	$6.38 \cdot 10^{-2}$	$3.62 \cdot 10^{-2}$
K^+	M	$2.06 \cdot 10^{-2}$	$2.06 \cdot 10^{-2}$	$2.87 \cdot 10^{-2}$	$2.87 \cdot 10^{-2}$	$2.24 \cdot 10^{-2}$	$2.24 \cdot 10^{-2}$	$7.88 \cdot 10^{-2}$	$7.88 \cdot 10^{-2}$	$1.33 \cdot 10^{-1}$	$1.33 \cdot 10^{-1}$	$1.06 \cdot 10^{-1}$	$1.06 \cdot 10^{-1}$
Na^+		3.08	3.08	4.87	4.87	3.54	3.54	$8.94 \cdot 10^{-1}$	$8.94 \cdot 10^{-1}$	1.59	1.59	1.27	1.27
Ca^{2+}		$2.11 \cdot 10^{-1}$	$2.15 \cdot 10^{-1}$	$3.49 \cdot 10^{-1}$	$3.47 \cdot 10^{-1}$	$2.33 \cdot 10^{-1}$	$2.37 \cdot 10^{-1}$	$1.03 \cdot 10^{-1}$	$1.04 \cdot 10^{-1}$	$1.82 \cdot 10^{-1}$	$1.77 \cdot 10^{-1}$	$1.99 \cdot 10^{-1}$	$1.96 \cdot 10^{-1}$
Mg^{2+}		$7.53 \cdot 10^{-2}$	$7.53 \cdot 10^{-2}$	$4.61 \cdot 10^{-2}$	$4.61 \cdot 10^{-2}$	$6.43 \cdot 10^{-2}$	$6.43 \cdot 10^{-2}$	$4.23 \cdot 10^{-3}$	$4.23 \cdot 10^{-3}$	$4.29 \cdot 10^{-3}$	$4.29 \cdot 10^{-3}$	$3.25 \cdot 10^{-3}$	$3.25 \cdot 10^{-3}$
Sr^{2+}		$5.53 \cdot 10^{-3}$	$3.38 \cdot 10^{-3}$	$8.57 \cdot 10^{-3}$	$5.70 \cdot 10^{-3}$	$5.61 \cdot 10^{-3}$	$3.80 \cdot 10^{-3}$	$2.58 \cdot 10^{-3}$	$2.70 \cdot 10^{-3}$	$4.16 \cdot 10^{-3}$	$8.83 \cdot 10^{-3}$	$5.09 \cdot 10^{-3}$	$1.06 \cdot 10^{-2}$
Ba^{2+}		NA	$2.71 \cdot 10^{-5}$	NA	$1.30 \cdot 10^{-4}$	$4.43 \cdot 10^{-5}$	$3.77 \cdot 10^{-5}$	NA	$1.89 \cdot 10^{-5}$	NA	$9.53 \cdot 10^{-5}$	$8.69 \cdot 10^{-5}$	$1.10 \cdot 10^{-4}$
$Fe^{2+/3+}$		$1.73 \cdot 10^{-3}$	$1.73 \cdot 10^{-3}$	$2.61 \cdot 10^{-3}$	$2.61 \cdot 10^{-3}$	$1.26 \cdot 10^{-3}$	$1.26 \cdot 10^{-3}$	$1.84 \cdot 10^{-3}$	$1.84 \cdot 10^{-3}$	$3.73 \cdot 10^{-3}$	$3.73 \cdot 10^{-3}$	$4.03 \cdot 10^{-4}$	$4.03 \cdot 10^{-4}$
Cl^-		3.79	3.67	5.85	5.69	4.19	4.15	1.30	1.18	2.06	2.10	1.88	1.79
Br^-		$4.04 \cdot 10^{-3}$	$4.04 \cdot 10^{-3}$	$6.73 \cdot 10^{-3}$	$6.73 \cdot 10^{-3}$	$5.30 \cdot 10^{-3}$	$5.30 \cdot 10^{-3}$	$1.29 \cdot 10^{-3}$	$1.29 \cdot 10^{-3}$	$2.61 \cdot 10^{-3}$	$2.61 \cdot 10^{-3}$	$2.84 \cdot 10^{-3}$	$2.84 \cdot 10^{-3}$
SiO_2		NA	$4.15 \cdot 10^{-4}$	NA	$4.25 \cdot 10^{-4}$	NA	$4.16 \cdot 10^{-4}$	NA	$1.09 \cdot 10^{-3}$	NA	$1.89 \cdot 10^{-3}$	$2.75 \cdot 10^{-3}$	$2.12 \cdot 10^{-3}$

T is temperature, P is pressure, ρ_s is solution density, IS is ionic strength, and NA-values are not available from sources. The sample names are North German Basin (NGB) and Upper Rhine Graben (URG) at 2 000 m (a) and 3 000 m (b), respectively, as well as the geothermal sites Neustadt-Glewe (NG) and Landau (LND). [a] Wolfgramm and Seibt (2008) [b] Naumann (2000) [c] Kühn et al. (1998) [d] Sanjuan et al. (2016) [e] Down-hole pressure derived from depth (Figure 5.1b) [f] Calculated iteratively with PHREEQC

Equilibrium models and barite scaling potential

The well established software PHREEQC (U.S. Geological Survey) (Parkhurst and Appelo 2013), version 3.6, was used to do all geochemical batch calculations. The pre-shipped database `pitzer.dat` was applied, which provides thermodynamic data for calculating temperature and pressure dependent solubility products of many common minerals, as well as coefficients for the Pitzer ion-interaction activity model (Pitzer 1986). It has been shown that using this database yields good result for predicting barite solubility at high ionic strengths up to 6 M (Hörbrand et al. 2018).

The equilibrium reaction of barite in an aqueous solution is defined as:

$$\mathrm{BaSO_{4(solid)}} \rightleftharpoons \mathrm{Ba^{2+}_{(aq)}} + \mathrm{SO^{2-}_{4(aq)}}. \tag{5.1}$$

Based on the law of mass action, the saturation state of barite in a solution is calculated with

$$\mathrm{SR_{barite}} = \frac{\mathrm{Ba^{2+}} \cdot \mathrm{SO_4^{2-}}}{K_{\mathrm{sp,barite}}} \cdot \gamma_{\mathrm{Ba^{2+}}} \cdot \gamma_{SO_4^{2-}} \tag{5.2}$$

where $\mathrm{SR_{barite}}$ is the saturation ratio, $K_{\mathrm{sp,barite}}$ is the temperature and pressure dependent solubility constant, and γ_i is the activity coefficient of the respective species. A solution is undersaturated if $\mathrm{SR_{barite}} < 1$ and supersaturated if $\mathrm{SR_{barite}} > 1$. The relationship of solubility with regard to temperature, pressure and NaCl-equivalent ionic strength is shown in Fig. 5.2.

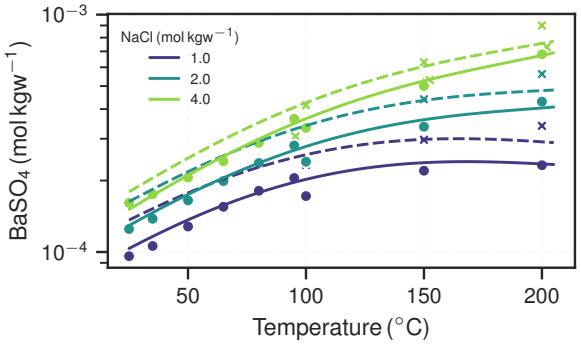

Figure 5.2: Model predictions of barite solubility using PHREEQC and the Pitzer database at ambient/vapor pressure (solid lines) and 50 MPa (dashed lines) for various temperatures and NaCl-contents. The circle and cross markers represent experimental values from Blount (1977) and Templeton (1960), respectively.

Furthermore, the initial ratio of the aqueous $\mathrm{SO_4^{2-}}$ and $\mathrm{Ba^{2+}}$ concentrations constrains the total precipitation amount, which follows from Eqs. 5.1 and 5.2. To illustrate this, two unitless example cases are considered: (A) $a_1 = 1$ and $a_2 = 1$; (B) $b_1 = 0.5$ and $b_2 = 2$. Both have the same initial product: $\zeta = a_1 \cdot a_2 = b_1 \cdot b_2 = 1$, but their ratios differ. If, for both cases, the two reactants are reduced uniformly due to precipitation by 0.1, the resulting products are $\zeta_\mathrm{A} = 0.9 \cdot 0.9 = 0.81$ and $\zeta_\mathrm{B} = 0.4 \cdot 1.9 = 0.76$. The product for the case B reduces more strongly and equilibrium is reached earlier. Therefore, the stronger the initial ratio deviates from unity, the less precipitation can be expected at thermodynamic equilibrium. The resulting ion ratios of the cases are shown in Tab. 5.1.

The target Mesozoic sandstones predominantly consist of quartz. Accessory barite content is reported to exist in the host rock in both regions (Bruss 2000; Wolfgramm 2002), with concentrations ranging from (100–300) ppm (max. 1 000 ppm). It appears paragenetically next to minerals such as anhydrite and celestite, and calcite, or in fracture fillings (Wolfgramm 2002). Aqueous Ba-concentrations are only provided for the reservoir fluids of NG and LND. Based on these compositions, the fluids appear to be close to equilibrium with respect to barite at reservoir conditions. Thus, the commonly applied assumptions is used that the fluids are in equilibrium with the mineral assemblage of the formation

rock (Kühn et al. 2002). As the starting point for all consecutive equilibrium and reactive transport calculations, the concentrations reported in the literature were adjusted to achieve equilibrium with all mentioned minerals (Tab. 5.1). The Cl^--content was adjusted to achieve charge balance.

The maximum barite scaling amount was derived from equilibrium modelling by changing the initial P and T state with respect to the production-injection cycle (Fig. 5.1a). Re-injection temperatures usually lie in the range (45–65) °C. The system pressure usually is in the order of 1 MPa (Seibt and Thorwart 2011; Wiersberg et al. 2004). P increases again at the injection well, which is in the order of the reservoir's down-hole pressure. The concentration difference between the initial and altered state represents the maximum amount of barite that can precipitate from the thermodynamic point of view.

Crystal growth kinetics

Crystal growth kinetics were considered in order to yield information on time and therefore location of scale formation. Pristine barite content in the rock matrix constitutes growth sites. Nucleation from solution can lead to an increase in the amount of active growth sites over time. This process was disregarded here, however, because the respective supersaturation ratios are assumed to be too low in the investigated cases for it to be growth determining. The reactive surface area of the available barite S_{barite} ($\text{m}^2\,\text{m}^{-3}$) determines the magnitude of the reaction rate, which was approximated using

$$S_{\text{barite}} = \phi_{\text{barite}} \cdot S \cdot \text{SF} \tag{5.3}$$

where ϕ_{barite} ($\text{m}^3\,\text{m}^{-3}$) is the initial volume fraction of barite in the rock, S ($\text{m}^2\,\text{m}^{-3}$) is the specific inner surface area of the rock, and SF is a dimensionless scaling factor for converting the specific into the effective reactive surface area. S was assumed to be $3 \cdot 10^4$ $\text{m}^2\,\text{m}^{-3}$ for the considered sandstones (Rabbani and Jamshidi 2014; Schumacher et al. 2020). Barite was found to exist in aggregations or fracture veins (Wolfgramm 2002), hence it was assumed that fluid accessibility is reduced. SF was therefore set to 0.05 accounting for the reduced volume fraction that is accessible to the pore network (Beckingham et al. 2016). From measured weight fractions of the mineral assemblage, the volume fraction of barite is

$$\phi_{\text{barite}} = (1-\phi)\frac{\frac{w_{\text{barite}}}{\rho_{\text{barite}}}}{\frac{w_{\text{barite}}}{\rho_{\text{barite}}} + \frac{1-w_{\text{barite}}}{\rho_{\text{quartz}}}} \tag{5.4}$$

where w_{barite} ($\text{kg}\,\text{kg}^{-1}$) is the weight fraction of barite in the rock and ρ_i ($\text{kg}\,\text{m}^{-3}$) is the respective density of barite (= 4 480 $\text{kg}\,\text{m}^{-3}$) and quartz (= 2 650 $\text{kg}\,\text{m}^{-3}$). For sake of simplicity, only quartz and barite were assumed to be in the rock for these calculation. The weight fraction of barite in the Bunter sandstones is reported to be in the range (0.01–0.10) wt% in the NGB (Wolfgramm 2002) or in traces in the URG (Bruss 2000), hence 0.10 wt% was used to have a conservative estimate.

A general formulation of the reaction mechanism was applied (Lasaga 1998):

$$R = -k_{\text{p}}(1 - \text{SR}) \tag{5.5}$$

where R ($\text{mol}\,\text{m}^{-2}\text{s}^{-1}$) is the surface area normalised precipitation rate and k_{p} is the temperature and ionic strength dependent rate constant. It has been shown that it is independent from pH in the range 3–9 (Ruiz-Agudo et al. 2015).

The kinetic rate constant k_{p} for bulk precipitation of barite was derived from unseeded batch experiments at low supersaturation SR < 8 (Zhen-Wu et al. 2016). k_{p} is temperature and ionic strength dependent. It was fitted with a first-order linear regression by minimising the averaged residuals:

$$\log_{10} k_{\text{p}} = -\frac{2532}{(T + 273)} + 0.694\sqrt{\text{IS}} + 0.29 \tag{5.6}$$

where T °C) is the temperature and IS (M) is the ionic strength. The data is given in Tab. 5.2. The underlying experimental data was conducted in the ranges (25–60) °C and (0–1.5) M, respectively. An extrapolation outside of these ranges can be seen in Fig. 5.3.

Table 5.2: Rate constants for bulk precipitation of barite at varying conditions used for the linear regression. The parameters T and IS are the input factors. Comparing experimental and model rates yields $R^2_{\text{adj}} = 0.88$.

T (°C)	IS (M NaCl)	$\log_{10} k^a_{\text{p,exp}}$ ($\text{mol m}^{-2}\,\text{s}^{-1}$)	$\log_{10} k_{\text{p,model}}$ ($\text{mol m}^{-2}\,\text{s}^{-1}$)
25	0.0	−8.46	−8.21
25	0.1	−7.62	−7.99
25	1.0	−7.60	−7.51
25	1.5	−7.55	−7.36
60	0.1	−7.22	−7.09
60	0.7	−6.60	−6.73
60	1.0	−6.54	−6.62
60	1.5	−6.52	−6.46
25	1.0	−7.40	−7.51

[a] Experimental data on bulk precipitation (Zhen-Wu et al. 2016)

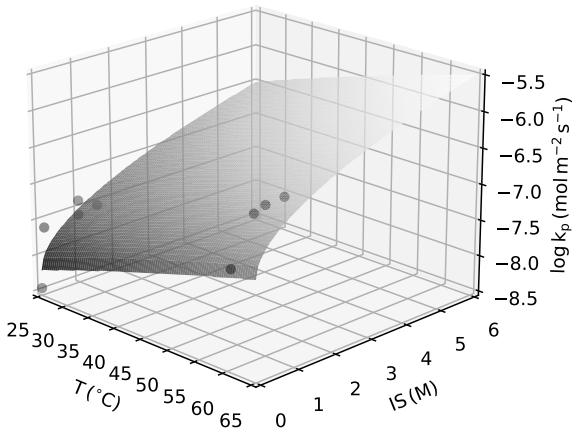

Figure 5.3: Kinetic rate constant for barite bulk precipitation as a function of temperature and ionic strength (Eq. (5.6)). The dots represent experimental data from Zhen-Wu et al. (2016).

5.2.2 Flow

Reservoir hydraulics

The injectivity index J ($\text{m}^3\,\text{s}^{-1}\,\text{Pa}^{-1}$) quantifies an injection well's efficiency for flow rate Q ($\text{m}^3\,\text{s}^{-1}$) and corresponding pressure build-up dP (Pa). The applied pressure difference follows from the planned flow rate and the transmissivity of the target reservoir. It can be approximated with Dupuit-Thiem's well equation, if Darcy flow is assumed (Dupuit 1863):

$$Q = 2\pi T \frac{s}{\ln \frac{r_\text{e}}{r_\text{w}}} \tag{5.7}$$

where T ($\text{m}^2\,\text{s}^{-1}$) is the transmissivity, s (m) is the water column corresponding to the pressure build-up, r_e (m) is the reach of the pressure difference and r_w (m) is the well radius. Transmissivity and reach are both determined by permeability K (m^2), hence solving this equation with regard to s must be

done iteratively using an adequate relationship for r_e and K. However, in the following it will suffice to consider only the relative injectivity loss resulting from pore clogging. It can be shown that it approximately equals permeability loss if the reach is large compared to the well bore radius ($r_e \gg r_w$).

Franz et al. (2018b) report that circulation rates need to be around 100 $m^3\,h^{-1}$ in order to achieve the necessary thermal output for a profitable and long-term operation. Higher reservoir temperatures compensate lower flow rates and vice versa. Further, J should be at least 50 $m^3\,h^{-1}\,MPa^{-1}$ in order to achieve these circulation rates with realistic pressure differences. The minimum hydraulic parameters for a porous hydrothermal reservoir are given it Tab. 5.3. K, M, and ϕ constitute mean reservoir properties and were accepted to be the starting point for all cases in order to compare them regarding barite scale formation. All reservoirs were thus simplified in the models to isotropic and homogeneous porous aquifers.

Table 5.3: Hydraulic parameters of a potential hydrothermal reservoir based on Franz et al. (2018b).

r_w (m)	Q ($m^3\,h^{-1}$)	K (mD)	M (m)	ϕ (−)
0.22	100	500	20	0.2

r_w is the well radius, Q is the flow rate, K is the permeability, M is the aquifer thickness, and ϕ is the porosity.

Reactive transport modelling

Flow from an injection well into a porous aquifer can be described by radially diverging flow (Bear 1988; Langevin 2008). If the regional hydraulic gradient is neglected and assuming homogeneous and isotropic flow properties of the aquifer, the injection well exhibits radial symmetry. Further, for fully penetrating injection wells, flow can be assumed to be planar and horizontal. Thus, a one-dimensional reactive transport model was set up to model the injection of supersaturated fluids into the aquifer. The governing equations are given in Section 4.3. To take barite precipitation kinetics into account, the advection-reaction-equation (4.27) is modified to:

$$\frac{\partial c_i}{\partial t} = -\frac{V}{r}\frac{\partial c_i}{\partial r} - R\,\frac{S_{\text{barite}}}{m_{\text{water}}}. \tag{5.8}$$

where c_i (M) is the solute concentration of a respective solute species i, t (s) is time, V ($m^2\,s^{-1}$) is a proxy for flow ($= Q/2\pi\,M\,\phi$), r (m) is the radial distance from the well-centre, R ($mol\,s^{-1}\,m^{-2}$) is the barite precipitation rate (Eq. (5.5)), and m_{water} ($kg\,m^{-3}$) is the solvent amount. Equation 5.8 is similar to Eq. (4.29), which was solved numerically and validated with an analytical solution Eq. (4.42). However, because the kinetic rate depends on changing activity coefficients, there is no straightforward analytical solution for this. Therefore, it was split and the resulting advective and reactive operators were solved separately by applying the sequential non-iterative approach. The upwind differences in space numerical method was used to solve the advection term ($V\,\partial c_i/r\,\partial r$). The reaction term ($R\,S_{\text{barite}}/m_{\text{water}}$) was solved with PHREEQC's batch kinetic solver, which uses an implicit Runge-Kutta algorithm (Parkhurst and Appelo 2013). A regular grid with 300 nodes and a constant time step was used, which fulfilled the Courant-Friedrich-Lewy stability criteria of the upwind scheme. Temperature and pressure were set to constant injection conditions. Solute concentrations (Ba^{2+} and SO_4^{2-}) at the inlet boundary were taken from equilibrated, initial reservoir data. All other species were used as constant background concentration. V and S_{barite} were kept constant during a simulation, as feedback from reaction on flow or reactive surface area were not taken into account. The solute concentration profiles therefore reached steady-state at one point.

The shape of steady-state concentration profiles are determined by the relationship of advection to reaction. If advection is increased, the profiles will be flattened and vice versa. A way to describe this relationship, is to use the dimensionless Damköhler number Da (Lichtner 1988):

$$\mathrm{Da}(r) = \frac{r r_\mathrm{c}}{V} \frac{R}{\phi c_{i,\mathrm{eq}}} \tag{5.9}$$

where r_c m) is a characteristic length set arbitrarily to 15 m. It follows that Da is a linearly increasing function along the flow path r, since all other parameters were assumed to be constant. The steeper this function, the shorter the equilibrium length scale and precipitation can be expected to happen closer to the point of origin. This is illustrated in Fig. 5.4 for various Da-slope values. The slope of Da(r) can be calculated simply with:

$$m_\mathrm{Da} = \frac{\mathrm{dDa}}{\mathrm{d}r} = \frac{\mathrm{Da}(r)}{r} \tag{5.10}$$

or written out:

$$m_\mathrm{Da} = \frac{r_\mathrm{c}}{V} \frac{R}{\phi\, c_{i,\mathrm{eq}}} = \frac{2\pi\, M\, r_\mathrm{c}}{Q} \frac{R}{c_{i,\mathrm{eq}}} \tag{5.11}$$

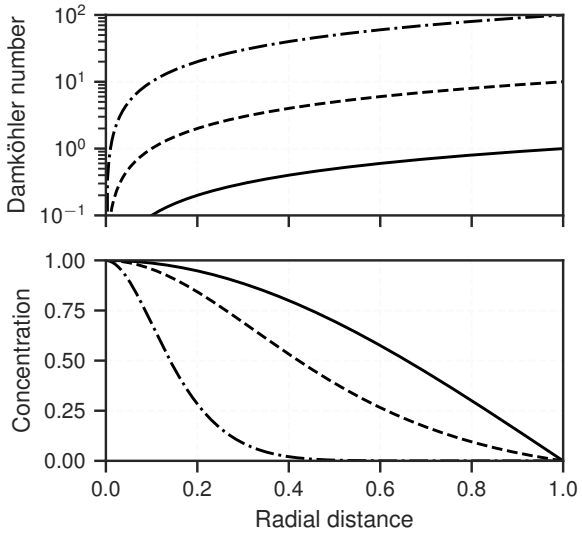

Figure 5.4: Concentration profiles for reactive transport problems with Damköhler ranges from 0–1 (solid), 0–10 (dashed) and 0–100 (dash-dotted).

Barite precipitation leads to porosity decrease, which can be expressed by volume fraction:

$$\frac{\mathrm{d}\phi_\mathrm{barite}}{\mathrm{d}t} = V_\mathrm{m,barite}\, R \tag{5.12}$$

where $V_\mathrm{m,barite}$ (m^3/mol) is the molar volume of barite. From this expression, the altered porosity was obtained for each domain node. Note that only quartz and barite were taken into account. To approximate the change in permeability, the widely used Kozeny-Carman relationship was applied (Carman 1937; Hommel et al. 2018):

$$\frac{K_j}{K_0} = \frac{\phi_j^3 (1-\phi_0)^2}{\phi_0^3 (1-\phi_j)^2} \tag{5.13}$$

where ϕ_0 and ϕ_j are the initial porosity and porosity at time step j, respectively. The effective permeability follows from a series of blocks; it was calculated using the harmonic mean of the individual blocks'

permeability (Renard and de Marsily 1997). Due to the radial diverging flow field, the logarithmic harmonic mean must be used:

$$K = \frac{\ln\left(\frac{r_n}{r_w}\right)}{\sum_{j=1}^{n} \frac{\ln \frac{r_j}{r_{j-1}}}{K_j}} \tag{5.14}$$

where r_j is the radial distance of a node j from the center of the injection well and r_w is the well radius. r_n was chosen so as to capture the saturation length scale.

The order of steps used for assessing the temporal permeability loss is as follows:

1. Calculate reactive surface area (Eq. (5.3)).
2. Calculate rate constant (Eq. (5.6)).
3. Calculate flow constant V.
4. Evaluate Damköhler number along the r-axis (Eq. (5.9)) and the corresponding slope (Eq. (5.11)).
5. Solve ARE (Eq.(5.8)) with numerical simulations until solutes reach steady-state.
6. Extrapolate porosity change at steady-state for each node over ten years.
7. Evaluate permeability loss using both the porosity-permeability relationship (Eq. (5.13)) and the effective permeability expression for the radial diverging flow field (Eq. (5.14)).

Each geothermal sample case was evaluated this way, representing the respective base scenario by using values described in the previous sections (Tabs. 5.1 and 5.3). In order to illustrate the effects of various parameters on the simulation results, additional scenarios were examined as in a one-at-a-time sensitivity analysis (Tab. 5.4).

Table 5.4: Varied parameters in the respective scenarios for a one-at-a-time sensitivity analysis. Decreasing Q and w_{barite} corresponds to decreasing flow velocity and precipitation rate, respectively.

Scenario	Parameter	Value	Unit
$T + 10$ °C	T	65	°C
$T - 10$ °C	T	45	°C
$Q/2$	Q	50	$m^3\,h^{-1}$
$R/10$	w_{barite}	0.01	–

5.3 Results

5.3.1 Equilibrium models

The scaling potential results from equilibrium calculations are shown in Fig. 5.5. The whole range from the respective reservoir temperature down to 25 °C illustrates the effect of temperature reduction, expressed as $dT = T_{res} - T_i$. Furthermore, the influence of pressure reduction dP from reservoir to surface condition is shown.

Figure 5.5a presents the respective barite saturation associated to dT and dP. The curves show an exponentially increasing trend for all cases with increasing dT. The URG cases (grey tones) generally exhibit higher saturation ratios than the NGB cases (red tones) at equal depths. The considered pressure reduction increases the saturation additionally, however not as strong as the accompanying temperature

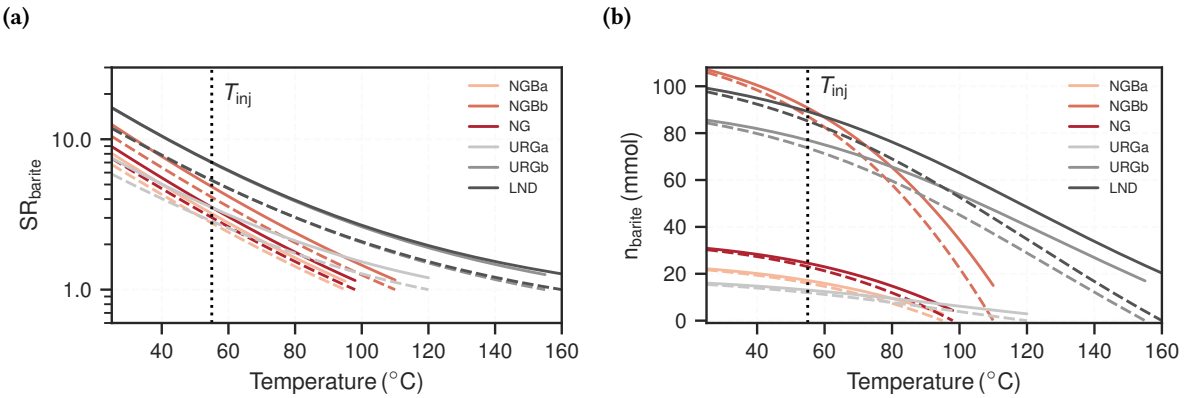

Figure 5.5: (**a**) Barite saturation according to reducing temperature for the various geothermal cases. $SR_{barite} = 1$ represents equilibrium with respect to barite. (**b**) The associated precipitation potential in units of millimoles per produced cubic metre of formation fluid. At respective reservoir conditions, the values are zero since equilibrium is assumed to be the initial state. The solid lines assume system pressures (1 MPa) and the dashed lines assume the respective reservoir pressures. The dotted vertical lines indicate the assumed injection temperature (T_{inj}).

reduction. Concerning the flow path in geothermal installations, saturation increases during the passageway through the production well and the heat exchanger due to temperature and pressure reduction, respectively. Supersaturation reaches its highest magnitude up to the point where the fluid is pressurised again and re-injected through the injection well. Assuming a temperature and pressure reduction down to 55 °C and 1 MPa, respectively, SR values for the various cases lie between 3.2 and 7.1. If these values overstep the supersaturation threshold, nucleation can be expected in the surface installation. SR values representative for the injection location are between 2.7 and 5.3, which are lower again due to the increased fluid pressure.

Figure 5.5b presents the associated total amount of barite that can precipitate from a cubic metre of produced formation fluid, which has been subjected to change in temperature and pressure. The cases representing greater depths (NGBb, URGb and LND) have a higher scaling potential than the shallower cases (NGBa, URGa, NG). Regarding fluid injection, values lie between (74–88) mmol m^{-3} and (12–23) mmol m^{-3} for the deeper and shallower cases, respectively. The results for injection conditions are also shown in Tab. 5.5. Lower injection temperatures result in more scaling potential, although the curve flattens off, meaning that it does not grow linearly. This further indicates that the potential scaling amount is not linearly correlated to the previously reported exponentially increasing saturation ratios. Generally, the higher the fluid's ionic strength, the more scaling can be expected. The same applies to the degree of temperature and pressure reduction, although the drop from reservoir to system pressure has a generally smaller effect on precipitation than temperature. The NGB cases tend to exhibit higher values, although their dT values to reach injection temperature are lower. For instance, temperature reduction for the NGBb case is close to half compared to the URGb case, however scaling potential is almost 20% higher for the NGBb case.

The initial ion ratios of aqueous SO_4^{2-} and Ba^{2+} are shown in Tab. 5.5. SO_4^{2-} concentrations are generally higher, between 30 and 300 times the concentration of Ba^{2+}. The ratios of the deeper cases are about one order closer to unity than the shallower cases. Cases with ion ratios closer to unity are reflected in steeper curve slopes in Fig. 5.5b.

5.3.2 Reactive transport models

The Damköhler number increases linearly for the considered flow model, originating from zero along the r-axis. The associated slopes m_{Da} (Eq. (5.10)) for all scenarios are shown in Tab. 5.5. The higher m_{Da}, the faster the advection time decreases along the r-axis compared to the reaction rate, and thus

Table 5.5: Summary of results of the equilibrium calculations and the reactive transport simulations for all considered geothermal cases and scenarios. Further, the developed empirical scaling score X_{score} is shown (Eq. (5.15)).

Case	Scenario	n_{barite} (mmol/m^3)	m_{Da} (1/m)	Loss (1/year)	X_{score} (10^{-4} mol/m year)
NGBa	Base	16	4.4	0.018	6.1
NGBa	T+10 °C	16	5.6	0.018	7.9
NGBa	T−10 °C	16	3.3	0.016	4.7
NGBa	$Q/2$	16	8.7	0.016	6.1
NGBa	$R/10$	16	0.43	0.0026	0.61
NGBb	Base	87	2.8	0.064	22
NGBb	T+10 °C	87	3.6	0.069	27
NGBb	T−10 °C	87	2.1	0.056	16
NGBb	$Q/2$	87	5.6	0.06	22
NGBb	$R/10$	87	0.28	0.01	2.1
NG	Base	23	4.1	0.024	8.3
NG	T+10 °C	23	5.3	0.025	11
NG	T−10 °C	23	3.2	0.022	6.4
NG	$Q/2$	23	8.2	0.022	8.3
NG	$R/10$	23	0.41	0.0036	0.83
URGa	Base	12	1.6	0.0057	1.7
URGa	T+10 °C	12	2.3	0.0066	2.4
URGa	T−10 °C	12	1.2	0.0048	1.2
URGa	$Q/2$	12	3.3	0.0051	1.7
URGa	$R/10$	12	0.16	0.0008	0.17
URGb	Base	74	1.1	0.024	6.9
URGb	T+10 °C	74	1.4	0.029	9.2
URGb	T−10 °C	74	0.79	0.02	5.1
URGb	$Q/2$	74	2.1	0.022	6.9
URGb	$R/10$	74	0.11	0.0034	0.69
LND	Base	85	0.8	0.022	6
LND	T+10 °C	85	1.0	0.026	7.8
LND	T−10 °C	85	0.58	0.018	4.3
LND	$Q/2$	85	1.6	0.02	6
LND	$R/10$	85	0.08	0.003	0.6

T is the injection temperature, Q is the flow rate, R is the precipitation rate, n_{barite} is the total precipitation potential, m_{Da} is the slope of the Damköhler number along the r-axis, and loss represents the relative, effective permeability decrease per year, as in $K/K_0 - 1$.

the more precipitation will occur more concentrated close to the injection well. All URG cases have comparably low slope values, whereas the NGBa and NG cases have the highest values. Reducing the flow rate increases, while reducing the reaction rate reduces m_{Da} proportionally. In accordance with the kinetic rate expression (Eq. (5.6)), increasing temperature increases m_{Da}.

In the following, the reactive transport simulation results are presented. In Figs. 5.6 and 5.7, the NGB and URG cases are shown, respectively. On the left-hand side, the temporal porosity changes at steady-state are plotted against the r-axis. Porosity changes result from increase of barite volume fraction. Note that the porosity-change-plots are cut off at 10^{-4} per year, as lower values are assumed to be negligible with regard to their impact on permeability during the lifetime of a geothermal installation. This corresponds to a porosity loss of −0.1% over the course of ten years. All curves show flipped parabola shapes in the semi-log plot, with the porosity change maximum close to the origin, i.e., the outflow of the injection well. The NGBb case generally exhibits the highest porosity changes with a maximum of 0.7% porosity loss per year. The URGa case has the least loss of more than one order of magnitude less than that of NGBb. It can be seen that the URG cases have flatter curves and broader widths of significant precipitation along the axis. Precipitation is concentrated closer to the well for the NGB cases. They have ranges of about (4.5–6.5) m, compared to (5.5–10.5) m for the URG cases.

Changing the injection temperature within in the considered ranges of the sensitivity analysis only has a small effect compared to the base case. A temperature increase accelerates precipitation and vice versa. As such, lower injection temperature increases the reach and also lowers the maximum porosity decline close to the well. Smaller flow rates generally result in less precipitation in total, which can be anticipated by the total area under the curves; compared to the base case, the maximum porosity changes at the inlet still has the same order of magnitude, however the reach is reduced by about 30%. Lower reaction rates (R) flatten the curves significantly, meaning precipitation is more distributed along the flow path. If the magnitude of R is one order lower compared to the base case, the porosity change peak is also one order of magnitude lower and the reach is increased by about 50%.

The associated temporal permeability ratios (K/K_0) over the course of ten years are shown on the right-hand side of Figs. 5.6 and 5.7. Notably, all curves illustrate a linear decline of permeability over time. The related injectivity losses per year ($1 - K/K_0$) are shown in Tab. 5.5. In the base case, the NGBb case exhibits the strongest permeability decline by over 6% per year. It slightly deviates from a linear curve towards the end of the considered time. The URGa case shows the lowest permeability decline of just below 0.6% per year; the others have between 1.8% and 2.4% loss per year. Concerning the sensitivity analysis scenarios, change in reactivity has the strongest impact on the permeability decline. If the reaction rate is reduced by one order of magnitude compared to the base case, the resulting permeability loss after 10 years is also reduced by almost one order of magnitude. For the shallower cases (NGBa, URGa, and NG), the other sensitivity analysis scenarios regarding temperature and flow rate show only negligible deviations from the base case. For the deeper cases (NGBb, URGb, and LND), increasing temperature (lower dT) accelerates permeability loss and decreasing temperature (higher dT) slows the decline down. Decreasing the flow rate reduces the permeability loss. However, this effect is small, about 10% deviation from the base case.

The final effective permeability changes after ten years for all investigated cases and scenarios are summarised in Fig. 5.8. It can be seen that the reservoirs of greater depth generally are affected more strongly by permeability losses. The NGB cases are generally affected more strongly than the URG cases; NGBb has by far the highest permeability loss (64%). Further, NG is similarly affected than URGb and LND, although it is not as deep; all exhibit a loss of approximately 24%. URGa has the least loss of just below 6%. Again, for all shallower cases (NG, NGBa, URGa), varying injection temperature or flow rate only has a little to no effect compared to the base case. There is a noticeable effect, however, with regard to injection temperature variation for the deep cases. As such, decreasing temperature reduces the permeability loss, whereas increasing temperature results in more loss. If reactivity is reduced compared to the base case, permeability loss is significantly less. Especially for the NGBb case, loss after ten years drops from 64% to only 10% in this scenario. The loss of the URGa case goes down to virtually zero in this scenario.

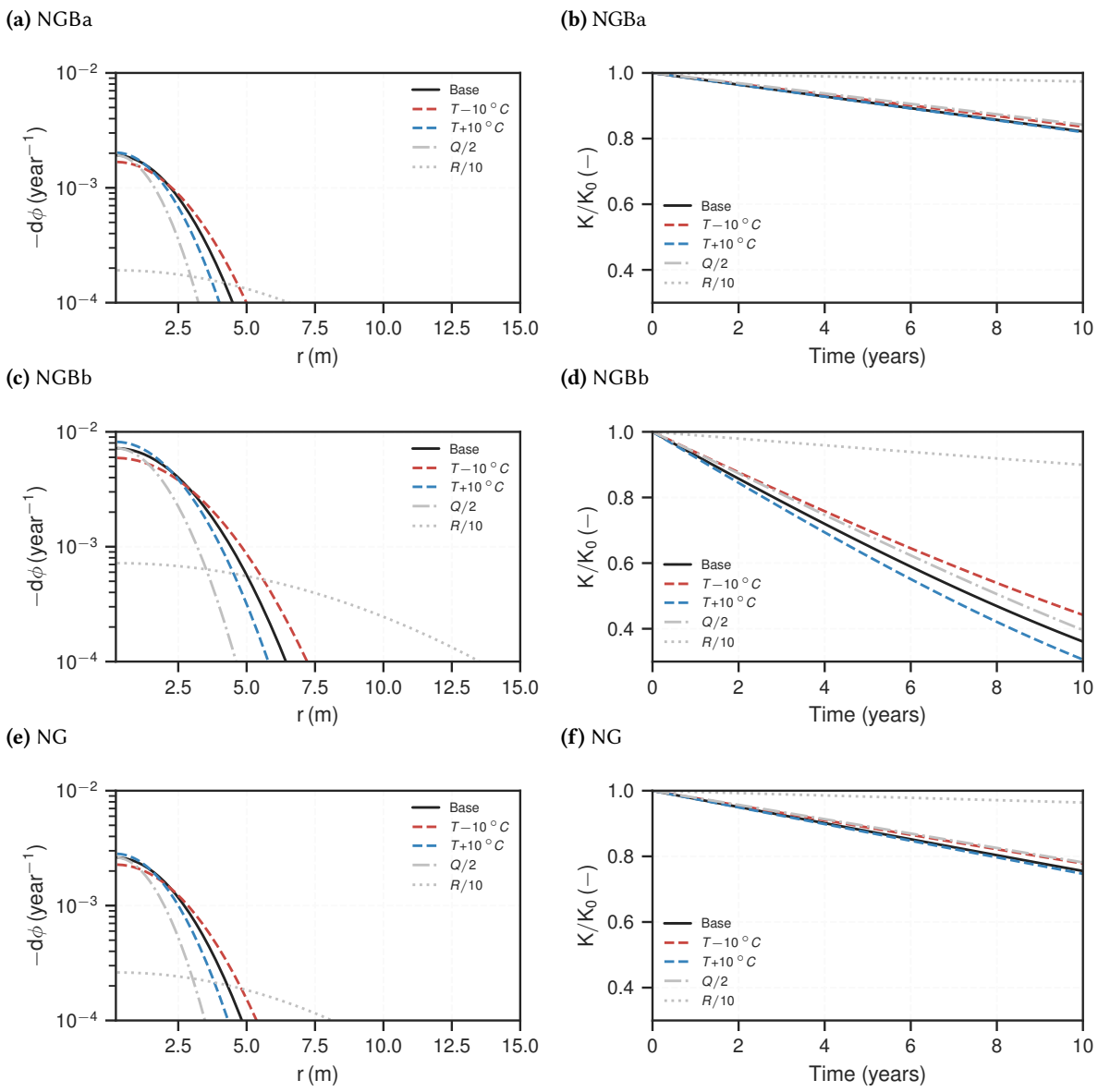

Figure 5.6: Reactive transport simulation results for the NGB cases. The lines represent respective scenarios. Plots on the left hand side show the distribution of porosity change per year for steady-state. Plots on the right hand side illustrate the resulting relative, effective permeability loss (Eq. (5.14)) based on the porosity-permeability relationship (Eq. (5.13)) over the course of ten years.

5.4 Discussion

Total barite scaling potential is determined by fluid composition, temperature reduction, pressure reduction, and ion ratio of Ba^{2+} and SO_4^{2-}. For the presented geothermal cases in the NGB and the URG, formation fluid temperature and salinity increase with greater reservoir depth. The deeper cases also showed ion ratios closer to unity. These factors all increase the precipitation potential and thus increase the scaling risk for deeper reservoirs. Furthermore, for cases at similar depths, fluid salinity is higher in the NGB and temperature is higher in the URG, but total scaling potential is in the same order of magnitude. As the corresponding saturation ratios were significantly higher for the URG cases, this illustrates that these values are not linearly correlated. Saturation ratios can only be taken as an indication, whether precipitation can be expected or not. Scaling amounts need to be investigated in detail for a specific location, taking the mentioned factors into consideration.

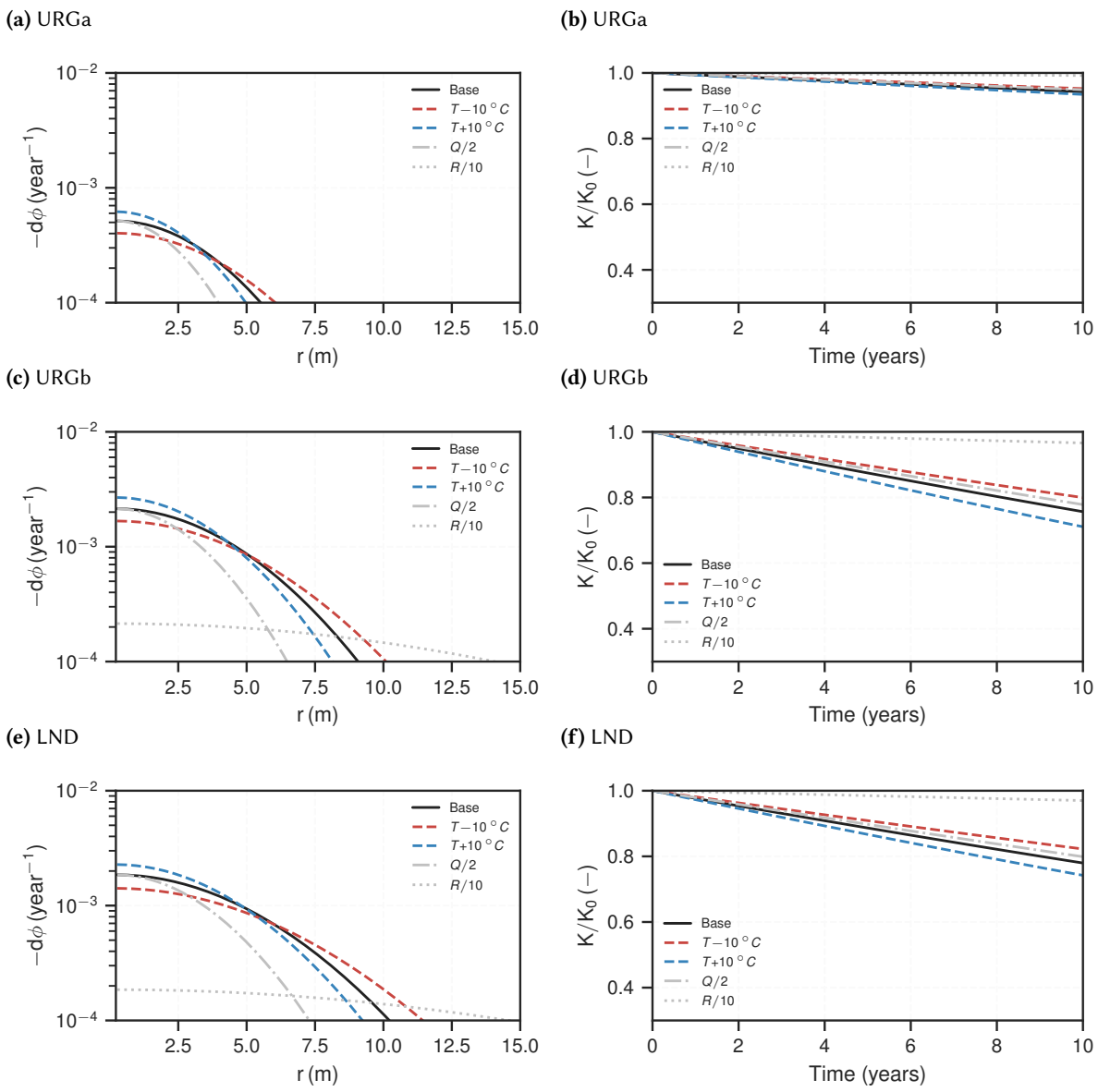

Figure 5.7: Reactive transport simulation results for the URG cases. The lines represent respective scenarios. Plots on the left hand side show the distribution of porosity change per year for steady-state. Plots on the right hand side illustrate the resulting relative, effective permeability loss (Eq. (5.14)) based on the porosity-permeability relationship (Eq. (5.13)) over the course of ten years.

An irreversible injectivity decline of about 35% after 16 years of injection has been reported at the geothermal site Neustadt-Glewe (Birner et al. 2015). They attributed this mainly to formation of sparingly soluble scales in the reservoir, such as barite, celestite, and various sulfides (Birner et al. 2015; Wolfgramm et al. 2011a). This order of magnitude is in fact in accordance with calculated injectivity losses, even though only barite scaling was taken into consideration in the present study. In this regard, some conservative assumptions were made, to the effect that the upper range of risk associated to barite scaling was assessed. For instance, it was assumed that barite growth does not happen until the re-injected fluid comes into contact with active growth sites (solid barite) in the formation rock. Formation of additional active growth sites can occur through nucleation, increasing the precipitation and injectivity loss rate further. Whether this effect is significant depends on site characteristics like mineralogy of the in-situ rock. This process was disregarded in the models, hence the real precipitation rate will be underestimated to some degree. For the considered cases, nucleation was not considered to

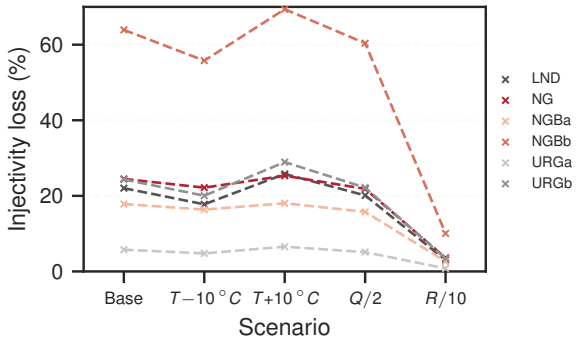

Figure 5.8: Effective permeability loss after ten years of injecting barite supersaturated fluids into the reservoir. T is the injection temperature, Q is the flow rate, R is the precipitation rate. Note that the connecting dashed lines are only plotted to help distinguish the cases from each other.

be a growth determining step, as the highest saturation ratios were presumed to be too low for this (He et al. 1994a; Prieto 2014). Nuclei formation can be promoted, however, by longer shut-in periods (Griffiths et al. 2016; Nitschke et al. 2014; Regenspurg et al. 2015). As a consequence, scale formation sets in prior to the fluid reaching the formation rock, thus not affecting the injectivity as strongly, but perhaps with other unwanted impediments (Regenspurg et al. 2015). Furthermore, re-injected fluids heat-up again gradually in the reservoir, depending on flow rate and heat transfer, which has not been taken into consideration. This increases barite solubility again and thus reduces scaling risk; more so if flow rate is reduced. In light of the simulated scaling reach of below 10 m, however, this effect appears to be negligible. Yet, injection pressure must be increased to maintain injection rates if permeability decreases. This could pose problems, as this increases the chance for loose particles to redistribute and clog pores. This process, however, is hard to quantify and also was not considered.

Supersaturation and kinetic rate both depend on the fluid's salinity and temperature. An increase in salinity therefore increases the precipitation rate two-fold. The relationship with regards to temperature is different: supersaturation increases further with temperature reduction (increased dT), whereas the rate constant is proportional to the absolute temperature. For quartz scaling in high-enthalpy systems, something similar has been shown by Pandey et al. (2015). Reducing temperature results in a counter effect of higher supersaturation, but lower kinetic rate constant. Temperature variations as part of the sensitivity analysis had no significant impact on calculated injectivity loss, at least in the considered ±10 °C range. This explains why the NGB cases are generally affected more strongly.

Scaling potential needs to be put into perspective with regard to distribution along the flow path in order to assess implications for system longevity. Due to the radial diverging flow, large spatial distribution of scale formation means less effective permeability loss. This is promoted by slower reaction rates and higher flow velocities. The URG cases generally showed widespread distribution along the flow path, i.e., flatter precipitation curves, attributable to lower reaction rates. An important point is that equal hydraulic properties were assumed for all cases, in order to be able to compare them with regard to fluid chemistry and precipitation kinetics. While the model assumptions of radial diverging and planar flow are reasonable for homogeneous and isotropic porous aquifers with fully penetrating injection wells, they are simplifying for partially penetrating wells and especially fractured aquifers. The former have spherical flow components, thus this model treatment overestimates flow velocities and underestimates the permeability loss in the near-vicinity of the injection well for these cases. Projects in the URG rely on multi-horizontal approaches in order to minimise exploration risk (Baumgärtner et al. 2010). Therefore, there are sections with slow flow through the porous matrix, but also sections with increased permeability due to fractures. Fracture permeability is characterised by preferential flow with increased flow velocities and also decreased water-rock contact, i.e., less effective reactive surface

area. Both factors hypothetically increase the scaling distribution in the formation rock, reducing the scaling risk for the URG even further compared to the NGB.

Scaling distribution patterns in the subsurface can be described by fluid flux, total scaling potential, and Damköhler number. The latter relates the respective magnitudes of advection and precipitation kinetics. Assuming that rock reactivity is homogeneous on a large scale, the Damköhler number increases linearly along the r-axis due to the radially diverging flow. The steeper the slope (m_{Da}), the closer the scaling distribution is to the injection well. Further, the volumetric scaling potential (n_{barite}) as well as fluid flux (Q) are also necessary to determine scaling in the subsurface with regard to injectivity decline, as these quantify the total amount that can precipitate from solution. In essence, these three factors provide insights into distribution and intensity of scaling in the subsurface. If they are simply lumped together, the following scaling score is derived:

$$X_{\mathrm{score}} = m_{\mathrm{Da}} \cdot n_{\mathrm{barite}} \cdot Q. \tag{5.15}$$

The resulting scores for the respective cases and scenarios are provided in Tab. 5.5. They qualitatively suggest, which cases' injectivity will be affected more than others and therefore generate a ranking fit. Although this score only yields an approximation, it can nevertheless be used as a quick comparative value, without having to run elaborate reactive transport simulations. Furthermore, this scaling score is correlated with the previously calculated injectivity losses. For instance, the NGBb case has the largest values, while URGa has the lowest, which corresponds closely to the simulation results. If plotted against each other, a clear linear correlation can be seen (Fig. 5.9). This is a valuable insight, since the calculated injectivity losses result from multiple non-linear considerations: (I) steady-state reactive transport simulations, (II) porosity-permeability relationship, and (III) effective permeability approximation. By calibrating the score with the reactive transport simulation results, the obtained linear correlation represents a lightweight score for approximating the temporal injectivity loss associated to barite scaling:

$$\mathrm{Loss}\,(\%\,\mathrm{year}^{-1}) = 2.89 \cdot 10^{-5} \cdot X_{\mathrm{score}}\,(\mathrm{mol\,m}^{-1}\,\mathrm{year}^{-1}). \tag{5.16}$$

It is easily applicable to new geothermal installations and may be calibrated further if additional data becomes available in this regard. The overall presented approach specifically treats barite as the sole scale formation agent. It can be adapted to make respective predictions for similar formation reactions of minerals exhibiting prograde solubility, for example silica or other sulfates. Though it is explicitly pointed out that the respective reaction mechanism needs detailed consideration.

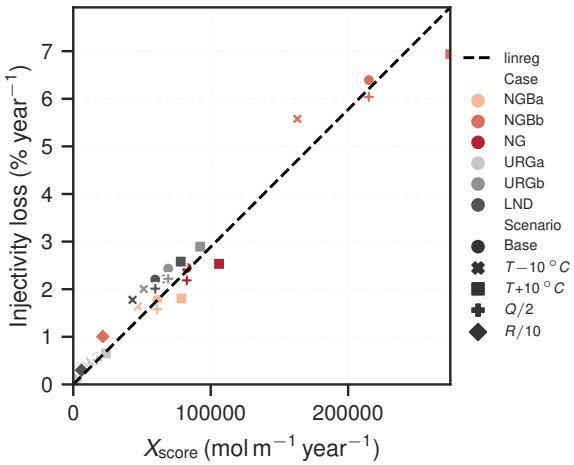

Figure 5.9: Scaling score plotted against injectivity loss per year as calculated from reactive transport simulations for the considered geothermal cases and different scenarios (Tab. 5.5). The dashed line is a linear regression without intercept. Using Eq. (5.15) for X_{score}, the slope is $2.89 \cdot 10^{-5}$ and $R^2 = 0.96$.

5.5 Conclusions

Two model concepts were presented to approximate barite scaling formation in geothermal systems of the North German Basin and Upper Rhine Graben regions: an equilibrium model approach and a transport model coupled with precipitation kinetics. It was shown that temperature and pressure reduction during the production-injection cycle results in supersaturated conditions for barite in all cases, which is accountable for scaling. Equilibrium models were used to calculate the total potential scaling amount, which gives a first indication on the related risk for a long-term operation. This scaling potential increases proportionally to the imposed degree of temperature and pressure reduction dependent on the respective geothermal system management, as well as to formation fluid salinity. These parameters are generally correlated with reservoir depth. Fluids encountered at similar depths are hotter in the URG, while they are more saline in the NGB. The scaling potential is similarly high for both regions, while deeper reservoirs tend to be affected more strongly.

A comprehensive assessment of scaling risk needs to include the respective scaling location and distribution along the flow path in order to quantify the accompanied injectivity decline. From reactive transport simulations, information on both the scaling distribution in the subsurface and the related injectivity loss was obtained. Precipitation kinetics are taken into account, which also depend on temperature and salinity, similarly to the total scaling potential. Injection temperatures are usually in the same order for different geothermal installations, thus the corresponding temperature reduction (dT) varies. The barite precipitation rate is higher for the NGB cases due to their higher fluid salinities. Thus, scaling will preferentially happen closer to the injection well and damage reservoir permeability more severely. Therefore, the NGB cases are generally at higher risk with regard to injectivity losses, while the shallow URG case showed almost no losses. A sensitivity analysis showed that varying temperature within a 10 °C margin, as well as significantly reducing the flow rate had negligible effects on injectivity loss. The kinetic rate, on the other hand, exhibited a strong sensitivity.

A scaling score was developed, which takes the total scaling potential, the Damköhler number and the flow rate into account. It correlates strongly with the results of the reactive transport simulations and may be calibrated with further data. It is easily applicable in order to get an indication on the accompanied scaling risk for a specific geothermal location, without having to run elaborate reactive transport simulations. The presented approach can be adapted to make scale formation and injectivity loss predictions for mineral formation reactions similar to that of barite.

CHAPTER 6

Barite scaling potential modelled for fractured-porous geothermal reservoirs

This is a reprint of an article published in the journal Minerals (MDPI)[1].

Abstract

Barite scalings are a common cause of permanent formation damage to deep geothermal reservoirs. Well injectivity can be impaired because the cooling of saline fluids reduces the solubility of barite, and the continuous re-injection of supersaturated fluids forces barite to precipitate in the host rock. Stimulated reservoirs in the Upper Rhine Graben often have multiple relevant flow paths in the porous matrix and fracture zones, sometimes spanning multiple stratigraphical units to achieve the economically necessary injectivity. While the influence of barite scaling on injectivity has been investigated for purely porous media, the role of fractures within reservoirs consisting of both fractured and porous sections is still not well understood. Here, we present hydro-chemical simulations of a dual-layer geothermal reservoir to study the long-term impact of barite scale formation on well injectivity. Our results show that, compared to purely porous reservoirs, fractured porous reservoirs have a significantly reduced scaling risk by up to 50%, depending on the flow rate ratio of fractures. Injectivity loss is doubled, however, if the amount of active fractures is increased by one order of magnitude, while the mean fracture aperture is decreased, provided the fractured aquifer dictates the injection rate. We conclude that fractured, and especially hydraulically stimulated, reservoirs are generally less affected by barite scaling and that large, but few, fractures are favourable. We present a scaling score for fractured-porous reservoirs, which is composed of easily derivable quantities such as the radial equilibrium length and precipitation potential. This score is suggested for use approximating the scaling potential and its impact on injectivity of a fractured-porous reservoir for geothermal exploitation.

6.1 Introduction

Barite ($BaSO_4$) scalings are a common cause of permanent formation damage to deep geothermal reservoirs. The continuous re-injection of priorly produced fluids may induce the sulfate mineral to precipitate in the host rock, as cooling reduces the solubility of barite (Tranter et al. 2020). Consequentially, these so-called mineral scalings may impair the well injectivity, a key performance indicator of geothermal power plants (Agemar et al. 2014). The scaling risk is particularly elevated when the geothermal fluids have a high mineralisation (> 100 g/L), and the cooling margin is high (> 40 °C) (Wolfgramm et al. 2011a). When conceptualising a geothermal project, it is crucial to take scaling into account, as it can be

[1]Morgan Tranter et al. (2021a). Barite Scaling Potential Modelled for Fractured-Porous Geothermal Reservoirs. *Minerals* 11(11):1198. DOI: 10.3390/min11111198.

a significant cause of expense or even the reason that a geothermal power plant fails (Regenspurg et al. 2015; Scheiber et al. 2013).

In a previous numerical study, we investigated the barite scaling potential and its impact on injectivity for porous reservoirs (Tranter et al. 2020). Scaling potential was quantified for geothermal fluids representative of the North German Basin and the Upper Rhine Graben (URG). We came to the conclusion that, disregarding variations in reservoir type, geothermal sites in the North German Basin have a higher scaling risk, since the respective brines are significantly more mineralised. Many geothermal reservoirs, however, rely on natural or engineered fractures to achieve the economically viable hydraulic yields (Vidal and Genter 2018). The overall fluid flow regime and inner surface area (reactivity) within fractured and fractured-porous media are fundamentally different, and need to be treated separately. This is where we follow up on in the present study.

The URG is an area of continuous interest for geothermal energy, where fracture networks in the sedimentary cover (Triassic/Permian sediments) and in the granitic basements (Paleozoic) play an essential role in brine circulation (Bächler et al. 2003; Guillou-Frottier et al. 2013). Fracture zones are often filled with secondary minerals and exhibit insufficient permeability (Dezayes et al. 2010; Genter et al. 1996). One common approach to improve a well's injectivity or productivity is to reactivate these natural fractures with hydraulic injection, which falls within the concept of Enhanced Geothermal Systems (EGS). Furthermore, a multi-horizon-concept was successfully applied to the commercial power plant Landau (Germany) (Baumgärtner et al. 2010; Schindler et al. 2010). The aim was to minimise exploration risk by crossing the fault system in the Buntsandstein, Perm and the granitic basement. These target horizons are located in Landau at depths of approximately 1 900 m to 3 000 m, exhibit temperatures of over 150 °C, and hold brines with mineral contents of over 107 g/L (Baumgärtner et al. 2010; Vidal and Genter 2018). The reservoir is classified as a fracture-porous aquifer, whereas the respective flow rate ratios of the porous and fracture components are hard to quantify.

Ngo et al. (2016) investigated the potential dissolution and precipitation behaviour of minerals specifically in the Soultz-sous-Forêts geothermal system, which also lies in the URG-area. They identified that, based on saturation state, as a reservoir cools, barite among other minerals shows a tendency to precipitate. At the same site, fracture veins filled with barite were documented in core samples (Griffiths et al. 2016), which indicates the associated risk of barite precipitation reducing fracture permeability. A related kinetic model illustrates that open fractures can seal within months or days, depending on temperature. The clogging process of barite precipitation in porous and fractured reservoir rock was investigated recently at the laboratory scale, showing significant permeability loss by up to one order of magnitude of the core samples (Orywall et al. 2017). Fracture aperture is a key parameter here; a numerical study suggests that large fractures are less susceptible to scaling-induced permeability loss, due to the variations in specific reactive surface area (Tranter et al. 2021b).

Rock permeability evolution as a consequence of altering pore space is a most important aspect of subsurface utilisation and focus of many recent studies (e.g., Hommel et al. 2018; Poonoosamy et al. 2020b; Wetzel et al. 2020b, 2021). Numerical studies of geochemical-reaction-driven transmissivity evolution in geothermal reservoirs include silica scaling in single-fracture models (Pandey et al. 2015), barite precipitation in porous reservoir models (Tranter et al. 2020), and acid stimulation in single- and double-porosity models (Lucas et al. 2020). The present study closes the gap for modelling barite-scaling-induced permeability loss in fractured-porous geothermal reservoirs. We coupled two one-dimensional, continuum-scale models (dual-layer) to study the impact of barite scaling on the injectivity of a geothermal well based on the Landau geothermal reservoir. By separating the fracture and porous aquifer into two individual layers, we investigate the influence of varying the uncertain hydraulic relevance of fractures. We applied a radial diverging flow field and barite precipitation kinetics, similar to Tranter et al. (2020). Moreover, we carried out a scenario analysis, in which flow rate, amount of active fractures, and fluid chemistry were varied, to quantify relationships between parameters. These provided the basis for an analytical scaling score, which can approximate the scaling potential for fractured-porous reservoirs without the need to run numerical simulations. This tool can be used to

quickly assess whether a substantial scaling risk exists for a geothermal site, which is beneficial for an initial screening.

6.2 Methods

In this study, the Landau deep geothermal reservoir was taken as the basis for the parametrisation of our models. At Landau, a multi-reservoir approach was adopted, which aims to utilise the sandstone formations Buntsandstein and Rotliegendes, as well as the altered section of the granitic basement (Baumgärtner et al. 2010; Schindler et al. 2010). The sandstone formations are porous to fractured-porous aquifers, whereas the granitic basement is a purely fractured aquifer with negligible matrix permeability (Bächler et al. 2003). The open-hole section of the injection well Gt La2 begins at 2 200 m and the total drilled length is 3 170 m (Vidal and Genter 2018). To simplify the modelling setup, a total utilised reservoir thickness of 1 000 m was assumed, subdivided into two horizontal aquifer layers of 500 m in thickness, each (Fig. 6.1b). This dual-layer reservoir simulation setup consists of a homogeneous, sedimentary-porous aquifer (upper layer), and a granitic-fractured aquifer with variable sizes and different amounts of horizontal fractures (lower layer). These assumptions allow for the development of a radial-symmetric system that can be represented by a set of 1D models. Interaction or mass transfer between the reservoir layers was not taken into account; therefore the approach using two parallel layers is viable. The total reservoir simulation time was ten years to model the lifecycle of a borehole until restoration is needed.

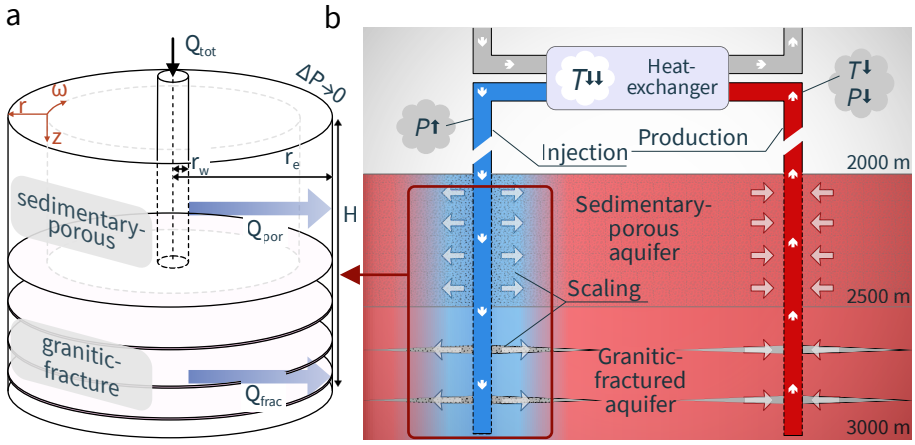

Figure 6.1: Conceptual model of radially diverging groundwater flow near an injection well of a geothermal system. (**a**) Injection flow components are split into two parts for the sedimentary-porous aquifer (upper layer) and the granitic-fractured aquifer with variable sizes and different amounts of horizontal fractures (lower layer). The boundary is the range of influence, i.e., where the induced pressure difference moves towards zero. (**b**) Produced fluids, originating from the deep reservoir, are cooled and depressurised along the flow path through the heat exchanger. Thermodynamically disequilibrated fluids are then re-injected via the injection well, where scaling and formation damage are anticipated.

6.2.1 Reservoir flow

Fluid flow from an injection well into an aquifer creates a radially diverging flow field that is advection dominated in its proximity (Fig. 6.1a) (Bear 1988). The flow through area of the aquifer perpendicular to the horizontal axis increases with radial distance to the well. Let us assume a constant injection rate and quasi-stationary state, a negligible regional hydraulic gradient, and a homogeneous and isotropic medium. Darcy velocity then is a function of radial distance (Eq. (6.1)).

$$q(r) = \frac{Q}{A(r)} = \frac{Q}{2\pi\, r\, H}, \tag{6.1}$$

where q (m/s) is the Darcy flow velocity, r (m) is the radial distance from the well-centre, Q (m^3/s) is the flow rate, and H (m) is the flow-through thickness. Now let us further assume n horizontally layered aquifers with differing hydraulic properties. The respective flow share through a layer i (subscript por for porous or frac for fracture) corresponds to its transmissivity $\mathcal{T}$ (m^3) share with respect to the reservoir transmissivity (Eq. (6.2)).

$$\frac{Q_i}{Q_{\text{tot}}} = \frac{\mathcal{T}_i}{\mathcal{T}_{\text{res}}}, \tag{6.2}$$

where Q_{tot} is the total well's injection rate, *res* refers to the screened section of the reservoir, and transmissivity defined here as

$$\mathcal{T}_i = \mathcal{K}_i \, H_i, \tag{6.3}$$

with the permeability $\mathcal{K}$ (m^2). The effective permeability of a reservoir for flow perpendicular to heterogeneity is the arithmetic mean of permeabilities of all layers (Eq. (6.4)) (Renard and de Marsily 1997).

$$\mathcal{K}_{\text{res}} = \frac{\sum_{i=1}^{n} \mathcal{K}_i \, H_i}{H_{\text{res}}}. \tag{6.4}$$

This effective reservoir permeability for a confined reservoir was derived from well tests assuming Darcy flow and quasi-stationary state. Dupuit-Thiem's well equation (Dupuit 1863) (Eq. (6.5)), the measured injectivity index (Eq. (6.6)), and the approximate hydraulic range of influence in the reservoir (Eq. (6.7)) were used for this (Genske 2006).

$$Q = 2\pi \, s \, \mathcal{K} \, \frac{\rho_f \, g}{\mu_f} \, H \, \frac{1}{\ln r_{\text{e}}/r_{\text{w}}}, \tag{6.5}$$

$$J = \frac{Q}{P} = \frac{Q}{s \, \rho_f \, g}, \tag{6.6}$$

$$r_{\text{e}} = 3000 \, s \, \sqrt{\mathcal{K} \, \frac{\rho_f \, g}{\mu_f}}, \tag{6.7}$$

where ρ_f (kg/m^3) is the fluid density, g (m/s^2) is the gravitational acceleration, μ_f (Pa s) is the fluid viscosity, r_{w} (m) is the well radius, r_{e} (m) is the hydraulic range of influence, J (m^3/Pa s) is the injectivity, P (Pa) is the pore pressure, and s (m) is the water column pressure.

For the Landau geothermal reservoir, we obtained the following (Schindler et al. 2010; Tischner et al. 2006): with $Q = 100$ m^3/h, $H = 1\,000$ m, $J = 40$ m^3/h MPa ($s \approx 240$ m), and constant fluid density and viscosity of 1 050 kg/m^3 and 4×10^{-4} Pa s, respectively, the effective reservoir permeability and transmissivity are $\mathcal{K} = 5 \cdot 10^{-15}$ m^2 and $\mathcal{T} = 5 \cdot 10^{-12}$ m^3, respectively. The well radius was set to $r_{\text{w}} = 0.22$ m. The range of influence (Eq. (6.7)) is approximately $r_{\text{e}} = 260$ m, which had to be fitted iteratively since Eqs. (6.5) and (6.7) cannot be readily resolved for $\mathcal{K}$.

The rock permeability of a fracture-dominated aquifer is generally determined by its fracture properties, such as density, aperture, length, geometry, dip, and connectivity. The simple case of infinitely extending, horizontal, parallel plates was assumed here for the fracture layer. Consequently, the permeability of a single fracture was calculated with only its hydraulic aperture using the cubic law (Eq. (6.8)) (Witherspoon et al. 1980).

$$\mathcal{K}_{\text{frac}} = \frac{(2\delta)^2}{12}, \tag{6.8}$$

where δ (m) is the half-fracture aperture. The total flow-through height of an aquifer and its transmissivity with n_{frac} uniform fractures assuming negligible matrix permeability was calculated with Eqs. (6.9) and (6.10), respectively (Paillet et al. 1987).

$$H_{\text{frac}} = (2\delta) \, n_{\text{frac}}, \tag{6.9}$$

$$\mathcal{T}_{\text{frac}} = \frac{(2\delta)^3 \, n_{\text{frac}}}{12}, \tag{6.10}$$

where n_{frac} is the amount of fractures. Given a certain flow share with respect to a reservoir and the amount of uniform fractures, the hydraulic aperture and permeability was determined.

6.2.2 Reactive transport

Three fluid samples were considered as input concentrations that are representative of deep geothermal reservoirs in the Upper Rhine Graben (Tab. 6.1). URG 2000 m and URG 3000 m are averaged samples from the respective depths (Wolfgramm and Seibt 2008); LND is the fluid concentration of the Landau geothermal reservoir (Sanjuan et al. 2016). All three samples are Na-Cl-type waters. The shallow URG sample has the lowest ionic strength (1.3 M), followed by LND (2.0 M) and then URG 3000 m (2.3 M). Each of these samples were modified using the PHREEQC code v3.7 (Parkhurst and Appelo 2013) to achieve equilibrium at initial reservoir conditions with minerals that are expected to be present in the reservoir rocks (Tranter et al. 2020). The `pitzer.dat` database was used to account for the high ionic strengths of the aqueous solutions.

Table 6.1: Chemical compositions of the geothermal fluids samples. All concentrations are given in (mM), except for pH. LND is a sample from the Landau geothermal reservoir (Sanjuan et al. 2016). URG 2000 m and URG 3000 m are averaged samples from the Upper Rhine Graben at respective depths (Wolfgramm and Seibt 2008). The samples have been further modified to achieve equilibrium with respect to the common reservoir minerals barite, quartz, anhydrite, celestite, and calcite at reservoir conditions; chloride was fitted to reach charge balance (Tranter et al. 2020).

Sample	LND	URG 2000 m	URG 3000 m
K	106	78.8	133
Na	1 270	894	1 590
Ca	196	104	177
Mg	3.25	4.23	4.29
Sr	10.6	2.7	8.83
Ba	0.11	0.0189	0.0953
Fe	0.403	1.84	3.73
Cl	1 790	1 180	2 100
Br	2.84	1.29	2.61
S(6)	3.02	5.93	3.61
C(4)	4.14	4.04	7.42
Si	2.12	1.09	1.89
pH	5.41	5.66	5.28
I	2 010	1 320	2 310

Reactive transport modelling was done using the TRANSPORT keyword of PHREEQC, similar to Tranter et al. (2020). Each reservoir simulation consisted of two one-dimensional simulations, one for each aquifer layer with 100 elements each. The flow rate was kept constant and the influence of porosity change on pore flow velocity caused by mineral reactions was not considered. Details of the implementation of radial flow in PHREEQC are given in Section 4.2. The model inlet was set to the well exit ($r_{\text{w}} = 0.22$ m) and the model length was derived for each simulation based on the approximated radial equilibrium length r_{eq} (m) using Eq. 6.11 (see Section 4.4 for its derivation).

$$r_{\text{eq}} = \sqrt{\frac{2V\, c_{\text{eq}}}{S\, k} + r_{\text{w}}^2}, \tag{6.11}$$

where $V = Q/2\pi\, H$, and c_{eq} ($\mathrm{mol/m^3_{rock}}$) is the fluid concentration of barium in equilibrium. Finally, the model end was set to $\min(r_{\mathrm{e}}, 3\, r_{\mathrm{eq}})$ to capture the relevant reactive flow section, but also not to extend over the range of influence. A constant boundary condition was set at the inlet using concentrations shown in Tab. 6.1, and flux boundary conditions at the outlet. The initial conditions of the aqueous solution in the domain were calculated based on the inlet chemistry, but in thermodynamic equilibrium with barite at domain P/T-conditions. Temperature and pressure were constant at 55 °C and 30 MPa.

A general kinetic rate law was used to calculate barite precipitation with PHREEQC (Eq. (6.12)) (Lasaga 1998).

$$\frac{\mathrm{d}m}{\mathrm{d}t} = -S\, k\, (1 - \mathrm{SR}), \tag{6.12}$$

where m ($\mathrm{mol/m^3_{rock}}$) is the mineral amount, t (s) is time, S ($\mathrm{m^2/m^3_{rock}}$) is the specific reactive surface area, k ($\mathrm{mol/m^2\ s}$) is the rate constant, and SR (-) is the saturation ratio, i.e., the ratio of the activity IAP and solubility product K_{sp}. The surface area normalised reaction rate constant was calculated as a function of temperature T (K) and ionic strength I (M) with Eq. (6.13) (Tranter et al. 2020) based on data from (Zhen-Wu et al. 2016).

$$\log_{10} k_{\mathrm{barite}} = -\frac{2532}{T} + 0.694\ \sqrt{I} + 0.29. \tag{6.13}$$

Besides barite precipitation, the chemical system was considered to be inert. From a thermodynamic perspective, it was found that only barite, celestite, and quartz could precipitate from solution due to the temperature decrease during fluid circulation. Quartz is known to have a negligible low precipitation rate at respective injection temperatures (Rimstidt and Barnes 1980). Celestite may co-precipitate (Heberling et al. 2017; Vinograd et al. 2018), although the saturation ratio of celestite for the respective geothermal fluids at 55 °C is about 1 or even below; thus, it is not expected to precipitate in noteworthy amounts, if at all. Solid-solutions were not taken into account as the additional precipitation potential is assumed to be comparably small for the same reason.

The initial porosity of the porous layer was $\varphi_{0,\mathrm{por}} = 0.2$; the fracture open space of the fracture layer was $\varphi_{0,\mathrm{frac}} = 1.0$. The reactive surface area of barite S_{barite} ($\mathrm{m^2/m^3_{rock}}$) (Eq. (6.14)) was calculated based on the inner specific surface area of the rock S_{S} ($\mathrm{m^2/m^3_{rock}}$) and an additional scaling factor SF (−) to account for reduced mineral accessibility, armouring, and surface roughness (Beckingham 2017).

$$S_{\mathrm{barite}} = \varphi_{\mathrm{barite}} \cdot S_{\mathrm{S},i} \cdot \mathrm{SF}_i, \tag{6.14}$$

where $\varphi_{\mathrm{barite}}$ (−) is the volume fraction of barite in the rock. The initial volume fraction of barite in the rock was 5×10^{-5} (Bruss 2000; Tranter et al. 2020) for all aquifers. The inner surface area of the porous aquifer was set to $S_{\mathrm{S,por}} = 3 \times 10^4\ \mathrm{m^2/m^3_{rock}}$ (Rabbani and Jamshidi 2014). For the fracture aquifer, it was calculated from its respective fracture aperture ($S_{\mathrm{S,frac}} = 1/(2\delta)$). The scaling factors for the porous and fracture aquifer were set to $\mathrm{SF_{por}} = 0.05$ and $\mathrm{SF_{frac}} = 0.1$, respectively (Beckingham 2017). The fracture scaling factor is higher to also account for fracture surface roughness (Deng and Spycher 2019). The reactive surface area of each mineralogical component in the rock accessible to circulating fluids is extremely hard to quantify (Beckingham 2017; Beckingham et al. 2016; Deng and Spycher 2019; Deng et al. 2018a,b; Seigneur et al. 2019), especially for hardly accessible rocks of deep geothermal reservoirs. The uncertainty may be significant and is investigated in more detail in a previous work by the authors (Tranter et al. 2020).

To relate porosity and permeability change, the Kozeny-Carman relationship (Carman 1937; Kozeny 1927) was used for the porous layers (Eq. (6.15)). It is widely accepted for the use in porous media and is comparably simple as only the initial porosity needs to be assumed (Hommel et al. 2018). The cubic law holds for flow between two parallel plates; thus, it was applied to the fracture layer (Eq. (6.16)).

$$\frac{\boldsymbol{\mathcal{K}}_1}{\boldsymbol{\mathcal{K}}_0} = \frac{\varphi_1^3 (1 - \varphi_0)^2}{\varphi_0^3 (1 - \varphi_1)^2}, \tag{6.15}$$

$$\frac{\boldsymbol{\mathcal{K}}_1}{\boldsymbol{\mathcal{K}}_0} = \frac{\varphi_1^2}{\varphi_0^2}, \tag{6.16}$$

where φ (−) is the porosity of the layer, and subscripts 0 and 1 refer to the initial state and state after time t. The effective permeability of a layer for flow parallel to heterogeneity in a radial diverging flow field was calculated with the log-harmonic mean of permeabilities of its elements (Eq. (6.17)) (King 1989; Renard and de Marsily 1997).

$$\mathcal{K} = \frac{\ln\left(\frac{r_e}{r_w}\right)}{\sum_{j=1}^{n} \frac{\ln\left(\frac{r_j}{r_{j-1}}\right)}{\mathcal{K}_j}}, \tag{6.17}$$

where subscript j refers to a grid element. Here, the range of influence r_e from Eq. (6.7) was used for all layers, whereas the undisturbed section, if $r_e > r_{eq}$, was also taken into account. The effective permeability loss $\mathcal{L}$ (Eq. (6.18)) was taken as a measure for injectivity loss (Eq. (6.18)).

$$\mathcal{L} = 1 - \frac{\mathcal{K}_1}{\mathcal{K}_0}. \tag{6.18}$$

6.2.3 Scenarios

Injectivity loss was investigated in detail with a scenario analysis using variables and their ranges given in Tab. 6.2. The impact of fluid chemistry was taken into consideration using three different fluid samples (Tab. 6.1). The total injection flow rate was varied significantly from the mean rate of 100 m^3/h, which is usually an approximate target value (Baumgärtner et al. 2010). Moreover, the flow rate fraction of the fracture layer as well as the amount of fractures were varied significantly.

Table 6.2: Reservoir simulation variables and their ranges that were considered for the exhaustive scenario analysis. Each unique parameter combination represents a scenario ($3^4 = 81$ scenarios).

Variable	Range
Sample	[LND, URG 2000 m, URG 3000 m]
Q_{tot}	[50, 100, 200] m^3/h
Q_{frac}/Q_{tot}	[0.1, 0.5, 0.9]
n_{frac}	[1, 10, 100]

6.3 Results

6.3.1 Reservoir simulation scenarios

The results of two of the 81 reservoir simulation scenarios are shown exemplary in detail in Figs. 6.2 and 6.3. Both are based on the same input sample (LND), amount of fractures (100), and total well injection rate of 100 m^3/h. They differ in their flow rate fraction with respect to the porous and fracture aquifers. Figure 6.2 shows scenario 1, where the fracture layer drains 90% of the total injection volume. This corresponds to a fracture aquifer permeability of 9×10^{-15} m^2 with a mean fracture aperture of 80 µm, and a permeability of the porous layer of 1×10^{-15} m^2. Scenario 2 is shown in Fig. 6.3, which has a fracture aquifer flow rate ratio of 10%, corresponding to a permeability of 1×10^{-15} m^2 and a mean fracture aperture of 40 µm.

The rock porosity changes along the horizontal axis after the final simulation time of ten years are shown in Figs. 6.2b and 6.3b. In both scenarios and in each layer, the maximum porosity change is close to the well and decreases with various gradients along the r-axis. The porous aquifers of both scenarios have a similar maximum porosity reduction of about 9% and an affected range of only 1 m to 2 m around the well. The fracture aquifer with the higher flow rate has a maximum porosity loss of 3%,

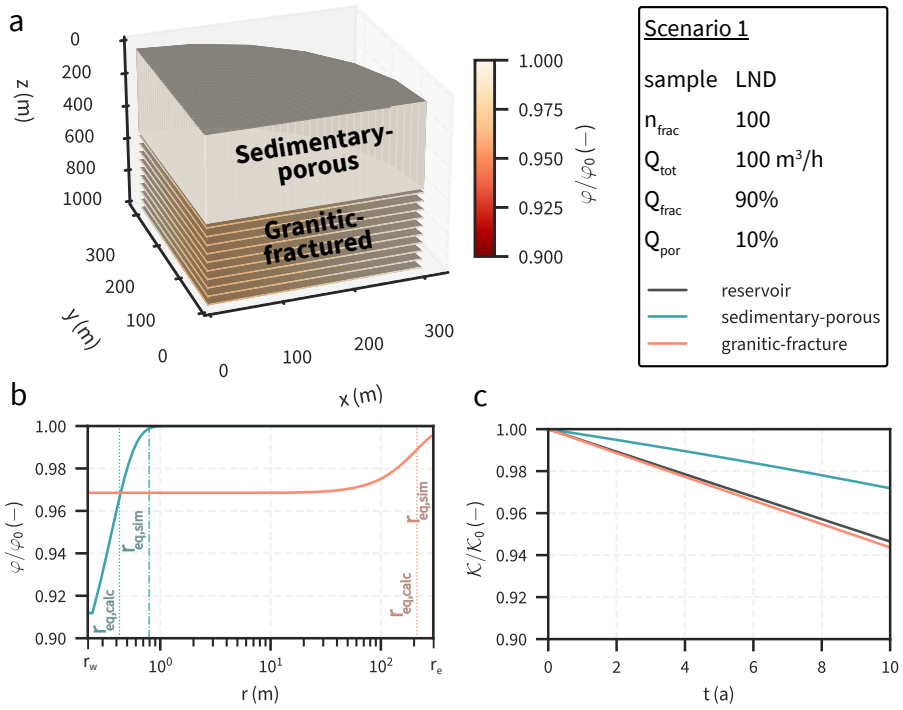

Figure 6.2: Reservoir simulation results of scenario 1. (**a**) Conceptual view of the reservoir model with the injection well at the origin. (**b**) Porosity change along the horizontal flow axis at the end of the simulation as well as the previously calculated and simulated equilibrium lengths. (**c**) Effective permeability change in the layers and the reservoir over the duration of the simulation.

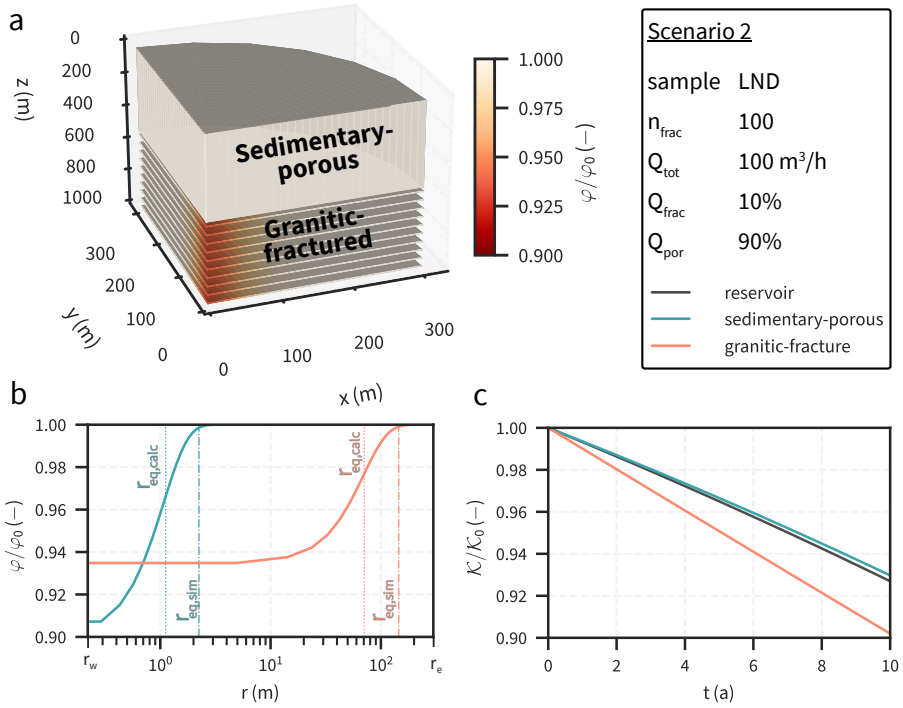

Figure 6.3: Reservoir simulation results of scenario 2. (**a**) Conceptual view of the reservoir model with the injection well at the origin. (**b**) Porosity change along the horizontal flow axis at the end of the simulation as well as the previously calculated and simulated equilibrium lengths. (**c**) Effective permeability change in the layers and the reservoir over the duration of the simulation.

while the lower flow rate scenario has a higher maximum porosity loss of slightly more than 6%. The respective affected ranges are orders of magnitudes higher than the porous layers: scenario 1 (higher flow rates) has a range of 300 m and scenario 2 (lower flow rates) about 150 m.

Changes in effective permeabilities are shown in Figs. 6.2c and 6.3c. Over the period of the simulation time, effective permeabilities decrease almost linearly for all layers and reservoirs. In both scenarios, the respective fracture layer has a stronger decline in effective permeability than the porous layer. Moreover, a main difference between aquifer types is that permeability loss is greater for fracture layers if the flow rate is lower. Reducing the flow rate ratio of the fracture layer from 90 to 10%, increases its final permeability loss from 6 to 10%. The opposite applies to the porous layers, where the permeability loss is proportional to flow rate. As a consequence, however, the loss in effective permeability of the reservoir varies less (Eq. (6.4)); about 5% for high fracture layer flow rates (scenario 1) and about 7% for high porous layer flow rates (scenario 2).

6.3.2 Scenario analysis

For all scenarios, the calculated equilibrium lengths using Eq. 6.11 underestimate the simulated values, as shown in Fig. 6.4. The simulated equilibrium length was defined as the point where the initial saturation ratio has decreased by 99%. The previously calculated and the simulated scenarios are also shown as vertical lines in Figs. 6.2b and 6.3b. In general, the equilibrium length is correlated with the flow rate. The fracture layers are consistently underestimated by slightly less than half. For the porous layers, the calculated lengths lie between 65% and 45% of the simulated values and decrease proportionally to these. Furthermore, equilibrium lengths of all scenarios for the fracture layers range from 73 m to 660 m; for the porous layers, the range is with 0.4 m to 3.3 m significantly lower. The various fluid samples have no impact on this relationship.

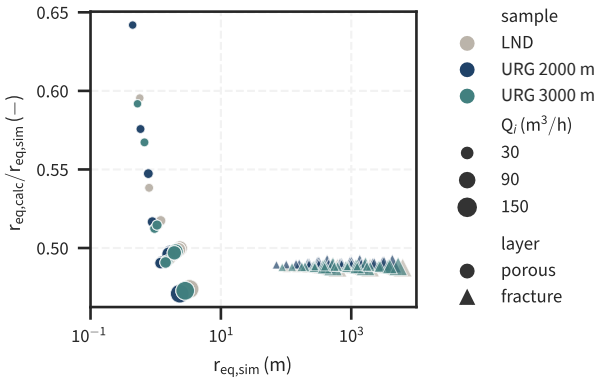

Figure 6.4: Previously calculated ($r_{eq,calc}$, Eq. (6.11)) and simulated equilibrium lengths ($r_{eq,sim}$) are correlated. $r_{eq,calc}$ can thus be used as a predictive parameter. Q_i refers to the flow rate of the respective porous or fractured layer.

In Fig. 6.5, the effective permeability losses of the fracture layers are shown against the respective mean fracture half-apertures. Firstly, fracture apertures directly correspond to the amount of fractures that were set, and the flow rate share. The mean fracture apertures lie between 40 µm and 400 µm. If more fractures are introduced, a lower mean fracture aperture suffices to reach the target transmissivity. The target transmissivity directly follows from the imposed flow rate share (Eq. (6.2)). Thus, higher fracture apertures are needed to reach a certain flow rate. The permeability loss of a fracture layer is generally lower if fracture apertures are larger, and the fewer fractures are introduced. Furthermore, the input fluid sample has a significant impact on the loss factor. While the deep mean sample URG 3000 m has similar, but slightly higher losses (1.5–12%) compared to the LND sample (1.3–10%), the shallow mean sample URG 2000 m has significantly lower losses, with a range of only 0.4–2.7%.

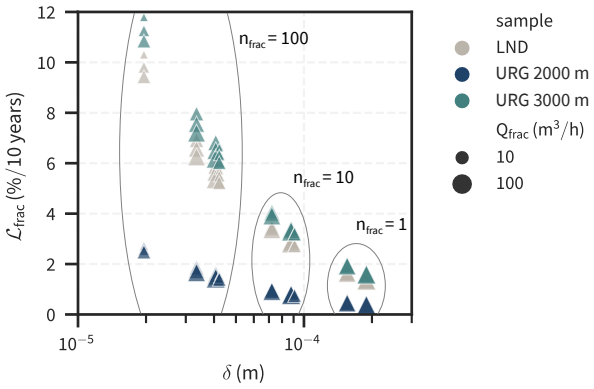

Figure 6.5: Permeability loss of the fracture layer ($\mathcal{L}_{\text{frac}}$) is dependent on the fracture half-aperture (δ), amount of fractures (n_{frac}), flow rate (Q_{frac}), and fluid sample, i.e., fluid chemistry. The relationships are shown for all scenarios after the final simulation time of ten years.

Figure 6.6 shows the flow rate share of the fracture layer in relation to the effective reservoir permeability loss. Only the scenarios with the base injection flow rate of 100 m^3/h are shown. Most notably, if sample URG 2000 m is applied as an input concentration, the absolute lowest losses were recorded. URG 3000 m and LND are again similar, with LND-scenarios having slightly lower losses. Generally, the reservoir permeability loss is lower if the flow rate share of the fracture layer is higher. On average, loss is reduced by about 50% if the flow rate share of the fracture layer increases from 10% to 90%. For the URG 2000 m sample, this reduction is slightly smaller. Furthermore, increasing the amount of fractures in the model always increases the final loss. This relationship becomes more prevalent as the fracture flow rate share increases. At a flow rate share of 10%, this effect is negligible. If the flow rate share is high, an increase of active fractures by one order of magnitude almost doubled the loss. The highest reservoir permeability loss of 8% was calculated with the scenario using the sample URG 3000 m, 100 fractures, and a fracture flow rate share of 10%. The scenario with the sample URG 2000 m, 1 fracture, and a fracture flow rate share of 90% had the lowest loss of 0.4%.

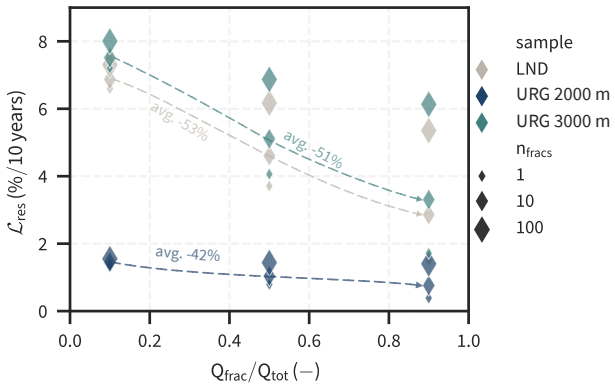

Figure 6.6: Effective reservoir permeability loss ($\mathcal{L}_{\text{res}}$) decreases as the flow rate ratio of the fracture layer ($Q_{\text{frac}}/Q_{\text{tot}}$) increases. Only the scenario with the base injection flow rate of 100 m^3/h are shown after the final simulation time of ten years. The average losses for each input fluid sample are indicated as dashed lines.

6.3.3 Scaling score

Parameter relationships are examined in more detail based on the reported simulation results and the scenario analysis. The calculated radial equilibrium lengths for layers of all scenarios are shown

in Fig. 6.7a. If plotted against the respective layer permeability losses, the relationship is different, depending on the considered layer type (fractured or porous). While for the porous layer, losses are positively correlated to r_{eq}, the corresponding fracture layer losses are negatively correlated. The figure also shows that flow rate comparably increases loss, irrespective of layer type. Furthermore, fluid chemistry has a significant impact on permeability loss. In this regard, the initial ion ratio of Ba^{2+} to SO_4^{2-} of the fluid sample affects the precipitation (or scaling) potential N_{eq} mol/m^3), i.e., the amount of barite that can precipitate from a cubic metre of injected fluid, assuming equilibrium is reached. The closer the ion ratio is to unity, the higher the precipitation potential indicated for the three considered samples in Fig. 6.7b. Lastly, from Fig. 6.5 it was previously derived that a higher flow-through thickness reduces the resulting permeability loss. If these relationships are combined into a single statement, we can obtain a definition for a predictive scaling score $\mathcal{X}$ for a layer i (Eq. (6.19)).

$$\mathcal{X}_i = \frac{N_{\mathrm{eq}}\, Q_i}{r_{\mathrm{eq}}^a\, H_i\, \varphi_{i,0}}, \tag{6.19}$$

where a is an exponent that depends on the considered layer type. Using linear regression, a was fitted to 1.5 for the porous layers and to 1.9 for the fracture layers. The scaling score then linearly relates the a priori known input parameters of a reservoir and its layers to the simulated layer permeability losses. The resulting linear relationships are shown in Fig. 6.7c, which both have a very high R^2 correlation coefficient of over 0.99. To yield the total reservoir permeability loss, one can then take the arithmetic mean of the layer losses with the respective flow rate ratio as weights (Eq. (6.20)).

$$\mathcal{L}_{\mathrm{res}} = \sum_{n=1}^{i} \mathcal{L}_i\, Q_i / Q_{\mathrm{tot}} \tag{6.20}$$

6.4 Discussion

Our aim for the present study was to investigate the barite scaling potential and the corresponding injectivity loss of wells within fractured-porous reservoirs. We assumed the modelled reservoir consisted of two separate, horizontal aquifers, one porous and one fractured layer. With this, we build upon a previous study, in which we assessed the situation for purely porous media, focussing on fluid compositions and temperature variations representative of deep geothermal systems in Germany and restricting precipitation to pure barite (Tranter et al. 2020), i.e., disregarding solid-solution and other potential mineral scaling agents (Heberling et al. 2017; Wolfgramm et al. 2011a). Open fractures, natural or engineered, are needed for many geothermal reservoirs to achieve the economically viably hydraulic yield, since porous matrix permeability is often insufficient. We expected that fractures crossing a well, provided they make up a significant amount of the total reservoir's transmissivity, will decrease the impact of scalings compared to purely porous reservoirs. Open fractures are essentially preferential flow paths, with higher local flow velocities compared to the matrix flow, and thus mineral scalings are distributed more along the flow path. Our simulation results confirm this hypothesis, in which reservoirs with a 90% transmissivity share regarding fractures had, on average, only half the injectivity loss compared to a fracture transmissivity-share of 10% under otherwise equal conditions.

6.4.1 Simulation results

We value the overall simulated injectivity losses of the Landau geothermal system as low (< 8% after ten years), compared to effects related to, for example, mechanical fault compaction or non-sustainable, hydraulically induced fractures. Experiments on the laboratory and reservoir scale show that this can happen within an even shorter timeframe and could account for losses by more than a factor of three (Blöcher et al. 2016; Kluge et al. 2021). We also showed that scaling is a creeping process that occurs

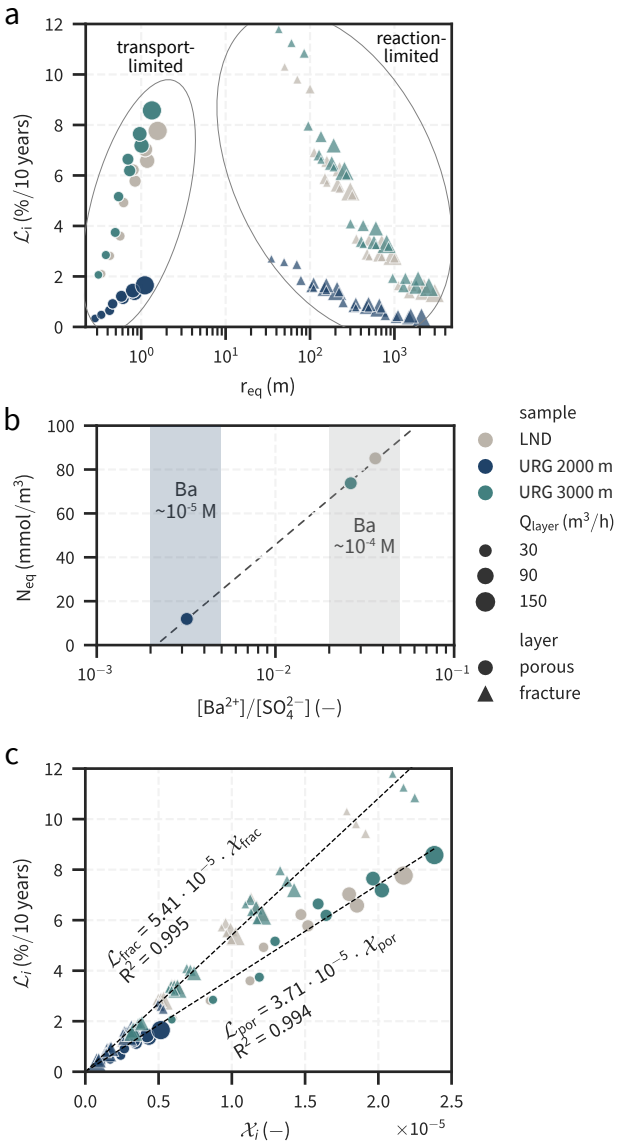

Figure 6.7: (**a**) The porous layers show clear signs of being transport-limited with respect to loss due to scaling, whereas the fracture layers are rather reaction-limited. (**b**) Initial ion ratios for the considered samples versus the precipitation potential (N_{eq}), i.e., the maximum amount of barite that can precipitate, provided thermodynamic equilibrium is reached, show a positive correlation. (**c**) The final layer permeability loss can be fitted with an analytical scaling score (Eq. (6.19)). The upper dashed line for the fracture layers is a linear regression using an exponent $a = 1.9$. The lower dashed line is for the porous layers and uses an exponent of $a = 1.5$.

linearly in the investigated time frame, principally allowing for time to react with countermeasures. Furthermore, a crucial value for the interpretation of our results is the precipitation potential of barite (N_{eq}), i.e., the maximum amount of barite that can precipitate from a defined volume of fluid. This mainly depends on fluid chemistry, and temperature reduction (Tranter et al. 2020). Here, we assumed it to be located in the upper range of what is possible. Precipitation within the technical system (Scheiber et al. 2013) and fluid re-heating in the rock due to thermal conduction could both reduce the potential, but were not taken into account. While temperature variations will play a progressively smaller role, as the injection location will cool down over time, the precipitated amount in the well, pipes, and above-ground system is hard to quantify. A comprehensive assessment would need to take precipitation kinetics within the system into account (e.g., Banks 2013), although studies have shown that barite can be kinetically inhibited in this environment (Canic et al. 2011), justifying our approach.

It is known that barite and celestite form slightly non-ideal regular solid-solution (Heberling et al. 2017; Vinograd et al. 2018), which could increase the precipitation potential compared to the sum of the end members; this is a source of uncertainty when modelling only the pure mineral phases. Sr-bearing barite scales have been reported for various geothermal sites (Regenspurg et al. 2015; Wolfgramm et al. 2011a), and the abilities of modelling solid-solutions in reactive transport simulators has been demonstrated in a recent study (Poonoosamy et al. 2021). The saturation ratio of celestite for the here considered cooled geothermal fluids at injection conditions is either negligibly supersaturated ($SR < 1.1$) or slightly undersaturated. The precipitation potential of pure celestite can thus be assumed to be negligible. Using parameters for the $(Ba, Sr)SO_4$ solid-solution given in Vinograd et al. (2018), the additional precipitation amount, compared to modelling only barite precipitation, is approximated to be around 20%. This is within acceptable limits for the present study, but preliminary results show that this may be even more at higher injection temperatures (70 °C). For more detailed and site-specific assessments, solid-solutions can be subject to future work in this context.

The presented results strongly depend on the assumed reservoir thickness and reactivity. In this study, the reservoir was based on the Landau geothermal reservoir, using a comparably large porous aquifer thickness of 500 m. If the same fluid samples are applied to a purely porous reservoir with a thickness of only 20 m, representative of the North German Basin (e.g., Franz et al. 2018b), losses are higher by a factor from three to four (Tranter et al. 2020). For the same reason, the fracture layers, which had flow-through areas of four orders of magnitude lower than their porous counterparts, systematically exhibited higher permeability losses. Mineral scaling locations are concentrated more vertically along the well-axis, although this is opposed to some degree by the higher flow rates and increased horizontal distribution in the rock. While one could come to the conclusion that a larger flow-through area reduces scaling related injectivity loss, the relationship is further dependent on the overall reactivity of the aquifer. The accessible barite surface area in the rock, which controls the overall precipitation rate, is notoriously hard to quantify (Beckingham et al. 2016), and primarily depends on the barite content in the rock and the inner rock surface area, both of which can vary significantly between and within stratigraphic layers (Beckingham 2017; Bruss 2000; Rabbani and Jamshidi 2014). Moreover, the scaling itself provides further reactive surface area, which was not taken into account here.

Our dual-layer simulation approach is an abstraction of the multi-horizon reservoir at the Landau geothermal system. The underlying model framework follows from the limited data that are available on the subsurface. Foremost, the assumption of radial-symmetry facilitates one-dimensional transport models, which are reasonable considering the adopted conditions of isotropic hydraulic behaviour. However, if it becomes evident that mass transfer between and within aquifer units significantly contributes to the overall flow regime, the model could be improved by taking the interaction between layers into account. An example of complexity being added in this way is the dual-porosity approach (e.g., Deng and Spycher 2019; Lucas et al. 2020). However, the matrix permeability of the granitic basement in the URG is negligible (Bär 2012; Vidal and Genter 2018), and thus dual-porosity approaches appear unfounded here.

6.4.2 Scenario analysis

The calculated equilibrium length (Eq.(6.11)) was used to approximate the radial area of interest around an injection well concerning barite scaling. On this basis, the model lengths for the reactive transport simulations were determined. Given that its derivation (cf. Section 4.4) is based on a first-order chemical reaction (Lichtner 1988), compared to the second-order mineral reaction of barite used in the simulations (Zhen-Wu et al. 2016), the results correspond exceptionally well to the simulated equilibrium lengths. This is due to the fact that Ba^{2+} concentration is about two orders of magnitude lower than that of SO_4^{2-} for the considered fluid samples. Consequentially, the sulfate concentration changes during barite precipitation are almost negligible in comparison, resulting in a practically pseudo-first order reaction. For the fracture layers, the calculated and simulated lengths are related by merely a constant,

making it an excellent predictive value for the presented cases. For the porous layers, a dependency on the flow rate seems apparent, though the overall fluctuation of the relationship is small. We hypothesise that this is a grid effect resulting from the high-flow velocities close to the well ($v \propto 1/r$). In a separate test (not shown), decreasing the grid elements increased the discrepancy, providing support for this assumption. Although there is no apparent dependency on the fluid sample, it remains unclear whether the calculated equilibrium length is generally applicable for other fluid compositions.

In case of the Landau geothermal reservoir, the Buntsandstein was more permeable before stimulation, but the granitic fractures provide the most productive zones afterwards (derived from temperature logs) (Schindler et al. 2010). However, it is unclear if this shift is permanent or if circulation over a longer period could change the flow regime again. The impedance of the injection well is known to reduce slightly (Blöcher et al. 2016; Tischner et al. 2006), at least in the first months of circulation, but self-propping fractures may close again over time due to mechanical failure of asperities (Blöcher et al. 2016). The scenario analysis, covering the range of flow fractions of fractures and porous matrix, showed that activating the granitic fractures would reduce barite-scaling-related injectivity loss. Thus, ensuring fractures are the dominant flow path is favourable in this sense, e.g., by the use of proppants (Blöcher et al. 2016; Schindler et al. 2010; Vidal and Genter 2018).

The amount and, coincidentally, the aperture of hydraulically active fractures in the aquifer both influence permeability loss. It was shown that one order of magnitude more fractures doubles the scaling induced loss. Furthermore, smaller apertures were associated with an increased scaling risk. This finding corresponds to a numerical study for single fractures on the laboratory scale (Tranter et al. 2021b), where low fracture aperture was identified as the most important parameter, next to barite supersaturation. This was attributed to the specific inner surface area, which is inversely related to the aperture for an idealised fracture. These characteristic values are usually hard to determine *in situ*, and thus constitute uncertainties for the models (Genter et al. 1996; Griffiths et al. 2016; Vidal and Genter 2018). Genter et al. (1996) carried out a fracture analysis at the Soultz geothermal site and found that only about 30, 1% of the total recorded fractures, were open and unsealed. The measured apertures were of the order of a few mm, about one or two orders of magnitude larger than the calculated apertures in this study. The latter were derived from hydraulic apertures, but using the cubic law and assuming infinitely extending horizontal plates parallel to flow. In reality, fractures may not be ideally connected within a fracture zone and may be oriented divergent to flow. Further, they could be partly sealed, and thus exhibit significant aperture fluctuations (Genter et al. 1996). The corresponding inner surface area of fracture zones are expected to be higher, thus actual permeability losses may be underestimated. However, there are indications that flow, especially in stimulated fractured reservoirs, is determined by a discrete set of individual fractures (Schindler et al. 2010; Tischner et al. 2006; Zimmermann et al. 2010), in accordance with our assumptions.

6.4.3 Scaling score and implications for geothermal systems

We presented an analytical scaling score, which combines the investigated parameter relationships of the scenario analysis to approximate mono-mineralogical-scaling-induced permeability losses in fractured–porous media. A similar approach was presented in a previous study (Tranter et al. 2020) for a porous reservoir type representative of the North German Basin. There, the local Damköhler number was used to quantify the influenced range along the flow path. Here, we extended this score to be generically applicable to fractured and porous aquifers with varying thicknesses and porosity. Furthermore, the radial equilibrium length was identified to be exceptionally suitable to approximate the range of scaling influence around an injection well under the assumption of quasi-stationary state. Compared to the Damköhler number, this does not depend on an arbitrary characteristic length, and therefore yields an easily, interpretable value. The main benefit of an analytical scaling score is that it enables a quick initial screening of geothermal sites to assess the scaling risk in advance. Elaborate

numerical simulations can be carried out at a later stage of a geothermal project, when more detailed information is available on the subsurface and reservoir parameters.

The scaling score was demonstrated with the single mineral precipitation reaction of barite, but it may be applicable to other scaling minerals in fractured-porous geothermal reservoirs, such as quartz (Kumar and Ghassemi 2005; Pandey et al. 2015), celestite (Nitschke et al. 2014; Regenspurg et al. 2015), or calcite (Wanner et al. 2017). The radial equilibrium length must be adapted accordingly to account for the kinetic rate law of the respective mineral. If multiple minerals are anticipated to precipitate in the reservoir, one score for each mineral must be calculated and the effects can be simply summed to yield a first approximation. This, however, does not account for any interaction of the chemical reaction system, which could lead to non-linear effects. One example is the aforementioned solid-solution barite–celestite, which may lead to an increased precipitation potential compared to the sum of the endmembers. Another example would be the dissolution of anhydrite within the reservoir due to cool water injection, which could facilitate further barite and celestite precipitation due to the release of sulfate into solution (Forjanes et al. 2020). A comprehensive assessment of the chemical system and possible interaction effects may be needed for specific sites, and is subject to future work.

There are two essential differences between the fractured and porous layers, which the scaling score takes into account with the exponent a for the radial equilibrium length. Firstly, the loss factor must be seen in light of the respectively applied porosity–permeability relationship. The Kozeny–Carman relationship was used for porous media and the cubic law was used for the fractures. While these idealised model approaches are commonly used in this regard (Hommel et al. 2018), significant deviations are possible under certain conditions (e.g., Beckingham 2017; Poonoosamy et al. 2020a,b; Wetzel et al. 2021). For fractures, many characteristics can be attributed to a departure from the cubic law, including aperture fluctuations, surface roughness, and pore fluid exchanges with the surrounding matrix (Blöcher et al. 2019). The porosity–permeability relationship for porous rocks may become strongly non-linear, for example, if pore-throats are preferentially closed (Wetzel et al. 2021).

Poonoosamy et al. (2020b) used flow-through column experiments involving the concurrent dissolution of celestite and precipitation of barite to demonstrate that the Kozeny-Carman relationship does not hold for the investigated case, but that the relationship proposed by Verma and Pruess (1988) provides better estimates. One drawback of this relationship is that it introduces an additional, potentially highly uncertain parameter: the critical porosity, below which the permeability is zero. Furthermore, barite supersaturation was orders of magnitude higher (this study: SR < 10, experiment: SR $\gg 1\,000$). Thus, nucleation was an important precipitation process in the experiments (Poonoosamy et al. 2020b; Tranter et al. 2021c), but there is evidence that it is negligible for this study (Tranter et al. 2020, and references therein). Microstructural rock alteration patterns are, therefore, expected to be distinctly different; accordingly, we used the Kozeny–Carman relationship as a default. Ultimately, the choice of porosity–permeability law can be adapted according to specific site conditions. However, this is reflected in the a exponent, and thus each law needs to be calibrated with additional reactive transport simulations. It may be an interesting topic for future work to systematically investigate the relationship of the a exponent and the applied porosity–permeability. Ideally, an analytical relationship can be derived to completely bypass the numerical simulations.

The second difference is that the investigated porous layers are transport-limited, while the fractured layers exhibit reaction-limited precipitation. This can be derived from Fig. 6.7a, where radial equilibrium length and loss factor are positively correlated for porous, but negatively correlated for fractured, layers. An increase of the radial equilibrium length corresponds to an increase in flow rate, which, in turn, means a higher solute influx, but also an increased distribution of precipitates along the flow path the further scaling happens away from the well; however, its influence on injectivity decreases logarithmically (Eq. (6.17)). An increase in solute influx thus only increases the loss of the porous layer, but not that of the fracture layers, which have a spatial scaling reach into the reservoir that is about two orders of magnitude higher.

6.5 Conclusions

The present study assessed the barite scaling potential, and the related injectivity loss for geothermal wells within fractured-porous reservoirs, particularly for the expected fluids encountered at the Landau geothermal site in the Upper Rhine Graben. We highlight here the beneficial role of natural and engineered fractures with respect to mitigating the impact of barite scaling in this context. Preferential flow paths, while resulting in concentrated solute influx into the reservoir, cause mineral scaling to be more spatially spread within the reservoir. Our simulation results show that cases with a high fracture flow share are affected by up to 50% less regarding injectivity loss compared to purely porous reservoirs. The numerical results of a previous study quantified the injectivity loss for Landau after ten years of circulation as around 20%, but fractures were disregarded in that case. Here, we yielded lower losses of 3%–8%, depending on the amount, aperture, and flow rate share of the applied fractures. Increasing aperture and flow rate share generally decreased, whereas more fractures increased injectivity loss. Overall, we rate the barite-scaling-related injectivity loss in the Upper Rhine Graben to be small over the entire lifetime of a geothermal power plant compared to other known risks, such as the mechanical closing of fractures.

An analytical scaling score was developed for fractured–porous reservoirs. It features a quick screening method for geothermal sites to assess the associated scaling risk based on easily derivable reservoir and transport parameters, which can be conducted during the exploration phase. We identified the radial equilibrium length to be a key parameter to quantify the range of scaling influence around an injection well. After calibration to account for the respectively applied porosity–permeability relationship, there was excellent agreement with the simulation results. This confirms that this is a valuable tool to anticipate the barite scaling influence under expected system conditions, which is of practical importance for the conceptualisation of future geothermal power plants. As a next step, this conceptual model is planned to include a more complex geochemical system, including solid-solutions and multi-mineral reactions, to take potential non-linear effects into account.

CHAPTER 7

Discussion

Barite scale formation in geothermal reservoirs constitute a risk for a sustainable heat or power plant operation. In the search for suitable new sites for geothermal energy, it is therefore necessary to be able to evaluate this risk in figures, so that feasibility can be proven and the associated additional costs can be taken into account. There is a large geothermal potential in Germany in deep, dense rock formations, which could be made accessible with stimulation methods. Natural or engineered fractures are needed for these reservoir types to achieve the economically viably hydraulic yield. However, these preferential flow paths also introduce more heterogeneity regarding subsurface flow and rock reactivity. Especially the utilisation of multiple stratigraphic units (multi-horizontal approach) introduces uncertainties and makes the setting more complex. Geochemical reservoir models that quantify the involved processes are therefor indispensable for assessing the operational risk related to reservoir scaling.

This thesis provides predictive models for assessing scale formation in geothermal reservoir, and evaluates the geothermal regions North German Basin (NGB) and Upper Rhine Graben (URG) in this regard. The main objective is broken down into the following subitems: (1) identification and modelling of the effective precipitation processes taking place on the macro-scale in fractures and pores, (2) evaluation of the sensitive parameters for precipitation, (3) transfer of laboratory-scale to field-scale models, and finally (4) assessment of barite scaling potential and the corresponding injectivity loss of wells within fractured-porous reservoirs. The relevance of specific precipitation mechanisms for reservoir scale formation, as well as the predictive power of the presented approaches for quantifying injectivity loss are discussed in the following. This chapter is concluded with implications for geothermal energy and a verdict regarding barite scale formation in relevant reservoirs.

7.1 Relevance of different precipitation mechanisms for barite scales

To develop prediction models for mineral scale formation, a mechanistic understanding of the water-rock reactions in the Ba-S-system is required. Furthermore, the parameters measured in experiments have to be transferred to those that can be incorporated into the model representations. The aim of the laboratory-scale models is to assess the processes taking place on the microscopic scale and to relate them to the decisive macroscopic level, which ultimately allows one to predict changes in mineralogical rock composition and hydraulic rock properties.

For barite, the main driving force for precipitation results from thermodynamic supersaturation (Christy and Putnis 1993; Templeton 1960), which—in the context of geothermal systems—happens mainly through temperature reduction. Precipitation is principally subdivided into the processes crystal growth and nucleation, whereas nucleation can be further distinguished between heterogeneous nucleation on to existing crystal surfaces (HET), and homogeneous nucleation in free solution (HON) (Christy and Putnis 1993; Kashchiev 2000; Lasaga 1998). These processes are discussed individually in the following regarding their relevance for reservoir scaling in geothermal systems based on the findings of this thesis.

7.1.1 Uncertainty of nucleation

The widely accepted model representation of barite nucleation is the Classical Nucleation Theory (CNT), which quantifies the amount of nuclei per time and volume unit (Eq. 2.3) (Kashchiev 2000; Prasianakis et al. 2017; Weber et al. 2021). The coupling of this process into reactive transport models is a key element for describing barite precipitation in more detail, as opposed to models considering only kinetics or even just thermodynamics. There are numerous examples of laboratory experiments, which demonstrate that nucleation is a rate determining step under specific conditions (Dai et al. 2019; Lu et al. 2020; Orywall et al. 2017; Poonoosamy et al. 2020b; Putnis et al. 1995). Yet, current state-of-the-art reactive transport simulators (Poonoosamy et al. 2021; Steefel et al. 2015) do not provide means to take this process into account explicitely, and it must still be considered an experimental tool. This particular topic has gained more attention in recent years, specifically with regard to simulating laboratory experiments with prevalent nucleation on the pore scale (e. g., Curti et al. 2019; Fazeli et al. 2020; Nooraiepour et al. 2021; Prasianakis et al. 2017). To my knowledge, Steefel and Van Cappellen (1990) provide one of the first examples for this coupling. However, the parameters determining barite nucleation are still quite uncertain, and thus need to be analysed in the context of geothermal conditions.

Tranter et al. (2021b) shows that one crucial parameter to look out for in geothermal systems is the threshold supersaturation (SR_{thresh}). This is the value above which nucleation becomes "noticeable", conventionally above 10^{10} $1/s\,m^3$ solution (Prieto 2014). If the saturation ratio stays below this value at all times, scale formation is inhibited. Otherwise, nucleation becomes relevant and facilitates further precipitation. This can potentially be catastrophic for a geothermal plant, as was demonstrated in this thesis for the Groß Schönebeck site using educated guesses for approximating SR_{thresh} (Tranter et al. 2021b). According to the models, decreasing the fluid temperature by more than 70 °C in this specific case, HET is induced and fracture permeability within the reservoir could consequentially decrease by one order of magnitude due to barite scaling over the course of days to months. Indeed, a considerable amount of barite was found at Groß-Schönebeck within the pipe-network and filters (Banks 2013; Regenspurg et al. 2015). In contrast, a barite-supersaturated solution can theoretically stay meta-stable if SR_{thresh} is not reached, because neither crystal growth nor nucleation happens, provided it is a reactive-surface-area-free domain (Tranter et al. 2021b). As a consequence, scale formation is suppressed within the system and the related risk for efficiency loss is significantly lower.

Based on various laboratory experiments, Fig. 7.1 illustrates for which values of saturation ratio (SR), nucleation can be expected, i. e., $SR > SR_{thresh}$ (Poonoosamy et al. 2020b; Prasianakis et al. 2017; Zhen-Wu et al. 2016; Zuber 2021). It indicates that solutions stay meta-stable for the geothermal sites Neustadt-Glewe and Landau, but heterogeneous nucleation is possible for Groß Schönebeck (the respective SR-values were taken from Tranter et al. (2021b, 2020)). Homogeneous nucleation appears to be an unlikely process for all considered geothermal plants, as the necessary saturation ratio is over three orders of magnitude higher. Such high supersaturations seem unlikely to happen by temperature changes alone (Tranter et al. 2020). Accordingly, homogeneous nucleation was not taken into account here in this thesis for modelling geothermal systems. The presented ranges in Fig. 7.1 must be treated qualitatively, nevertheless, as SR_{thresh} is also influenced by other parameters, such as the interfacial tension and the contact angle (Kashchiev 2000). Moreover, higher temperature principally decreases SR_{thresh} (Eq. 2.3), and experimental time can also play a role (He et al. 1995). Yet, since the saturation ratio has the largest range of possible values (Tranter et al. 2021b), spanning multiple orders of magnitude, Fig. 7.1 provides evidence for occurrence of nucleation within a system. A reliable prediction of SR_{thresh} is crucial in order to determine the risk of nucleation in a geothermal plant. To fill the gaps, more experimental data are needed at respective geothermal conditions.

The contact angle, which is the parameter that determines the reduced energy barrier of HET compared to HON, is currently not available or is uncertain for specific substrates from experimental data. Therefore, CNT must be treated with care when applying it to reactive transport models. A common approximate solution is to simply assume a "pancake"-habitus of the nucleus (Lasaga 1998),

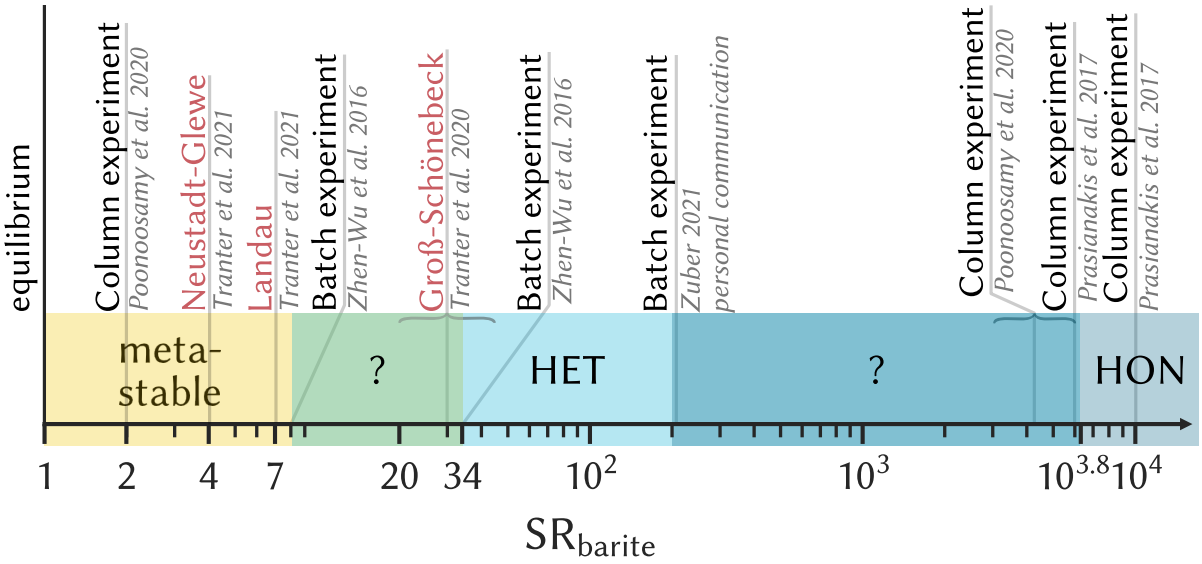

Figure 7.1: Saturation ratio has the greatest influence on nucleation, and thus gives an indication on whether a solution stays meta-stable. Experimental observations show, homogeneous nucleation only happens at extreme supersaturations. The cooled solutions from geothermal sites (red) are expected to behave meta-stable, though for Groß Schönebeck it is unclear. This diagram must be considered qualitatively, as (heterogeneous) nucleation further depends on other parameters, such as temperature, interfacial tension, and substrate material.

which corresponds to a contact angle of 90°. However, my sensitivity analysis shows it can have drastic consequences for the modelling results (Tranter et al. 2021b), as it is a very sensitive parameter of the nucleation rate. In some recent studies, the parameter is considered as inherently uncertain by treating nucleation as a stochastic process (Fazeli et al. 2020; Nooraiepour et al. 2021). Though, using the classical deterministic approach has benefits, too: the parameters (e. g., contact angle) can be calibrated by inverse modelling laboratory experiments, which can provide the basis for related forward modelling. Thus, additional inverse modelling studies similar to Tranter et al. (2021c), but at varying conditions, can help to reduce the uncertainty.

Nucleation and crystal growth, both, can increase the reactive surface area, so that subsequent crystal growth is accelerated (Lasaga 1998). They can be regarded as competing processes relying on surplus barium and sulfate ions. Accordingly, experiments with nucleation taking place are often described by an initial surge of nuclei formation in the early stage, and then are dominated by subsequent crystal growth (Lu et al. 2020; Orywall et al. 2017; Poonoosamy et al. 2015, 2016; Poonoosamy et al. 2020b; Prieto 2014). I demonstrate that this phenomenon can be reproduced with continuum-scale reactive transport models (Tranter et al. 2021c) on the basis of experiments conducted by Poonoosamy et al. (2020b). The respective reactor flow experiments (celestite grain packed columns, flowed through with variously barite-supersaturated solutions) were modelled by coupling barite crystal growth, celestite dissolution kinetics, heterogeneous nucleation, and explicit crystal surface increase. The model calibration of the nucleation process against the experimental data yielded an estimate for the contact angle barite-celestite of 32° (Tranter et al. 2021c). A similar value (30°) was fitted previously with a different modelling approach based on pore-size dependent nucleation (Poonoosamy et al. 2016). Contact angles between 0° and 180° are theoretically possible, which correspond energetically to crystal growth and homogeneous nucleation, respectively; the lower this value, the lower the energy barrier (Kashchiev 2000). The relatively low calibrated value of 32° can be explained by the structural similarity of celestite and barite crystals (Weber et al. 2021).

Modelling nucleation in natural environments remains a challenge. For a perfect representation, heterogeneous nucleation needs to be considered for all existing crystal faces in the domain, though the respective properties of other substrates (e. g., quartz, feldspar, etc.) are largely not available (Kashchiev

2000). Furthermore, the interfacial tension of barite has been determined experimentally in multiple studies (Fernandez-Diaz et al. 1990; Gardner and Nancollas 1983; He et al. 1995; Nielsen and Söhnel 1971). However, some open questions remain in this regard: studies suggest that this parameter depends on barite solubility and/or on the ionic strength of the solution (He et al. 1995; Li and Jun 2019), which currently is not taken into account and again introduces more uncertainty, especially for the geothermal context (elevated solubility, elevated ionic strength). Nevertheless, I demonstrated that the presented modelling framework is capable of explicitly implementing heterogeneous nucleation into continuum-scale reactive transport simulators, and that laboratory experiments can be reproduced successfully using this approach. If more detailed data on nucleation becomes available, this approach could be extended for field scale applications in future modelling work.

7.1.2 What influences the precipitation rate of barite?

To calculate the precipitation rate (R) of a mineral in continuum-scale reactive transport models, the respective rate constant (k) under specific conditions is needed (Lasaga 1998). This constant can be derived from experimental batch or flow-through tests, and is normalised to the available reactive surface area (discussed later in this section). For its derivation, an empirical expression of the macroscopic reaction rate must be assumed, which is then fitted against the data by taking the deviation from thermodynamic equilibrium into account, for example:

$$R = -k\,(1 - \mathrm{SR}). \tag{7.1}$$

Further common kinetic rate laws for minerals and their analytical solutions are provided in Section 4.2.

A comprehensive set of affinity based kinetic rate parameters for dissolution and precipitation of common rock-forming minerals is compiled by Palandri and Kharaka (2004). To my knowledge, it is the most often used kinetic database for mineral reactions in earth sciences (currently over 1 100 citations on Google Scholar, e. g., Deng et al. 2018a; Poonoosamy et al. 2021). Two main parameter dependencies are taken into account in this study: the temperature with an Arrhenius correction factor, and pH with separately catalysed reaction mechanisms for H^+ and OH^-. One crucial assumption of this work, is the principle of microscopic reversibility (Lasaga 1998). This states that the precipitation rate constant can be derived from the dissolution rate constant, which can be much harder to obtain experimentally than dissolution rates. For this assumption to hold, the forward and backward reaction must proceed by the same reversible mechanism. The provided kinetic data for the specific case of barite is derived from dissolution experiments (Dove and Czank 1995). However, more recent studies suggest that the precipitation and dissolution mechanism are not reverse, equivalent processes (Stack et al. 2012; Weber et al. 2021). This stands in contradiction to claims of Zhen-Wu et al. (2016), who suggest that similar slopes of dissolution and precipitation rate versus saturation ratio are an indication of micro-reversibility. Furthermore, other experimental data suggests that pH has no significant impact on barite growth in the range 3–9 (Ruiz-Agudo et al. 2015), which covers the largest part of naturally occurring waters, and relevant geothermal fluids (Sanjuan et al. 2016). Consequentially, the kinetic data given in Palandri and Kharaka (2004) is not appropriate to describe barite precipitation.

For a more reliable prediction of the kinetic rate constant, I developed a linear regression model (Tranter et al. 2021b), which accounts for the ionic strength and temperature dependency. A recent experimental study provides the data for this at various ionic strengths (0–1.5 M NaCl) and temperatures up to 60 °C (Zhen-Wu et al. 2016). One of their main finding is that the precipitation rate is correlated to the square root of the ionic strength (at least in the investigated range), which is not accounted for in the Palandri and Kharaka-model. At very low ionic strengths (< 0.1 M), the rate constants of both studies are on the same order of magnitude. However, there is more than one order of magnitude deviation for higher ionic strengths (Palandri and Kharaka 2004; Tranter et al. 2021b). This is relevant for modelling barite precipitation in the geothermal context because ionic strengths of the respective

fluids are commonly high (> 1 M), sometimes even up to 6 M (Tranter et al. 2020). A similar dependency on ionic strength was also found for the mineral gypsum (He et al. 1994b), but only up to 3 M NaCl, above which the rate declined again slightly.

Zotzmann et al. (2021), who investigated barite precipitation rates at geothermal conditions using a fibre-optical approach, make a contradictory statement in this regard. They concluded that the rate is negatively correlated to the ionic strength (up to 5 M), depending on the temperature (25 °C to 150 °C). But, they varied the ionic strength and temperature without taking the according change in solubility of barite into account, i. e., initial barium and sulfate concentrations were always the same. Accordingly, the initial conditions are differently far away from equilibrium, which could entail nucleation processes of different magnitudes. This makes it difficult to distinguish the two precipitation processes for parametrisation, especially since the reactive surface area was disregarded. Nevertheless, their approach for measuring precipitation kinetics using fibre-optics seems very promising and could contribute to filling the data gaps.

The reactive surface area is used as a parameter that serves as a proxy for the crystal reactivity in macroscopic modelling (Beckingham et al. 2016). A reliable determination is a challenging topic, especially for heterogeneous natural rocks (Fischer et al. 2014). The general approach I used for the reservoir models is to derive it from the mineral volume fraction and the total inner surface area of the rock (Tranter et al. 2021a, 2020), which is an accepted approximation (Beckingham et al. 2016; Lasaga 1998). For larger scale models, this makes sense because the reliable determination of individual crystal reactivity is principally not feasible. The reactive surface area of minerals in rocks is known to be a magnificently uncertain parameter (Beckingham et al. 2016, 2017; Deng et al. 2018b; Rabbani and Jamshidi 2014), and it must be regarded as a general weak point of reactive transport modelling on the field scale. To account for this uncertainty, I conducted a scenario analysis for geothermal reservoirs in this regard (Tranter et al. 2020). Pristine barite is commonly found as an accessory mineral (100–1 000 ppm) in NGB and URG geothermal host rocks (Behr and Gerler 1987; Bruss 2000; Wolfgramm 2002). Coincidentally, this also explains why the corresponding geothermal fluids are suggested to be initially in thermodynamic equilibrium with barite at reservoir conditions because it can be assumed that fluids have had sufficient time to equilibrate with their environment (Regenspurg et al. 2015; Sanjuan et al. 2016). Using this range, showed that it is indeed a sensitive parameter for injectivity loss predictions, which varied by a factor of about six. Thus, it is important that this property is determined as best as possible, preferably within one order of magnitude.

My investigations on barite precipitation in fractures revealed that the fracture aperture is the most influential parameter for scaling-facilitated fracture closing (Tranter et al. 2021b). The respective reactive transport models that were conducted in this regard show that the lower the initial aperture, the faster the permeability decreases by one order of magnitude. For instance, a fracture with barite covered surfaces and an aperture of 0.1 mm had a closing time on the order of tens of days, whereas for a fracture with an aperture of 10 mm it took about ten times longer. Griffiths et al. (2016) also investigated barite scaling facilitated fracture closing and yielded a time frame on the same order of magnitude. For an ideal fracture (two parallel plates), the aperture is linked to the specific inner surface area (L^2/L^3); the further the plates are apart, the more fluid can exist between them in relation to the fracture surface area. This surface area to fluid volume ratio essentially determines the reactivity and the magnitude of the water-rock-interaction (Steefel and Lasaga 1994). A further point to consider is the permeability-aperture relationship, which is commonly described with the cubic law: permeability $\propto$ aperture^2 (Neuzil and Tracy 1981).

The investigated single-fracture plug flow experiments showed predominantly homogeneous coating with precipitates, which means that the precipitation rate was similar within the whole column (Tranter et al. 2021b). The equilibrium length provides an explanation for this, which is the flow path a solution travels in reactive transport until it reaches equilibrium. In the respective experiments, the core length was much smaller than the calculated equilibrium lengths (0.15 m versus 12–205 m, on average). Accordingly, the saturation state of barite was more or less constant within the core. On the field-scale,

however, the equilibrium length may be smaller than the investigated domain. Thus, a homogeneous covering cannot be assumed and the distribution of scale formation in the subsurface becomes significant for the permeability development. The flow rate to reaction rate ratio ultimately determines the precipitation pattern within the investigated domain and is discussed in more detail in Section 7.2.

There are further potentially influencing factors that were disregarded in the studies of this thesis, mostly because they are currently either impossible to quantify reliably in natural environments, or are not determined sufficiently in an experimental setting for this matter:

- Using atomic force microscopy, a strong deviation from unity of the Ba^{2+}/SO_4^{2-} ratio has been shown to decrease the crystal step advancement (Bracco et al. 2016; Kowacz et al. 2007). However, it is unclear how this translates to bulk precipitation rates.
- Impurities within the solution (other cations, anions, and organic molecules) all affect growth (Weber et al. 2021), though experiments have shown that calcium, magnesium, and strontium do not have a significant influence (Zhen-Wu et al. 2016).
- Barite and celestite ($SrSO_4$) are known to form a non-ideal regular solid-solution (Heberling et al. 2017; Vinograd et al. 2018), but kinetic data for this is sparse and inconclusive (Poonoosamy et al. 2020a,b; Weber et al. 2021). In a preliminary study, I showed that for the geothermal sites in the URG about 20% more precipitates can be expected if this were taken into account (Tranter et al. 2021a).
- Deliberate influence can be taken on the growth rate with inhibitors, which mitigate precipitation either by disabling ion activity (complexation) or by binding to the surface (chemisorption) (He et al. 1996, 1994a; Jones et al. 2007; Weber et al. 2021).

7.2 Impact of barite reservoir scales on injectivity loss

One hypothesis made in this thesis is that barite reservoir scaling can lead to a significant injectivity loss of geothermal wells. To test this, the barite scaling potential and the related injectivity loss for fractured-porous reservoirs in the NGB and the URG were assessed using the previously developed precipitation models. A key achievement was the transfer of the plug flow model onto the field-scale for geothermal reservoirs. As a result, the two factors that determine the impact of scale formation on injectivity were identified: the amount and distribution in the subsurface, which are discussed in the following.

7.2.1 Quantification of the precipitation mass

The calculated barite precipitation potentials for both geothermal regions URG and NGB are similar, but show a clear reservoir-depth dependency (Tranter et al. 2020). The amounts were in the range 12–16 mmol/m^3 fluid for the 2000 m deep reservoirs, and between 74–87 mmol/m^3 fluid for reservoirs of 3000 m depth. In mass units, this corresponds to a total range of 2.8–20.2 g/m^3 fluid, or, if a constant flow rate of 100 m^3/h is assumed, to a total volume of around 0.5 m^3 to 4 m^3 per year. The 20 g/m^3 fluid reported for the Groß Schönebeck site is within this range (Regenspurg et al. 2015). However, there are some differences regarding the evaluation basis: the Groß Schönebeck reservoir is significantly deeper (over 4 000 m), and the injection temperature in my models was assumed to be 55 °C (e. g., Genter et al. 2009), while for Groß Schönebeck it was 80 °C. But, since the mass amounts are in the same order of magnitude, this is an indication that the models yield realistic results.

The precipitation potential is the starting point for an assessment, but on its own has no quantitative value for determining the impeding effects on the geothermal plant's efficiency. Nevertheless, it can give

an indication for whether a scaling risk can be anticipated, and it is therefore worthwhile to understand the influencing parameters. The key parameters are the fluid properties that determine the solubility: temperature, pore/system pressure, and fluid composition. In the investigated range, decreasing the temperature and the pressure, each decrease the solubility of barite. Yet, the effect of pressure change in the range 1 MPa to 30 MPa is much lower than the effect of temperature alteration in the range of 55 °C to 160 °C (Blount 1977), which are the approximate ranges of the considered geothermal cases (Tranter et al. 2020). Furthermore, the pressure increases again when fluids are re-injected into the reservoir, mitigating this effect even further. Thus, the main driving force for the precipitation potential is the induced temperature difference (dT).

A higher ionic strength generally enhances the solubility differences at various temperatures (Blount 1977). This partly explains why the precipitation potential for the URG and the NGB are similar, as discussed in Tranter et al. (2020): dT is higher for the URG regions (assuming the same injection temperature), but the NGB fluids have a higher mineral content. Accordingly, both regions have different influencing sources for their magnitude of precipitation potential. To yield reliable solubility estimates, even at high ionic strengths up to 6 M, a thermodynamic database relying on the Pitzer ion-interaction approach (Hörbrand et al. 2018; Pitzer 1986) was used in Tranter et al. (2021a, 2020).

Four additional points are to be considered: (1) the barium to sulfate ratio has a significant impact; the more it deviates from unity, the lower the precipitation potential (Tranter et al. 2020). (2) Any precipitation taking place before the fluid reaches the reservoir, of course, lowers the amount that can precipitate in the reservoir. For which cases this phenomenon can be expected, is discussed in Section 7.1. Not taking this into account leaves us with a conservative estimate of the precipitation potential for reservoir scale formation. (3) Fluids are expected to heat up again to some degree if they are re-injected into the reservoir, which lowers the precipitation potential again to some degree (provided they are still supersaturated). However, for a long-term, continuous injection of cold water, this effect can be expected to subside over time. A sensitivity analysis in this regard could be subject to future work. My presented iso-thermal models provide a conservative estimate. (4) The saturation ratio and the precipitation potential are not linearly correlated. Judging the scaling risk based on the saturation ratio alone is inappropriate, and can only be used as an indication if precipitation and nucleation can be expected.

7.2.2 Determination of the subsurface scaling distribution and the role of fractures

The presented models of the NGB cases yielded porosity reductions of the host rock due to barite precipitation in the range 0.2%–1.0% per year, with an approximate radial influence of 5 m around the injection well (Tranter et al. 2020). Applying the Kozeny-Carman porosity-permeability relationship, this corresponds to 1.8%–6.4% injectivity loss per year. This is within the range of the injectivity loss which was observed at the Neustadt-Glewe geothermal site, about 35% after 16 years of injection, or 2.2% per year on average (Birner et al. 2015). This rate of loss is significant, and could expose the geothermal plant to serious economic risk if the flow rates also decline to that effect. This depends on the feasibility to increase the injection well head pressure. However, the modelling results presented in this thesis also showed a strong sensitivity towards the reactivity of the reservoir (Tranter et al. 2020). As discussed in the previous section, the reactive surface area is an uncertain parameter, which was approximated here based on the barite content in the host rock. Using the lower bound from the literature (Wolfgramm 2002), resulted in significantly less injectivity loss between 0.3% and 1.0% per year. The range of the scaling influence around the well roughly doubled, accordingly. Nevertheless, the results suggest that barite played an important role in reducing rock permeability at the Neustadt-Glewe site, possibly even a dominant one. Potentially, other scaling minerals also contributed to this. Lead, lead-sulfides and Sr-bearing barite were also observed at this site, which could be investigated further in future work.

I was able to show that the predicted impact of barite reservoir scaling in the URG region is significantly lower, in comparison to the NGB region (Tranter et al. 2021a). The modelling results of

the scenario analysis yield a range of < 0.1%–1.2% injectivity loss per year (using the upper bound for reactive surface area). Indeed, there are more reports of severe barite scaling in the NGB area, e. g., Neustadt-Glewe and Groß Schönebeck (Regenspurg et al. 2015; Wolfgramm et al. 2012, 2011a), than in the URG. I am not aware of any reports that make barite directly responsible for well injectivity loss in the URG area, although it has been hypothesised to be a contributing factor (Griffiths et al. 2016; Scheiber et al. 2013). Particularly, it is self-evident that barite reservoir scaling happens to some extent because there is proof of barite precipitates in the surface system equipment and in the injection well (Nitschke et al. 2014; Scheiber et al. 2013). Yet, the subsurface distribution of scales is a crucial factor for the injectivity loss.

The results showing that the URG is affected less (Tranter et al. 2021a, 2020), can be interpreted as follows: (1) The investigated samples show that the URG fluids have ionic strengths that are lower by a factor of 3–4 compared to the NGB fluids, depending on the reservoir depth (Wolfgramm and Seibt 2008). Accordingly, the kinetic rate constant is lower for the URG (assuming the same injection temperature), and thus scales form more dispersed along the flow path away from the well (Fig. 7.2). (2) The reservoir thickness is significantly higher in the URG. In the NGB models, a porous-reservoir thickness of 20 m was assumed, which is the target minimum value for exploration (Franz et al. 2018b). In contrast, the URG model was based on the Landau geothermal site, which has a reservoir thickness on the order of 1 000 m, though it is partly porous, partly fractured dense rock (Vidal and Genter 2018). Nevertheless, the higher aquifer thickness results in a precipitation pattern that is more vertically dispersed compared to the NGB. (3) The existing fractures found in the geothermal reservoirs of the URG constitute preferential flow paths with flow velocities exceeding those in porous media by many magnitudes. This also causes precipitation to happen more dispersed along the flow paths in the fractures (Fig. 7.2).

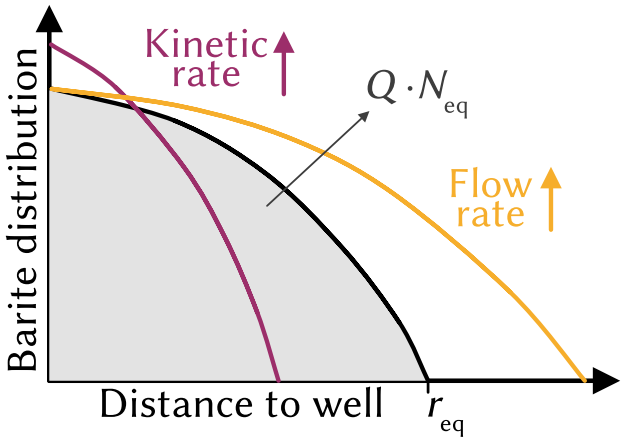

Figure 7.2: Schematic illustration of the barite reservoir scaling pattern shows that a higher flow rate (Q) extends the range of influence around a well and a higher kinetic rate skews the distribution towards the well. The total amount of scales, i. e., the area under the curve, is determined by the precipitation potential (N_{eq}) and the flow rate. The range of influence can be approximated with the radial equilibrium length (r_{eq}). The influence of scales on injectivity declines logarithmically with distance to the well.

It becomes clear that the spatial distribution of scales has a significant impact on the related injectivity loss. Though the calculated precipitation potential is similar for both geothermal regions (Tranter et al. 2020), the subsurface distributions of scales and also the predicted injectivity losses differ. Especially, the role of fractures must be emphasised in this context, which was further assessed in this thesis with a scenario analysis (Tranter et al. 2021a). While fractures showed to have a minimising influence on the scaling related risk in general, due to the aforementioned reason, there are fracture parameters that are specifically relevant in this regard. For instance, the amount of hydraulically active fractures as well as their corresponding apertures were determined to be influential parameters. Corresponding to my previous findings regarding single fractures on the laboratory scale (Tranter et al. 2021b), scale formation affects the reservoir transmissivity more strongly if there is a high number of small fractures

compared to reservoirs with few large ones. For a fractured-porous aquifer, the flow rate ratio of each flow component is important. The respective results show that reservoirs with dominating porous flow had roughly a doubled transmissivity loss compared to reservoirs with mainly fracture flow (Tranter et al. 2021a).

7.2.3 Development of a scaling score

Based on the findings above, I developed a screening tool for assessing the reservoir scaling risk of geothermal systems (Tranter et al. 2021a, 2020). This tool encompasses an analytical *scaling score*, which provides an estimate of the induced injectivity loss over time by taking the discussed precipitation potential and the subsurface scaling distribution pattern into account. The incentive was to provide a quick method for evaluating the related risk in terms of investment decisions. The main benefit is its practicability compared to cumbersome reservoir-scale numerical models, which can both take a lot of time to set up and to carry out. Elaborate numerical models can be conducted at a later stage of a project, when more data is available and an in-depth analysis of the reservoir reaction due to fluid injection becomes necessary. A suggested workflow for approximating the reservoir scaling induced injectivity loss is presented in Fig. 7.3.

A crucial value for determining the spatial distribution of scaling in the subsurface is the radial equilibrium length. It is derived similarly to the Damköhler number by relating the flow rate and the reaction rate, and, as such, is derived from the underlying advection-reaction transport equation. The original application of the equilibrium length in the literature was to analytically assess mineral weathering, but for a constant, linear flow field (Lichtner 1988, 1996; Steefel 2008). For the present case, I adapted this method to account for the radial flow field around an injection well, which entails non-constant flow velocities in the model domain (see Section 4.4 for its derivation). The radial equilibrium length gives the approximate range of influence of scaling around an injection well, provided there is radial-symmetry. Two further assumptions had to be made: (1) quasi-stationary state of the subsurface flow field (2) and constant spatial and temporal reservoir reactivity (i. e., reactive surface area). Its applicability is therefore best met for long injection periods, as well as for ideal fractures and homogeneous porous media. For the investigated geothermal cases, the analytically determined equilibrium lengths of barite were linearly correlated to the numerical simulations (Tranter et al. 2021a), making it an excellent analytical predictor for this application.

To translate the scaling score into tangible values for injectivity loss, it was calibrated with numerical simulations (Tranter et al. 2021a). After calibration, the analytical and numerical injectivity loss results showed a close match. This procedure implicitly accounts for the different responses with regard to the porosity-permeability relationship, both for porous and fractured aquifers. Thus, a calibration has to be done for each porosity-permeability relationship. The Kozeny-Carman relationship was chosen by default for porous aquifers (Carman 1937; Kozeny 1927), and the cubic law was used for the fractures, which are both widely accepted approaches (Hommel et al. 2018). If a different relationship is needed, the numerical simulations have to be carried out again for calibration of the score.

This screening tool is generically applicable to homogeneous porous media and individual sets of uniform fractures with varying thickness and porosity, and to all mineral reservoir scalings, provided it is calibrated regarding its kinetic rate law. It must be noted that only a mono-mineralogical precipitation reaction is considered, so the chemical system is comparably simple. If multiple minerals precipitate in the reservoir, an initial approach would be to calculate a scaling score for each mineral individually, and then sum up the response. This does not take any interaction effects between mineral reactions into account, but yields a quick estimate.

7.2.4 Other sources of injectivity loss

Injectivity loss over time is often reported for EGS and where there are briny, basinal fluids in play (Blöcher et al. 2016; Seibt et al. 2010b). The presented models indicate that barite reservoir scaling can be relevant

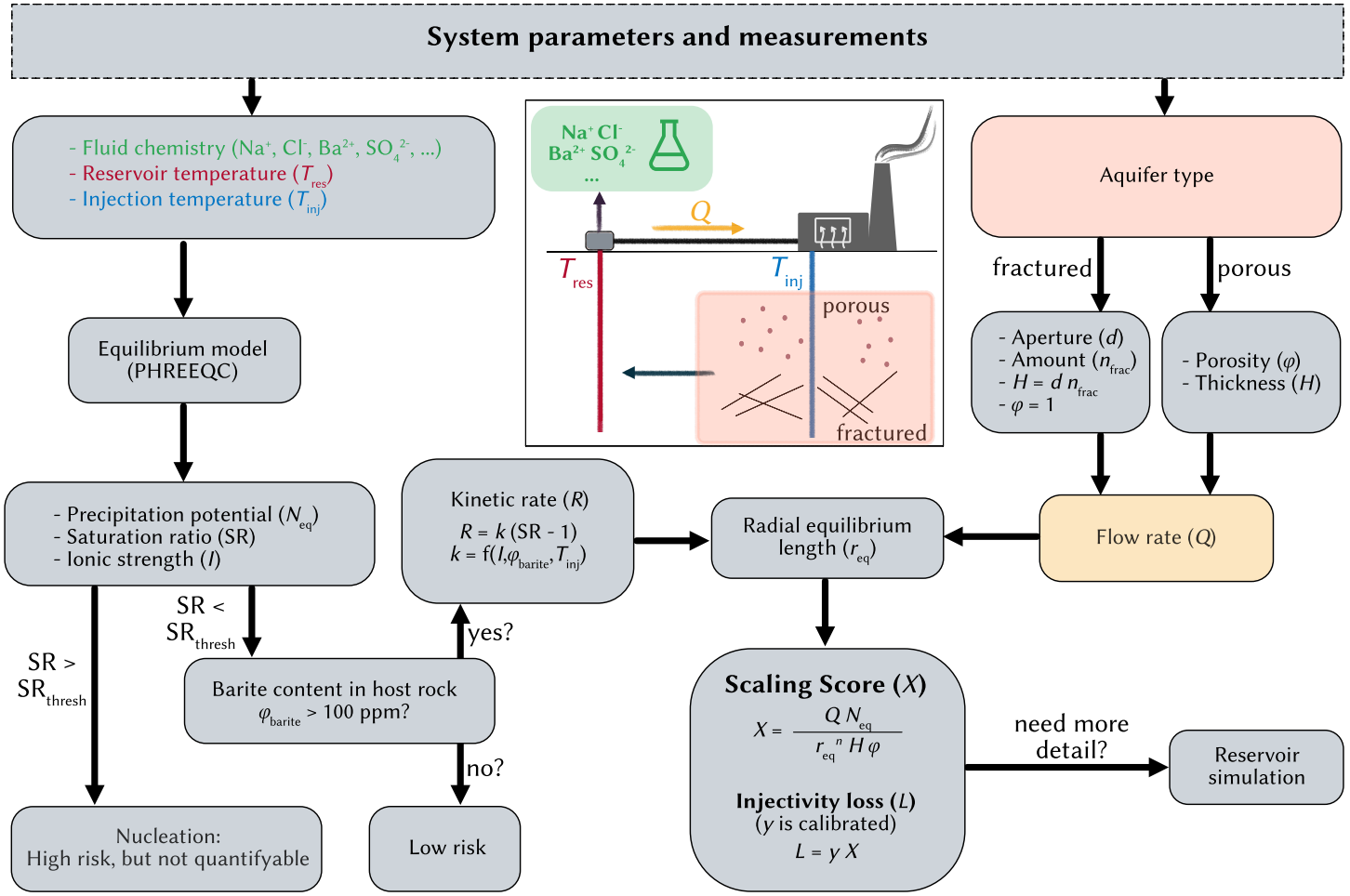

Figure 7.3: Suggested workflow for determining the influence of reservoir scaling on injectivity using the developed scaling score. SR_{thresh} is the threshold supersaturation, φ_{barite} is the volume fraction of barite in the host rock, k is the kinetic rate constant.

in this regard under certain circumstances. The calculated range of injectivity loss is indeed on the same order of magnitude of what was observed at the Neustadt-Glewe geothermal site (Tranter et al. 2020). However, there are other possible reasons, which could also impact injectivity over time: (1) reservoir clogging by washed in particles previously loosened from pipe walls, newly formed particles by homogeneous nucleation, or redistribution in the subsurface (Wolfgramm et al. 2011a); (2) fluid viscosity decrease at the cool water injection location (Blöcher et al. 2016); (3) mechanical (e. g., thermal or shear dilation) closing of natural and engineered fractures (Blöcher et al. 2016; Genter et al. 1996); (4) porosity reduction by other scaling minerals (Hesshaus et al. 2013; Wolfgramm et al. 2011a). Furthermore, formation fluids often exhibit a free gas phase (mostly CO_2 and N_2) leading to a reduced effective permeability due to two-phase flow (Sanjuan et al. 2016). The pressure drop during production could lead to further degassing, which has been considered as a factor for productivity loss (Blöcher et al. 2016). However, commonly a degasser is deployed before the heat exchanger, therefore the impact of two-phase flow on injectivity loss is assumed to be small. A comprehensive assessment of a geothermal site with regard to long-lasting plant operation must take all these possibilities into account to pinpoint the relevant processes.

7.3 Implications for geothermal energy

7.3.1 Summary of contributing factors for reservoir scaling in geothermal systems

The following points are contributing factors for reservoir scaling and should be taken into account when assessing the related risk of a geothermal site.

Threshold supersaturation This is the saturation ratio above which nucleation can be expected within a domain. I come to a general conclusion that this value should not be overstepped within a geothermal system, otherwise the precipitation rate can increase exponentially. Following the Classical Nucleation Theory, nucleation is not expected to play a role for the Neustadt-Glewe or Landau sites, but for Groß Schönebeck it is probable.

Barite ubiquity Sedimentary basin reservoirs usually contain barite in trace amounts. This is something to look out for in general because then it must be assumed that (1) the fluids are initially in thermodynamic equilibrium with barite and (2) this provides the reactivity for reservoir scaling (even if no nucleation has happened).

Precipitation potential The main influencing factor for precipitation potential is the induced temperature change within the system. Deeper reservoirs have a generally higher precipitation potential because the initial reservoir temperature and accordingly the induced temperature difference are higher. Higher salinity also enhances the temperature-change-induced precipitation potential. Since fluid salinity is correlated with depth, deeper reservoirs are even more at risk. Finally, the closer the barium to sulfate ratio is to unity, the higher the precipitation potential, which is also more frequent for deeper reservoir fluids. The precipitation potential therefore needs to be determined site specifically using thermodynamic equilibrium models, which are able to take high ionic strengths into account, e. g., the Pitzer ion-interaction approach.

Scaling distribution pattern The scaling distribution in the subsurface is determined by the flow rate to kinetic rate ratio. If the kinetic rate is high, scales form closer to the well and injectivity loss progresses faster. Factors which enhance the kinetic rate are the ionic strength and the magnitude of the reactive surface area. The temperature has an ambivalent effect on the kinetic rate: a low temperature decreases the rate constant, but increases the deviation from the thermodynamic equilibrium and hence increases the saturation ratio. High flow rates enlarge the radius of the occurring scalings around the well.

Fractures Fractures are preferential flow paths in the subsurface and therefore influence the scaling distribution by extending the scaling reach, i. e., dispersing precipitates further away from the well. Accordingly, fractures crossing the injection well potentially lower the impact of scaling on injectivity compared to purely porous reservoirs. However, fractures with lower apertures experience more permeability loss than larger ones due to their higher specific reactive surface area.

7.3.2 Verdict for exemplary geothermal regions

Geothermal system in the NGB region, especially the deeper reservoirs ($\approx$ 3000 m), bear all the described barite-precipitation-enhancing features: fluids with high ionic strengths, barium to sulfate ratio closer to one, and few to no fractures. The modelling results suggest that these geothermal systems are likely to experience severe reservoir scaling induced injectivity loss over time with according economical consequences. The URG is significantly less at risk, mainly due to lower ionic strength of the fluids, a higher number of fractures, and reservoirs with higher thicknesses, translating into a more dispersed precipitation in the subsurface. The simulated injectivity losses for the URG are judged to be low compared to effects related to mechanical fault compaction or non-lasting, hydraulically induced fractures. But, the multi-horizontal EGS approach applied in the URG (e. g., at Landau) entails uncertainty with regard to the subsurface flow field, which makes related predictions more complex. Depending on the hydraulic dominance of the fractures or the porous matrix, the scaling risk is either lower or higher, respectively. The flow distribution may even change over time due to mechanical or chemical closing, underlining the importance to monitor the flow paths. Yet, the nature of the described scaling occurrence is rather a creeping process, permitting a time frame to react with countermeasures.

7.3.3 Strategies for mitigating barite scale formation

The presented models provide a clear message that fractures mitigate the effect of reservoir scaling compared to purely porous reservoirs. From this perspective, reservoir prospection and engineering should focus on exploiting fractured reservoirs, which incidentally can also provide high hydraulic yields. Particularly, the presence of few fractures with large hydraulic apertures further reduces the impact of reservoir scaling. Ensuring that fractures remain the dominant flow path in the subsurface is vital, e. g., by using effective proppants to keep fractures open.

Further, the presented results suggest that the threshold supersaturation should not be exceeded if possible. If the induced supersaturation is higher, nucleation can become a rate determining step, which accelerates the overall precipitation rate. Determining the threshold supersaturation for a specific site experimentally is a difficult undertaking, but models can give supporting evidence. If the threshold is indeed expected to be exceeded, increasing the injection temperature to some degree could be beneficial. However, it must be taken into account that a higher injection temperature also increases the reaction rate constant. These effects need to be weighed up, depending on the fluid composition and the initial reservoir temperature.

Other strategies possibly worth examining further are the following: (1) The application of inhibitors to suppress scale formation has been tested for various geothermal sites (Scheiber et al. 2013). While the experience was successful to some degree for preventing scales in the heat exchanger and the piping system, it remains unclear if it is suitable for preventing reservoir scaling. Questions regarding thermal stability, environmental concerns and the perturbation of the precipitation mechanism need to be answered for specific inhibitors. (2) Newly formed and washed-in particles from the reservoir can lead to sedimentation in the pipework and clogging in reservoir (Wolfgramm et al. 2011a). Fine mesh particle filters can mitigate this aspect, but there is a trade-off between possible flow-rate and filter size. (3) Deliberately provoking precipitation of barite ex situ before fluids enter the reservoir could reduce the precipitation potential leading to injectivity loss. In a similar way, removing barium or sulfate from the solution, e. g., with membranes, would reduce scaling. However, due to the high flow rates ($>$ 50 l/s) this is not feasible with current technologies.

7.3.4 Value of models

Models are an essential tool for predicting processes in the subsurface and to assess the feasibility of its utilisation. Although models have limits due to their simplified representation of the heterogeneous, natural subsurface, they provide great value for long-lasting subsurface applications. They are particularly necessary to evaluate the risk of reservoir scaling because no field methods are currently available to verify this processes in situ. In the present thesis, models provide means of testing the hypothesis whether barite reservoir scaling is of relevance for the NGB and the URG geothermal regions. Not only do they yield evidence for scaling risk in these regions, but they also allow the determination of the influencing factors, indicating which reservoir parameters need to be focused on. This also gives insights into which prevention-measures are feasible to mitigate the issue. Moreover, the developed modelling framework has the potential to be extended if more detailed subsurface data becomes available. For instance, a more complex chemical system with concurrent dissolution and precipitation of multiple minerals or solid-solutions is envisaged to describe the influence of reservoir scales more comprehensively. The benefit of analytical approaches, e. g., the scaling score, must be emphasised in this context, as the applicability of their numerical counterparts is often limited due to their computing time intensity. This is especially true for chemically coupled models on the reservoir scale, so surrogate models are vital to make practical advances in this field.

CHAPTER 8

Conclusions and outlook

Deep geothermal energy has the potential to contribute to the goal of net-zero carbon emissions by providing a base-load capable alternative to fossil fuels. A widespread adoption in Germany is impeded by various challenges, such as the finding risk of high hydraulic yields and temperature anomalies as well as the specific operational demands for a long-term deployment. In this thesis, one of the major obstacles with regard to plant longevity, namely barite reservoir scaling, was addressed on the basis of the promising geothermal regions North German Basin (NGB) and Upper Rhine Graben (URG). Reservoir scaling in general is the accumulation of secondary mineral formation close to the cool water injection location. This can have severe negative impacts on the efficiency of a system, as it alters the microstructure and consequently the hydraulic properties of the rock. In this regard, specifically barite has been presumed to be responsible for irreversible injectivity loss. Hydrogeochemical models are indispensable to quantify the impact of scalings on a system's efficiency, since direct field-measurements of reservoir scales is not feasible. The aim of this thesis is to provide such models for fractured-porous geothermal reservoirs, to estimate the related permeability loss by means of reactive transport simulations as well as analytical approaches. The achieved objectives for advancing the application of geothermal energy are: (1) evaluation of the individual precipitation mechanisms and their controlling parameters, (2) assessment of the impact of barite reservoir scaling on injectivity using numerical reservoir models and (3) direct screening methods.

To determine the location of barite scale formation in the system, knowledge on the kinetic reaction properties is fundamental. Barite precipitation is represented by a two-step process involving nucleation and crystal growth, whereby the main driving force is the temperature change induced supersaturation. Additional important parameters to consider are the ionic strength of the fluid, the available reactive surface area as well as the existence of fractures and their hydraulic properties. The ionic strength enhances the induced supersaturation as well as the kinetic rate constant, hence accelerating the kinetic rate two-fold. The initial barite in the rock determines the reactive surface area, which can be further enhanced by nucleation. However, nucleation becomes only relevant if the supersaturation exceeds a certain threshold, which can only be roughly approximated with the available databases. The reactivity of a fracture is reversely correlated to its aperture. The influence of fractures on reservoir scaling is controlled by their respective apertures, which is inversely correlated to the reactivity. The aforementioned theoretical factors have substantial consequences for geothermal systems: Scales form closer to the well if the kinetic rate is high, which progresses injectivity loss faster. Thus, it is beneficial if the threshold supersaturation is not exceeded. For the investigated exemplary sites Neustadt-Glewe and Landau, the results suggest that nucleation is negligible, but not for Groß Schönebeck. Generally, it can be deduced that geothermal sites circulating fluids with high ionic strength are more at risk for accelerated injectivity loss. Furthermore, fractures are preferential flow paths and contribute to dispersing scales further away from the well, more so if fractures are large.

The conducted reservoir simulations give evidence that injectivity loss due to barite scaling is significant in the NGB and can affect the longevity of the plant, especially for deeper reservoirs (3000 m). In contrast, the results of the URG sites do not indicate a significant role of barite in this regard. The

reservoir models show that two factors control the scaling induced injectivity loss: the distribution and potential of precipitation. The precipitation potential rises with increasing reservoir depth, since fluids typically have (1) a higher ionic strength, (2) a barium to sulfate ratio closer to unity as well as (3) a higher temperature and consecutively a higher induced temperature difference. Regarding the investigated study areas, both the NGB and the URG regions reach similar depth-dependent precipitation potentials, but for different reasons. While the URG can profit from less ionic strength fluids, it is impacted by a higher temperature difference between reservoir and injection. Conversely, within the NGB temperature does not vary as much, but the ionic strength of circulating fluids is significantly higher. Despite the comparable precipitation potential, the scaling patterns are skewed more towards the well for the NGB cases, i.a., due to the higher kinetic rates. The relevance of scales on injectivity increases logarithmically the closer they are to the well. In the URG, barite scale formation occurs additionally dispersed because reservoir thickness is generally larger and existing fractures serve as preferential flow paths within the rock.

Finally, a screening tool was developed for approximating the reservoir scaling risk of geothermal systems. This tool encompasses an analytical scaling score, which provides an accurate estimate of the induced injectivity loss over time by taking the discussed precipitation potential and the scaling pattern into account. The score was calibrated for porous media and single sets of fractures using numerical simulations and specific porosity-permeability relationships. Although the screening tool was developed for barite specifically, it can be certainly transferred to other minerals, provided the kinetic rate law is adjusted accordingly. The major advantage compared to cumbersome reservoir simulations lies in its simplicity, making it more accessible for plant operators and decision makers. Thus, it can find broader application in geothermal engineering, e. g., in search of potential plant sites and estimation of long-term efficiency.

The presented thesis provides a modelling framework for quantifying reservoir scaling and their net effect on the efficiency of geothermal systems. Still, there are some aspects on which future modelling studies could focus to additionally improve the process understanding and prediction of reservoir scaling:

Multi-mineral chemistry Other scaling minerals, such as Pb, Pb-sulfides, calcite and $(Ba, Sr)SO_4$ solid solutions have been observed to accompany barite precipitates in geothermal systems. Assessing the corresponding scaling risk of each, especially including the interaction with each other, is a logical continuation of this thesis. Moreover, a comprehensive treatment of the chemical system should check if interaction with other minerals in the reservoir is relevant to consider, e. g., the concurrent dissolution of anhydrite.

Complex flow models Scaling distribution can be considerably affected by the overall flow regime of the system. Thus, the presented geochemical models should be coupled to more elaborate flow models, e. g., discrete fracture network or dual-porosity models, if detailed data on the hydraulic rock properties suggest that these are required.

Porosity-permeability relationships The actual permeability loss response of a host rock due to barite precipitation could deviate from generic porosity-permeability assumptions, which then should be assessed reservoir-specifically with accompanying pore-scale models. Furthermore, the presented scaling score takes the permeability response with a calibrated exponent factor into account. It would be worthwhile to investigate whether this exponent can be deduced analytically from a respective porosity-permeability relationship.

Scaling inhibitors The use of inhibitors to prevent scaling in the surface system has been tested at various pilot sites with mixed success. Modelling investigations of their efficiency and the specific mechanisms involved could prove to be an important step towards mitigating the issue and thus could further improve the longevity of geothermal plants.

APPENDIX A

Appendix

A.1 Supplements for Chapter 2

Numerical investigation of barite scaling kinetics in fractures.

A.1.1 Example PHREEQC input file

```
TITLE PhreeqSim
RATES
Barite # phreeqsim
-start
# (mol), temporary variable
10 moles = 0
# (mol m-2 s-1), dissolution rate constant
20 k_d = 10^PARM(1)
# (mol m-2 s-1), growth rate constant
30 k_p = 10^PARM(2)
40 sa = PARM(3)  # (m2)
# (-), reaction order dissolution
50 n_d = 0.2
# (-), reaction order growth
60 n_p = 1.0
70 IF (SR("Barite") < 1.0)
AND (M <= 0.0) THEN GOTO 100
# Crystal dissolution
80 IF SR("Barite") < 1.0 THEN
moles = k_d * sa * (1 - SR("Barite")^n_d)
# Crystal growth
90 IF SR("Barite") > 1.0 THEN
moles = k_p * sa * (1 - SR("Barite")^n_p)
100 SAVE moles * TIME
-end
SELECTED_OUTPUT
-high_precision True
-reset false
USER_PUNCH
-headings step_no # base
-headings pH pe # sol
-headings Ba S Na Cl # element
-headings Ba+2 SO4-2 # species
-headings sr_Barite # sr_solid
-headings Barite # kin_solid

-start
10 PUNCH STEP_NO
20 PUNCH -LA('H+'), -LA('e-')
30 PUNCH TOT('Ba'), TOT('S'), TOT('Na'), TOT('Cl')
40 PUNCH MOL('Ba+2'), MOL('SO4-2')
50 PUNCH SR('Barite')
60 PUNCH KIN('Barite')
-end
END
# ============================================
SOLUTION 0
units mol/kgw
water 958.29329
temperature 60
pressure 98.692327
pH 6.0071915
pe 4
Ba 0.00089862195
S(6) 0.00089862195
Na 1.5
Cl 1.5
KINETICS 0
-steps 1 in 1 steps seconds
Barite
-m0 13.125398
-parms -5.96 -6.46 100000 # log_kd, log_kp, sa
END
```

A.1.2 Model input parameters

Table A.1: Transport model input parameters for the various sensitivity analysis and scenarios. OAT refers to the one-at-a-time parameter screening after Morris (2.3.2). A, B, and C refer to the sensitivity analysis scenarios after Sobol (2.3.3). GSB refers to the scenario for Groß-Schönebeck site (2.3.4). Parameters: nodes (−), maximum time steps $\mathrm{nt}_{\max}$ (−), length x (m), fracture aperture $\log d$ ($\log$ m), temperature T (°C), pressure $\log P$ ($\log$ Pa), flow velocity $\log u_{\mathrm{x}}$ ($\log \mathrm{m\,s^{-1}}$), pH (−), elemental concentrations ($\mathrm{mol\,kgw^{-1}}$), saturation state at inlet Ω_{in} (−), temperature at inlet T_{in} (°C), diffusion coefficient D_{m} ($\mathrm{m^2\,s^{-1}}$), interfacial energy γ ($\mathrm{J\,m^{-2}}$), contact angle θ (°), molar volume V_{m} ($\mathrm{cm^3\,mol^{-1}}$). A single value means it was fixed. Two values mean it was varied uniformly in this range. If T_{in} is not defined, it is the same as the domain temperature T.

parameter	OAT (Morris)	A (Sobol)	B (Sobol)	C (Sobol)	GSB
nodes	6	6	6	6	6
$\mathrm{nt}_{\max}$	200	200	200	200	200
x	0.15	0.15	0.15	0.15	0.15
$\log d$	$(-4, -2)$	$(-4, -2)$	$(-4, -2)$	$(-4, -2)$	$(-4, -2)$
T	$(50, 70)$	$(50, 70)$	$(50, 70)$	$(50, 70)$	$(25, 150)$
$\log P$	$(7.0, 7.7)$	$(7.0, 7.7)$	$(7.0, 7.7)$	$(7.0, 7.7)$	7.7
$\log u_{\mathrm{x}}$	$(-3, 0)$	$(-3, 0)$	$(-3, 0)$	$(-3, 0)$	-1
pH	$(5, 7)$	$(5, 7)$	$(5, 7)$	$(5, 7)$	5.7
Na^+	$(0.1, 1.5)$	$(0.1, 1.5)$	$(0.1, 1.5)$	$(0.1, 1.5)$	1.67
K^+	-	-	-	-	7.4×10^{-2}
Ca^{2+}	-	-	-	-	1.35
Mg^{2+}	-	-	-	-	1.8×10^{-2}
Ba^{2+}	-	-	-	-	2.469×10^{-3}
Sr^{2+}	-	-	-	-	2.2×10^{-2}
Cl^-	$(0.1, 1.5)$	$(0.1, 1.5)$	$(0.1, 1.5)$	$(0.1, 1.5)$	4.521
SO_4^{2-}	-	-	-	-	3.719×10^{-3}
HCO_3^-	-	-	-	-	3.1×10^{-4}
Ω_{in}	$(1.1, 31.6)$	15	20	30	1
T_{in}	-	-	-	-	150
D_m	1.0×10^{-9}	1.0×10^{-9}	1.0×10^{-9}	1.0×10^{-9}	1.0×10^{-9}
γ	$(0.07, 0.134)$	0.08	0.08	0.08	0.08
θ	$(1, 179)$	85	85	85	85
V_m	$(50.26, 55.55)$	$(50.26, 55.55)$	$(50.26, 55.55)$	$(50.26, 55.55)$	52.9

A.2 Supplements for Chapter 5

Barite scale formation and injectivity loss models for geothermal systems.

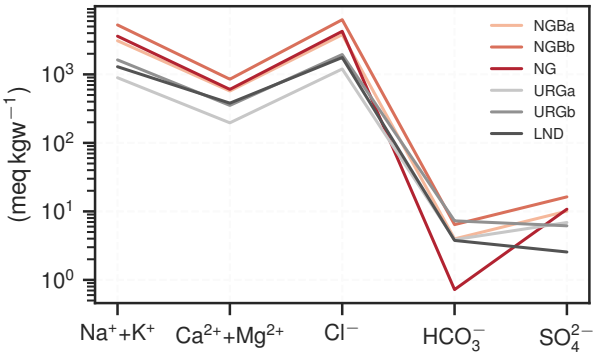

Figure A.1: Chemical composition of the considered geothermal fluids illustrated in Schoeller-diagrams. All shown waters are Na-Cl(-Ca)-types.

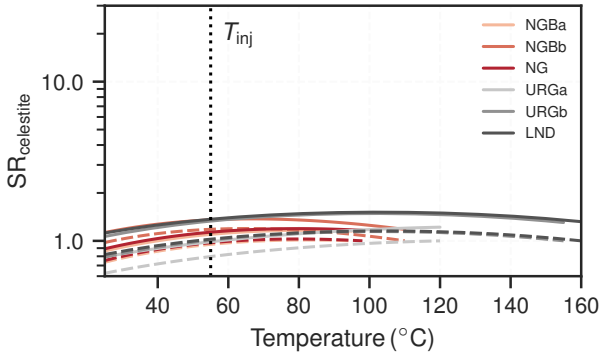

Figure A.2: Celestite saturation ratio according to reducing temperature for the various geothermal cases. The solid lines assume system pressures (1 MPa) and the dashed lines assume the respective reservoir pressures. The dotted vertical lines indicate the assumed injection temperature (T_{inj}).

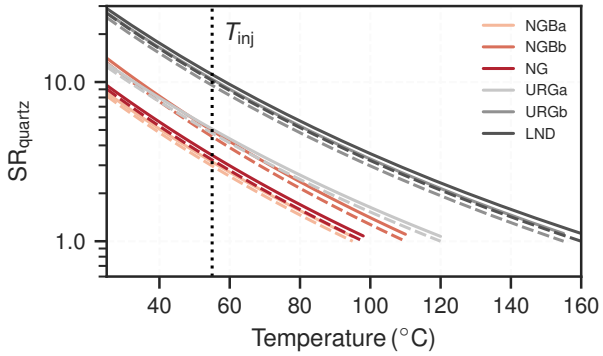

Figure A.3: Quartz saturation ratio according to reducing temperature for the various geothermal cases. The solid lines assume system pressures (1 MPa) and the dashed lines assume the respective reservoir pressures. The dotted vertical lines indicate the assumed injection temperature (T_{inj}).

Bibliography

Agemar, Thorsten, Rüdiger Schellschmidt, and Rüdiger Schulz (2012). Subsurface Temperature Distribution in Germany. *Geothermics* 44:65–77. DOI: 10.1016/j.geothermics.2012.07.002.

Agemar, Thorsten, Evelyn Suchi, and Inga Moeck (2018). *Die Rolle der tiefen Geothermie bei der Wärmewende - Wie Deutschland 60 % erneuerbare Wärme bis 2050 schaffen könnte*. Hannover, Germany: Leibniz-Institut für Angewandte Geophysik LIAG, p. 14.

Agemar, Thorsten, Josef Weber, and Rüdiger Schulz (2014). Deep Geothermal Energy Production in Germany. *Energies* 7(7):4397–4416. DOI: 10.3390/en7074397.

Aichi, Masaatsu and Kento Akitaya (2018). Analytical Solution for a Radial Advection-Dispersion Equation Including Both Mechanical Dispersion and Molecular Diffusion for a Steady-State Flow Field in a Horizontal Aquifer Caused by a Constant Rate Injection from a Well. *Hydrological Research Letters* 12(3):23–27. DOI: 10.3178/hrl.12.23.

Al Ibrahim, Mustafa A., Abdulla Kerimov, Tapan Mukerji, and Gary Mavko (2019). Particula: A Simulator Tool for Computational Rock Physics of Granular Media. *GEOPHYSICS* 84(3):F85–F95. DOI: 10.1190/geo2018-0481.1.

Appelo, C. A. J. and Dieke Postma (2010). *Geochemistry, Groundwater and Pollution*. 2nd ed., 5th corr. repr. Boca Raton: CRC Press. 649 pp.

Appelo, C.A.J. (2015). Principles, Caveats and Improvements in Databases for Calculating Hydrogeochemical Reactions in Saline Waters from 0 to 200 °C and 1 to 1000 Atm. *Applied Geochemistry* 55:62–71. DOI: 10.1016/j.apgeochem.2014.11.007.

Appelo, C.A.J., D.L. Parkhurst, and V.E.A. Post (2014). Equations for Calculating Hydrogeochemical Reactions of Minerals and Gases Such as CO2 at High Pressures and Temperatures. *Geochimica et Cosmochimica Acta* 125:49–67. DOI: 10.1016/j.gca.2013.10.003.

Bächler, D, T Kohl, and L Rybach (2003). Impact of Graben-Parallel Faults on Hydrothermal Convection––Rhine Graben Case Study. *Physics and Chemistry of the Earth, Parts A/B/C* 28(9-11):431–441. DOI: 10.1016/s1474-7065(03)00063-9.

Banks, Jonathan (2013). Sulfate Mineral Scaling during the Production of Geothermal Energy from Sedimentary Basin Formation Brines: A Case Study at the Groß Schönebeck in-Situ Geothermal Laboratory, Germany. Berlin: Freie Universität Berlin.

Banks, Jonathan, Simona Regenspurg, and Harald Milsch (2014). Experimental Method for Determining Mixed-Phase Precipitation Kinetics from Synthetic Geothermal Brine. *Applied Geochemistry* 47:74–84. DOI: 10.1016/j.apgeochem.2014.05.016.

Bär, Kristian Manuel (2012). Untersuchung Der Tiefengeothermischen Potenziale von Hessen. Darmstadt: Technische Universität.

Baumgärtner, Jörg, Dimitra Teza, Thomas Hettkamp, and Peter Hauffe (2010). Stimulierung Tiefer Geothermischer Systeme. *BBR-Sonderheft*:13–23.

Bear, Jacob (1988). *Dynamics of Fluids in Porous Media*. Dover Books on Physics and Chemistry. New York: Dover. 764 pp.

Beckingham, Lauren E. (2017). Evaluation of Macroscopic Porosity-Permeability Relationships in Heterogeneous Mineral Dissolution and Precipitation Scenarios. *Water Resources Research* 53(12):10217–10230. DOI: 10.1002/2017wr021306.

Beckingham, Lauren E. et al. (2016). Evaluation of Mineral Reactive Surface Area Estimates for Prediction of Reactivity of a Multi-Mineral Sediment. *Geochimica et Cosmochimica Acta* 188:310–329. DOI: 10.1016/j.gca.2016.05.040.

Beckingham, Lauren E. et al. (2017). Evaluation of Accessible Mineral Surface Areas for Improved Prediction of Mineral Reaction Rates in Porous Media. *Geochimica et Cosmochimica Acta* 205:31–49. DOI: 10.1016/j.gca.2017.02.006.

Behr, H.-J. and J. Gerler (1987). Inclusions of Sedimentary Brines in Post-Variscan Mineralizations in the Federal Republic of Germany — A Study by Neutron Activation Analysis. *Chemical Geology* 61(1-4):65–77. DOI: 10.1016/0009-2541(87)90028-3.

Birner, J et al. (2012). Hydraulic Characterisation of the Malm Aquifer in the South German Molasse Basin and Its Impact on Geothermal Exploitations. *Z geol Wiss* 40(2):133–56.

Birner, Johannes, Andrea Seibt, Peter Seibt, and Markus Wolfgramm (2015). Removing and Reducing Scalings – Practical Experience in the Operation of Geothermal Systems. *Proceedings World Geothermal Congress*. World Geothermal Congress. Melbourne, Australia.

Blöcher, Guido et al. (2016). Hydraulic History and Current State of the Deep Geothermal Reservoir Groß Schönebeck. *Geothermics* 63:27–43. DOI: 10.1016/j.geothermics.2015.07.008.

Blöcher, Guido et al. (2019). Permeability of Matrix-Fracture Systems under Mechanical Loading – Constraints from Laboratory Experiments and 3-D Numerical Modelling. *Advances in Geosciences* 49:95–104. DOI: 10.5194/adgeo-49-95-2019.

Bloomquist, R.Gordon (2003). Geothermal Space Heating. *Geothermics* 32(4-6):513–526. DOI: 10.1016/j.geothermics.2003.06.001.

Blount, C. W. (1977). Barite Solubilities and Thermodynamic Quantities up to 300°C and 1400 Bars. *American Mineralogist* 62(9-10):942–957.

BMWi (2019). *Energiedaten: Gesamtausgabe—Stand: Oktober 2019*. Berlin: Bundesministerium für Wirtschaft und Energie.

Bozau, Elke, Steffen Häußler, and Wolfgang van Berk (2015). Hydrogeochemical Modelling of Corrosion Effects and Barite Scaling in Deep Geothermal Wells of the North German Basin Using PHREEQC and PHAST. *Geothermics* 53:540–547. DOI: 10.1016/j.geothermics.2014.10.002.

Bracco, Jacquelyn N., Yiscka Gooijer, and Steven R. Higgins (2016). Hydrothermal Atomic Force Microscopy Observations of Barite Step Growth Rates as a Function of the Aqueous Barium-to-Sulfate Ratio. *Geochimica et Cosmochimica Acta* 183:1–13. DOI: 10.1016/j.gca.2016.03.009.

Brehme, Maren et al. (2018). Injection-Triggered Occlusion of Flow Pathways in Geothermal Operations. *Geofluids* 2018:1–14. DOI: 10.1155/2018/4694829.

Bromley, Chris et al. (2010). Contribution of Geothermal Energy to Climate Change Mitigation: The IPCC Renewable Energy Report. *Proceedings World Geothermal Congress*. World Geothermal Congress. Bali, Indonesia, p. 5.

Bruss, Dietfried (2000). *Zur Herkunft der Erdöle im mittleren Oberrheingraben und ihre Bedeutung für die Rekonstruktion der Migrationsgeschichte und der Speichergesteinsdiagenese*. Berichte des Forschungszentrums Jülich 3831. Jülich: Forschungszentrum Jülich GmbH Zentralbibliothek, Verlag. 222 pp.

Canic, Tina et al. (2011). Kinetik von Barytausfällungen Aus Geothermalwasser – Einfluss Der Scherung. *DGK*. DGK.

Carman, P. C. (1937). Fluid Flow through Granular Beds. *Transactions of the Institution of Chemical Engineers* 15:150–166.

Cataldi, Raffaele et al., eds. (1999). *Stories from a Heated Earth: Our Geothermal Heritage*. Sacrament Calif: Geothermal Resources Council: International Geothermal Association. 569 pp.

Chamorro, César R. et al. (2012). World Geothermal Power Production Status: Energy, Environmental and Economic Study of High Enthalpy Technologies. *Energy* 42(1):10–18. DOI: 10.1016/j.energy.2011.06.005.

Charlton, Scott R. and David L. Parkhurst (2011). Modules Based on the Geochemical Model PHREEQC for Use in Scripting and Programming Languages. *Computers & Geosciences* 37(10):1653–1663. DOI: 10.1016/j.cageo.2011.02.005.

Chen, Chia-Shyun (1985). Analytical and Approximate Solutions to Radial Dispersion From an Injection Well to a Geological Unit With Simultaneous Diffusion Into Adjacent Strata. *Water Resources Research* 21(8):1069–1076. DOI: 10.1029/wr021i008p01069.

Chen, Jui-Sheng, Chen-Wuing Liu, and Chung-Min Liao (2002). A Novel Analytical Power Series Solution for Solute Transport in a Radially Convergent Flow Field. *Journal of Hydrology* 266(1-2):120–138. DOI: 10.1016/s0022-1694(02)00119-1.

Christy, Andrew G and Andrew Putnis (1993). The Kinetics of Barite Dissolution and Precipitation in Water and Sodium Chloride Brines at 44–85°C. *Geochimica et Cosmochimica Acta* 57(10):2161–2168. DOI: 10.1016/0016-7037(93)90557-d.

Curti, Enzo et al. (2019). Modelling Ra-bearing Baryte Nucleation/Precipitation Kinetics at the Pore Scale: Application to Radioactive Waste Disposal. *European Journal of Mineralogy* 31(2):247–262. DOI: 10.1127/ejm/2019/0031-2818.

Dai, Zhaoyi et al. (2019). Two-Stage Model Reveals Barite Crystallization Kinetics from Solution Turbidity. *Industrial & Engineering Chemistry Research* 58:DOI: 10.1021/acs.iecr.9b01707.

De Lucia, Marco and Michael Kühn (2013). Coupling R and PHREEQC: Efficient Programming of Geochemical Models. *Energy Procedia* 40:464–471. DOI: 10.1016/j.egypro.2013.08.053.

De Lucia, Marco and Michael Kühn (2021). DecTree v1.0 – Chemistry Speedup in Reactive Transport Simulations: Purely Data-Driven and Physics-Based Surrogates. *Geoscientific Model Development* 14(7):4713–4730. DOI: 10.5194/gmd-14-4713-2021.

Degering, Detlev, Matthias Koehler, and Mario Hielscher (2011). Occurrence and behaviour of natural radionuclides in aquifer, fluid and precipitates of the geothermal facility Neustadt-Glewe, Germany. *Zeitschrift für Geologische Wissenschaften* 39(3-4):275–290.

Demir, Mustafa M., Alper Baba, Vedat Atilla, and Mustafa İnanlı (2014). Types of the Scaling in Hyper Saline Geothermal System in Northwest Turkey. *Geothermics* 50:1–9. DOI: 10.1016/j.geothermics.2013.08.003.

Deng, Hang and Nicolas Spycher (2019). Modeling Reactive Transport Processes in Fractures. *Reviews in Mineralogy and Geochemistry* 85(1):49–74. DOI: 10.2138/rmg.2019.85.3.

Deng, Hang, Carl Steefel, Sergi Molins, and Donald DePaolo (2018a). Fracture Evolution in Multimineral Systems: The Role of Mineral Composition, Flow Rate, and Fracture Aperture Heterogeneity. *ACS Earth and Space Chemistry* 2(2):112–124. DOI: 10.1021/acsearthspacechem.7b00130.

Deng, Hang et al. (2018b). Pore-Scale Numerical Investigation of the Impacts of Surface Roughness: Upscaling of Reaction Rates in Rough Fractures. *Geochimica et Cosmochimica Acta* 239:374–389. DOI: 10.1016/j.gca.2018.08.005.

Dezayes, Chrystel, Albert Genter, and Benoît Valley (2010). Structure of the Low Permeable Naturally Fractured Geothermal Reservoir at Soultz. *Comptes Rendus Geoscience* 342(7-8):517–530. DOI: 10.1016/j.crte.2009.10.002.

Dickson, Mary H. and Mario Fanelli (2013). *Geothermal Energy*. Routledge. DOI: 10.4324/9781315065786.

Dove, Patricia M. and Carol A. Czank (1995). Crystal Chemical Controls on the Dissolution Kinetics of the Isostructural Sulfates: Celestite, Anglesite, and Barite. *Geochimica et Cosmochimica Acta* 59(10):1907–1915. DOI: 10.1016/0016-7037(95)00116-6.

Dupuit, Jules (1863). *Études Théoriques et Pratiques Sur Le Mouvement Des Eaux Dans Les Canaux Découverts et à Travers Les Terrains Perméables*. Dunod (Paris).

Dussel, M. et al. (2016). Forecast for Thermal Water Use from Upper Jurassic Carbonates in the Munich Region (South German Molasse Basin). *Geothermics* 60:13–30. DOI: 10.1016/j.geothermics.2015.10.010.

Duyvesteyn, Willem P.C. (1992). Recovery of Base Metals from Geothermal Brines. *Geothermics* 21(5-6):773–799. DOI: 10.1016/0375-6505(92)90030-d.

Eyerer, S. et al. (2020a). Combined Heat and Power from Hydrothermal Geothermal Resources in Germany: An Assessment of the Potential. *Renewable and Sustainable Energy Reviews* 120:109661. DOI: 10.1016/j.rser.2019.109661.

Eyerer, Sebastian, Fabian Dawo, Christoph Wieland, and Hartmut Spliethoff (2020b). Advanced ORC Architecture for Geothermal Combined Heat and Power Generation. *Energy* 205:117967. DOI: 10.1016/j.energy.2020.117967.

Fazeli, Hossein et al. (2020). Pore-Scale Modeling of Nucleation and Growth in Porous Media. *ACS Earth and Space Chemistry* 4(2):249–260. DOI: 10.1021/acsearthspacechem.9b00290.

Fernandez-Diaz, Lurdes, Andrew Putnis, and Toby J. Cumberbatch (1990). Barite Nucleation Kinetics and the Effect of Additives. *European Journal of Mineralogy* 2(4):495–502. DOI: 10.1127/ejm/2/4/0495.

Fischer, Cornelius, Inna Kurganskaya, Thorsten Schäfer, and Andreas Lüttge (2014). Variability of Crystal Surface Reactivity: What Do We Know? *Applied Geochemistry* 43:132–157. DOI: 10.1016/j.apgeochem.2014.02.002.

Forjanes, Pablo, José Manuel Astilleros, and Lurdes Fernández-Díaz (2020). The Formation of Barite and Celestite through the Replacement of Gypsum. *Minerals* 10(2):189. DOI: 10.3390/min10020189.

Franz, Matthias et al. (2018a). Deep Geothermal Resources of the North German Basin: The Hydrothermal Reservoirs of the Stuttgart Formation (Schilfsandstein, Upper Triassic). *Zeitschrift der Deutschen Gesellschaft für Geowissenschaften* 169(3):353–387. DOI: 10.1127/zdgg/2018/0164.

Franz, Matthias et al. (2018b). Geothermal Resources of the North German Basin: Exploration Strategy, Development Examples and Remaining Opportunities in Mesozoic Hydrothermal Reservoirs. *Geological Society, London, Special Publications* 469(1):193–222. DOI: 10.1144/sp469.11.

Gardner, G. L. and G. H. Nancollas (1983). Crystal Growth in Aqueous Solution at Elevated Temperatures. Barium Sulfate Growth Kinetics. *The Journal of Physical Chemistry* 87(23):4699–4703. DOI: 10.1021/j100246a031.

Genske, Dieter D. (2006). *Ingenieurgeologie: Grundlagen und Anwendung*. Berlin Heidelberg: Springer. 588 pp.

Genter, A. et al. (1996). Fracture Analysis and Reservoir Characterization of the Granitic Basement in the HDR Soultz Project (France). *International Journal of Rock Mechanics and Mining Sciences & Geomechanics Abstracts* 33(2):A69. DOI: 10.1016/0148-9062(96)83915-5.

Genter, Albert et al. (2009). Overview of the Current Activities of the European Egs Soultz Project: From Exploration to Electricity Production. *Proceedings, 34th Workshop on Geothermal Reservoir Engineering*. Workshop on Geothermal Reservoir Engineering. Stanford University, Stanford, California.

Godinho, Jose R. A. and Andrew G. Stack (2015). Growth Kinetics and Morphology of Barite Crystals Derived from Face-Specific Growth Rates. *Crystal Growth & Design* 15(5):2064–2071. DOI: 10.1021/cg501507p.

Granbakken, Dag et al. (1991). Scale Formation in Reservoir and Production Equipment During Oil Recovery. III. A Kinetic Model for the Precipitation/Dissolution Reactions. *Acta Chemica Scandinavica* 45:892–901. DOI: 10.3891/acta.chem.scand.45-0892.

Griffiths, L. et al. (2016). Geothermal Implications for Fracture-Filling Hydrothermal Precipitation. *Geothermics* 64:235–245. DOI: 10.1016/j.geothermics.2016.06.006.

Grünthal, Gottfried, Rutger Wahlström, and Dietrich Stromeyer (2013). The SHARE European Earthquake Catalogue (SHEEC) for the Time Period 1900–2006 and Its Comparison to the European-Mediterranean Earthquake Catalogue (EMEC). *Journal of Seismology* 17(4):1339–1344. DOI: 10.1007/s10950-013-9379-y.

Guillou-Frottier, Laurent et al. (2013). Structure of Hydrothermal Convection in the Upper Rhine Graben as Inferred from Corrected Temperature Data and Basin-Scale Numerical Models. *Journal of Volcanology and Geothermal Research* 256:29–49. DOI: 10.1016/j.jvolgeores.2013.02.008.

Haarberg, Torstein et al. (1992). Scale Formation in Reservoir and Production Equipment During Oil Recovery: An Equilibrium Model. *SPE Production Engineering* 7(01):75–84. DOI: 10.2118/19449-pa.

Hano, T. et al. (1992). Recovery of Lithium from Geothermal Water by Solvent Extraction Technique. *Solvent Extraction and Ion Exchange* 10(2):195–206. DOI: 10.1080/07366299208918100.

He, Shiliang, Amy T. Kan, and Mason B. Tomson (1996). Mathematical Inhibitor Model for Barium Sulfate Scale Control. *Langmuir* 12(7):1901–1905. DOI: 10.1021/la950876x.

He, Shiliang, John E. Oddo, and Mason B. Tomson (1994a). The Inhibition of Gypsum and Barite Nucleation in NaCl Brines at Temperatures from 25 to 90°C. *Applied Geochemistry* 9(5):561–567. DOI: 10.1016/0883-2927(94)90018-3.

He, Shiliang, John E. Oddo, and Mason B. Tomson (1994b). The Seeded Growth of Calcium Sulfate Dihydrate Crystals in NaCl Solutions up to 6 m and 90°C. *Journal of Colloid and Interface Science* 163(2):372–378. DOI: 10.1006/jcis.1994.1116.

He, Shiliang, John E. Oddo, and Mason B. Tomson (1995). The Nucleation Kinetics of Barium Sulfate in NaCl Solutions up to 6 m and 90°C. *Journal of Colloid and Interface Science* 174(2):319–326. DOI: 10.1006/jcis.1995.1397.

Heberle, Florian, Christopher Schifflechner, and Dieter Brüggemann (2016). Life Cycle Assessment of Organic Rankine Cycles for Geothermal Power Generation Considering Low-GWP Working Fluids. *Geothermics* 64:392–400. DOI: 10.1016/j.geothermics.2016.06.010.

Heberling, Frank, Dieter Schild, Detlev Degering, and Thorsten Schäfer (2017). How Well Suited Are Current Thermodynamic Models to Predict or Interpret the Composition of (Ba,Sr)SO4 Solid-Solutions in Geothermal Scalings? *Geothermal Energy* 5(1):9. DOI: 10.1186/s40517-017-0068-x.

Hesshaus, Annalena, Georg Houben, and Robert Kringel (2013). Halite Clogging in a Deep Geothermal Well - Geochemical and Isotopic Characterisation of Salt Origin. *Physics and Chemistry of the Earth* 64:127–139. DOI: 10.1016/j.pce.2013.06.002.

Hina, A. and G. H. Nancollas (2011). Precipitation and Dissolution of Alkaline Earth Sulfates: Kinetics and Surface Energy. *Reviews in Mineralogy and Geochemistry* 40(1):277–301. DOI: 10.2138/rmg.2000.40.5.

Hommel, Johannes, Edward Coltman, and Holger Class (2018). Porosity–Permeability Relations for Evolving Pore Space: A Review with a Focus on (Bio-)Geochemically Altered Porous Media. *Transport in Porous Media* 124(2):589–629. DOI: 10.1007/s11242-018-1086-2.

Hörbrand, Thorsten, Thomas Baumann, and Helge C. Moog (2018). Validation of Hydrogeochemical Databases for Problems in Deep Geothermal Energy. *Geothermal Energy* 6(1):20. DOI: 10.1186/s40517-018-0106-3.

Hsieh, Paul A. (1986). A New Formula for the Analytical Solution of the Radial Dispersion Problem. *Water Resources Research* 22(11):1597–1605. DOI: 10.1029/wr022i011p01597.

Huttrer, Gerald (2020). Geothermal Power Generation in the World 2015-2020 Update Report. *Proceedings World Geothermal Congress 2020*. World Geothermal Congress 2020. Reykjavik, Iceland, p. 17.

IAEA (2016). *Climate Change and Nuclear Power 2016*. Vienna: International Atomic Energy Agency.

IPCC (2021). Summary for Policymakers. *Climate Change 2021: The Physical Science Basis. Contribution of Working Group I to the Sixth Assessment Report of the Intergovernmental Panel on Climate Change*. Cambridge University Press.

Jones, Franca et al. (2007). The Interaction of EDTA with Barium Sulfate. *Journal of Colloid and Interface Science* 316(2):553–561. DOI: 10.1016/j.jcis.2007.09.005.

Karlsdottir, Marta R., Jukka Heinonen, Halldor Palsson, and Olafur P. Palsson (2020). Life Cycle Assessment of a Geothermal Combined Heat and Power Plant Based on High Temperature Utilization. *Geothermics* 84:101727. DOI: 10.1016/j.geothermics.2019.101727.

Kashchiev, D. and G. M. van Rosmalen (2003). Review: Nucleation in Solutions Revisited. *Crystal Research and Technology* 38(78):555–574. DOI: 10.1002/crat.200310070.

Kashchiev, Dimo (2000). *Nucleation: Basic Theory with Applications*. Oxford ; Boston: Butterworth Heinemann. 529 pp.

Kaufmann-Knoke, Ruth (1992). *Zur Problematik von Mineralausfällungen insbesondere von (Ba, Sr)SO4-Mischkristallen bei der Erdölförderung*. Version 1.0. Geologisch-Paläontologisches Institut und Museum, Christian-Albrechts-Universität, Kiel, 110 pages. DOI: 10.2312/REPORTS-GPI.1992.53.

King, P.R. (1989). The Use of Renormalization for Calculating Effective Permeability. *Transport in Porous Media* 4(1):DOI: 10.1007/bf00134741.

Kluge, Christian et al. (2021). Permeability Evolution During Shear Zone Initiation in Low-Porosity Rocks. *Rock Mechanics and Rock Engineering*:DOI: 10.1007/s00603-020-02356-0.

Kowacz, M., C. V. Putnis, and A. Putnis (2007). The Effect of Cation:Anion Ratio in Solution on the Mechanism of Barite Growth at Constant Supersaturation: Role of the Desolvation Process on the Growth Kinetics. *Geochimica et Cosmochimica Acta* 71(21):5168–5179. DOI: 10.1016/j.gca.2007.09.008.

Kozeny, J. (1927). Über Kapillare Leitung Des Wassers Im Boden. *Sitzungsberichte Wiener Akademie* 136:(2a), 271–306.

Kühn, Michael (1997). Geochemische Folgereaktion Bei Der Hydrogeothermalen Energiegewinnung. Universität Bremen.

Kühn, Michael, Jörn Bartels, and Joachim Iffland (2002). Predicting Reservoir Property Trends under Heat Exploitation: Interaction between Flow, Heat Transfer, Transport, and Chemical Reactions in a Deep Aquifer at Stralsund, Germany. *Geothermics* 31(6):725–749. DOI: 10.1016/s0375-6505(02)00033-0.

Kühn, Michael et al. (1997). Experimentelle Untersuchungen zur Barytübersättigung einer Thermalsole. *Grundwasser* 2(3):111–117. DOI: 10.1007/s767-1997-8532-2.

Kühn, Michael et al. (1998). Onsite Experimental Simulation of Brine Injection into a Clastic Reservoir as Applied to Geothermal Exploitation in Germany. *Applied Geochemistry* 13(4):477–490. DOI: 10.1016/s0883-2927(97)00081-4.

Kumar, G. Suresh and Ahmad Ghassemi (2005). Numerical Modeling of Non-Isothermal Quartz Dissolution / Precipitation in a Coupled Fracture–Matrix System. *Geothermics* 34(4):411–439. DOI: 10.1016/j.geothermics.2005.04.003.

Lai, Keng-Hsin et al. (2016). A Novel Method for Analytically Solving a Radial Advection-Dispersion Equation. *Journal of Hydrology* 542:532–540. DOI: 10.1016/j.jhydrol.2016.09.027.

Langevin, Christian D (2008). Modeling Axisymmetric Flow and Transport. *Ground Water* 46(4):579–590. DOI: 10.1111/j.1745-6584.2008.00445.x.

Lasaga, A. C. (1998). *Kinetic Theory in the Earth Sciences*. Princeton Series in Geochemistry. Princeton, N.J: Princeton University Press. 811 pp.

Leal, Allan M. M., Dmitrii A. Kulik, William R. Smith, and Martin O. Saar (2017). An Overview of Computational Methods for Chemical Equilibrium and Kinetic Calculations for Geochemical and Reactive Transport Modeling. *Pure and Applied Chemistry* 89(5):597–643. DOI: 10.1515/pac-2016-1107.

Legland, David, Ignacio Arganda-Carreras, and Philippe Andrey (2016). MorphoLibJ: Integrated Library and Plugins for Mathematical Morphology with ImageJ. *Bioinformatics* 33(22):3532–3534. DOI: 10.1093/bioinformatics/btw413.

Li, Ling et al. (2018). Lithium Recovery from Aqueous Resources and Batteries: A Brief Review. *Johnson Matthey Technology Review* 62(2):161–176. DOI: 10.1595/205651317X696676.

Li, Qingyun and Young-Shin Jun (2019). Salinity-Induced Reduction of Interfacial Energies and Kinetic Factors during Calcium Carbonate Nucleation on Quartz. *The Journal of Physical Chemistry C* 123(23):14319–14326. DOI: 10.1021/acs.jpcc.9b00378.

Li, Tianyu, Sogo Shiozawa, and Mark W. McClure (2016). Thermal Breakthrough Calculations to Optimize Design of a Multiple-Stage Enhanced Geothermal System. *Geothermics* 64:455–465. DOI: 10.1016/j.geothermics.2016.06.015.

Lichtner, Peter C. (1988). The Quasi-Stationary State Approximation to Coupled Mass Transport and Fluid-Rock Interaction in a Porous Medium. *Geochimica et Cosmochimica Acta* 52(1):143–165. DOI: 10.1016/0016-7037(88)90063-4.

Lichtner, Peter C. (1996). Continuum Formulation of Multicomponent-Multiphase Reactive Transport. *Reviews in Mineralogy and Geochemistry* 34(1):1–81.

Liu, S.T., G.H. Nancollas, and E.A. Gasiecki (1976). Scanning Electron Microscopic and Kinetic Studies of the Crystallization and Dissolution of Barium Sulfate Crystals. *Journal of Crystal Growth* 33(1):11–20. DOI: 10.1016/0022-0248(76)90074-9.

Liu, X. Y. (1999). A New Kinetic Model for Three-Dimensional Heterogeneous Nucleation. *The Journal of Chemical Physics* 111(4):1628–1635. DOI: 10.1063/1.479391.

Lu, Alex Yi-Tsung et al. (2020). Kinetics of Barium Sulfate Deposition and Crystallization Process in the Flowing Tube. *Industrial & Engineering Chemistry Research* 59(16):7299–7309. DOI: 10.1021/acs.iecr.0c00112.

Lu, Chunhui, Pengfei Du, Yiming Chen, and Jian Luo (2011). Recovery Efficiency of Aquifer Storage and Recovery (ASR) with Mass Transfer Limitation. *Water Resources Research* 47(8):DOI: 10.1029/2011wr010605.

Lucas, Yann et al. (2020). Modelling Acid Stimulation in the Enhanced Geothermal System of Soultz-sous-Forêts (Alsace, France). *Geothermics* 85:101772. DOI: 10.1016/j.geothermics.2019.101772.

Lund, John W and Aniko Toth (n.d.). Direct Utilization of Geothermal Energy 2020 Worldwide Review:(), 39.

Martin, Gunther, Lars Rentsch, Michael Höck, and Martin Bertau (2017). Lithium Market Research – Global Supply, Future Demand and Price Development. *Energy Storage Materials* 6:171–179. DOI: 10.1016/j.ensm.2016.11.004.

Moench, A. F. and A. Ogata (1981). A Numerical Inversion of the Laplace Transform Solution to Radial Dispersion in a Porous Medium. *Water Resources Research* 17(1):250–252. DOI: 10.1029/wr017i001p00250.

Morris, Max D. (1991). Factorial Sampling Plans for Preliminary Computational Experiments. *Technometrics* 33(2):161–174. DOI: 10.1080/00401706.1991.10484804.

Nancollas, G. H. and N. Purdie (1963). Crystallization of Barium Sulphate in Aqueous Solution. *Transactions of the Faraday Society* 59:735. DOI: 10.1039/tf9635900735.

Nancollas, G.H. and S.T. Liu (1975). Crystal Growth and Dissolution of Barium Sulfate. *Society of Petroleum Engineers Journal* 15(06):509–516. DOI: 10.2118/5300-pa.

Naumann, D. (2000). *Salinare Tiefenwässer in Norddeutschland: gas- und isotopengeochemische Untersuchungen zur Herkunft und geothermische Nutzung*. Scientific Technical Report STR00/21. Deutsches GeoForschungsZentrum Potsdam.

Neuzil, C. E. and James V. Tracy (1981). Flow through Fractures. *Water Resources Research* 17(1):191–199. DOI: 10.1029/wr017i001p00191.

Ngo, Viet V., Yann Lucas, Alain Clément, and Bertrand Fritz (2016). Modeling the Impact of Temperature on the Saturation State and Behavior of Minerals in the Soultz-sous-Forêts Geothermal System. *Geothermics* 64:196–208. DOI: 10.1016/j.geothermics.2016.06.001.

Nielsen, Arne E. (1964). *Kinetics of Precipitation*. Oxford: Pergamon, Oxford.

Nielsen, Arne E. and O. Söhnel (1971). Interfacial Tensions Electrolyte Crystal-Aqueous Solution, from Nucleation Data. *Journal of Crystal Growth* 11(3):233–242. DOI: 10.1016/0022-0248(71)90090-x.

Nitschke, Fabian, Julia Scheiber, Utz Kramar, and Thomas Neumann (2014). Formation of Alternating Layered Ba-Sr-sulfate and Pb-sulfide Scaling in the Geothermal Plant of Soultz-sous-Forêts. *Neues Jahrbuch für Mineralogie - Abhandlungen* 191(2):145–156. DOI: 10.1127/0077-7757/2014/0253.

Nooraiepour, Mohammad, Mohammad Masoudi, Nima Shokri, and Helge Hellevang (2021). Probabilistic Nucleation and Crystal Growth in Porous Medium: New Insights from Calcium Carbonate Precipitation on Primary and Secondary Substrates. *ACS Omega*:acsomega.1c04147. DOI: 10.1021/acsomega.1c04147.

Orywall, Pia et al. (2017). Flow-through Experiments on the Interaction of Sandstone with Ba-rich Fluids at Geothermal Conditions. *Geothermal Energy* 5(1):20. DOI: 10.1186/s40517-017-0079-7.

Paillet, F. L., A. E. Hess, C. H. Cheng, and E. Hardin (1987). Characterization of Fracture Permeability with High-Resolution Vertical Flow Measurements During Borehole Pumping. *Ground Water* 25(1):28–40. DOI: 10.1111/j.1745-6584.1987.tb02113.x.

Palandri, James L. and Yousif K. Kharaka (2004). *A Compilation of Rate Parameters of Water-Mineral Interaction Kinetics for Application to Geochemical Modeling*. Report 2004-1068. USGS.

Pandey, S.N., A. Chaudhuri, H. Rajaram, and S. Kelkar (2015). Fracture Transmissivity Evolution Due to Silica Dissolution/Precipitation during Geothermal Heat Extraction. *Geothermics* 57:111–126. DOI: 10.1016/j.geothermics.2015.06.011.

Parkhurst, David L. and C.A.J. Appelo (2013). *Description of Input and Examples for PHREEQC Version 3: A Computer Program for Speciation, Batch-Reaction, One-Dimensional Transport, and Inverse Geochemical Calculations*. Report 6-A43. Reston, VA: USGS.

Paschen, H, D Oertel, and R Grünwald (2003). *Möglichkeiten Geothermischer Stromerzeugung in Deutschland*. TAB-Arbeitsbericht 84. Berlin: Büro für Technikfolgenabschätzung beim Deutschen Bundestag (TAB).

Pauwels, Hélène, Christian Fouillac, and Anne-Marie Fouillac (1993). Chemistry and Isotopes of Deep Geothermal Saline Fluids in the Upper Rhine Graben: Origin of Compounds and Water-Rock Interactions. *Geochimica et Cosmochimica Acta* 57(12):2737–2749. DOI: 10.1016/0016-7037(93)90387-c.

Phillips, O. M. (1991). *Flow and Reactions in Permeable Rocks*. Cambridge [England] ; New York: Cambridge University Press. 285 pp.

Pitzer, Kenneth S. (1973). Thermodynamics of Electrolytes. I. Theoretical Basis and General Equations. *The Journal of Physical Chemistry* 77(2):268–277. DOI: 10.1021/j100621a026.

Pitzer, Kenneth S. (1986). *Theoretical Considerations of Solubility with Emphasis on Mixed Aqueous Electrolytes*. LBNL Report LBL-21961. Lawrence Berkeley National Laboratory.

Poonoosamy, J., Georg Kosakowski, Luc R. Van Loon, and Urs Mäder (2015). Dissolution-Precipitation Processes in Tank Experiments for Testing Numerical Models for Reactive Transport Calculations: Experiments and Modelling. *Journal of Contaminant Hydrology* 177–178:1–17. DOI: 10.1016/j.jconhyd.2015.02.007.

Poonoosamy, J. et al. (2016). Barite Precipitation Following Celestite Dissolution in a Porous Medium: A SEM/BSE and μ-XRD/XRF Study. *Geochimica et Cosmochimica Acta* 182:131–144. DOI: 10.1016/j.gca.2016.03.011.

Poonoosamy, J. et al. (2021). Benchmarking of Reactive Transport Codes for 2D Simulations with Mineral Dissolution–Precipitation Reactions and Feedback on Transport Parameters. *Computational Geosciences* 25(4):1337–1358. DOI: 10.1007/s10596-018-9793-x.

Poonoosamy, Jenna et al. (2020a). Combination of MRI and SEM to Assess Changes in the Chemical Properties and Permeability of Porous Media Due to Barite Precipitation. *Minerals* 10(3):(3), 226. DOI: 10.3390/min10030226.

Poonoosamy, Jenna et al. (2020b). Effects of Solution Supersaturation on Barite Precipitation in Porous Media and Consequences on Permeability: Experiments and Modelling. *Geochimica et Cosmochimica Acta* 270:43–60. DOI: 10.1016/j.gca.2019.11.018.

Prasianakis, N. I. et al. (2017). Deciphering Pore-Level Precipitation Mechanisms. *Scientific Reports* 7(1):1–9. DOI: 10.1038/s41598-017-14142-0.

Prieto, M. (2014). Nucleation and Supersaturation in Porous Media (Revisited). *Mineralogical Magazine* 78(6):1437–1447. DOI: 10.1180/minmag.2014.078.6.11.

Przybycin, Anna M., Magdalena Scheck-Wenderoth, and Michael Schneider (2017). The Origin of Deep Geothermal Anomalies in the German Molasse Basin: Results from 3D Numerical Models of Coupled Fluid Flow and Heat Transport. *Geothermal Energy* 5(1):1. DOI: 10.1186/s40517-016-0059-3.

Putnis, Andrew, Manuel Prieto, and Lurdes Fernandez-Diaz (1995). Fluid Supersaturation and Crystallization in Porous Media. *Geological Magazine* 132(1):1–13. DOI: 10.1017/s0016756800011389.

Rabbani, Arash and Saeid Jamshidi (2014). Specific Surface and Porosity Relationship for Sandstones for Prediction of Permeability. *International Journal of Rock Mechanics and Mining Sciences* 71:25–32. DOI: 10.1016/j.ijrmms.2014.06.013.

Regenspurg, Simona, Elvira Feldbusch, Ben Norden, and Marion Tichomirowa (2016). Fluid-Rock Interactions in a Geothermal Rotliegend/Permo-Carboniferous Reservoir (North German Basin). *Applied Geochemistry* 69:12–27. DOI: 10.1016/j.apgeochem.2016.03.010.

Regenspurg, Simona et al. (2010). Geochemical Properties of Saline Geothermal Fluids from the In-Situ Geothermal Laboratory Groß Schönebeck (Germany). *Geochemistry* 70:3–12. DOI: 10.1016/j.chemer.2010.05.002.

Regenspurg, Simona et al. (2015). Mineral Precipitation during Production of Geothermal Fluid from a Permian Rotliegend Reservoir. *Geothermics* 54:122–135. DOI: 10.1016/j.geothermics.2015.01.003.

Renard, Ph. and G. de Marsily (1997). Calculating Equivalent Permeability: A Review. *Advances in Water Resources* 20(5-6):253–278. DOI: 10.1016/s0309-1708(96)00050-4.

Rimstidt, J.D. and H.L. Barnes (1980). The Kinetics of Silica-Water Reactions. *Geochimica et Cosmochimica Acta* 44(11):1683–1699. DOI: 10.1016/0016-7037(80)90220-3.

Risthaus, Peter, Dirk Bosbach, Udo Becker, and Andrew Putnis (2001). Barite Scale Formation and Dissolution at High Ionic Strength Studied with Atomic Force Microscopy. *Colloids and Surfaces A: Physicochemical and Engineering Aspects* 191(3):201–214. DOI: 10.1016/s0927-7757(00)00843-8.

Ruiz-Agudo, Cristina, Christine V. Putnis, Encarnación Ruiz-Agudo, and Andrew Putnis (2015). The Influence of pH on Barite Nucleation and Growth. *Chemical Geology* 391:7–18. DOI: 10.1016/j.chemgeo.2014.10.023.

Saltelli, Andrea (2002). Making Best Use of Model Evaluations to Compute Sensitivity Indices. *Computer Physics Communications* 145(2):280–297. DOI: 10.1016/s0010-4655(02)00280-1.

Sanjuan, B. et al. (2016). Major Geochemical Characteristics of Geothermal Brines from the Upper Rhine Graben Granitic Basement with Constraints on Temperature and Circulation. *Chemical Geology* 428:27–47. DOI: 10.1016/j.chemgeo.2016.02.021.

Scheiber, Julia et al. (2013). Application of a Scaling Inhibitor System at the Geothermal Power Plant in Soultz-sous-Forêts: Laboratory and On-site Studies. *Proceedings European Geothermal Congress*. European Geothermal Congress. Pisa, Italy.

Schindler, Marion et al. (2010). Successful Hydraulic Stimulation Techniques for Electric Power Production in the Upper Rhine Graben, Central Europe. *Proceedings World Geothermal Congress*. World Geothermal Congress, p. 7.

Schröder, H et al. (2007). Long Term Reliability of Geothermal Plants – Examples from Germany. *Proceedings European Geothermal Congress*. European Geothermal Congress.

Schumacher, Sandra, Roberto Pierau, and Wolfgang Wirth (2020). Probability of Success Studies for Geothermal Projects in Clastic Reservoirs: From Subsurface Data to Geological Risk Analysis. *Geothermics* 83:101725. DOI: 10.1016/j.geothermics.2019.101725.

Seibt, Andrea and Kirsten Thorwart (2011). Untersuchungen Zur Gasphase Geothermischer Genutzter Tiefenwässer Und Deren Relevanz Für Den Anlagenbetrieb. *Zeitschrift für Geologische Wissenschaften* 39(3/4):264–274.

Seibt, Peter, Frank Kabus, Markus Wolfgramm, and Jörn Bartels (2010a). *Monitoring Geothermischer Anlagen - Praxisbeispiele*. 2028. VDI.

Seibt, Peter et al. (2010b). Monitoring of Hydrogeothermal Plants in Germany – an Overview. *Proceedings World Geothermal Congress*. World Geothermal Congress. Bali, Indonesia.

Seigneur, Nicolas, K. Ulrich Mayer, and Carl I. Steefel (2019). Reactive Transport in Evolving Porous Media. *Reviews in Mineralogy and Geochemistry* 85(1):197–238. DOI: 10.2138/rmg.2019.85.7.

Smith, York, Pankaj Kumar, and John McLennan (2017). On the Extraction of Rare Earth Elements from Geothermal Brines. *Resources* 6(3):39. DOI: 10.3390/resources6030039.

Sobol′, I.M (2001). Global Sensitivity Indices for Nonlinear Mathematical Models and Their Monte Carlo Estimates. *Mathematics and Computers in Simulation* 55(1-3):271–280. DOI: 10.1016/s0378-4754(00)00270-6.

Sorbie, K.S and E.J Mackay (2000). Mixing of Injected, Connate and Aquifer Brines in Waterflooding and Its Relevance to Oilfield Scaling. *Journal of Petroleum Science and Engineering* 27(1-2):85–106. DOI: 10.1016/s0920-4105(00)00050-4.

Stack, Andrew G., Paolo Raiteri, and Julian D. Gale (2012). Accurate Rates of the Complex Mechanisms for Growth and Dissolution of Minerals Using a Combination of Rare-Event Theories. *Journal of the American Chemical Society* 134(1):11–14. DOI: 10.1021/ja204714k.

Steefel, C. I. and A. C. Lasaga (1994). A Coupled Model for Transport of Multiple Chemical Species and Kinetic Precipitation/Dissolution Reactions with Application to Reactive Flow in Single Phase Hydrothermal Systems. *American Journal of Science* 294(5):529–592. DOI: 10/dfk3md.

Steefel, C. I. et al. (2015). Reactive Transport Codes for Subsurface Environmental Simulation. *Computational Geosciences* 19(3):445–478. DOI: 10.1007/s10596-014-9443-x.

Steefel, Carl I. (2008). Geochemical Kinetics and Transport. *Kinetics of Water-Rock Interaction*. Ed. by Susan L. Brantley, James D. Kubicki, and Art F. White. New York, NY: Springer New York, pp. 545–589. DOI: 10.1007/978-0-387-73563-4_11.

Steefel, Carl I. and Philippe Van Cappellen (1990). A New Kinetic Approach to Modeling Water-Rock Interaction: The Role of Nucleation, Precursors, and Ostwald Ripening. *Geochimica et Cosmochimica Acta* 54(10):2657–2677. DOI: 10.1016/0016-7037(90)90003-4.

Stober, Ingri, Markus Wolfgramm, and Johannes Birner (2013). Hydrochemie Der Tiefenwässer in Deutschland. *Zeitschrift für Geologische Wissenschaften* 42(5/6):339–380.

Stober, Ingrid and Kurt Bucher (2014). *Geothermie*. 2nd ed. Lehrbuch. Berlin: Springer Spektrum. 302 pp.

Taebi, Behnam and Sabine Roeser, eds. (2015). *The Ethics of Nuclear Energy: Risk, Justice and Democracy in the Post-Fukushima Era*. Cambridge, United Kingdom: Cambridge University Press. 286 pp.

Templeton, C. C. (1960). Solubility of Barium Sulfate in Sodium Chloride Solutions from 25° to 95° C. *Journal of Chemical & Engineering Data* 5(4):514–516. DOI: 10.1021/je60008a028.

Tesmer, M. et al. (2007). Deep Reaching Fluid Flow in the North East German Basin: Origin and Processes of Groundwater Salinisation. *Hydrogeology Journal* 15(7):1291–1306. DOI: 10.1007/s10040-007-0176-y.

Tischner, T, M Pfender, and D Teza (2006). *Hot Dry Rock Projekt Soultz: Erste Phase der Erstellung einer wissenschaftlichen Pilotanlage*. Abschlussbericht 0327097. BGR, p. 87.

Toride, Nobuo, Feike J. Leij, and Martinus T. van Genuchten (1993). A Comprehensive Set of Analytical Solutions for Nonequilibrium Solute Transport with First-Order Decay and Zero-Order Production. *Water Resources Research* 29(7):2167–2182. DOI: 10.1029/93wr00496.

Tranter, Morgan (2021). *Phreeqsim*. Version 0.3.0. Zenodo. DOI: 10.5281/ZENODO.5482132.

Tranter, Morgan, Marco De Lucia, and Michael Kühn (2021a). Barite Scaling Potential Modelled for Fractured-Porous Geothermal Reservoirs. *Minerals* 11(11):1198. DOI: 10.3390/min11111198.

Tranter, Morgan, Marco De Lucia, and Michael Kühn (2021b). Numerical Investigation of Barite Scaling Kinetics in Fractures. *Geothermics* 91:102027. DOI: 10.1016/j.geothermics.2020.102027.

Tranter, Morgan, Marco De Lucia, Markus Wolfgramm, and Michael Kühn (2020). Barite Scale Formation and Injectivity Loss Models for Geothermal Systems. *Water* 12(11):3078. DOI: 10.3390/w12113078.

Tranter, Morgan, Maria Wetzel, Marco De Lucia, and Michael Kühn (2021c). Reactive Transport Model of Kinetically Controlled Celestite to Barite Replacement. *Advances in Geosciences* 56:57–65. DOI: 10.5194/adgeo-56-57-2021.

Umweltbundesamt UBA (2010). *Energieziel 2050: 100% Strom aus erneuerbaren Quellen*. Dessau-Roßlau, p. 196.

Valdez, Benjamin et al. (2009). Corrosion and Scaling at Cerro Prieto Geothermal Field. *Anti-Corrosion Methods and Materials* 56(1):28–34. DOI: 10.1108/00035590910923437.

Van den Heuvel, Daniela B. et al. (2018). Understanding Amorphous Silica Scaling under Well-Constrained Conditions inside Geothermal Pipelines. *Geothermics* 76:231–241. DOI: 10.1016/j.geothermics.2018.07.006.

Verma, A. and K. Pruess (1988). Thermohydrological Conditions and Silica Redistribution near High-Level Nuclear Wastes Emplaced in Saturated Geological Formations. *Journal of Geophysical Research* 93(B2):1159. DOI: 10.1029/JB093iB02p01159.

Vidal, Jeanne and Albert Genter (2018). Overview of Naturally Permeable Fractured Reservoirs in the Central and Southern Upper Rhine Graben: Insights from Geothermal Wells. *Geothermics* 74:57–73. DOI: 10.1016/j.geothermics.2018.02.003.

Vinograd, V.L. et al. (2018). Thermodynamics of the Solid Solution - Aqueous Solution System (Ba,Sr,Ra)SO4 + H2O: I. The Effect of Strontium Content on Radium Uptake by Barite. *Applied Geochemistry* 89:59–74. DOI: 10.1016/j.apgeochem.2017.11.009.

Wallis, Ilka et al. (2012). Simulating MODFLOW-Based Reactive Transport Under Radially Symmetric Flow Conditions. *Ground Water*:no–no. DOI: 10.1111/j.1745-6584.2012.00978.x.

Wanner, Christoph, Florian Eichinger, Thomas Jahrfeld, and Larryn W. Diamond (2017). Causes of Abundant Calcite Scaling in Geothermal Wells in the Bavarian Molasse Basin, Southern Germany. *Geothermics* 70:324–338. DOI: 10.1016/j.geothermics.2017.05.001.

Weber, Josef, Britta Ganz, Burkhard Sanner, and Inga Moeck (2016). Geothermal Energy Use, Country Update for Germany. *European Geothermal Congress*. European Geothermal Congress. Strasbourg, France, p. 17.

Weber, Juliane et al. (2021). Studies of Mineral Nucleation and Growth Across Multiple Scales: Review of the Current State of Research Using the Example of Barite ($BaSO_4$). *ACS Earth and Space Chemistry*:DOI: 10.1021/acsearthspacechem.1c00055.

Wetzel, Maria, Thomas Kempka, and Michael Kühn (2020a). Digital Rock Physics Approach to Simulate Hydraulic Effects of Anhydrite Cement in Bentheim Sandstone. *Advances in Geosciences* 54:33–39. DOI: 10.5194/adgeo-54-33-2020.

Wetzel, Maria, Thomas Kempka, and Michael Kühn (2020b). Hydraulic and Mechanical Impacts of Pore Space Alterations within a Sandstone Quantified by a Flow Velocity-Dependent Precipitation Approach. *Materials* 13(14):3100. DOI: 10.3390/ma13143100.

Wetzel, Maria, Thomas Kempka, and Michael Kühn (2021). Diagenetic Trends of Synthetic Reservoir Sandstone Properties Assessed by Digital Rock Physics. *Minerals* 11(2):151. DOI: 10.3390/min11020151.

Wiersberg, T., A. Seibt, and M Zimmer (2004). *Gas-Geochemische Untersuchungen an Formationsfluiden Des Rotliegend Der Bohrung Groß Schönebeck 3/90*. Scientific Technical Report STR04/03. GeoForschungsZentrum, pp. 153–170.

Witherspoon, P. A., J. S. Y. Wang, K. Iwai, and J. E. Gale (1980). Validity of Cubic Law for Fluid Flow in a Deformable Rock Fracture. *Water Resources Research* 16(6):1016–1024. DOI: 10.1029/wr016i006p01016.

Wolfgramm, M. and A. Seibt (2008). Zusammensetzung von Tiefenwässern in Deutschland und ihre Relevanz für geothermische Anlagenteile. *DGK*. DGK. Karlsruhe, Germany, pp. 503–516.

Wolfgramm, Markus (2002). Fluidentwicklung und Diagenese im Nordostdeutschen Becken - Petrographie, Mikrothermometrie und Geochemie stabiler Isotope. Halle: Martin-Luther-Universität Halle-Wittenberg.

Wolfgramm, Markus (2020). *Personal Communication*. Landesamt für Umwelt, Naturschutz und Geologie Mecklenburg-Vorpommern.

Wolfgramm, Markus, Johannes Birner, Gerhard Lenz, and Frank Hoffmann (2012). Erfahrungen Bei Der Säurestimulation Geothermaler Aquifere Und Anlagen. *DGK*. DGK.

Wolfgramm, Markus, Kerstin Rauppach, and Andrea Seibt (2009). Langfristige Betriebsführung Und Monitoring Geothermischer Anlagen in Deutschland. *DGK*. DGK.

Wolfgramm, Markus, Kerstin Rauppach, and Peter Seibt (2008). Reservoir-Geological Characterization of Mesozoic Sandstones in the North German Basin by Petrophysical and Petrographical Data. *Zeitschrift für Geologische Wissenschaften* 36(4/5):249–265.

Wolfgramm, Markus, Kerstin Rauppach, and Kirstin Thorwart (2011a). Mineralneubildungen Und Partikeltransport Im Thermalwasserkreislauf Geothermischer Anlagen Deutschlands. *Zeitschrift für Geologische Wissenschaften* 39(3/4):213–239.

Wolfgramm, Markus, Kirsten Thorwart, Kerstin Rauppach, and Juliane Brandes (2011b). Zusammensetzung, Herkunft Und Genese Geothermaler Tiefengrundwässer Im Norddeutschen Becken (NDB) Und Deren Relevanz Für Die Geothermische Nutzung. *Zeitschrift für Geologische Wissenschaften* 39(3/4):173–193.

Wolfgramm, Markus et al. (2011c). Rasterelektronenmikroskopische Untersuchungen von Barytkristallen Nach Fällung Aus Salinarem Modell-Geothermalwasser – Zur Reduzierung von Barytscaling in Geothermischen Anlagen. *DGK*. DGK.

Wolfram|Alpha (2021). *Wolfram|Alpha: Making the World's Knowledge Computable*. URL: https://www.wolframalpha.com (visited on 10/23/2021).

Zarrouk, Sadiq J., Blair C. Woodhurst, and Chris Morris (2014). Silica Scaling in Geothermal Heat Exchangers and Its Impact on Pressure Drop and Performance: Wairakei Binary Plant, New Zealand. *Geothermics* 51:445–459. DOI: 10.1016/j.geothermics.2014.03.005.

Zhen-Wu, B.Y. et al. (2016). Experimental Determination of Barite Dissolution and Precipitation Rates as a Function of Temperature and Aqueous Fluid Composition. *Geochimica et Cosmochimica Acta* 194:193–210. DOI: 10.1016/j.gca.2016.08.041.

Zimmermann, Günter, Inga Moeck, and Guido Blöcher (2010). Cyclic Waterfrac Stimulation to Develop an Enhanced Geothermal System (EGS)—Conceptual Design and Experimental Results. *Geothermics* 39(1):59–69. DOI: 10.1016/j.geothermics.2009.10.003.

Zotzmann, Jörg et al. (2021). A Fibre-Optical Method for Monitoring Barite Precipitation at High Pressure/High Temperature Conditions. *Applied Geochemistry* 127:104906. DOI: 10.1016/j.apgeochem.2021.104906.

Zuber, Philipp (2021). *Personal Communication*. Ruhr-Universität Bochum.

List of Publications

Journal Publications

Tranter, Morgan, Marco De Lucia, and Michael Kühn (2021a). Barite Scaling Potential Modelled for Fractured-Porous Geothermal Reservoirs. *Minerals* 11(11):1198. DOI: 10.3390/min11111198.

Tranter, Morgan, Marco De Lucia, and Michael Kühn (2021b). Numerical Investigation of Barite Scaling Kinetics in Fractures. *Geothermics* 91:102027. DOI: 10.1016/j.geothermics.2020.102027.

Tranter, Morgan, Marco De Lucia, Markus Wolfgramm, and Michael Kühn (2020b). Barite Scale Formation and Injectivity Loss Models for Geothermal Systems. *Water* 12(11):3078. DOI: 10.3390/w12113078.

Tranter, Morgan, Ferry Schiperski, Johannes Zirlewagen, and Traugott Scheytt (2017). Hydraulic Linkage of a Storm Water Tank to a Karst Spring (Gallusquelle). *Grundwasser* 22(1):55–62. DOI: 10.1007/s00767-016-0346-8.

Tranter, Morgan, Maria Wetzel, Marco De Lucia, and Michael Kühn (2021d). Reactive Transport Model of Kinetically Controlled Celestite to Barite Replacement. *Advances in Geosciences* 56:57–65. DOI: 10.5194/adgeo-56-57-2021.

Conference Proceedings

De Lucia, Marco, Morgan Tranter, and Michael Kühn (2021). Acceleration of Reactive Transport Simulations with Data-Driven and Hybrid Physics-Artificial Intelligence Surrogates. Goldschmidt2021. Virtual: European Association of Geochemistry. DOI: 10.7185/gold2021.5922.

Tranter, Morgan, Marco De Lucia, and Michael Kühn (2020a). Barite Scaling in Fractures Simulated with Nucleation and Crystal Growth Kinetics. EGU General Assembly Conference. Online. DOI: 10.5194/egusphere-egu2020-417.

Tranter, Morgan and Michael Kühn (2019a). Geochemical Modelling of Barite Scalings in Geothermal Systems. 29. Doktoranden-Treffen FH-DGGV. Munic, Germany.

Tranter, Morgan and Michael Kühn (2019b). Geochemical Modelling of Sulfate Scalings in Geothermal Systems. 10th Geothermal PhD Day. Potsdam, Germany.

Tranter, Morgan and Michael Kühn (2020). Baryt Fällungspotenzial Modelliert Für Niedrigenthalpie Geothermieanlagen. Der Geothermiekongress. Online.

Tranter, Morgan and Michael Kühn (2021). Numerical Investigation of Barite Scaling Kinetics in Fractures and Their Impacts on Well Injectivity. Der Geothermiekongress. Online.

Tranter, Morgan, Maria Wetzel, Marco De Lucia, and Michael Kühn (2021c). Reactive Transport Model of Kinetically Controlled Celestite to Barite Replacement. EGU General Assembly Conference. Online. DOI: 10.5194/egusphere-egu21-9832.

Software Publications

Tranter, Morgan (2021). *Phreeqsim*. Version 0.3.0. Zenodo. DOI: 10.5281/ZENODO.5482132.

Selbstständigkeitserklärung

Hiermit erkläre ich, Morgan Alan Tranter, dass ich als Autor der vorliegenden Dissertation mit dem Titel *Numerical quantification of barite reservoir scaling and the resulting injectivity loss in geothermal systems*, die Arbeit selbstständig und ohne unerlaubte Hilfe angefertigt habe.

Ferner versichere ich, keine anderen als die angegebenen Quellen und Hilfsmittel benutzt zu haben. Alle Ausführungen, die anderen Schriften wörtlich oder inhaltlich entnommenen wurden, sind als solche kenntlich gemacht. Die vorliegende Arbeit wurde in keinem anderen Promotionsverfahren angenommen oder abgelehnt.

Potsdam, 20. September 2022